Modern Day Temperature Field, Central Graben, North Sea: Investigation of Conduction and Fluid Advection

A Thesis submitted for the degree of Doctor of Philosophy

by

Campbell George Fleming B.Sc. (University of Strathclyde)

Department of Geology and Applied Geology

University of Glasgow

March 1996

ProQuest LLC.
789 East Eisenhower Parkway
P.O. Box 1346
Ann Arbor, MI 48106 – 1346

The material presented in this thesis summarises the results of research carried out between October 1991 and March 1996 in the Department of Geology and Applied Geology, University of Glasgow, under the supervision of Gary D. Couples and R. Stuart Haszeldine.

This study is based on my own independent research and any previously published or unpublished results of other researchers used in this thesis has been given full acknowledgement in the text.

Campbell G. Fleming

March 1996

We certify that Campbell Fleming has undertaken the bulk of the work involved in this thesis, specifically data collation and analysis, and computer modelling. We have assisted with advice and help of a general, technical, conceptual nature, as would be expected in the course of normal Ph.D. supervision. Campbell Fleming has written the thesis himself, and is responsible for the content.

Gary D. Couples

R. Stuart Haszeldine

Acknowledgments

I am particularly grateful to Grant Garven for the use of his modelling package OILGEN, without which this project would not have been possible. Thanks also go to the Radian Corporation for use of CPS3. Temperature data supplied by Robertson Research International Ltd and seismic sections provided by British Petroleum Plc were also invaluable.

Special thanks go to Gill Scott of Robertson Research for her initial interest in this project and her help in obtaining the temperature data, the keystone to this project, and to Christian Hermanrud for his views and advice on the accuracies of temperature data in the early days of my research.

I am indebted to Gary Couples and Stuart Haszeldine for their unwavering support and guidance during my studentship.

My thanks also go to Karen Carder, and my family for their support without which I may never have completed my work, and to friends within and outwith the department who have been both my social and emotional crutches for too long.

NERC studentship GT4/91/GS/50 is most gratefully acknowledged.

Abstract

The purpose of this project is to define the modern subsurface temperature field of the central North Sea, and to develop a phenomenological explanation based on conduction and fluid-advective processes. The source of subsurface information is corrected bottom-hole temperatures (BHT's) from thirty wells located within the Central Graben and its flanking areas.

Temperature-depth patterns reveal considerable variability (24.6 to 44.6°C/km for the preferred method of calculation) which is further highlighted by 2-D contour plots of temperatures. The temperature pattern consists of both a long-wavelength, positive temperature anomaly (LWA) which is centred on the graben axis, and, superimposed upon it, a number of short-wavelength, high amplitude positive temperature anomalies (SWA's) which are 5-15 km in half-wavelength and up to 40°C in magnitude.

Computer modelling shows that conduction may account for the shape of the LWA, if there is a decrease in basal heat flow (from 70 to 65 mWm^{-2}) across the graben from west to east. SWA's, however, remain un-explained even by localised high thermal conductivity features such as salt domes. Models of fluid-advection consider both regional and local scale flows. Regional, topographically-driven fluid flow does not influence the temperature regime of the graben, but it provides a significant volume of fluid to the base of the sedimentary pile. Regional-scale convection in the Permian aged strata is an alternative explanation (compared to decrease in heat flow) for the cooler temperatures in the eastern end of the profile (LWA). No regional-scale fluid flow process is capable of producing the SWA's. Localised fluid flow associated with faults, including convective fluid flows within fault zones, can produce SWA's like those observed, with temperature anomalies of up to 50°C formed at realistic sediment and fault permeabilities. The fluid-flow models assume normally-pressured conditions and thus are very conservative. The release of overpressure within the Central Graben may be a more likely mechanism for causing such flows .

List of Contents

List of Figures

Chapter 1

Chapter 2

Chapter 3

Chapter 4

Chapter 5

Chapter 6

List of Tables

Chapter 2

Chapter 3

Chapter 4

Chapter 5

Chapter 6

CHAPTER 1

INTRODUCTION

In this chapter I describe the rationale for the project undertaken here, and I outline some of the key contributions which set the stage for this research. The specific aims of this project are also outlined, and a brief plan of the thesis is given.

1.1 Temperature Distribution in Basins

It is extremely important to understand the subsurface temperature regime of oil producing or exploration areas. Temperature affects many aspects of petroleum systems, including ancient source rock maturity calculations (Goff, 1983; Ungerer et al., 1990), and temperature-dependent diagenetic reactions (Wilkinson et al., 1992). Estimates of downhole temperature are also important for estimating the effects of present-day temperature gradient on the actual drilling of wells. Thus, both the present temperature state, and the history of temperature variation, are subjects of interest.

The research reported here avoids any palaeo-temperature calculation arguments by restricting its focus to the present-day. It seeks to identify the heat-transfer processes which are, or have recently been, active in the central North Sea region. Although I am cognisant of the possibility that similar heat-transfer mechanisms may have operated in the North Sea in the geological past, I keep my focus in the present, and leave the historical extrapolation of my results to others.

1.2 Previous Work

1.2.1 *Temperature Studies in the North Sea*

Compilations and analyses of present-day subsurface temperatures have been carried out in the North Sea by Carstens and Finstad (1981), Oxburgh and Andrews-Speed (1981) and Andrew-Speed et al. (1984). These studies indicate a significant variability in the subsurface temperature distribution. Andrews-Speed et al. (1984) identify regional variations in the heat-flow, and they argue that topographically-driven fluid flow arising from the Norwegian land mass may be part of the explanation of the thermal state in the Central Graben. Carstens and Finstad (1981) also suggest the involvement of migrating fluids in controlling the distribution of modern temperatures in the Viking Graben (in their case, the migration of fluids up faults). By contrast, other modelling studies conclude that the present-day temperature distributions can be readily explained without the involvement of rapidly migrating fluids (Viking Graben; Hermanrud et al (1990), Danish Basin; Yu et al (1995)).

1.2.2 *Thermal Effects of Fluid Flow*

In studies from around the world conduction has long been considered to be the dominant, or even the only heat transfer mechanism in sedimentary basins (Jessop and Majorowicz, 1994). However, a number of studies have shown that advection of heat by moving groundwaters can significantly modify the conductive temperature regime in sedimentary basins. Moving groundwaters within sedimentary basins can have effects on temperature (Bethke, 1986; Garven, 1989; Person and Garven, 1989; Deming et al, 1992; Le Carlier et al, 1994), petroleum migration (Tóth, 1980), and the occurrence or genesis of mineral deposits (Garven, 1985). Recent overviews

of the development of basins involving fluid migration (Garven, 1995; Jessop and Majorowicz 1994) describe some of the major advances made in understanding fluid flow proccesses and their effects.

Among others, Garven and Freeze (1984), Burrus et al. (1992) and Deming (1992), have shown that groundwater flow driven by topography/gravity can have significant thermal effects. For the central North Sea the Norwegian mainland may provide the drive for a similar fluid flow regime (Fig. 1.1). The thermal effects of convective fluid flow also have the potential to alter the thermal regime. Le Carlier (1994) has shown that in the Rhine Graben, regional convective fluid flow has a major effect on not only the temperature, but that it influences petroleum migration, and it has implications for the maturity of source rocks in the graben. Overpressure release and subsequent vertical fluid migration has been shown to have significant thermal effects, along with obvious effects on the migration of petroleum (Grauls and Baleix, 1994). The area selected for this study, the Central Graben (Fig. 1.1), has thick sequences of clastic sediments (Kent, 1975) that are, in part, highly overpressured (Gaarenstroom, 1992; Darby et al. 1996a and 1996b).

1.3 Research Objectives

The North Sea is an extensively explored basin with an abundance of high quality data. This region provides a convenient site to evaluate the modern thermal budget of a late stage rift-basin. The study is intended to assess the relative contributions of the various heat-transfer processees, and to establish the physical controls on them.

The specific objectives of this research are:

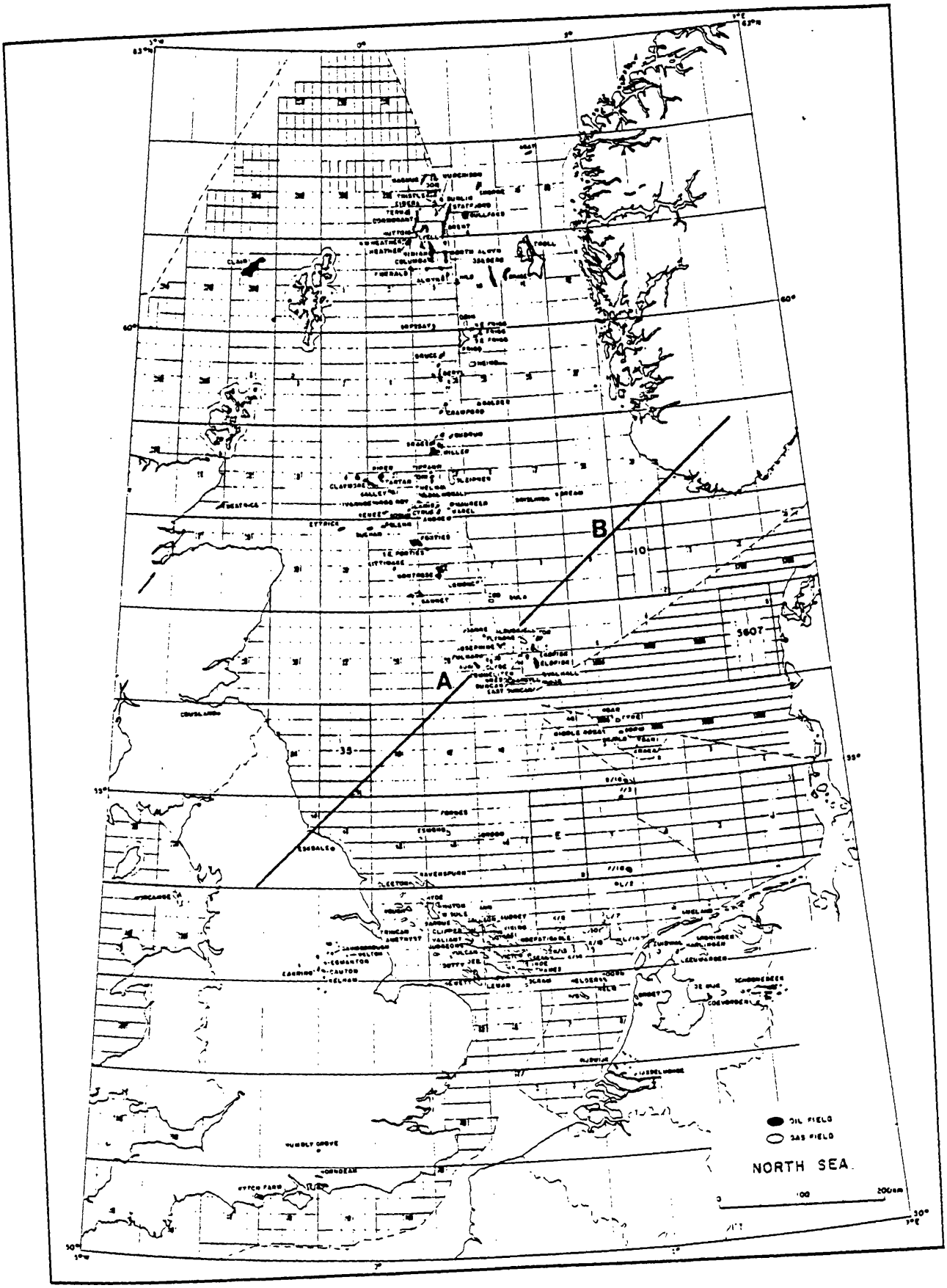

Figure 1.1 - Line of section for temperature study and finite-element models. Section line runs from the Pennines in England, to Norway, and is 800 km in length. The temperature study area, across the Central Graben, lies between points A and B (approximately). Base-map reproduced from Brooks and Glennie (1986).

- Define the present day temperature field across the Central Graben along a representative 2-D section (Fig. 1.1).

- Evaluate the contribution of conductive heat transfer to the present-day temperature field.

- Determine the role of regional fluid flow in transferring heat within the Central Graben.

- Determine the role of localised fluid flow in creating local-scale temperature anomalies.

- Discuss the implications of the present-day processes identified in this study for the thermal state of basins.

1.4 Plan of Thesis

The next chapter (Chapter 2) deals with the corrected bottom-hole measured temperature data obtained from Robertson Research International Ltd. I attempt to define as closely as possible the modern temperature field across the Central Graben along a given line of section. Having established temperature profiles across the Central Graben I attempt (in Chapter 3) to fit a conductive model to those profiles using finite-element modelling.

The conductive temperature model does **not** account fully for all the observed local variability of the temperature profiles. Therefore, Chapters 4 and 5 examine the hypothesis that another main heat transfer agent is

important within this sedimentary basin - fluid advection. This is approached in two stages.

First, in Chapter 4, I assess the potential of regional fluid flow mechanisms to alter the temperature field of the Central Graben. Again using finite-element models, I evaluate the effects of topographically-driven (gravity-driven) and regional convective fluid flows. These regional mechanisms are unable to account for all of the localised temperature anomalies revealed by the temperature profiles described in Chapter 2.

Chapter 5 assesses the thermal potential of localised fluid flow processes -- namely, small-scale convection, and fluid flow within fault or fracture zones -- in a Central Graben setting. These processes are capable of providing an explanation for all of the anomalous temperature features observed within the Central Graben.

I discuss the mechanisms responsible for such fluid flow processes, and the likelihood of each process, in Chapter 6. My conclusions are presented in Chapter 7.

CHAPTER 2

CENTRAL GRABEN TEMPERATURE STUDY

2.1 Introduction

2.1.1 *Aims*

In this chapter the aim is to define and characterise the present-day temperature field in a 2-D section across the Central Graben. The area investigated extends from the Mid-North Sea High, crosses the Auk field and continues north-east across the Norwegian Sector of the Central Graben (Fig. 2.1). The subsurface temperature data used in this investigation is derived from information supplied by Robertson Research International Ltd.

2.1.2 *Summary*

Using corrected bottom-hole temperatures (BHT's) temperature gradients are calculated for characteristic settings within the Central Graben. On a regional basis, wells located within the platform areas (i.e. rift shoulders) indicate lower temperature gradients (33.9±1.3°C) than do those located within the terrace and deep graben areas (36.7±0.9°C, and 35.5±1.5°C, respectively). On a local basis, temperature gradients calculated from individual wells further demonstrate local variability (gradients ranging from 20.1 - 51.5°C/km or 24.6 - 44.6°C/km, depending on the method of calculation). If all wells are plotted together the "average" gradient is 36.23±0.6°C/km.

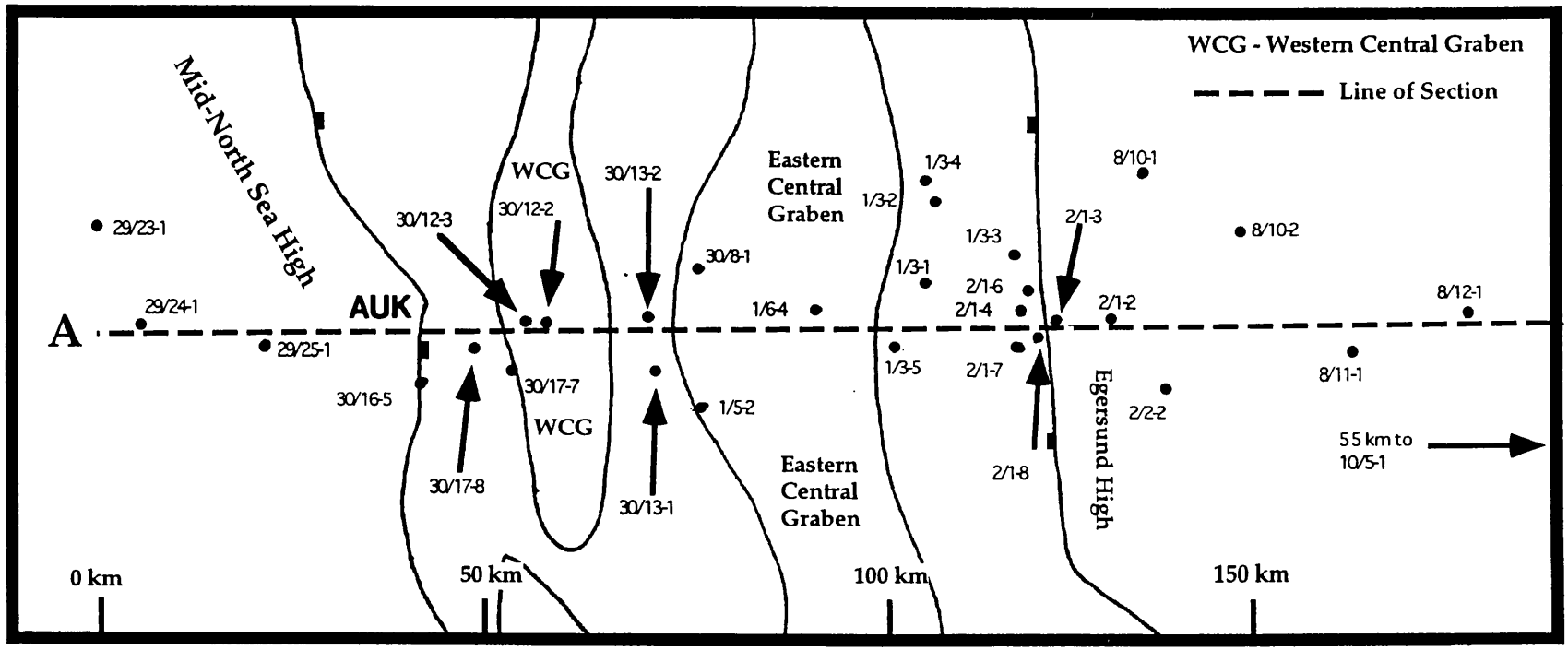

Figure 2.1 - Location of wells used in the temperature study of the Central Graben and flanking areas. Reference point for distance in all temperature plots (Figures 2.6, 2.7, 2.9 and 2.10) is well 29/23-1 (0 km). Point A corresponds to A in Figure 1.1.

Two methods were used to construct 2-D contour plots of the original BHT data. First the temperature data was hand contoured and subsequently gridded in a computer mapping software package (Fig. 2.6). The second method produces an entirely computer-generated contour plot of the original data set (Fig. 2.7); it is similar to the hand contoured plot in overall geometry. Both contour plots display a long-wavelength positive temperature anomaly centered on the graben, with superimposed short-wavelength, high-amplitude, positive temperature anomalies.

I interpolated temperatures at selected depths from the individual-well temperature plots; from these interpolated values I created two further displays (across the Central Graben). The most important of these was a simple line plot of the interpolated data which shows the temperature variations (Fig. 2.9). The second a computer generated contour plot of the interpolated data (Fig. 2.10). These plots again display both long-wavelength and short-wavelength temperature anomalies. The line plot of interpolated data is the primary reference for the thermal modelling reported in subsequent chapters.

2.2 Temperature Data Corrections

Downhole temperatures are obtained from thirty wells (see Table 2.1; Appendix 1) distributed along or close to a SW-NE profile (see Fig. 2.1 for well locations). These thirty wells contain multiple data points of sufficient quality to construct meaningful temperature/depth profiles, and it is this set of information, spanning both lateral and depth co-ordinates, that is used to define the present-day temperature field across the Central Graben.

The process of drilling a well disturbs the temperature field near the well-bore due to differences between the usually cooler drilling fluid and

the *in situ* rocks. Measured bottom-hole temperatures (BHT's) must, therefore, be adjusted so as to better approximate the true ambient temperature (Hermanrud 1988; Hermanrud et al 1990). The temperature data used in this study have been corrected (by Robertson Research International Ltd.) for this transient effect, as is normal practice, using either Horner plots (as described by Fertl & Wichmann 1977) or modified empirical graphs (Neglia 1979; Carstens & Finstad 1981). In cases where several temperatures are recorded at the same depth or within approximately 10 m of each other in the same well, and when these data are poorly correlated, the temperature reading with the longest 'time since circulation' (i.e. the temperature reading which has had longest time to re-equilibrate) is taken as being closest to equilibrium, and the other temperatures near that depth are disregarded.

The accuracy of BHT data is a much-debated subject. Several different methods have been suggested for calculating the true formation temperature (Lachenbruch & Brewer 1959; Cao et al 1988; Hermanrud 1988). According to Carstens & Finstad (1981), in favourable situations (e.g. good quality control at the time of the logging run) the uncertainty involved with BHT's can be reduced to as little as ±3°C, but they admit that in unfavourable cases, the errors may be as much as ±10°C or even greater. Friche and Schlosser (1980) suggest that uncertainties of ±5°C must be expected for BHT data, while Hermanrud et al (1990) states that logging derived temperatures result in a standard deviations between 8 and 10°C.

I have no independent means of determining the quality of the data acquisition stage for each recorded temperature. Therefore the uncertainties associated with the temperature data used in this study may be as low as ±3°C or may be as much as ±10°C or greater for data corrected by modified empirical graphs. BHT data corrected by the Horner Plot method will result in temperatures with a standard deviation of ±8.3°C (Hermanrud 1990). The

specific method of temperature correction is not known for most of the temperature data supplied by Robertson Research International Ltd., so in order to be as conservative as possible I assume the larger uncertainties (±10°C).

2.3 Temperature-Depth Relationships

In this study, investigation of the temperature field is carried out using only corrected BHT data (as described in the previous section). The wells used in this study (Fig. 2.1) are projected onto the 2-D profile perpendicular to the line of section (projection distances are shown in Table 2.1). Initially I calculate 1-D temperature gradients on a regional average basis, and subsequently on a well-by-well basis. This approach reveals variations in temperature gradient related to structural setting.

2.3.1 *Regional 1-D Temperature Gradients*

A temperature gradient approach is used in order to limit the interpreted errors caused by spurious temperature values. There is no way to guarantee the accuracy of any single data point; however, it may be that the interpretation is improved by fitting a line through several data points. A plot of all corrected temperature data against depth for the Central Graben gives a best-fit temperature gradient of 36.23±0.6°C/km (Fig. 2.2). However, when the temperature data is separated into three geographically-defined sub-areas -- platform, terrace, and deep graben (Fig. 2.1) according to PESGB (1990) -- local differences are apparent. The three areas have calculated temperature gradients of 33.9±1.3, 36.7±0.9, and 35.5±1.5°C/km respectively, with the platform area having the lowest overall temperature gradient (Fig. 2.3). These gradients compare favourably with the 33°C/km temperature

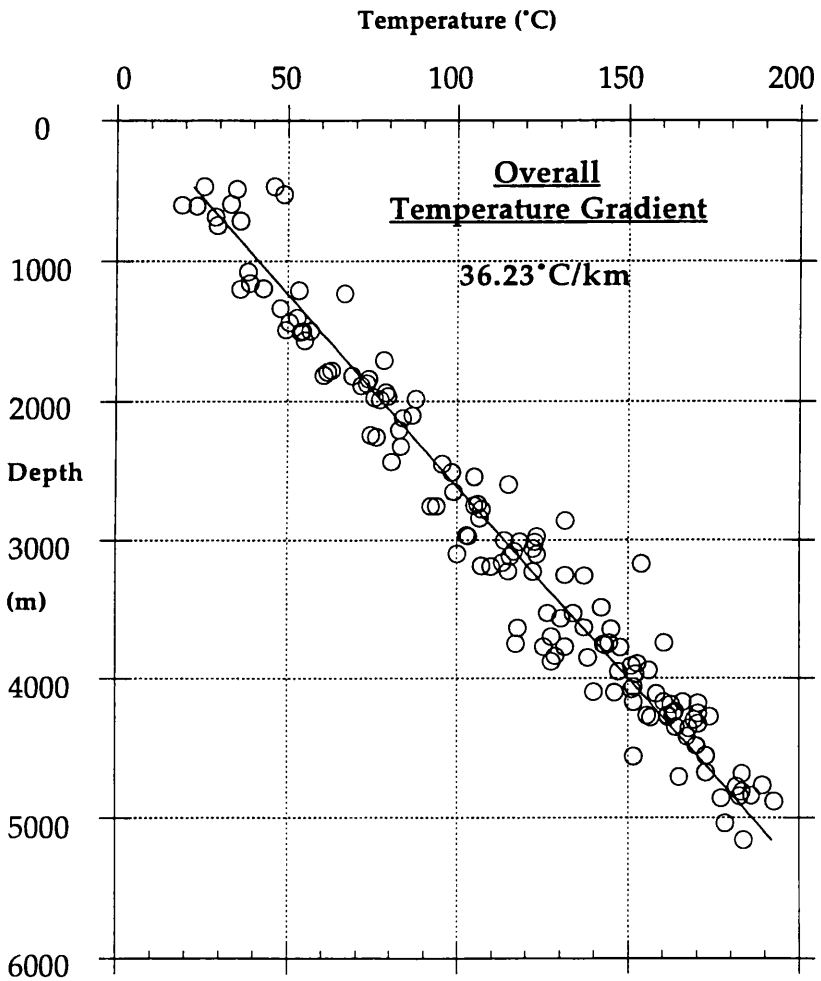

Figure 2.2 Subsurface temperature data and overall temperature gradient, for the Central Graben study area.

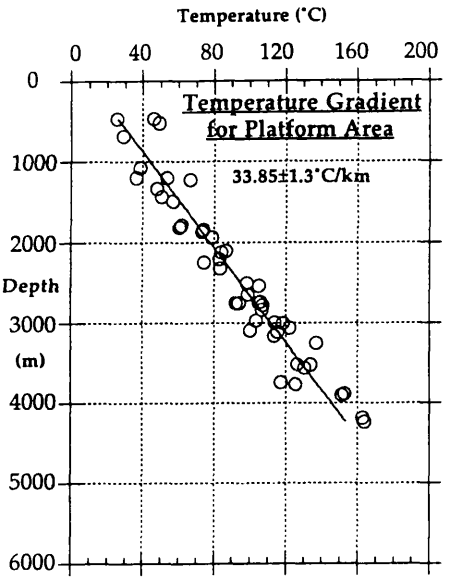

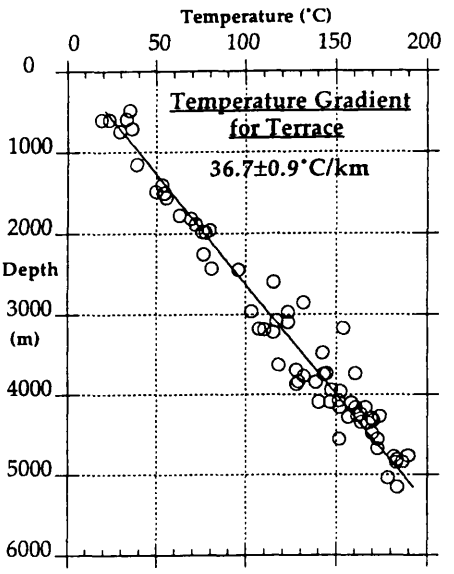

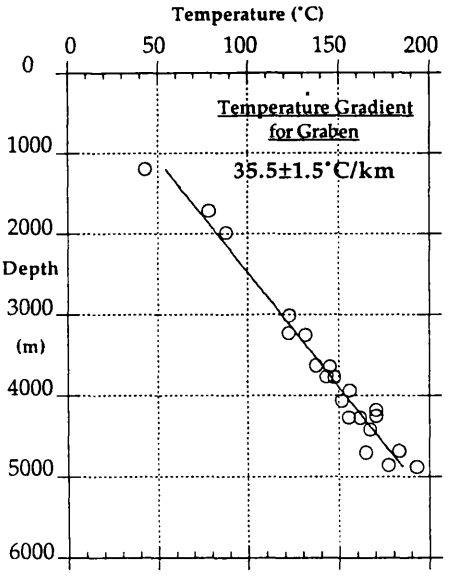

Figure 2.3

Calculated temperature gradients for platform, terrace and graben regions.

gradients reported by Barnard & Bastow (1991); Thomas et al (1985) report generally 30-35°C/km (Viking Graben) and 37.5°C/km or greater in the axis of the Central graben; and Carstens & Finstad (1981) deduce an average gradient of 30-35°C/km for studies in the northern North Sea.

Having established that the temperature gradients show variability across structural domains in the North Sea, I now undertake a more detailed study of the temperature data on a well-by-well basis. This more detailed study is undertaken to discover any more-localised variability.

2.3.2 *Well-by-Well Temperature Gradients*

Two methods are used in calculating temperature gradients for an individual well. The first is simply to find a best-fit line through only the available BHT data. In the second method, a surface temperature of 10°C (Harper 1971) is added to the data set in each well (as a single new data point; surface in this case the sea-bed). A best-fit line is then calculated through the revised data.

The first method is prone to suggesting overly high or low temperature gradients, especially where the available data within one well lies within a narrow depth range (see Fig. 2.4) It is still possible that the calculated values represent the actual temperature gradient over that limited depth range. The second method will reduce the problem associated with temperature data lying within a narrow depth range, and provides a more conservative calculated temperature gradient (individual well plots are shown in Appendix 2).

In this study, temperature gradients calculated on a well-by-well basis further demonstrate **local** variability. Table 2.1 shows the calculated overall temperature gradients for the thirty wells used in this Central Graben study. For the two methods (temperatures without and with the assigned surface

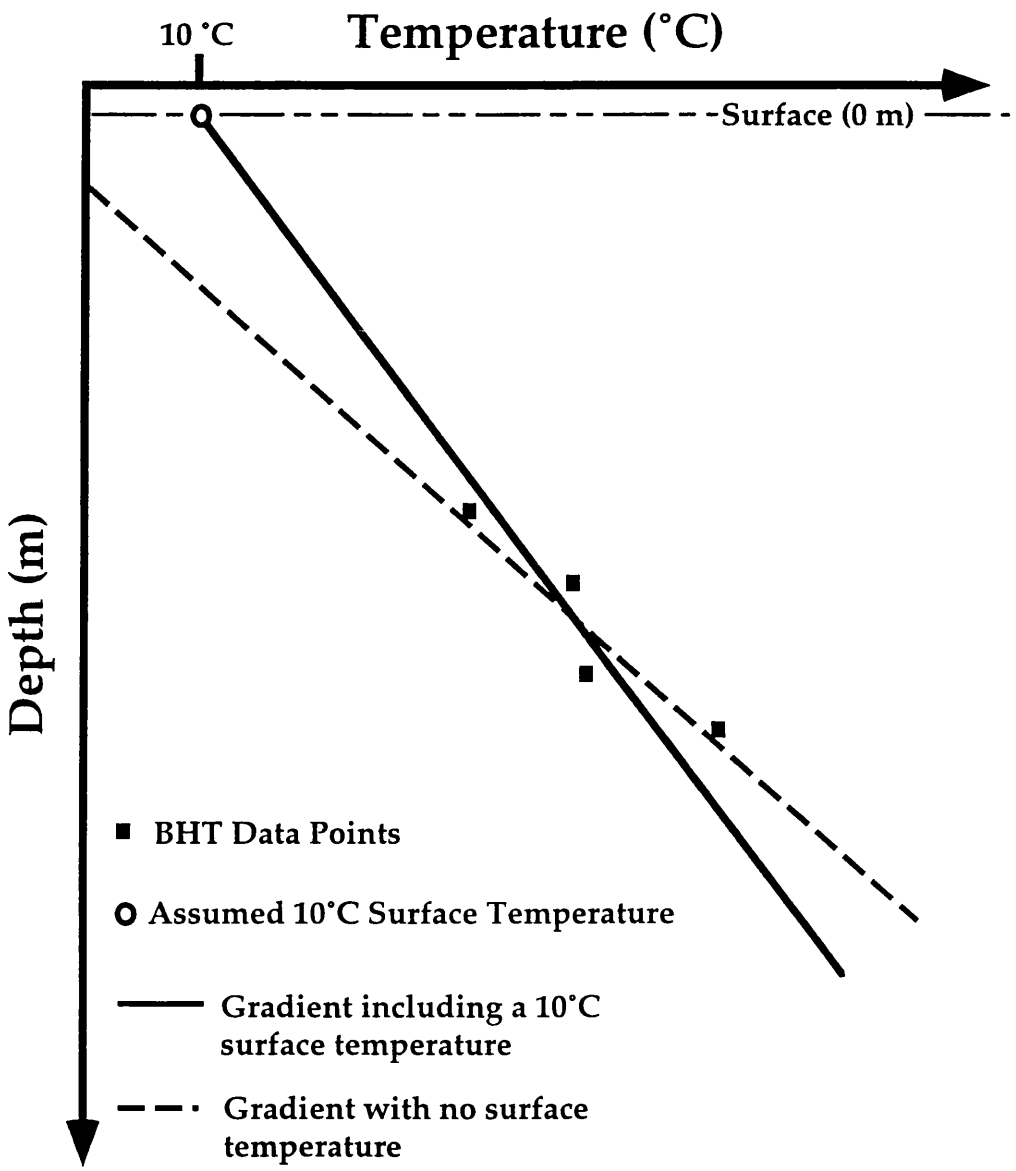

Figure 2.4 Schematic, showing the reduction of error in overall temperature gradient calculations by the addition of a surface temperature of 10°C(where data lies within a narrow depth range).

value), the range in temperature gradient is 20.1 - 51.5°C/km and 24.6 - 44.6°C/km respectively.

Well No.	Temperature Gradient (°C/km) **without** surface temperature	Temperature Gradient (°C/km) **with** surface temperature	Projected Distance (km)	Section Line Distance (km)
29/23-1	20.1	24.6	13	0
29/24-1	36.4	31.1	1	5.5
29/25-1	41.3	34.5	1	21.5
30/16-5	39.3	35.1	7	42
30/17-8	37.5	36.2	2	49
30/17-7	31.4	32.4	5	54
30/12-3	36.2	37.0	1	56.5
30/12-2	31.4	34.1	1	58
30/13-2	44.8	34.1	2	71
30/13-1	40.5	37.0	5	72
1/5-2	41.5	38.6	9	77
30/8-1	34.3	36.1	9	77.5
1/6-4	30.8	36.8	3	93
1/3-5	40.7	37.6	3	103
1/3-1	37.3	36.0	6	106.5
1/3-4	51.5	44.6	19	107
1/3-2	38.8	35.5	17	108.5
2/1-7	33.2	33.5	3	118.5
1/3-3	23.8	36.4	9	119.5
2/1-4	37.2	35.6	3	120.5
2/1-6	35.8	34.8	4	121
2/1-8	34.2	34.6	1	122
2/1-3	33.4	34.6	1	124
2/1-2	29.3	32.5	1	131
8/10-1	36.1	36.3	20	135
2/2-2	32.2	32.6	7	138
8/10-2	Insuff. Data	33.0	12	147.5
8/11-1	32.0	30.5	3	161.5
8/12-1	38.2	35.2	1	176
10/5-1	26.4	29.0	35	235
Min.	**20.1**	**24.6**	**1**	----------
Max.	**51.5**	**44.6**	**35**	----------

TABLE 2.1 - Calculated temperature gradients for the thirty wells used in the Central graben study. (Reference point for distance [in all sections] is well 29/23-1 which is taken to be at the origin)

As expected, temperature gradients calculated without the assumed surface temperature produce a wider range of values than do the calculated gradients which include an assumed surface data point. If these variations in temperature gradient are plotted against distance along the 2-D section (Fig. 2.5), the local variability is made clear. It is concluded that the use of a single (or even regional) temperature gradient for the study area would be an unacceptable means to estimate temperatures at points where measurements are lacking.

2.3.3 *Summary*

An overall temperature gradient for the Central Graben is calculated at 36.23±°C/km (Fig. 2.2). This gradient cannot, however, be reliably applied across the Central Graben. Subdivided plots of temperature gradients determined for platform, terrace, and deep graben areas show regional variability (Fig. 2.3). On a well-to-well basis, local variability of the temperature gradient is even more apparent (Fig. 2.5), with temperature gradients (for the 10°C surface temperature set) showing a range from 24.6 to 44.6°C/km across the graben. The higher values of temperature gradient are confined to the graben area especially the edges of structural highs and the graben edges, with the low values of temperature gradient found mostly on platform areas.

2.4 2-D Temperature Distribution (BHT Data)

Although a considerable range in temperature gradients across the Central Graben has been shown in Section 2.3, the variability of temperatures in two-dimensions is difficult to visualise from gradients

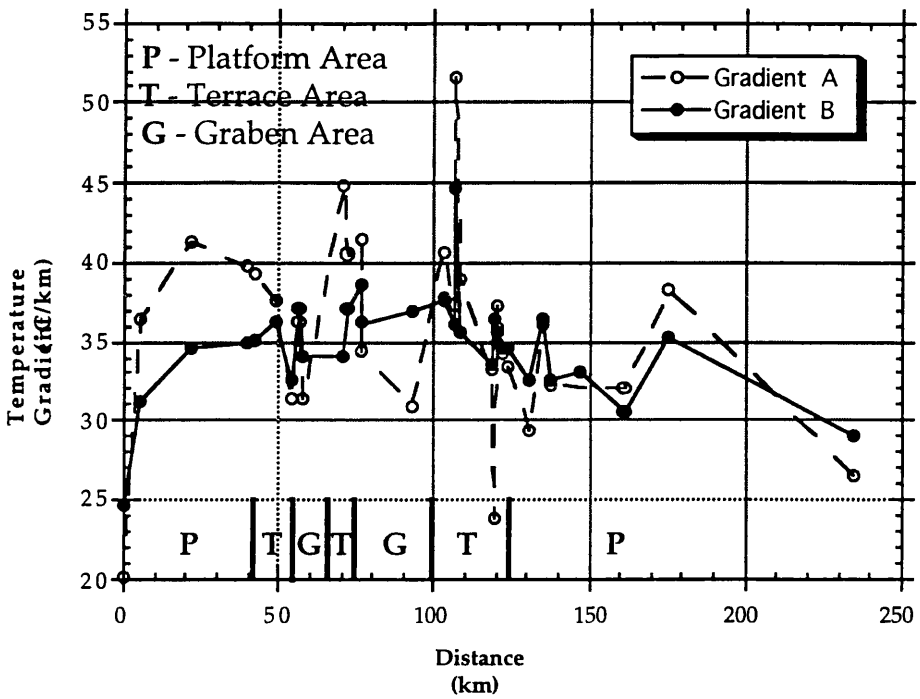

Figure 2.5 - Well-by-well temperature gradient versus distance, for the Central Graben study area showing Platform, Terrace and Graben sub-areas. [Gradient A calculated without an assigned surface temperature. Gradient B with an assigned surface temperature of 10°C.]

alone. To investigate the temperature distribution, both laterally and with depth, temperature contour plots of the original BHT data have been constructed. The reference point for distance in all sections is well 29/23-1 (0 km).

2.4.1 *Hand Contoured BHT Data*

A hand contoured plot of the corrected bottom-hole temperatures was constructed first. The individual contours from this plot are then digitised, and gridded using a computer mapping package, to produce a temperature contour plot (Fig. 2.6; the use of this mapping package permits a direct comparison to other plots introduced later). This plot shows a broad positive temperature anomaly centred over the deep graben most obvious at 3 to 5 km depth. The anomaly has a half-wavelength of approximately 120 km, and becomes more poorly defined towards the north-east. In subsequent discussion this regional variation in temperature is referred to as the long-wavelength anomaly (LWA). Superimposed onto this long-wavelength anomaly are several, significant (up to 40°C), narrow (<10 km half-wavelength), positive temperature variations. These are subsequently referred to as short-wavelength anomalies (SWA's). The main SWA's are documented in Table 2.2. The magnitude of these temperature anomalies (SWA's) range from 10 to 15°C (in well 30/12-3) to up to 40°C (in well 1/3-4), and their wavelengths range from 5 to 15 km.

2.4.2 *Computer Contoured BHT Data*

To provide an alternative interpretation, the same original corrected BHT data (Appendix 1) was gridded and contoured using a computer mapping package (Fig. 2.7). A broad, positive LWA is once again apparent

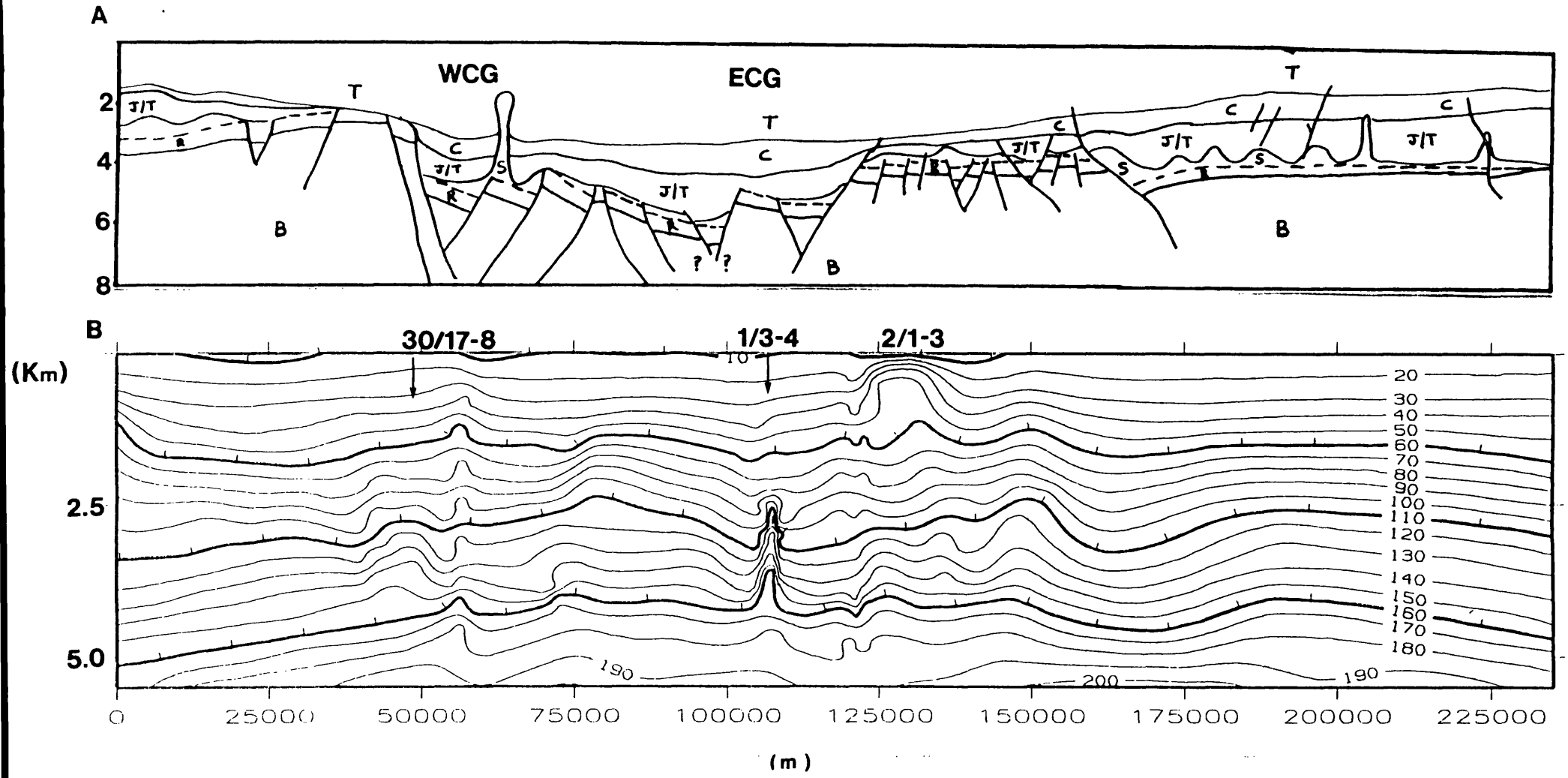

Figure 2.6 - Cross-section and hand-contoured plot of BHT temperature data. [A] KEY to cross-section; WCG - western Central Graben, ECG - eastern Central Graben, T - Tertiary, C - Cretaceous, J/T - Jurassic/Triassic, S - Zechstein Salt, R - Rotliegend and Pre-Permian Sediments and B - Basement. [B] Hand contoured plot of BHT data. Temperature contours are from 10 to 200 °C in 10°C intervals. NOTE vertical scale difference between [A] and [B]. Horizontal scale is in metres and significant well locations labelled.

on this plot (centred at approximately 90-100 km); it is especially obvious in that part of the plot between 110 and 210°C. The temperature field across the Central Graben also shows significant localised variability; there is a 40°C anomaly at approximately 110 km (Well 1/3-4); there is both a shallow (<2 km), 40°C temperature anomaly centred on 125 km (Wells 2/1-2 and 2/1-3), and a 20°C anomaly at depth in the same location; several other, smaller (up to 20°C) temperature anomalies occur at locations between 50 and 75 km on the section line.

Well Number	Distance (km)	Approximate Magnitude of SWA (°C)	Approximate Wavelength (km)	Comments
30/17-8	49	20	10	Terrace (West Central Graben)
30/12-3	56.5	10-15	5	Deep Graben (West Central Graben)
1/3-4	107	up to 40	5	Terrace (East Central Graben)
2/1-2 and 2/1-3	124-131	30	15	Edge of Egersund High. Temperatures in excess of 40°C at 500m depth.
8/10-2	147.5	15	10	Egersund High /Norwegian-Danish Basin

TABLE 2.2 - Location, magnitude and wavelength of significant SWA's observed in the temperature contour plot (hand-contoured) across the Central Graben (see Fig. 2.6).

The area of greatest temperature variability lies between approximately 100 and 140 km along the section line (Fig. 2.7). Of the thirty wells used in the study, thirteen (43%) lie within this 40 km stretch of the section. The remaining 57% of wells account for 195 km of the sections length. This relationship suggests that a greater density of well data within

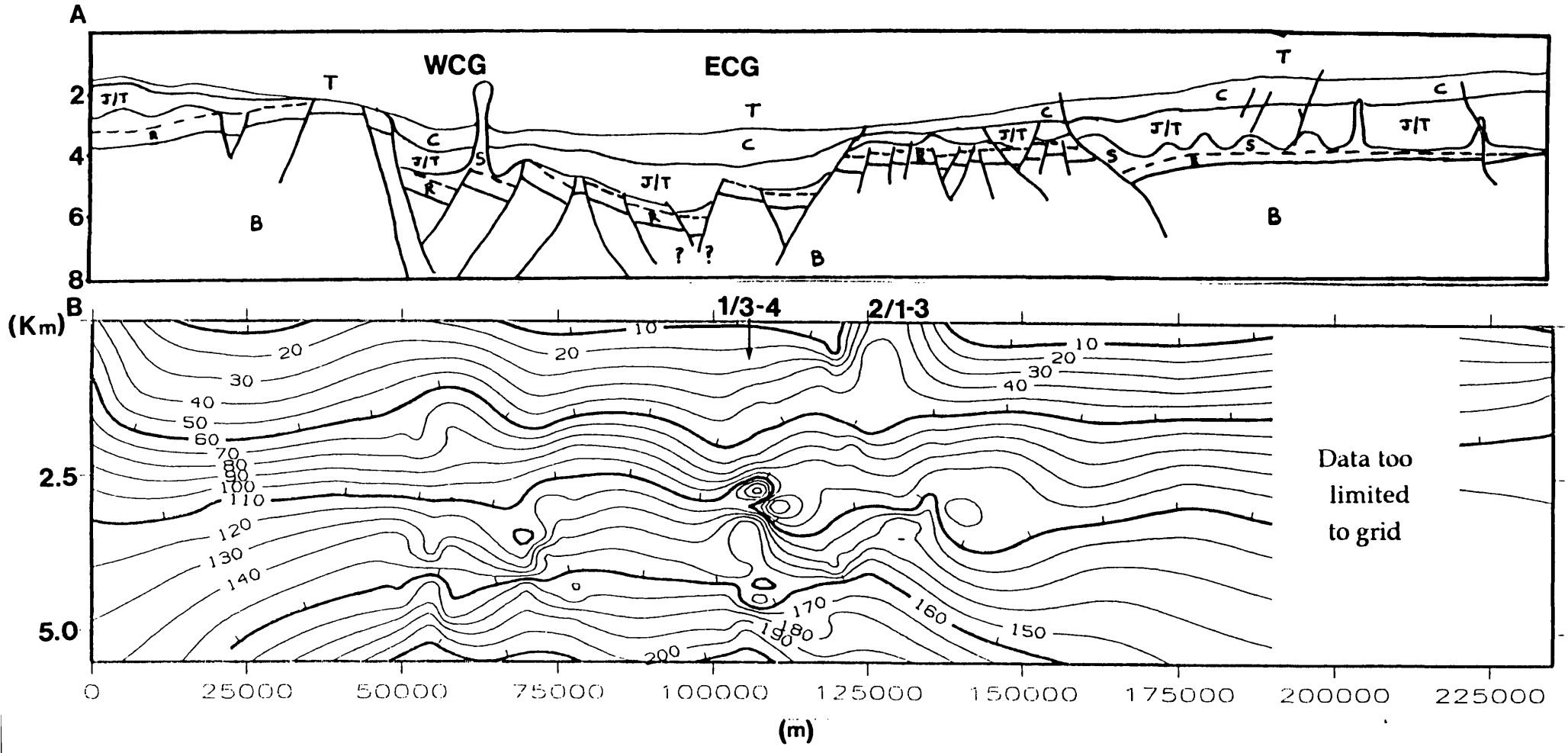

Figure 2.7 - Cross-section and computer-generated contour plot of BHT temperature data. [A] KEY to cross-section; WCG - western Central Graben, ECG - eastern Central Graben, T - Tertiary, C - Cretaceous, J/T - Jurassic/Triassic, S - Zechstein Salt, R - Rotliegend and Pre-Permian Sediments and B - Basement. [B] Temperature contours are from 10 to 200 °C in 10°C intervals. NOTE vertical scale difference between [A] and [B]. Horizontal scale is in metres and significant well locations are labelled.

the section would reveal even greater variability than is apparent from Figure 2.7.

2.4.3 *Discussion*

The two methods of contouring the original corrected BHT data are independent. However, both contour plots display broadly similar patterns of variability in temperature across the graben (compare Figs. 2.6 and 2.7).

Each contour plot shows a LWA centered on the graben. This broad anomaly is less well-defined in the hand-contoured plot (Fig. 2.6) than in the computer generated one (Fig. 2.7). The small-scale complexity of SWA's are also present within both contour plots, and their magnitudes range up to 40°C. The SWA's identified in the hand-contoured contour plot are compatible in location, magnitude and wavelength to those identified within the computer-generated plot. The identification of positive temperature anomalies at the present-day on long and short wavelength scales is robust to different interpretations. I conclude that the variability of temperature is therefore "real".

2.5 Depth-Specific Temperature Profiles (Interpolated Data)

2.5.1 *Interpolation of Data*

The well-by-well temperature gradients are used to interpolate temperatures at selected depths across the graben. This set of interpolated-temperature data is used in the construction of line and contour plots.

Two sets of temperature gradients have previously been calculated. The first, without an assumed surface temperature (Fig. 2.5), is prone to indicating overly high or low temperature gradients (and by implication,

high or low temperatures away from the actual data points). For this reason I use the more conservative set of temperature gradients with a 10°C assumed surface temperature (Fig. 2.5), to interpolate the temperatures at 2, 3, 4 and 5 km depths within each well.

The method of using the overall temperature gradient of a well to interpolate to desired depths will reduce the influence of anomalous data points (Fig. 2.8). In some wells (Figure 2.8A) the interpolated data points are close to the BHT data trend anyway. However the influence of anomalous (or unusual) data points is reduced by the use of an overall temperature gradient method (Fig. 2.8 B).

2.5.2 *2-D Interpolated Profiles*

Using these interpolated temperatures for each location, I construct depth-specific temperature profiles across the Central Graben (Fig. 2.9). These reveal the maximum and minimum *interpolated* temperatures at 2, 3, 4, and 5 km depths (Table 2.3), as well as the spatial variability in temperature across the Central Graben. Again, a positive LWA is evident, and it has superimposed positive SWA's.

The main SWA's of these profiles are documented in Table 2.4. These SWA's range in magnitude from 10 to 15°C (in well 30/17-8), to between 35 and 40°C (in well 1/3-4), and they have wavelengths ranging from <5 km to approximately 15 km. Only one of the observed temperature anomalies occurs within the deep graben. The majority occur in "terrace" areas, and at the margins of major structural features (horst/graben edges, see Fig. 2.9).

2.5.3 *Interpolated Data - Computer Contoured*

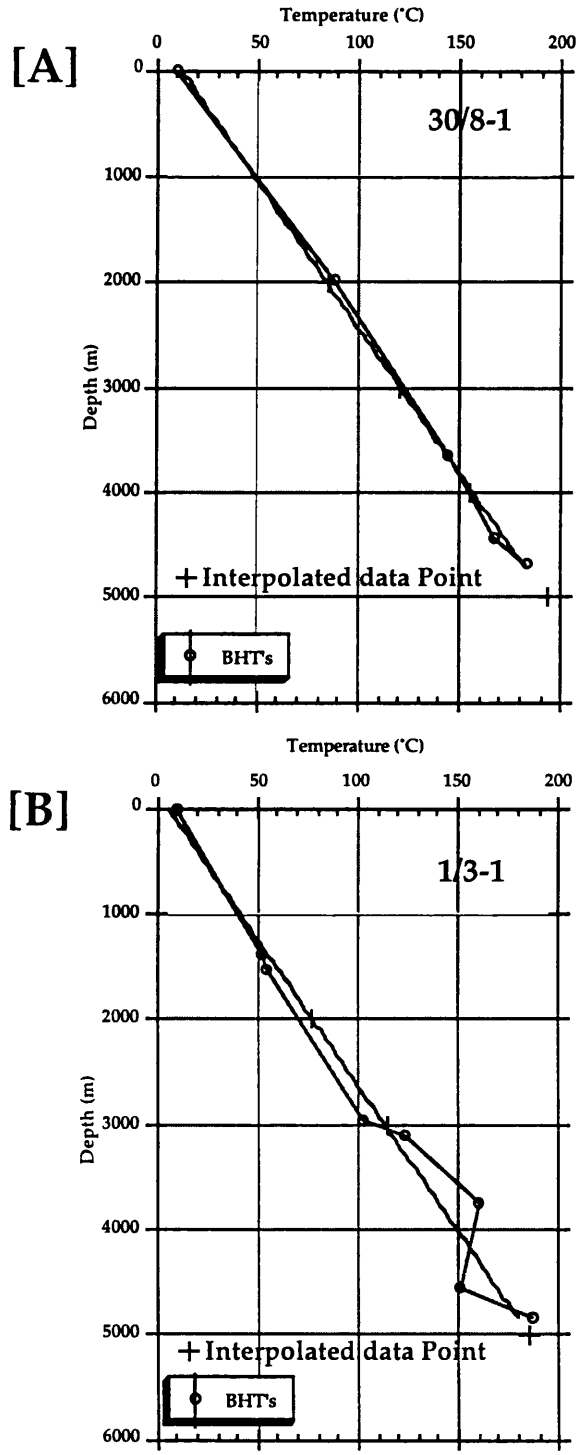

Figure 2.8 Examples of data interpolation from wells 30/8-1 and 1/3-1. In the case of [A] the interpolated temperatures are close to the best-fit temperature gradient. However, in case [B] the interpolated points smooth the effect of the irregular temperature gradient.

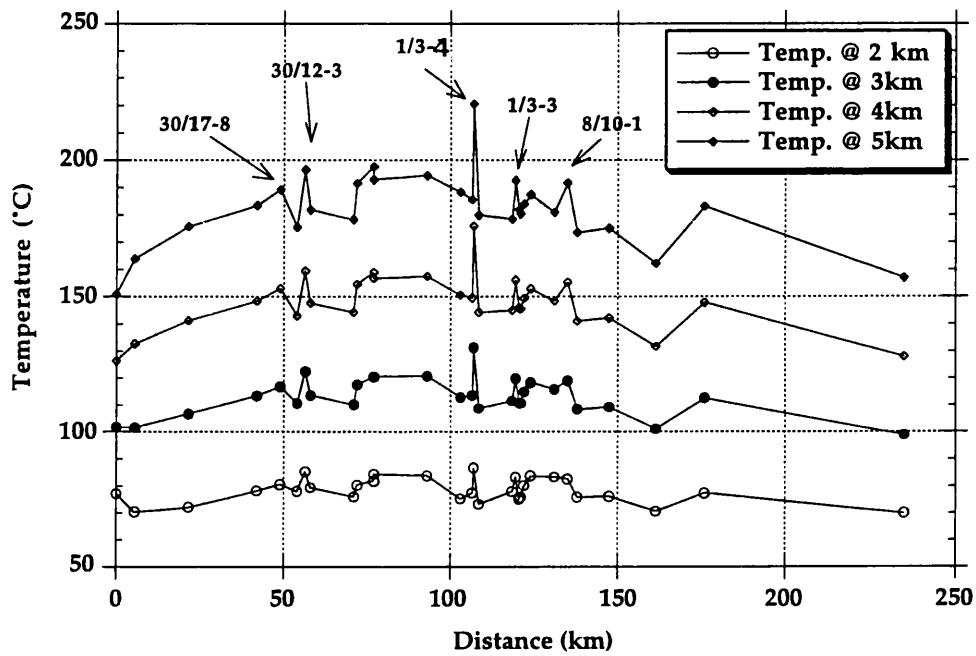

Figure 2.9 Interpolated-temperature profiles (calculated from temperature gradients) at 2, 3, 4, and 5 km depths across the Central Graben.

	Interpolated Temperatures		
Depth (km)	Lowest (°C)	Highest (°C)	Range (°C)
2 km	70.0	86.6	16.6
3 km	98.9	131.3	32.4
4 km	126.4	175.9	49.5
5 km	150.9	220.6	69.7

TABLE 2.3 - Calculated temperature variation at 2, 3, 4 and 5 km depths for the interpolated temperature data.

Well Number	Distance (km)	Approximate Magnitude of SWA (°C)	Approximate Wavelength (km)	Comments
30/17-8	49	10-15	10	Terrace (West Central Graben)
30/12-3	56.5	20	5	Deep Graben (West Central Graben)
1/3-4	107	35-40	5	Terrace (East Central Graben)
1/3-3	119.5	15	5	Graben Edge (East Central Graben /Egersund High)
8/10-1	135	12-20	10	Egersund High

TABLE 2.4- Location, magnitude and wavelength of significant SWA's observed in the interpolated temperature profiles across the Central Graben (see Fig. 2.9).

The interpolated data set is gridded and contoured in the computer mapping package (the identical procedure to that of Section 2.42, but using the smoothed interpolated data). The resulting plot (Fig. 2.10) shows much less variability than the hand or computer contoured BHT data (Figs. 2.6 & 2.7). This is partly to be expected as Figure 2.10 constitutes the most conservative projected temperature field for the Central Graben. It has undergone smoothing through the use of a best-fit temperature gradient as described above, and a further smoothing through the gridding and contouring process. However, Figure 2.10 still shows a positive LWA,

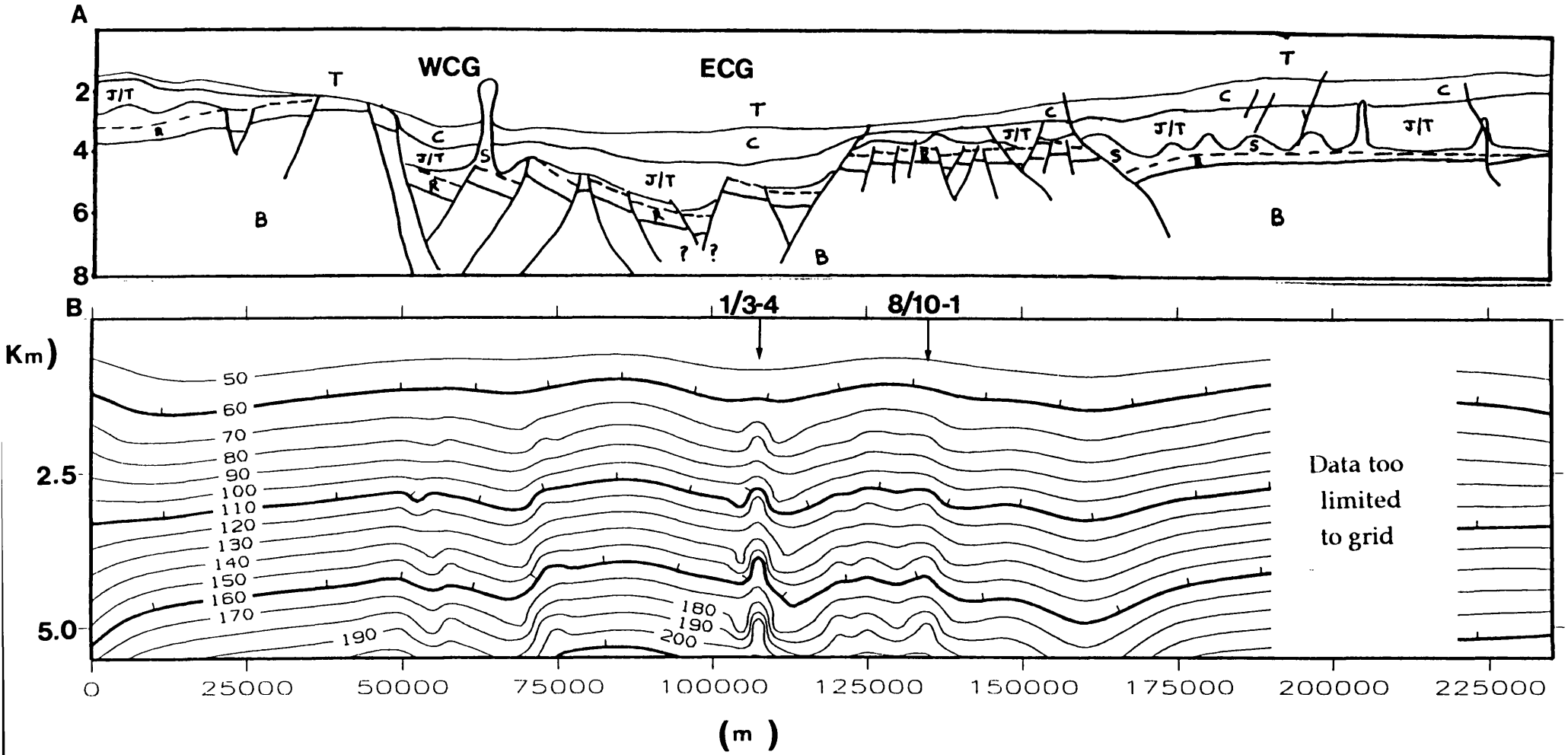

Figure 2.10 - Cross-section and computer-generated contour plot of interpolated-temperatures. [A] KEY to cross-section; WCG - western Central Graben, ECG - eastern Central Graben, T - Tertiary, C - Cretaceous, J/T - Jurassic/Triassic, S - Zechstein Salt, R - Rotliegend and Pre-Permian sediments and B - Basement. [B] Temperature contours are from 10 to 200 °C in 10°C intervals. NOTE vertical scale difference between [A] and [B]. Horizontal scale is in metres and significant well locations labelled.

although of shallower amplitude than those revealed by the other methods described previously. Wells 1/3-4 (107 km) and 8/10-1 (135 km) also show small SWA's, of approximately 15 and 10°C in magnitude respectively and of approximately 5 km half-wavelength.

2.5.4 *Summary*

The depth-specific line profiles of the interpolated data (Fig. 2.9), reveal SWA's of between 10 and 40 °C in magnitude, with maximum wavelengths of 10 km (Table 2.4). The variability of temperature across the graben at 2 to 5 km depths is documented in Table 2.3 and shows variability of up to 69.7°C at 5 km depth.

The computer generated contour plot of the interpolated data is undoubtedly the most conservative of the temperature plots, however, it too displays a broad LWA and two SWA's, located at 110 and 135 km, of 30°C and 10°C, respectively.

Thus, the LWA and SWA's persist through all data smoothing processes and alternative contouring exercises. These anomalies are consequently believed to be robust and not to be artefacts of poor data.

2.6 Comparison of BHT Data Plots to Interpolated Data Plots

Of the four 2-D temperature plots (Figs. 2.6, 2.7, 2.9 & 2.10) the computer generated contour plot of interpolated temperature data (Fig. 2.10) shows the least variability in temperature. Although it has the least overall variability, it still shows some of the temperature features observed in **all** other temperature plots -- namely SWA's located at wells 1/3-4 (107 km) and 8/10-1 (135 km), and an overall elevation of temperatures towards the centre of the graben (LWA).

The 2-D contour plots of the original corrected BHT data (Figs. 2.6 & 2.7 -- A hand-contoured plot, and a computer-generated BHT contour plot, respectively) show much wider variability in temperatures with depth and distance than does the computer-generated contour plot of interpolated-temperature data (Fig. 2.10). Comparing Figures 2.6 and 2.7, the overall geometries are essentially the same but the computer-generated BHT data plot shows more localised complexity.

The main features of both the hand contoured BHT data plot (Fig. 2.6), and the interpolated profiles (Fig. 2.9), indicate a LWA with superimposed SWA's. However, in the hand-contoured plot, the LWA is less well defined in the Norwegian sector (due to a lack of BHT data from depths in excess of 3 km, see Appendix 1). The temperature ranges for the two profiles differ considerably for the shallow portion of the graben (Table 2.5). At 2 km depth, the hand-contoured plot shows almost twice the temperature range of the interpolated-temperature profiles. This is due to the shallow temperature anomaly observed in wells 2/1-2 and 2/1-3 (Fig. 2.6, Table 2.2) which is "smoothed" by the best-fit line method adopted for the calculation of individual temperature gradients. The ranges in temperature at 3 and 4 km depths are in broad agreement for both profiles. At 5 km the lack of deep BHT measurements on the graben margins does not allow a meaningful estimation of the temperature range for the hand-contoured profile.

The short-wavelength anomalies observed in both the interpolated and hand-contoured profiles are closely comparable, each set having ranges in magnitude, and wavelength, of approximately 10 to 40°C, and 5 to 15 km, respectively (compare Tables 2.2 & 2.4). For both profiles, wells 30/17-8, 30/12-3, and 1/3-4 are located at significant SWA positions, with closely compatible magnitudes and wavelengths.

Depth (km)	Temperature Range (°C) Interpolated	Temperature Range (°C) Hand-contoured
2 km	16.6	30.8
3 km	32.4	40.0
4 km	49.5	47.0
5 km	69.7	Limited Data

TABLE 2.5 - Calculated maximum temperature variation at 2, 3, 4 and 5 km depth for interpolated and hand-contoured profiles.

The two remaining **interpolated** anomalies, at wells 1/3-3 and 8/10-1 (Table 2.4), are **not** observed within the hand-contoured profiles. This is because the BHT data in each of these wells falls within a restricted depth range (4 to 5 km, and 2 to 3 km respectively, see Appendix 1) and therefore does not provide a sufficient spread in depth to show any anomaly on the hand contoured plot. Likewise, the temperature anomalies observed in wells 8/10-2 and wells 2/1-2 and 3, within the hand-contoured profiles, are NOT observed in the interpolated profiles as they too occur over a narrow depth range (<1 km) and are "overlooked" by a best-fit line temperature gradient.

The interpolated-temperature profiles will reduce the effects of poor quality data by the interpolation of data points from a best-fit line. They also, however, smooth depth-limited temperature anomalies such as that observed in wells 2/1-2 and 2/1-3 (Figs. 2.6 and 2.7). Therefore, the use of both BHT data plots, and interpolated data plots, is essential in observing all the natural variability, and establishing the robust nature of the LWA and SWA's.

2.7 Conclusions/Observations

2.7.1 *Temperature-Depth Interpretation*

Thirty wells have been used to calculate present-day temperature gradients within the Central Graben. These show local variations, and regional differences from platform, to terrace, and graben areas (Fig. 2.3). When temperature gradients are calculated on a well-by-well basis with an assigned surface temperature, the local variation is even more apparent (Fig. 2.5). A range in temperature gradient occurs across the Central Graben from 24.6 to 44.6°C/km. The well-by-well range in temperature gradient is comparable to that established by Carstens and Finstad (1981) for the northern North Sea: "mean geothermal gradients generally vary between 25 and 40°C/km, higher and lower values being rare."

2.7.2 *2-D Temperature Study*

Several methods of constructing 2-D profiles are utilised in this study of temperatures across the Central Graben. The main observations from these profiles follow:-

- In each case a positive low-amplitude, long-wavelength, positive temperature anomaly is observed, centred on the graben axis (LWA).

- 2-D plots of the corrected BHT data (whether hand-contoured or computer generated) display short-wavelength, positive temperature anomalies (SWA's) of up to 40°C. These SWA's are consistent for both methods used to construct BHT data plots.

- Interpolated data profiles (Fig. 2.9) show SWA's of up to 40°C, and maximum of 10 km wavelength; these are comparable to those observed within the BHT data contour plots.

- A computer-generated contour plot of the interpolated temperature data (the most smoothed and conservative of all the temperature plots) again shows both the LWA and two SWA's of up to 30°C.

- Therefore, for all methods of 2-D temperature profiling, the thirty wells considered display a broad, long-wavelength, positive temperature anomaly (LWA) across the Central Graben, with superimposed, localised temperature highs (SWA's) of, in cases, up to 40°C. These anomalies are considered to be robust and not artefacts of data quality.

Each method of temperature profiling results in slightly different geometries of LWA, and different magnitudes of the superimposed SWA's. However, in each case it is equally true that the subsurface temperature field shows considerable spatial variability. Subsequent chapters assess the possible causes of this variability through both conductive temperature models, and regional and localised fluid flow models. In order to proceed, the relatively conservative interpolated-temperature profiles in Figure 2.9 (the basis for Figure 2.10) have been used as the definitive present-day temperature plot. In reality, as Figures 2.6 and 2.7 show, the temperature field is likely to be significantly more complex.

CHAPTER 3

CONDUCTIVE HEAT TRANSPORT

3.1 Introduction

3.1.1 *Summary*

The present day temperature field in the Central North Sea can be decomposed into a long-wavelength anomaly (LWA), with short-wavelength anomalies (SWA's) superimposed onto it (Chapter 2, Fig. 2.9). In this, Chapter 3, I investigate the contribution of *conductive* heat transport to the observed present-day temperature field to assess whether the observed temperatures are explicable purely in terms of conductive heat transfer. If so, what is the conductive architecture (in relation to basal heat flow, and thermal conductivity of sediments and basement)?

Using numerical models, I show that the LWA can be fully explained by conduction-only processes, i.e. lateral and vertical variation in thermal conductivities, and changes in basal heat flow. The observed LWA can be matched for a basal heat flow ranging between 65 and 70 mWm^{-2}, a basement thermal conductivity of 3.5 $Wm^{-1}°C^{-1}$, and an average sediment thermal conductivity of approximately 2.5 $Wm^{-1}°C^{-1}$, given the geometries of these units as defined by geological studies. However, other models are possible -- radically different geology (unlikely), or advection of heat by fluids (see Chapter 4).

The SWA's observed within the "real" temperature profiles have such narrow wavelengths that only anomalous conduction features (for example, salt pillars or wedges) could produce temperature anomalies of similar wavelengths. However, the temperature anomalies produced by

such salt features are here shown to be of much smaller magnitude than the observed SWA's, and so another explanation is required (see Chapter 4).

3.1.2 *Methodology*

The thermal modelling of the Central Graben is accomplished through the use of the modelling package OILGEN (Garven, 1989) -- a two-dimensional, steady-state/transient, finite element computer code that is capable of simulating both conductive heat transfer and advection of heat by moving groundwaters. The approach adopted in OILGEN is to define up to nine distinct material types from which a model is constructed.

In order to calculate the thermal models, I select a section line that runs from the Pennines in north-east England to southern Norway; it crosses the Mid-North Sea High, the Central Graben, and the Norwegian-Danish Basin (Fig. 1.1), and it has a total length of 800 km. A generalised cross-section Figure 3.1) was constructed from: an interpreted seismic section (line no. 17, provided by British Petroleum plc); public well data (from Robertson Research International Ltd.); in conjunction with cross-sections and isopach maps (Ziegler 1982). This cross-section is discretised into a finite element mesh of 20 rows and 39 columns of quadrilateral elements (Figure 3.2). The geometry of the top of the basement will remain constant throughout the modelling, but the sub-division of the sedimentary fill of the Central Graben may be changed according to the required complexity of a particular model (by assigning material types to each of the elements). However, although the material properties and the number of individual units may change, the mesh remains essentially unchanged throughout modelling.

The main factors affecting the conductive temperature field in this section are the basement thermal conductivity, the distribution of thermal

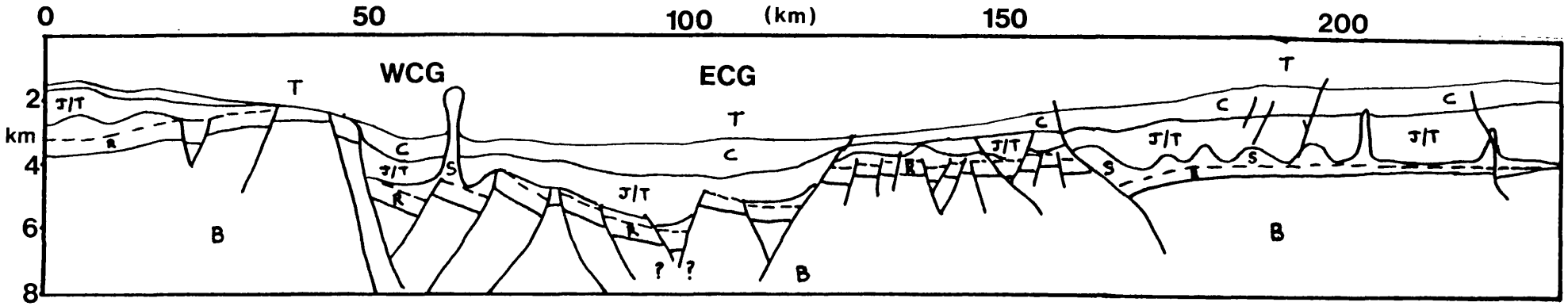

Figure 3.1 - Cross-section created for the Central Graben study area (see text for sources of information; Section 3.1.2). All distances in kilometres. Maximum depth of section 8 km, length of section 235 km (0 km distance corresponds to well number 29/23-1).

KEY to cross-section; WCG - western Central Graben, ECG - eastern Central Graben, T - Tertiary, C - Cretaceous, J/T - Jurassic/Triassic, S - Zechstein Salt, R - Rotliegend and Pre-Permian Sediments and B - Basement.

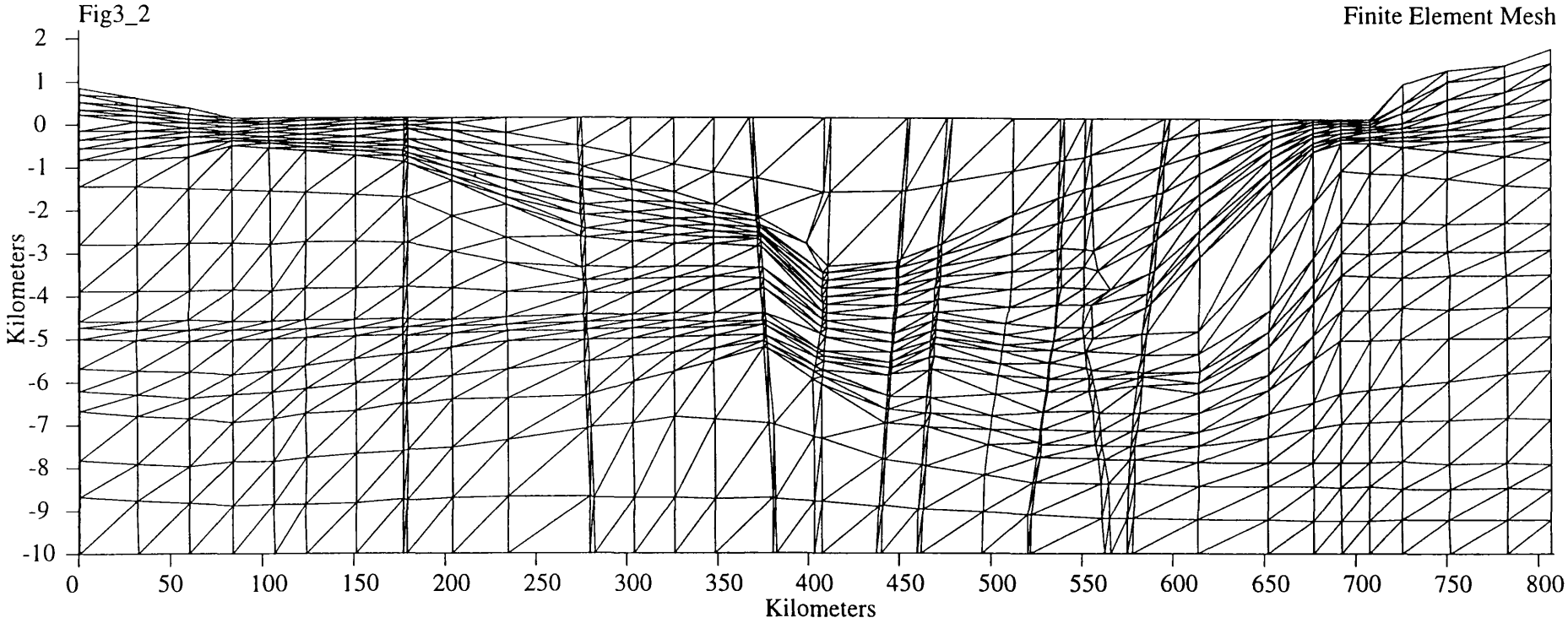

Figure 3.2 - Finite element mesh created from discretized section (Fig. 3.1). Total length of section 800 km, maximum depth of section 10 km (below sea-bed).

conductivity within the basin sediments, and lateral variations in basal heat flow (the sides of the model are insulated, and the top is held constant at 10°C). Published thermal conductivity data for the central North Sea sediments is limited, and basal heat flow and basement thermal conductivity values may be estimated (Evans & Coleman 1974; Del Rey & Hamza 1989; Raffensberger and Garven 1995) but remain essentially unknown. Therefore, it is not possible to create a definitive thermal model of the Central Graben. Instead, using the published data, I establish a likely range for basement and sediment thermal conductivities, and a range for basal heat flow. I use these ranges to undertake sensitivity studies. In the following sections, each of these parameters is investigated in turn, and comparisons are made with the observed temperature profiles (Fig. 2.9), in order to identify a best-fit model.

3.2 Long-Wavelength Anomaly: Effects of Basin Geometry

3.2.1 *Aims*

For a constant basal heat flow, differences in thermal conductivity between basement highs and the adjacent sedimentary fill, and variations in the thermal conductivities of sedimentary units within the basin, will result in changes to the predicted temperature field (Lovering 1936). I here quantify the magnitude of temperature changes in the Central Graben associated with these differences and compare them to the real temperature field (Fig. 2.9).

3.2.2 Basement Highs

To determine the temperature effects of basement vs sediments (e.g. to assess rift margins, and intra-rift highs), I first use a model in which the sedimentary fill of the basin (Carboniferous to Holocene) is treated as one uniform unit ("sediments"), with all pre-Carboniferous rock treated as a second uniform unit ("basement"). The geometry of this "basement high" model (Fig. 3.3) is simplified from the full geological interpretation (Fig. 3.1). The material properties for the "sediments" (thermal conductivity and porosity; Table 3.1) are chosen to encompass the range of measured thermal conductivity values for Central North Sea sediments (Andrews-Speed et al, 1984). The range in thermal conductivity for basement (Table 3.1) is assumed, but is comparable to values tabulated by Raffensberger & Garven (1995), and Del Rey & Hamza (1989). For these models, basal heat flow is held constant at 70 mWm^{-2} (value approximated from Andrews-Speed et al, 1984).

	Thermal Conductivity (mWm^{-2})	ø (%)
Sediments	1.0, 2.0, 2.5, 3.0, 3.5, 4.0, 5.0	5.0
Basement	2.5, 3.5, 4.5	0.01

Table 3.1 - Set of thermal conductivity and porosity values used in "Basement High" models (ø - porosity, sediment thermal conductivity ranges taken from Andrews-Speed et al, 1984).

For each of the estimated values of basement conductivity, I run a suite of simulations using the full range of sedimentary-fill thermal conductivities (Table 3.1; sediment in each case treated as uniform and homogeneous). For each simulation, the full temperature field is calculated for all elements (Fig. 3.4). In order to quantify the difference in temperature (ΔT) between basement highs and the sediments adjacent to them, I extract

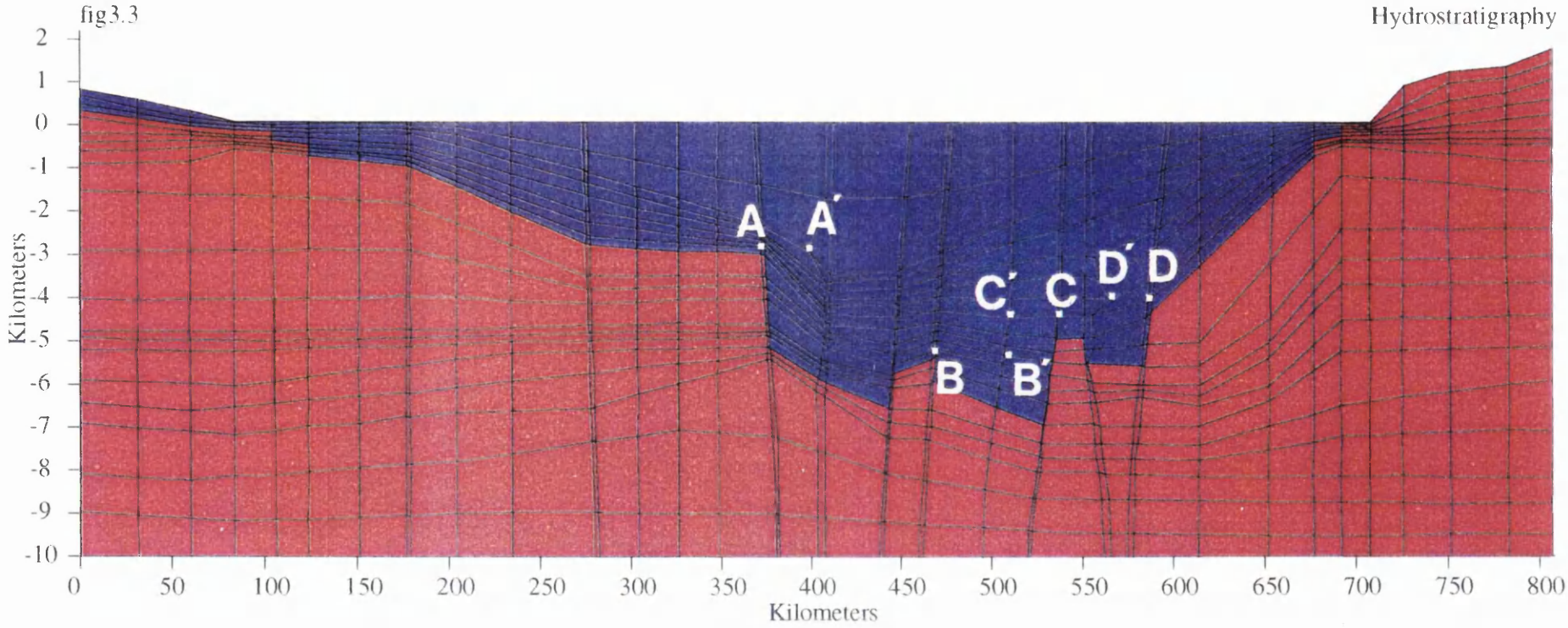

Figure 3.3 - 2-D finite-element section along the line of Figure 1.1. Geometry of basement high models showing basement (red) and sedimentary fill (blue). Temperature changes are monitored at points A to D and A' to D'.

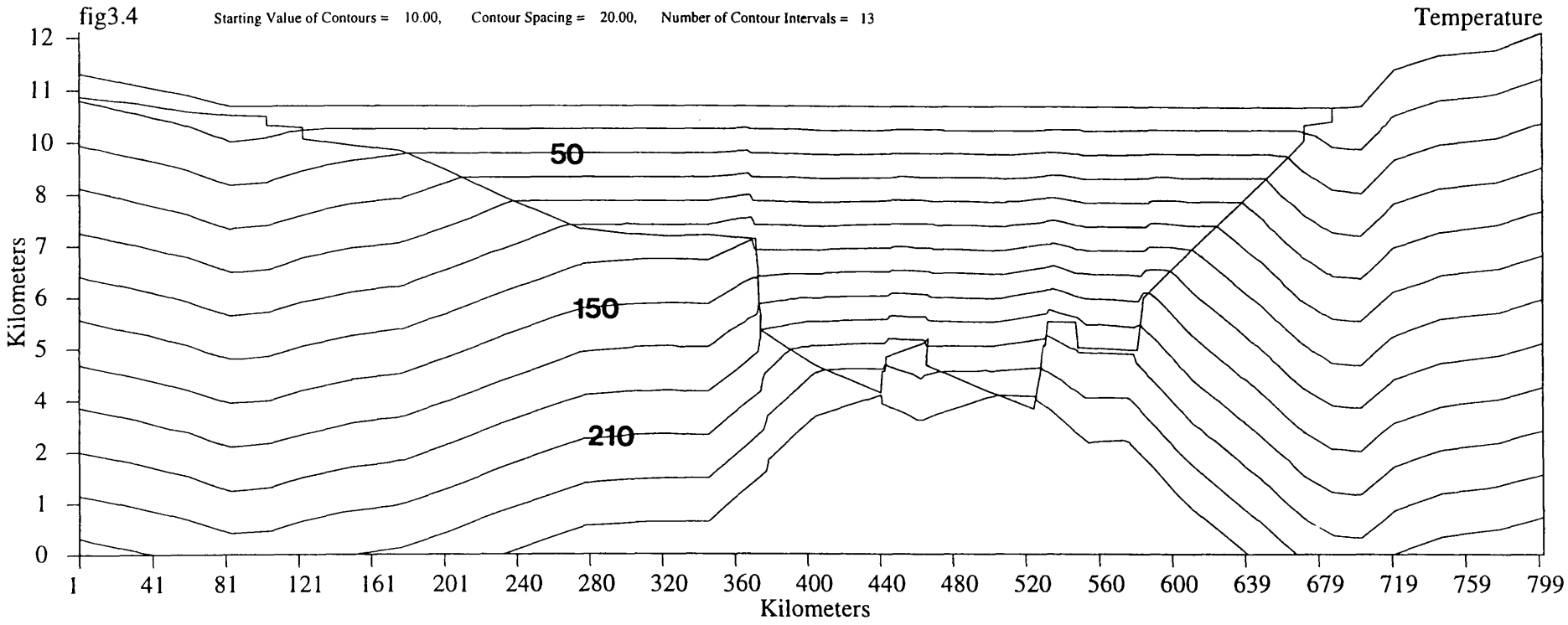

Figure 3.4 - Example of the calculated temperature field for a "basement high" model. Temperature contours are in degrees Centigrade, start at 10 and increase in 20 degrees C intervals. In this model Bsmt = 3.5 Wm*-1C*-1, Sediments = 2.0 Wm*-1C*-1.

the modelled temperature from points A to D and A' to D' (see Fig. 3.3). The unprimed letters refer to points at/on basement highs, and the primed letters denote locations at the same depth but some 10 to 15 km away, and within the sedimentary fill.

I define ΔT as the temperature at A minus the temperature at A', and similarly at the other points ($\Delta T = T_A - T_{A'}$) When I plot ΔT against the average value of conductivity of the sedimentary fill, I find that the temperature anomalies over the basement highs (ΔT) increase with decreasing sediment thermal conductivities (Fig. 3.5). However, only when sediment thermal conductivity values are lower than 2 $Wm^{-1}°C^{-1}$ does ΔT significantly exceed 10°C.

Based on published thermal conductivity values (Andrews-Speed et al, 1984; Fig. 3.6) it is apparent that the average thermal conductivity of the sedimentary fill is probably greater than 2.0 $Wm^{-1}°C^{-1}$. Of all the thermal conductivity measurements made on samples from the Central Graben, only the Tertiary and Carboniferous units record thermal conductivities as low as 2.0 $Wm^{-1}°C^{-1}$, with no measurements below 2.0 $Wm^{-1}°C^{-1}$ (Andrews-Speed et al 1984). Therefore, I subsequently do not give further consideration to sediment conductivities below 2.0 $Wm^{-1}°C^{-1}$. At the other extreme, for the average sediment thermal conductivity to be 5.0 $Wm^{-1}°C^{-1}$, the bulk of the sedimentary pile would have to consist of dolomite, halite and/or anhydrite; such lithologies are not dominant in the basin fill of the Central North Sea (Cayley 1986; Glennie 1990), and in the following discussion, I only consider sediment thermal conductivities of 4.0 $Wm^{-1}°C^{-1}$ or smaller.

Using these high and low limits (4.0 and 2.0 $Wm^{-1}°C^{-1}$), I next consider the effects of different basement thermal conductivities. If ΔT is plotted against basement thermal conductivity, the conductive temperature anomalies over basement highs within the Central Graben range from a

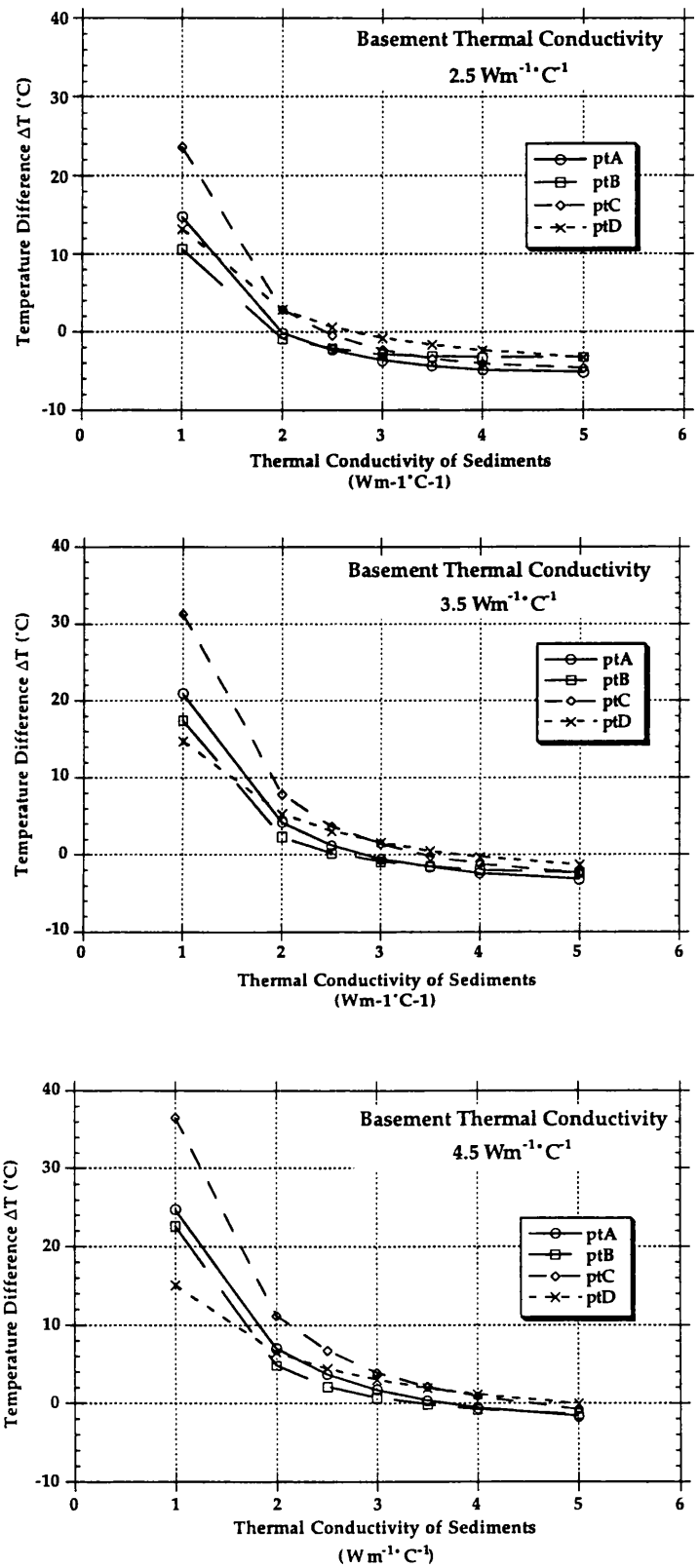

Figure 3.5 Temperature increase over basement highs (locations A, B, C, and D) for basement thermal conductivities of 2.5, 3.5 and 4.5 $Wm^{-1}°C^{-1}$. Each value of basement thermal conductivity is simulated over a sediment thermal conductivity range of 1.0 to 5.0 $Wm^{-1}°C^{-1}$.

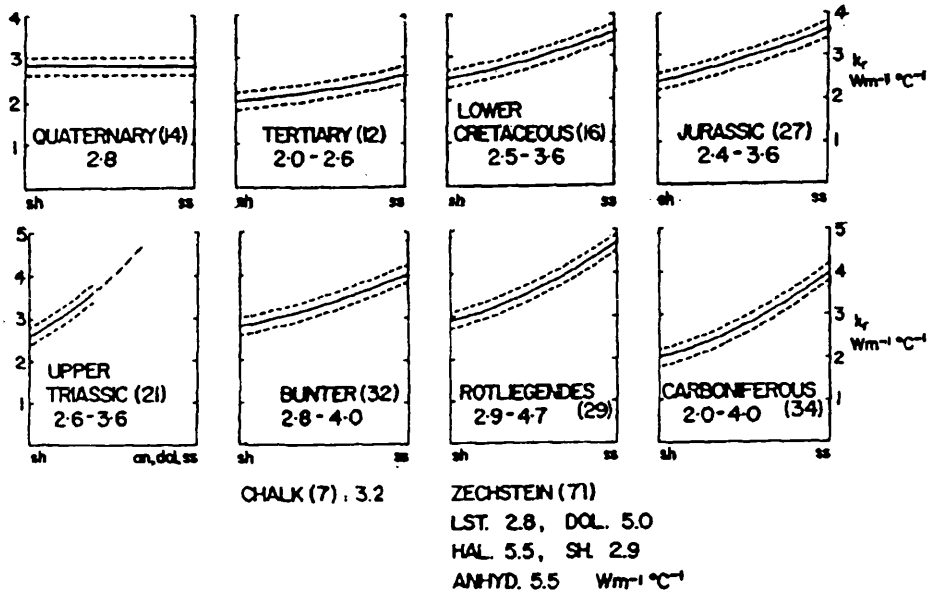

Figure 3.6 - Plots showing thermal conductivity ranges for each major stratigraphic unit of the southern and central North Sea. Dashed lines show margins of error. Number of samples given in parentheses.

Taken from Andrews-Speed et al. (1984).

maximum of ~10°C to essentially nil, or even negative (Fig. 3.7). Based on these modelled results I conclude that the magnitude of conductive temperature anomalies associated with basement highs falls within the range +11°C to -5°C.

Full-model temperature contours for the two *extreme cases* are shown in Figure 3.8. In Case 1 (minimum thermal conductivity of sediments and high basement thermal conductivity) small temperature peaks of 10°C or less are produced, but only at the edges of basement blocks, and a broad (flat topped) LWA is obtained. Case 2 (sediments at maximum thermal conductivity, and low basement thermal conductivity) produces a negative LWA and no substantial temperature peaks. Neither extreme case produces temperature profiles identical to those actually observed by wells (Fig. 2.9). However, Case 1, where the sediments have low conductivity and the basement conductivity is high, produces a LWA that is at least of the right sign. I conclude that the likely conductivity structure is one where basement conductivity is fairly high, and sediment conductivity is, on average, fairly low.

3.2.3 *The Sedimentary Pile*

The preceding section describes results of simple model configurations which constrain the range in both magnitude and shape of temperature anomalies associated with basement highs and especially their edges. I now focus on the temperature effects of variations in thermal conductivity distributions within the sedimentary pile.

In order to keep the complexity of the argument to a minimum, I divide the lithostratigraphy of the basin (Carboniferous to Holocene) into four conductivity units (Table 3.2). Each unit contains stratigraphic groups of similar measured thermal conductivities according to data reported by

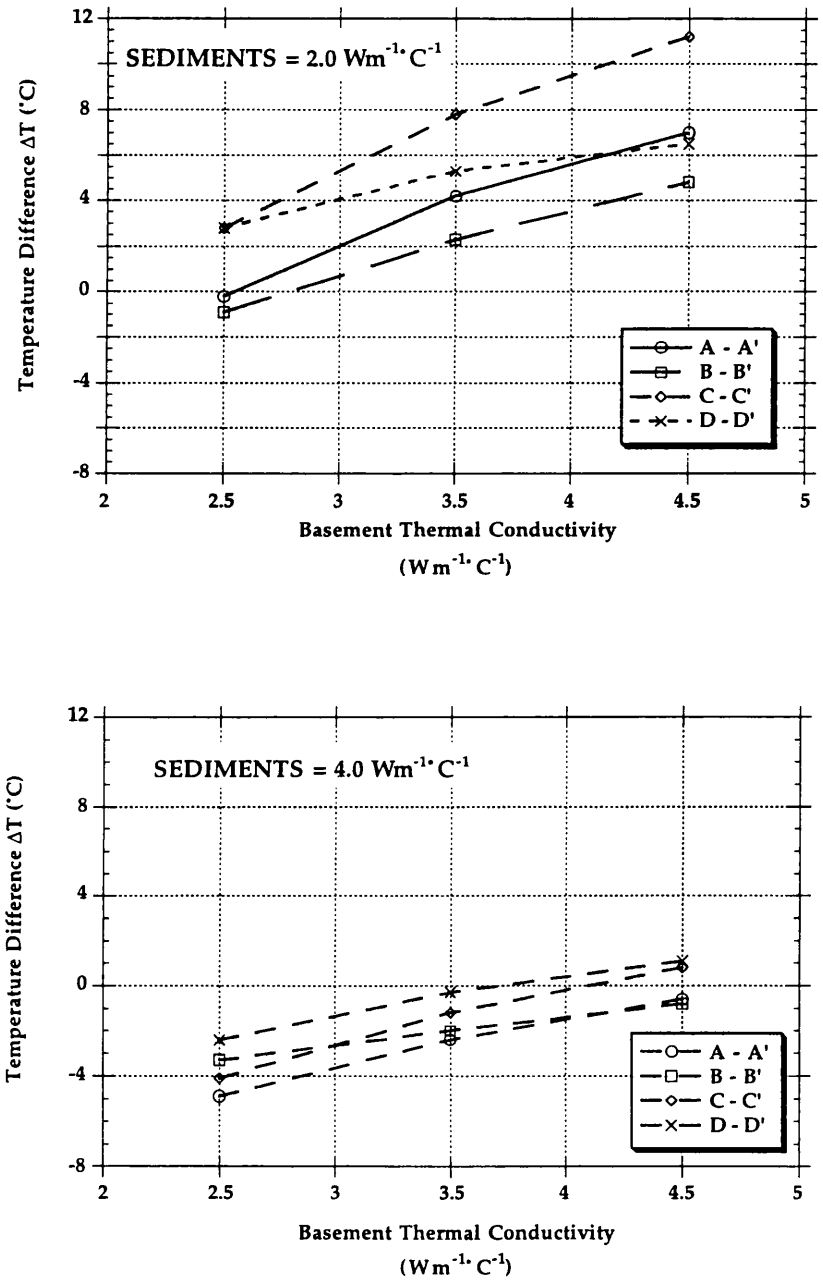

Figure 3.7 Temperature increase (ΔT) over basement highs at locations A, B, C and D for modelled sediment thermal conductivities of 2.0 and 4.0 Wm-1°C-1, over a range in basement thermal conductivity.

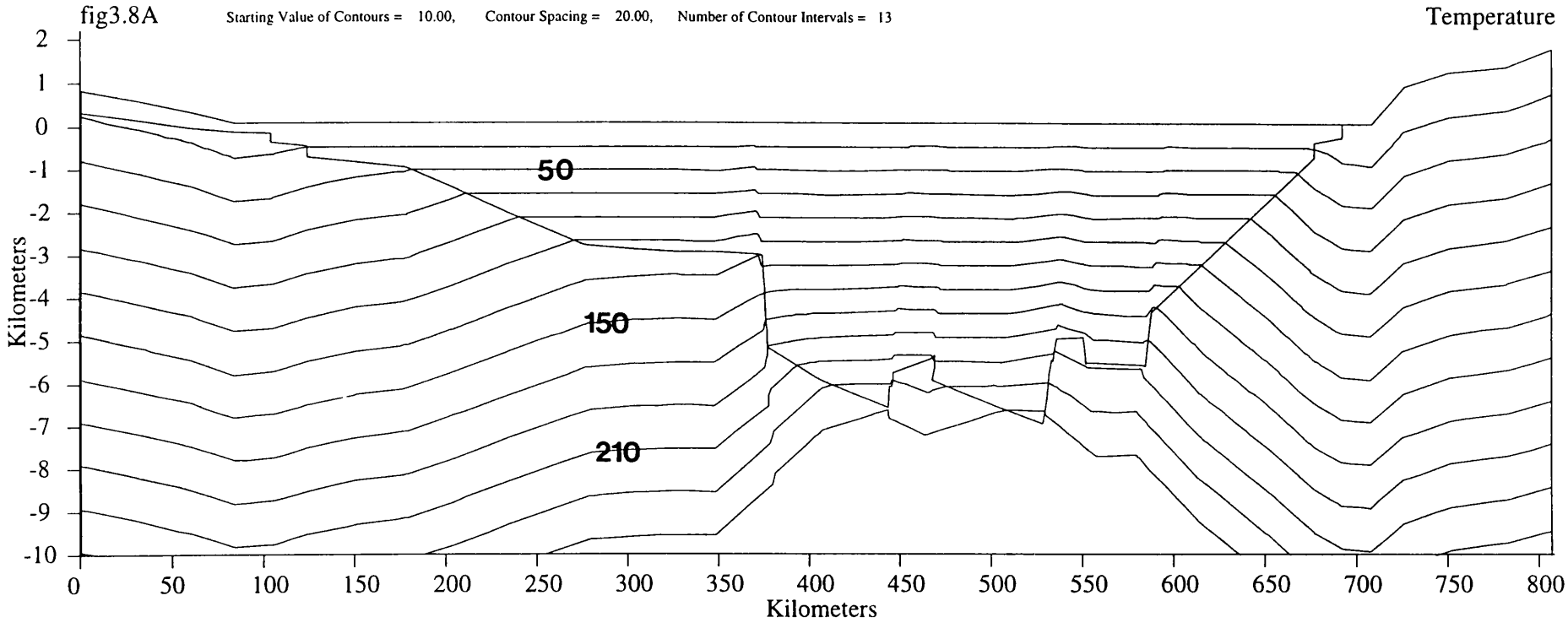

Figure 3.8A- The calculated temperature field for model with Bsmt = 4.5 Wm*-1C*-1, Sediments = 2.5 Wm*-1C*-1. Temperature contours start at 10 degrees C and increase in 20 degree C intervals.(This model is basement at maximum thermal conductivity, sediments at minimum).

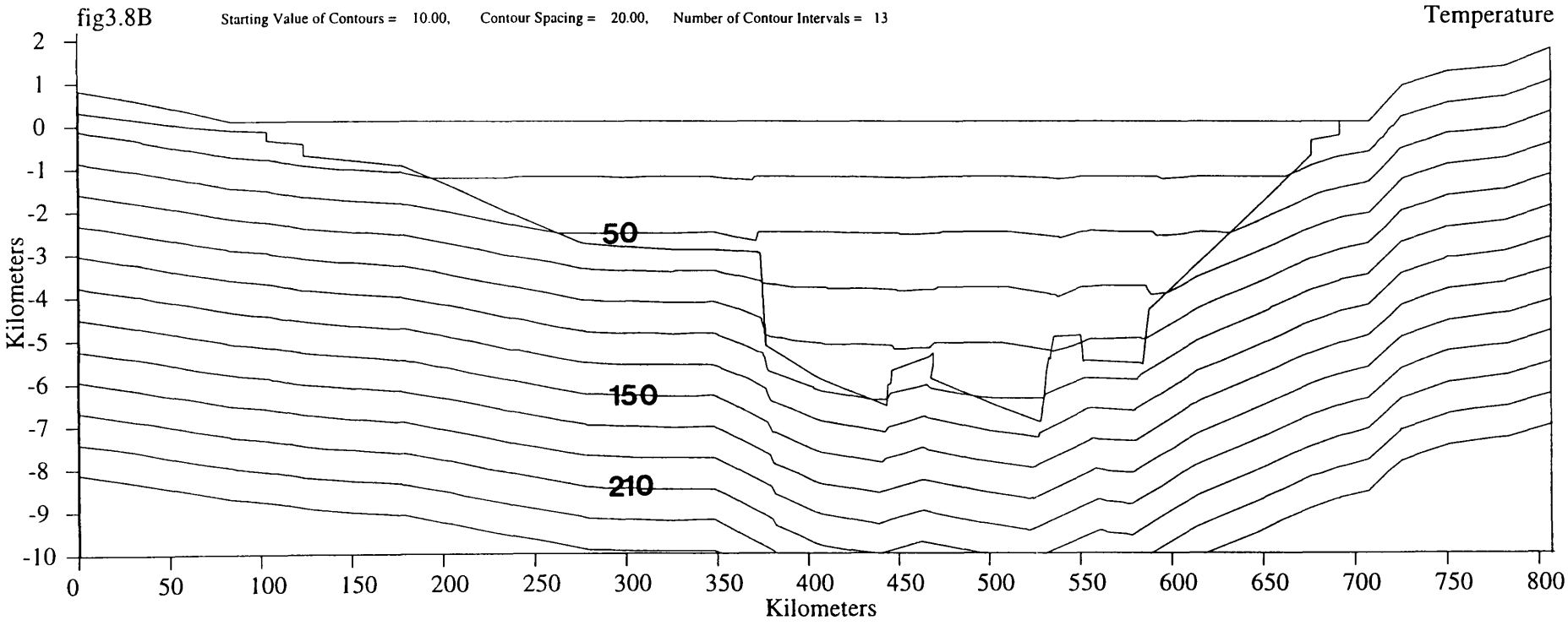

Figure 3.8B- The calculated temperature field for model with Bsmt = 2.5 Wm*-1C*-1, Sediments = 4.0 Wm*-1C*-1. Temperature contours start at 10 degrees C and increase in 20 degree C intervals.(This model represents basement at minimum thermal conductivity, with sediments at maximum)

Andrews-Speed et al (1984), (Fig. 3.6). From these four units a model is constructed with which to conduct the sensitivity studies (Fig. 3.9). This model shows the post-rift fill of the broad basin (Unit 1), the Upper Cretaceous "drape" (Unit 2), and the rift-fill (Units 3 & 4) which is restricted to the deep graben itself.

Unit 1	Cenozoic
Unit 2	Upper Cretaceous
Unit 3	Lower Cretaceous to Upper Triassic
Unit 4	Lower Triassic to Carboniferous

TABLE 3.2 - Conductivity units used in thermal modelling of the sedimentary pile, and their stratigraphic counterparts (see Fig. 3.9).

Five models are constructed to evaluate the range in thermal conductivities of these composite units (Table 3.3): all units at maximum thermal conductivity (Max); all at minimum (Min); units 1 & 3 at maximum, and units 2 & 4 at minimum (Mix 1); and vice versa (Mix 2); and units 1 to 4 at their approximate average (Avg). Each of these five models is used in simulations where the basement thermal conductivity is assumed to be 2.5, 3.5 or 4.5 $Wm^{-1}°C^{-1}$. This results in 15 simulations at a constant (70 mWm^{-2}) basal heat flow.

The temperature calculated in these simulations is extracted for a series of points at 4 km depth; the modelled temperatures are then compared (Fig. 3.10) to the actual temperatures at 4 km depth, interpolated in Chapter 2 (Fig. 2.9). The results of each simulation produce a broad, long wavelength anomaly (LWA), but none produce a temperature profile comparable to the observed temperature profile. In each case the modelled profiles are higher or lower than the real temperatures and are of lower amplitude.

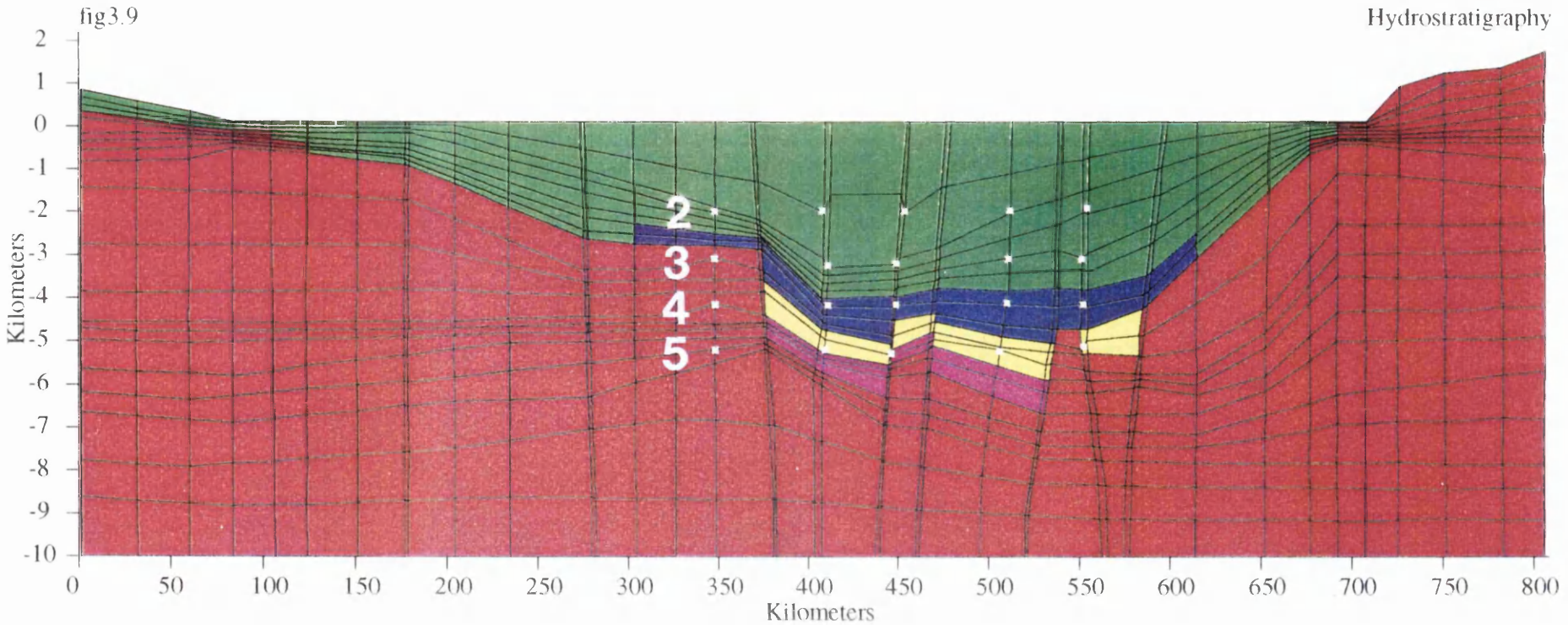

Figure 3.9 - Geometry of Sedimentary Pile model (Section 3.2.3). Points of data extraction are shown in white for 2, 3, 4 and 5 km depths. Basement - red, Cenozoic - green, Upper Cretaceous - blue, L. Cretaceous to U. Triassic - yellow, and L. Triassic to Permian - purple (see Table 3.2).

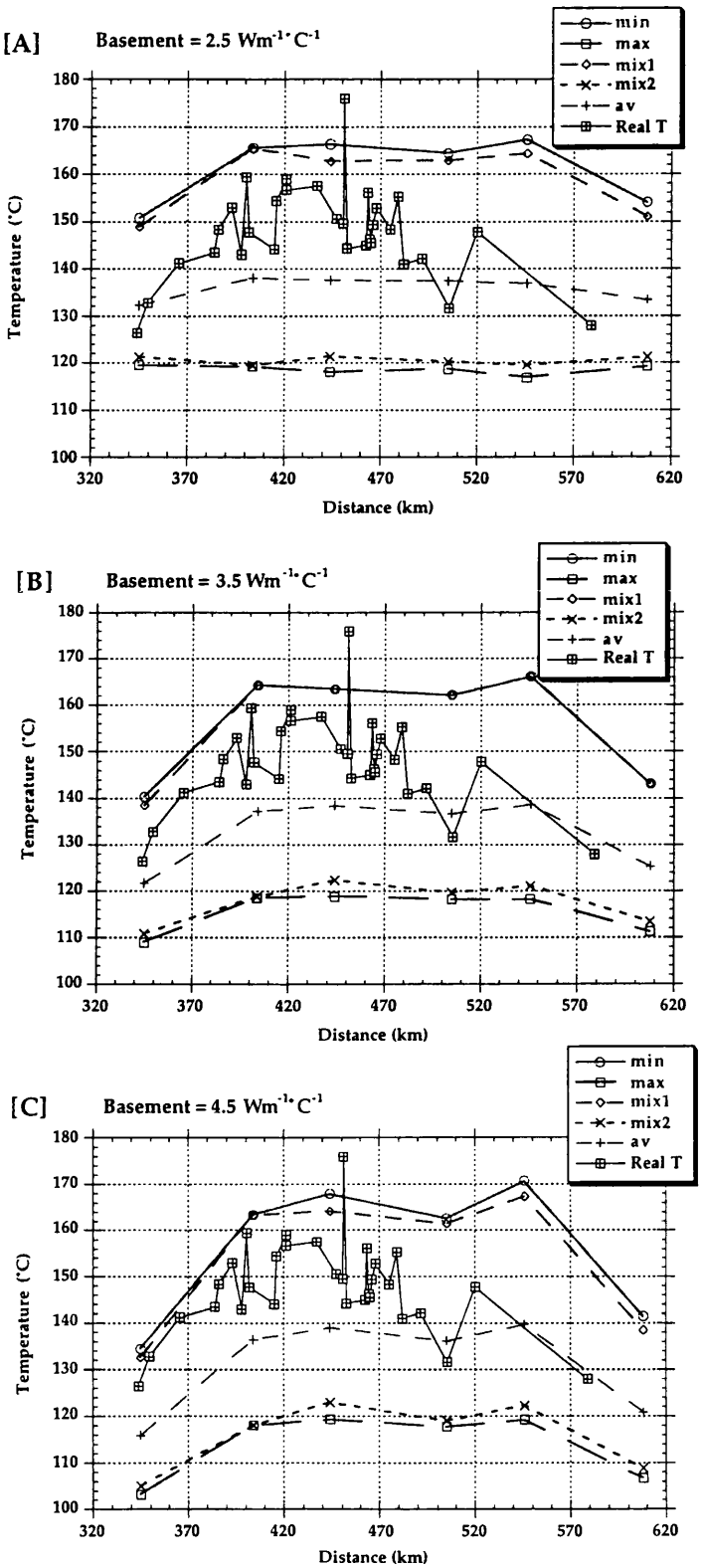

Figure 3.10 Comparison of modelled temperature profiles to observed temperature profile (Chapter 2) for basement thermal conductivities of 2.5, 3.5 and 4.5 Wm-1°C-1. All profiles from 4km depth.

UNIT (see Table 3.2 for stratig'ic. units).	Reported Range ($Wm^{-1}°C^{-1}$) (Andrews-Speed et al, 1984)	Assigned Thermal Conductivities ($Wm^{-1}°C^{-1}$)				
		MIN	MAX	MIX 1	MIX 2	AVG.
1	2.0 - 2.8	2.0	3.0	2.0	3.0	2.5
2	3.2	2.5	3.5	3.5	2.5	3.0
3	2.4 - 3.6	2.0	4.0	2.0	4.0	3.0
4	2.0 - 4.7	2.0	5.0	5.0	2.0	3.5

TABLE 3.3 - Assigned thermal conductivity values for the five models. Units 1 - 4 as defined in Table 2. Each case is run assuming basement conductivity values of 2.5, 3.5, and 4.5 $Wm^{-1}°C^{-1}$.

Which of these simulations is *closest* to reality? In Figure 3.10A (basement = 2.5 $Wm^{-1}°C^{-1}$), the temperature profiles produced by each of the five simulations (cases in Table 3) have amplitudes that are too small to match the observed LWA. Figures 3.10B and 10C (basement = 3.5 and 4.5 $Wm^{-1}°C^{-1}$ respectively) produce a closer fit to the amplitude of the LWA, although the shape of the curves would overestimate the actual temperature between 480 and 620 km. For either of these two basement values (3.5 and 4.5 $Wm^{-1}°C^{-1}$), a best-fit model to the observed LWA will have thermal conductivity values for each of the four sedimentary units somewhere between the Avg case, and the Min/Mix 1 cases.

3.2.4 *Best-Fit Model*

My aim is to find a best-fit model which will match (as closely as possible) the actual LWA at 2, 3, 4, and 5 km depths. Such a best-fit model

must have sedimentary thermal conductivity values which fall in the range between the Avg case, and Min/Mix 1 cases, for basement thermal conductivity of either 3.5 or 4.5 $Wm^{-1}°C^{-1}$ (Figs. 3.10B & 3.10C respectively). The observed temperature profile is judged to be best matched by the model with a basement thermal conductivity of 3.5 $Wm^{-1}°C^{-1}$. In order to keep the modelling as simple as possible, I continue the investigation using only a suite of simulations in which the basement thermal conductivity is assumed to be 3.5 $Wm^{-1}°C^{-1}$.

In order to judge the quality of the fit, the modelled temperatures from 2, 3, 4 and 5 km depths, for each of the Avg, Min, and Mix 1 cases, are compared against the actual (interpolated) temperature profiles at 2, 3, 4, and 5 km (Fig. 3.11). The Min and Mix 1 cases consistently over-estimate the temperature at any depth. The Avg model is a close match at 2 km but increasingly under-estimates the temperature with depth. Therefore, the input thermal conductivity values for each of the three cases (Table 3.4) define the ranges within which the best-fit model must lie. By trial and error, I find that the "Best-Fit model" (as defined in Table 3.4) closely matches the observed temperature field in the Central Graben (Fig. 3.12).

Although the temperatures calculated by the Best-Fit model (Fig. 3.12) match the LWA at 2, 3, 4, and 5 km depths within the Central Graben, the Best-Fit model does not produce significant SWA's. The full temperature field plot for the Best-Fit model (Fig. 3.13) reveals only small (approximately 5°C) temperature peaks over the edges of basement highs. This Best-Fit model, as is also the case in the other thermal models (see Figs. 3.10 & 3.11), overestimates the temperature between 480 and 620 km. This may simply be a local decrease in sediment thermal conductivity but there is no evidence to suggest that this is the likely explanation. Two alternative explanations of this phenomenon are: lateral variation in basal heat flow (the models discussed thus far have constant basal heat flow), OR, as postulated by

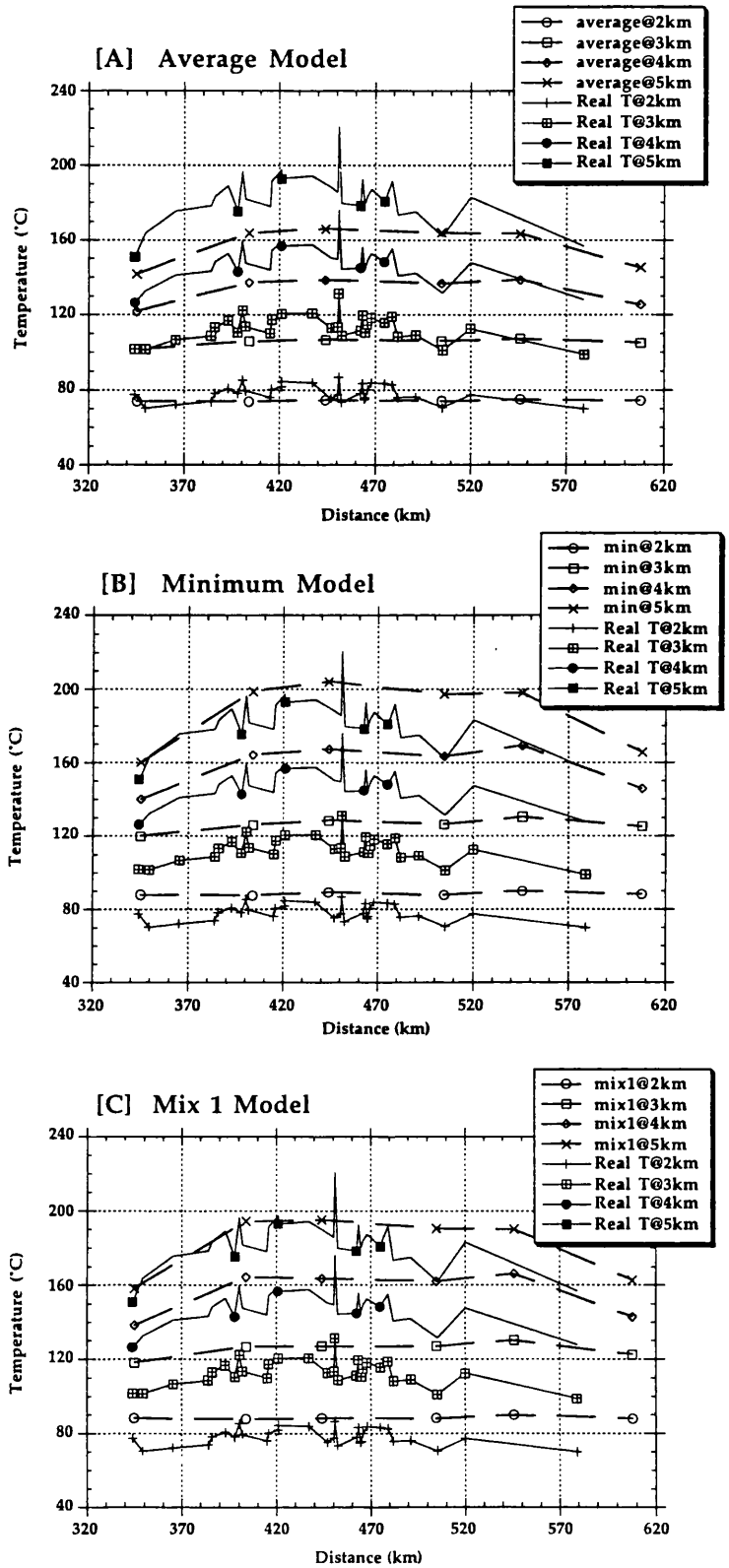

Figure 3.11 Comparison of modelled and observed temperatures within the Central Graben at 2, 3, 4, & 5 km depths for models Minimum, Average and Mix 1. Basement remains constant at 3.5 $Wm^{-1}°C^{-1}$.

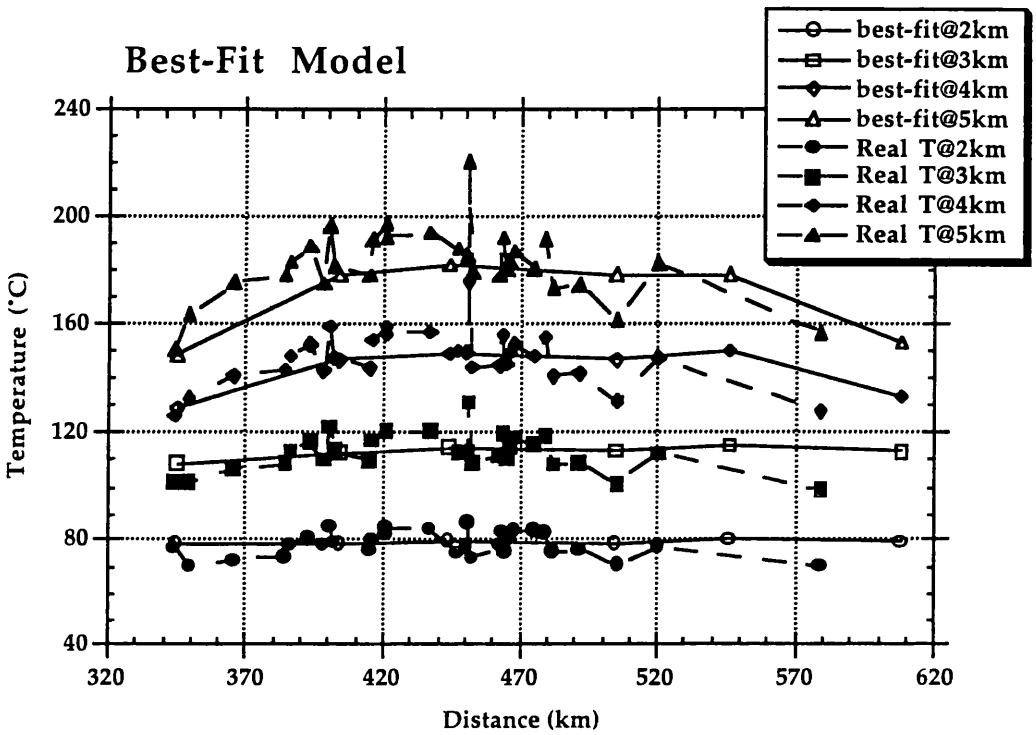

Figure 3.12 Comparison between calculated temperature profiles for Best-Fit Model (see Table 3.4), and observed temperature profiles (Chapter 2) at 2, 3, 4 & 5 km depths. Basal heat flow is constant at 70 mWm^{-2}.

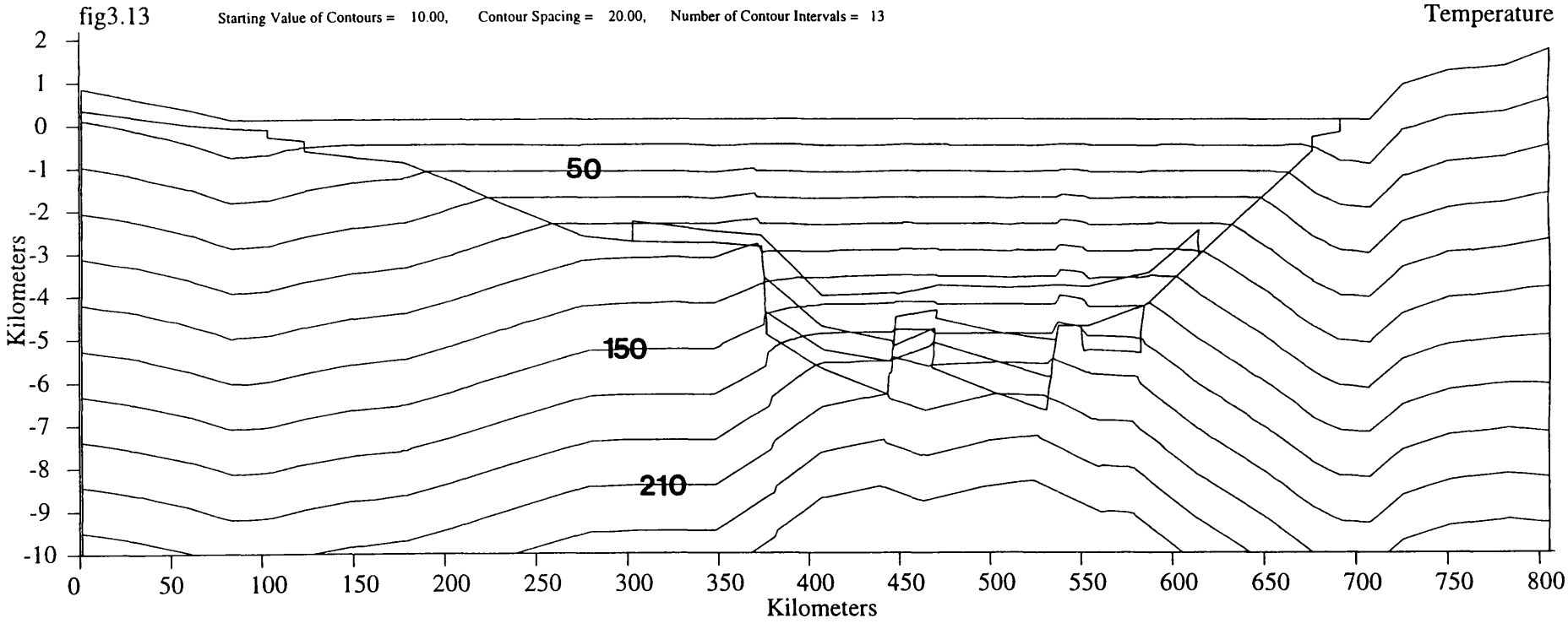

Figure 3.13 - Temperature contour plot for Best-Fit model (Section 3.2.4). Temperature contours reveal only small (approximately 5°C) temperature peaks over basement highs. This Best-Fit conductive model will provide the thermal conductivity parameters for the fluid flow models of subsequent chapters (see Table 3.4 for the thermal conductivity values of Units 1 - 4).

Temperature contours start at 10 °C (surface), and are in 20°C intervals.

Andrews-Speed et al (1984), cool groundwaters, descending through the sedimentary pile, driven by the hydraulic head provided by the Norwegian high, are removing heat. These possibilities are both considered: the first in the next section, and the second as part of the following chapter.

	Thermal Conductivity Values ($Wm^{-1}°C$)				
	Minimum	Mix 1	Average	(Range)	Best-Fit
Unit 1	2.0	2.0	2.5	(2.0 - 2.5)	2.3
Unit 2	2.5	3.5	3.0	(2.5 - 3.5)	2.5
Unit 3	2.0	2.0	3.0	(2.0 - 3.0)	2.5
Unit 4	2.0	5.0	3.5	(2.0 - 5.0)	2.8

TABLE 3.4 - Thermal Conductivity values for models Minimum, Mix 1, Average, and Best-Fit model (using geometry of Figure 9).

3.3 Long-Wavelength Anomaly: Variation in Basal Heat Flow

3.3.1 *Aims*

The modelling package OILGEN assumes a constant basal heat flow along the base of the modelled section. Previous heat flow studies of the North Sea and surrounding areas (Evans & Coleman 1974; Cermak 1979; Andrews-Speed et al. 1984) strongly suggest that this is not the case. I attempt here to constrain the possible maximum and minimum basal heat flow values along the chosen section line. Over-estimation of basal heat flow may be responsible for the consistent over-shoot of temperature between 480 and 620 km (Figs. 3.10 & 3.11) in the thermal models, and I therefore attempt to quantify the local decrease in basal heat flow necessary to account for these observations.

3.3.2 *Maxima and Minima of Basal Heat Flow*

In the thermal modelling of the sedimentary pile I have shown that I can match the LWA observed in the interpolated-temperature profiles of Chapter 2. To do this, the thermal conductivity values for the four sedimentary units must lie within the range of thermal conductivities in Table 3.4, with basement thermal conductivities of 2.5, 3.5 or 4.5 $Wm^{-1}°C^{-1}$, and a basal heat flow value of 70 mWm^{-2} is needed. The temperature profiles at 2, 3, 4, and 5 km are best matched by the Best-Fit model, which has a basement thermal conductivity of 3.5 $Wm^{-1}°C^{-1}$.

In the previous section, I found that the temperature curves are most closely matched for a basement thermal conductivity of 3.5 $Wm^{-1}°C^{-1}$ and thermal conductivity values within the range of the Avg, Min and Mix 1 cases. Therefore, I can model the four cases; Avg, Min, Mix 1 and Best-Fit (at a basement thermal conductivity of 3.5 $Wm^{-1}°C^{-1}$), for a range of basal heat flow values, and determine the effects of changed basal heat flow on the calculated temperature profiles. If the observed temperature profiles lie outwith the Avg, Min and Mix 1 modelled temperatures, this result will represent an unfeasible basal heat flow value for the Central Graben.

Figure 3.14 shows the four cases plotted for basal heat flow values of 60, 70, and 80 mWm^{-2} respectively. This cross-plot clearly shows that for basal heat flow values of 60 to 80 mWm^{-2} the known temperature profile falls within the likely range of thermal conductivity values (Avg, Min and Mix 1). [For heat flows of >80 mWm^{-2} we cannot expect to match modelled results to observed temperature data.] Therefore, a value of 70 mWm^{-2} for basal heat flow, while it may not be absolutely accurate along the entire length of the section, adequately serves as a broad average for modelling in the graben area. This average value of 70 mWm^{-2}, obtained by comparing the thermal models to the actual temperature profiles, matches well the

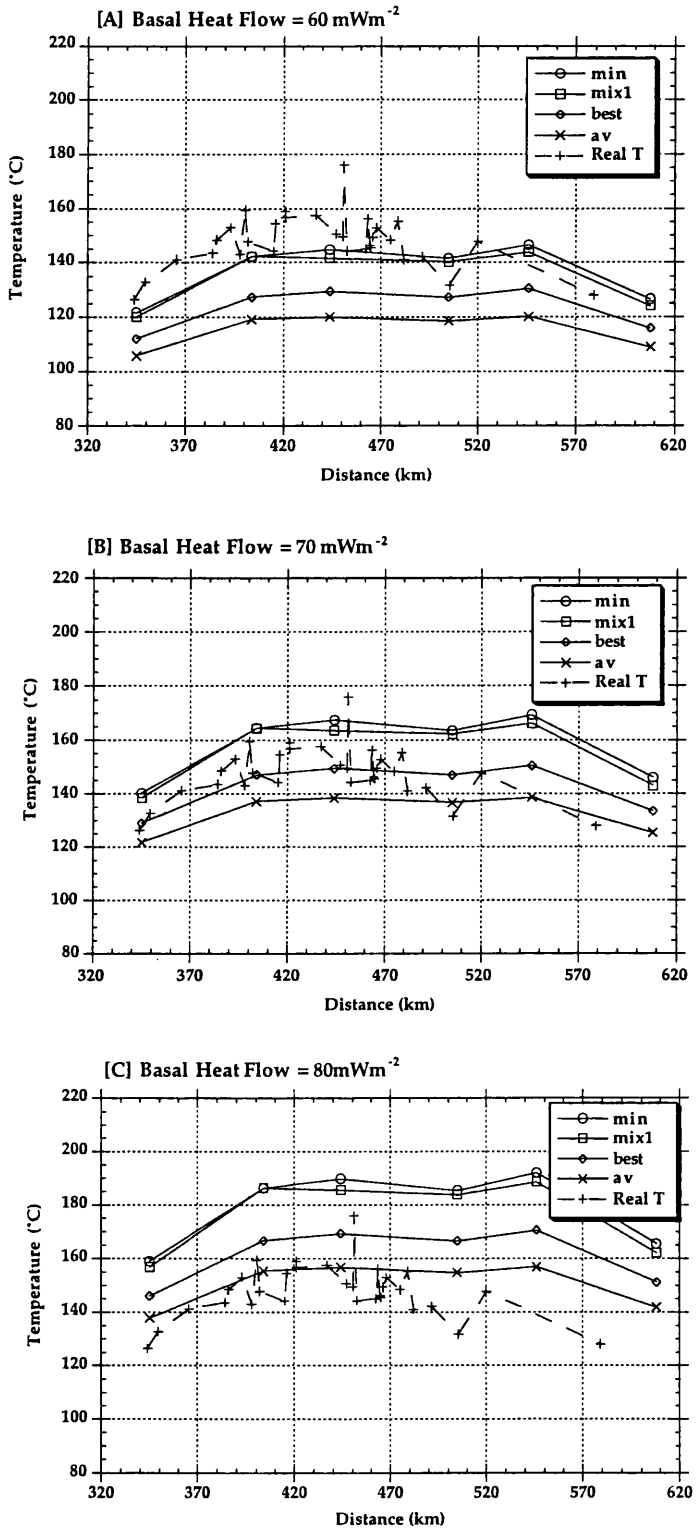

Figure 3.14 Modelled temperature profiles (for models Minimum, Mix 1, Best-Fit and Average) at 4 km for basal heat flow values of 60 , 70 and 80 mWm^{-2}. These are compared to the observed interpolated temperature profile from 4km (Chapter 2, Fig. 2.9).

mean estimated heat flow value for the central North Sea proposed from observations by Evans and Coleman (1974) of 71 mWm^{-2}.

3.3.3 *Lateral Variation in Basal Heat Flow*

The Best-Fit model shows a good match to the present day temperature field across much of the Central Graben (Fig. 3.12) when the basal heat flow value is assumed to be 70 mWm^{-2}. As discussed previously, the models consistently over-estimate the temperature between 480 and 620 km. One possible cause, as also suggested by Evans and Coleman (1974), is a decrease in basal heat flow across this portion of the section from west to east. However, fluid movement may also be responsible; see next chapter. If I plot the calculated temperature profiles for the Best-Fit model, using basal heat flow values of 50 to 90 mWm^{-2}, it is possible to estimate the change in basal heat flow necessary to account for the decrease in temperature between 480 and 620 km (see Fig. 3.15). The decrease in temperature between 480 and 620 km could be explained as being caused by a decrease in basal heat flow of approximately 5 mWm^{-2} in this area (reduction to 65 mWm^{-2} from 70 mWm^{-2}). Comparisons at other depths (not shown) support this conclusion.

3.4 Long-Wavelength Anomaly: Assessment of Conductive Models

A combination of variation of thermal conductivity within the sedimentary pile, and lateral variation in basal heat flow, is sufficient to explain the observed LWA. The Best-Fit model closely approximates the LWA of the observed temperature profiles (Fig. 3.12) at 2, 3, 4, and 5 km depths except that it over-estimates the observed temperatures between 480

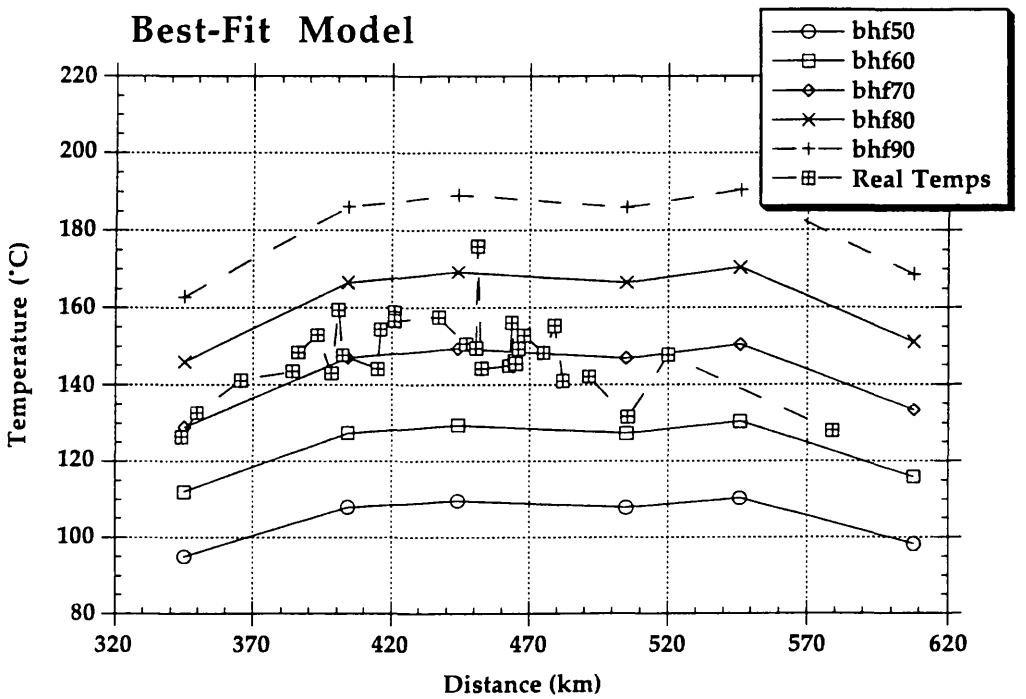

Figure 3.15 Best-Fit model temperature profiles from 4 km, for basal heat flow values of 50, 60, 70, 80, and 90 mWm^{-2}, compared to observed interpolated temperature profile from 4 km depth (see Fig. 2.9).

and 620 km. The excess temperatures may be explained by a lateral decrease in basal heat flow from 70 to 65 mWm^{-2} at the eastern end of the profile.

It must be emphasised, however, that the Best-Fit model is only one possible solution, and is not definitive. For example, small lateral variations in basal heat flow would result in a slightly different thermal conductivity architecture being necessary to match the observed temperature profiles. Changes in average basement thermal conductivity would also have a knock-on effect on the thermal conductivity distribution within the graben sediments, as would spatial variation in basement thermal conductivity. However, the sensitivity studies undertaken illustrate that small variations are not significant to the main conclusions, and that such small variations in thermal conductivity cannot account for the temperature spikes (SWA's) noted in Chapter 2. I therefore conclude that for the resolution attempted, the Best-Fit model, coupled with a lateral decrease in basal heat flow, can adequately represent the LWA of the Central Graben.

The effects of advection of heat by moving groundwaters have not been considered by these conduction-only models (see next chapter). For example, Andrews-Speed et al (1984) suggested, from their heat flow studies of the Central Graben, that the depression of temperatures in the east of the graben may be caused by cool groundwater descending through the sedimentary pile off the Norwegian high. Should this be the case, there would be no need to invoke a lateral variation in basal heat flow between 480 and 620 km along the line of section.

The Best-Fit model does match the LWA defined from the observed temperature profiles. Thermal conductivity and basal heat flow values that are used are as well constrained as is possible at this scale, and the resultant temperature field is a consistent match over the depth range considered (2 to 5 km). Although the conduction models produce a good match to the LWA, none of the simulations produce SWA's comparable to those on the

observed temperature profiles (Fig. 2.9). Possible localised conduction-only solutions to this mis-match are addressed in the following section.

3.5 Short-Wavelength Anomalies

3.5.1 *A Thermal Conduction Cause?*

The temperature profiles presented in Chapter 2 (Fig. 2.9) are composed of the LWA with superimposed short-wavelength anomalies (SWA's). These SWA's range up to 40°C in magnitude, and they generally have wavelengths of less than 10 km (when control points permit their resolution). The conductive models described thus far in this chapter explain the shape of the LWA, but these simulations do not result in short-wavelength temperature spikes comparable to those observed on the temperature profiles. This section describes the final possible way in which conductivity variations might explain the SWA's.

In order to produce a high magnitude, short-wavelength temperature anomaly in a conductive setting, a narrow "channel" of conductive material is necessary. To have a significant effect the channel needs to have a large vertical extent -- to conduct heat from greater depth into the shallow region of the temperature observations. Diapiric salt occurrences documented within the Central Graben (Glennie 1990) are the most likely geological candidates for such conductive anomalies. A salt wedge may also have a thermal effect, and this geometry is also considered. The models considered here are relatively extreme cases.

3.5.2 *Salt Models*

Two models are used to assess the effects of salt bodies within the Central Graben - the salt dome and salt wedge models (Figs. 3.16A & 3.16B respectively). A range of models is considered: varying the thermal conductivity of the basement and sediments, but holding the thermal conductivity of the salt constant at 5.5 $Wm^{-1}°C^{-1}$. The basement thermal conductivity is varied from 2.5 to 4.5 $Wm^{-1}°C^{-1}$, and the value for the sedimentary pile (considered homogeneous) ranges from 2.0 - 5.0 $Wm^{-1}°C^{-1}$. A comparison is made of the temperature over the top of the dome or wedge of salt against the temperature within the surrounding sediments at the same depth, but located at a distance approximately 10 km away (see Fig. 3.16; the salt dome model is patterned after an existing salt pillar approximately 25 km to the east of the Auk field (Glennie 1990)). ΔT is as defined before (being $\Delta T = T_A - T_{A'}$ and so on).

3.5.3 *Temperature Anomalies*

For both the salt dome and salt wedge models, a temperature anomaly develops (Figs. 3.17A & 3.17B). In each case the temperature above the salt is higher than in the adjacent sediments, and the difference (ΔT) is the local "anomaly". The temperature anomalies increase with decreasing average thermal conductivity for the sediments, for any of the modelled values of basement thermal conductivity. Thus, the greater the difference in thermal conductivity between salt and sediments, the greater the temperature anomaly. The *maximum* temperature "spike", or SWA, formed over a salt pillar or salt wedge, is 7°C or 6°C, respectively, using the minimum value (2.0 $Wm^{-1}°C^{-1}$) of homogeneous sedimentary fill thermal conductivity.

Our Best-Fit model shows, however, that in order to match the known temperature field, the average value of sediment thermal

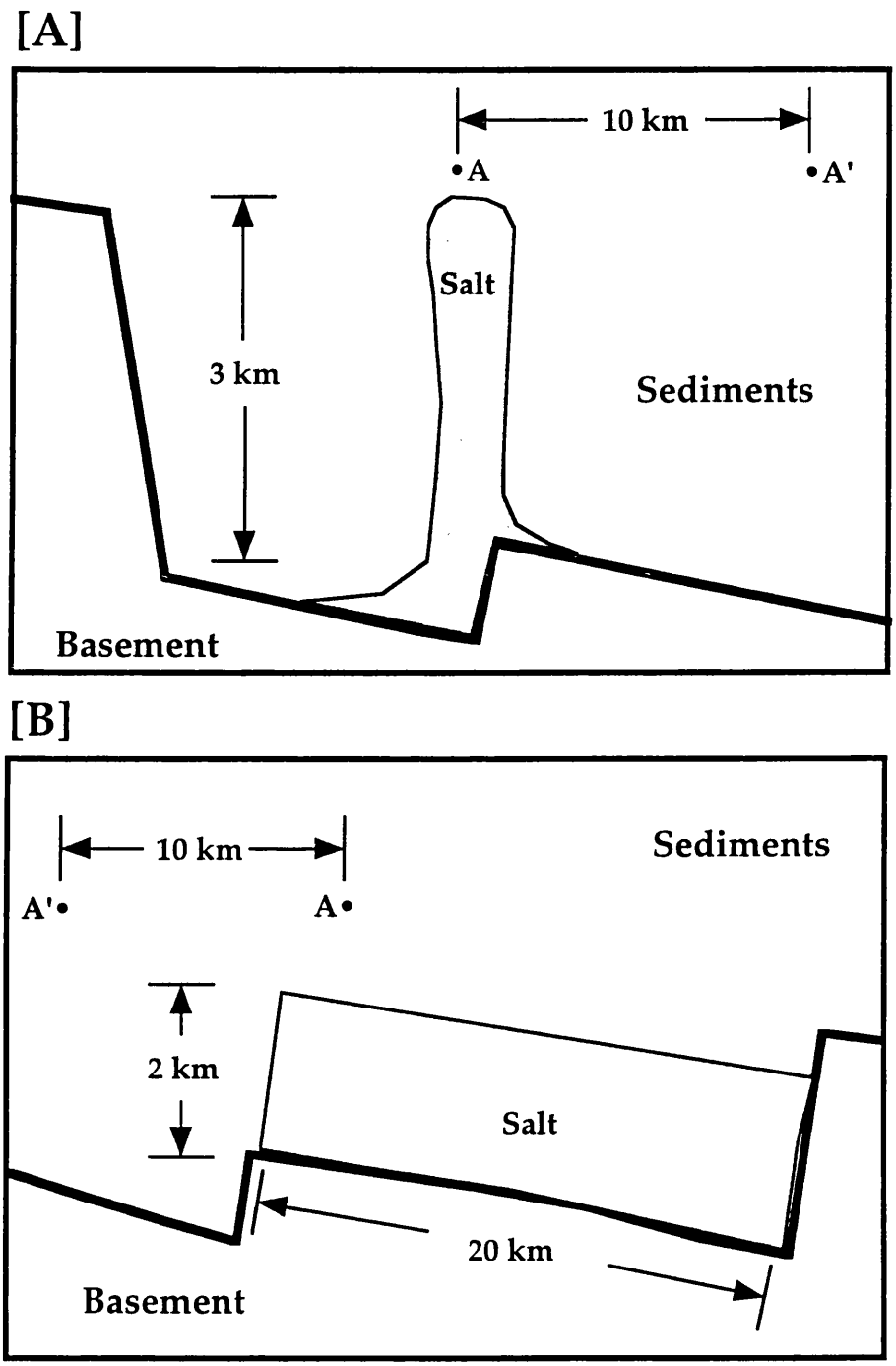

Figure 3.16 Sketch sections of Salt Dome and Salt Wedge models ([A] and [B] respectively), showing approximate dimensions.

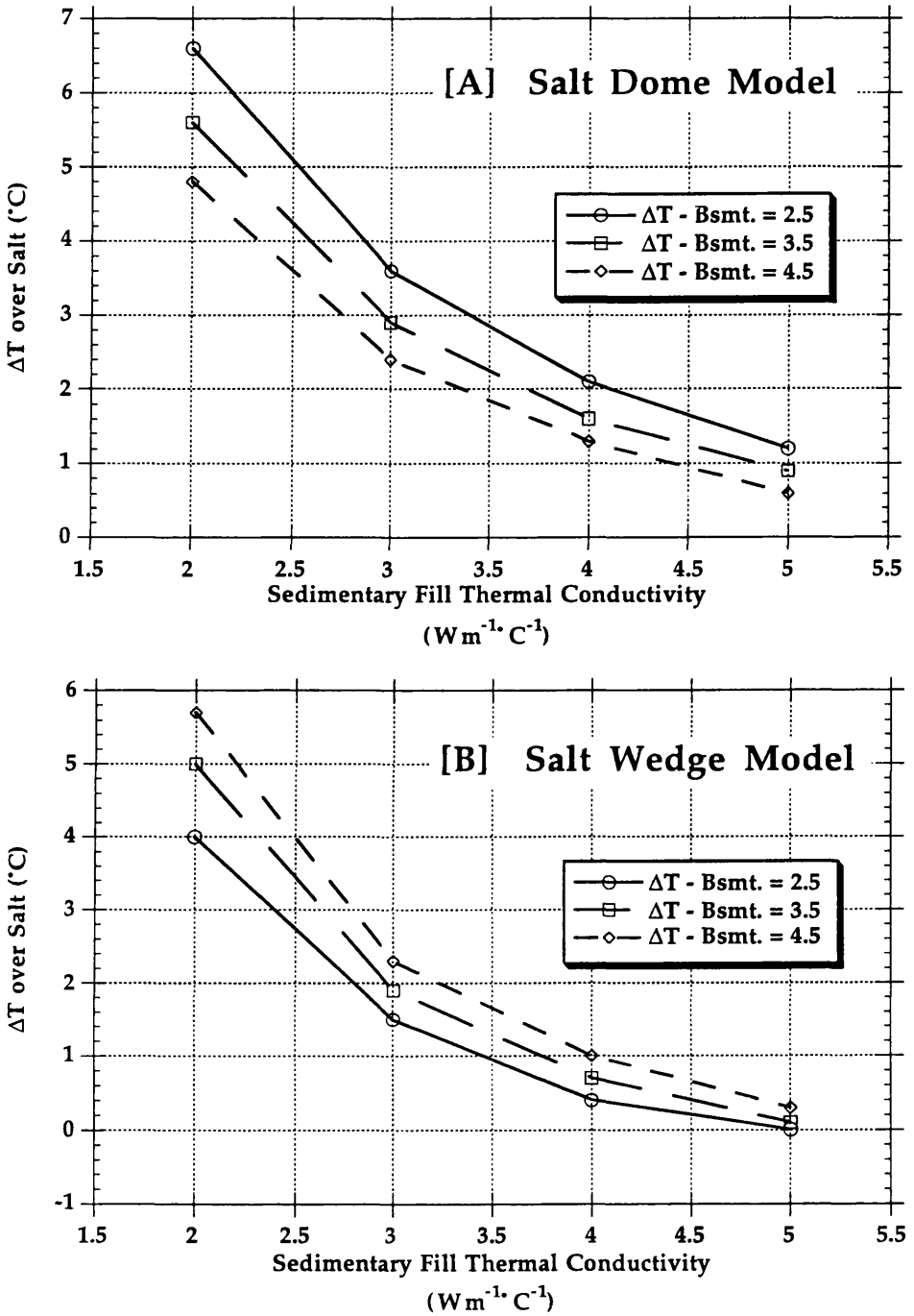

Figure 3.17 Temperature anomalies formed by Salt Dome and Salt Wedge models. Each model simulated at 2.5, 3.5 and 4.5 $Wm^{-1}{\cdot}C^{-1}$ basement thermal conductivity for a range in sediment thermal conductivity.

conductivity must be approximately 2.5 $Wm^{-1}°C^{-1}$. From Figure 3.17, the temperature anomalies associated with a salt dome or salt wedge must therefore be no larger than 5°C or 4°C, respectively. As these modelled salt bodies are extreme cases, the magnitude of a temperature anomaly associated with "real" salt and sediments within the Central Graben is likely to be less than this value.

The magnitude of the real SWA's shown in Chapter 2 (Fig. 2.9) ranges from 10 to 40°C. Therefore the observed SWA's can only be partly explained by preferential conduction of heat through anomalous salt bodies. Therefore, a process other than conduction of heat must be responsible for the magnitude of SWA's observed on the temperature profiles defined in Chapter 2.

3.6 Summary

3.6.1 *LWA*

The LWA identified from my original temperature profiles (Fig. 2.9) may be explained by conduction-only processes. Average thermal conductivities within the graben sediments, which are lower as compared to basement, readily form a long-wavelength, positive, low-amplitude temperature anomaly. Higher sediment thermal conductivity than basement leads to a negative LWA; this is unacceptable, as the observed temperature profiles all illustrate positive anomalies, (see Fig. 3.8B).

I attempt to match the observed LWA by running a suite of simulations encompassing the measured range of sediment thermal conductivities (see Table 3.3), using an estimated range of basement thermal conductivities, a uniform basal heat flow of 70 mWm^{-2}, and compare the modelled temperature field to that observed (Fig. 3.10). For any modelled

value of basement thermal conductivity, the observed temperature profile falls between the Avg and Min/Mix 1 cases, although a basement thermal conductivity of 3.5 $Wm\text{-}1°C^{-1}$ provides the best fit (Fig. 3.10).

When the three cases are compared to the observed temperature profiles at 2, 3, 4, and 5 km depth, none produce a good match over multiple depths (Fig. 3.11). However, the Avg and Min/Mix 1 cases define a range of thermal conductivity values within which a best-fit model must lie (Table 3.4). By a process of trial and error I was therefore able to define a thermal model -- the Best-Fit model -- which provides a good match to the LWA at 2, 3, 4, and 5 km depths (Fig. 3.12).

One unexplained feature of <u>all</u> the thermal models is their consistent over-estimation of temperature in the eastern portion of the section. Evans and Coleman (1974) suggested decreasing basal heat flow from west to east across the central North Sea as an explanation of this phenomena. From my thermal models (Fig. 3.15) it is evident that a decrease in basal heat flow from 70 mWm^{-2} to 65 mWm^{-2} would be sufficient to explain this mis-match between the thermal models and the actual LWA.

3.6.2 *SWA*

Although the LWA is well matched by the Best-Fit model, it is unable to account for the SWA's (Fig. 3.12 & 3.13). Two possible conductive solutions are considered; extreme thermal conductivity difference between basement and surrounding sediments, or vertical high-conductivity channels of salt.

In the case of extreme difference between basement and sediment thermal conductivity, I have shown that, even at the maximum measured difference between basement and sediment thermal conductivity, the temperature peaks formed over the edges of basement highs are smaller in

magnitude and greater in wavelength than some of the observed SWA's (compare Fig. 2.9 to Figs. 3.7 & 3.8). At these extremes of thermal conductivity difference, the LWA is not matched. Therefore, for the modelled temperatures to match the observed LWA, the thermal conductivity differences between basement and sediments cannot be so extreme as to form major temperature spikes (SWA's). Only the Best-Fit model is able to match the LWA's successfully, and it produces no SWA's (see Figs. 3.12 & 3.13). As the Best-Fit model defines the average thermal conductivities of basement (3.5 $Wm^{-1}°C^{-1}$), and sedimentary fill (approximately 2.5 $Wm^{-1}°C^{-1}$), I can estimate the range in magnitude of temperature peaks over basement highs for the Best-Fit model as being approximately 1°C to 5°C (Fig. 3.5).

Two models (Fig. 3.16), both extreme cases, are chosen to investigate the possible temperature effects of local conduction disturbances: salt domes and salt wedges (thermal conductivity of salt 5.5 $Wm^{-1}°C^{-1}$). For each simulation (using the range of basement and sediment thermal conductivities found earlier) a temperature anomaly forms over the salt dome or wedge (Fig. 3.17). The maximum temperature anomalies formed over them are 7 and 6°C, respectively.

The Best-Fit model is comparable to a model where the average thermal conductivity for the sedimentary pile is approximately 2.5 $Wm^{-1}°C^{-1}$. Returning to Figure 3.17, the maximum temperature anomaly formed over a salt dome or salt wedge in such a case will be 5 or 4°C, respectively -- much too small in magnitude to match the observed SWA's which range from 10°C to 40°C.

Within the Central Graben many salt domes/wedges are located on the edge of basement highs (Figure 2 (Zeigler 1982; Cayley 1986)). Therefore, *in some cases*, the temperature effect of a salt dome or wedge may be

combined with the preferential conduction of heat through a basement high. In the most extreme case (maximum possible temperature effect of salt + maximum temperature peak over a basement high), I can estimate that the resulting temperature anomaly would be 10°C, although the wavelength of the temperature anomaly would be greater than 10 km, and the magnitude of anomaly would still be too small to match the observed SWA's.

3.6.3 *Implications*

How then is it possible to produce the present-day temperature field? I have attempted to match the observed temperatures by purely conductive means and have been able to reproduce the LWA, but am unable to produce any temperature spikes or SWA's comparable to those in the observed temperature profiles. I can only conclude from this conductive thermal modelling that, in order to produce short-wavelength, high amplitude temperature spikes (SWA's, Fig. 2.9), a process in addition to conductive heat transfer must operate within the Central Graben. This process may possibly be advection of heat by moving groundwaters. In the following chapter I will investigate the influence of moving groundwaters on the temperature field .

CHAPTER 4

REGIONAL FLUID FLOW AND ASSOCIATED THERMAL EFFECTS

4.1 Introduction

Having shown, through thermal modelling, that it is *not* possible to match the temperature field of the Central Graben by conductive heat transfer, it is my intention in this chapter to assess the potential for modification of the temperature field within the Central Graben by regional fluid flow processes.

Topographically-driven fluid flow was proposed by Andrews-Speed et al (1984) to explain the interval heat flow values calculated across the Central Graben. They proposed that cool groundwater descending off the Norwegian high under gravity affected the temperature gradients. Theoretical studies by Smith & Chapman (1983) and Garven and Freeze (1984), along with basin specific studies by Majorowicz & Jessop (1981), Garven (1989), and Willett & Chapman (1989) among others, have shown that regional topographically-driven fluid flow can be responsible for significant modification of the conductive temperature field. Regional scale convection too, has the potential to significantly affect the thermal field (Le Carlier et al, 1994). I do not consider compaction-driven fluid flow in this chapter as Bethke (1985) has shown that the associated fluid velocities are too small to significantly effect the conductive temperature field.

Using a range of different models I aim to establish to what degree regional fluid flow, driven by either topography or by regional convective flows, affects temperature within the graben. I will also consider if any of the

regional fluid flow processes are responsible for the short-wavelength anomalies which remain unaccounted for in my conductive models.

4.1.1 *Methodology*

The modelling (using OILGEN) carried out in this chapter uses the same section line and basement geometry described within Chapter 3. In the following models however, fluid flow is coupled to heat flow so the thermal effects of any regional fluid flows can be ascertained.

I first quantify the thermal effects of fluid flow through basement on the thermal regime within the sedimentary pile, as the majority of the modelled section is composed of basement (Fig. 4.1). This is accomplished through a suite of simulations spanning a basement permeability range of 10^{-14} to 10^{-1} mD, at different sedimentary permeabilities. By this method it is possible to ascertain whether flow through basement (at realistic basement permeabilities) causes significant deviation of temperature within the Central Graben from the calculated conductive field established in Chapter 3. An estimate of fluid flux through basement is also made using these models.

Having established the role of basement I then consider the effects of the internal permeability architecture of the sedimentary pile. This is achieved by the investigation of three different geometries. From the first, (Fig. 4.1) where the sedimentary pile is considered as of homogeneous bulk permeability and assigned a range of bulk permeabilities I can establish an approximate upper limit to vertical permeability (potentially a major factor affecting the potential of fluid flow to modify the temperature field. By running simulations with the same suites of sediment permeabilities, but with different basement permeabilities, I may also confirm whether

basement permeability is a significant 'player' in the fluid flow regime within the sedimentary pile.

From this point I proceed to a more realistic four unit sedimentary pile permeability architecture. The four units (shown in Fig. 4.1) represent the Cenozoic, Cretaceous, Jurassic/Triassic, and the Palaeozoic sediments. This is the same stratigraphy as used for conductivity modelling in Chapter 3. To this geometry I assign base-case values to each of Units 1 to 4 and raise the vertical permeability of each Unit in turn comparing the effects on fluid flow and temperature, and matching modelled output to measured temperature data. This enables the establishment of three points;

1. A theoretical maximum vertical permeability for each Unit.

2. The likelihood of temperature changes within the graben being caused through either topographically-driven or convective fluid flow within each Unit, by comparison of the modelled permeabilities to calculated and measured permeability ranges for the Central Graben.

3. Whether the temperature changes caused by regional fluid flow are responsible for the SWA's established in Chapter 3.

4.2 Basement and the Sedimentary Pile: Bulk Permeability Models

4.2.1 *Basement Permeability and Temperature*

I here attempt to quantify the effect of fluid flow through *basement* on the present day temperature field, in and on the periphery of, the Central Graben. By varying basement permeability through many orders of

magnitude, for two suites of sediment permeabilities, it is possible to observe the threshold basement permeability at which modification of the conductive temperature field by moving groundwaters begins. This value can be compared to accepted values for crystalline basement permeability. My aim is to observe whether realistic basement permeabilities result in temperature patterns significantly different to that of the conductive models tested in the previous chapter.

I use the same 2-D section line, geometry and thermal conductivity parameters of the Best-Fit model, as described in Chapter 3 (Figs. 3.12 & 3.13), as the basis for modelling in this chapter, with the sedimentary pile remaining divided into Units 1 to 4. However, in this basement permeability modelling, Units 1 to 4 are assigned two suites (two extremes) of porosity and permeability values (Table 4.1) in order to compare the effect of basement permeability at relatively low and relatively high average sediment permeabilities. Both suites of sediment permeabilities (LOW and HIGH) are modelled for a range in basement permeability of 10^{-14} mD to 1.0 mD using OILGEN.

UNIT	Horizontal Permeability - **LOW**	Horizontal Permeability - **HIGH**	Porosity	Anisotropy
1	0.1	10	10	100
2	0.01	1	10	100
3	1	100	5	100
4	1	100	5	100

TABLE 4.1 - Permeability and porosity values used in basement permeability modelling (Units 1 to 4 shown in Fig. 4.1).

The suite of basement permeabilities is chosen to encompass values published in Garven and Freeze (1984), Black (1987), Clauser (1992) and Harms et al (1993). Sediment poro-perm values are generalised, but compare

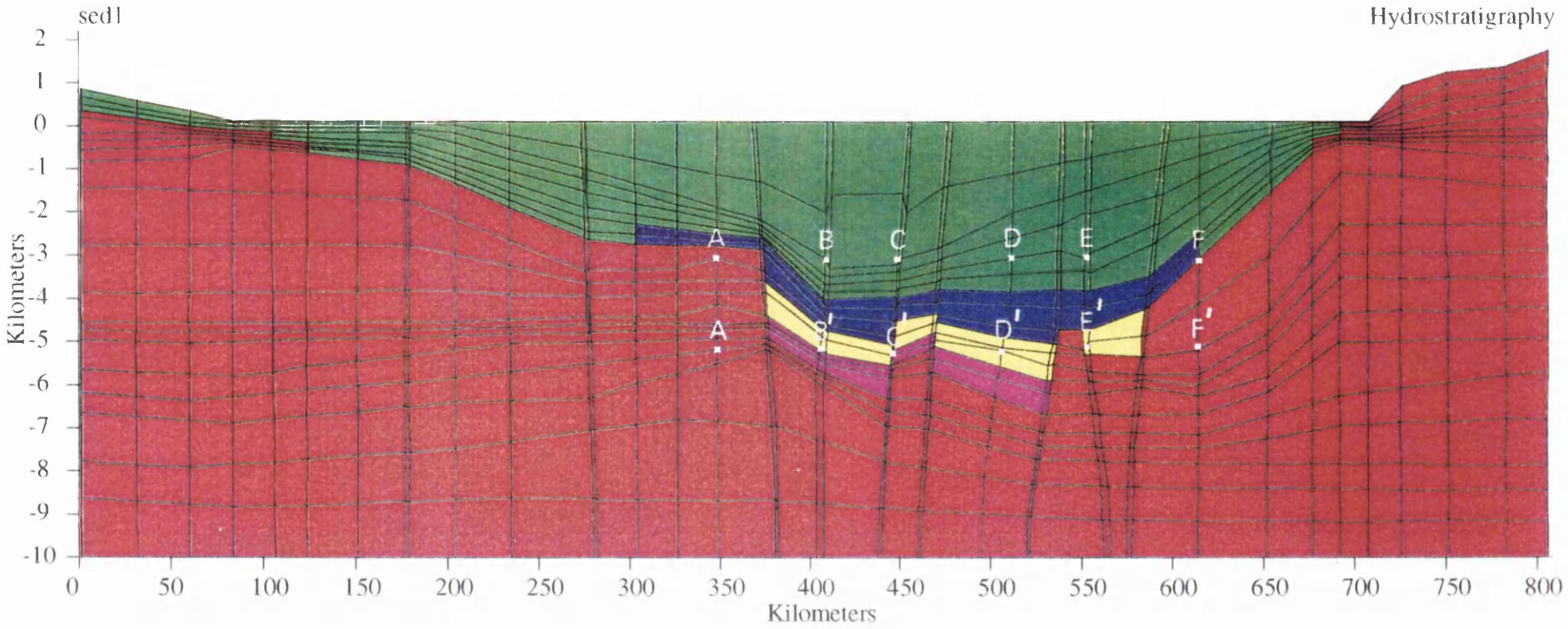

Figure 4.1 - Geometry of regional fluid flow models. Units 1 - 4 are green, blue, yellow and purple, respectively. Basement is shown in red (see Table 3.2 for stratigraphic definition of Units 1 to 4). The porosities of Units 1 - 4 are 10, 10, 5, and 5% respectively. Nodes of temperature extraction at 3 (A - F) and 5 km (A' - F') are labelled in white.

well to data in Garven and Freeze (1984) and Sclater and Christie (1980). It is important to point out that areas of recent geopressure exist within the Central Graben (Gaarenstroom 1992), which cannot be accounted for in these models. However, these models allow me to assess the scale of effects of fluid circulation within the graben, either during periods of low or no overpressure or within the normally pressured parts of the basin.

By extracting the calculated temperatures at nodes A to F and A' to F' (3 and 5 km depth respectively, Figure 4.1) for each of my simulations, I can observe at which basement permeability that a particular temperature change occurs within the basin. Figure 4.2 shows the calculated temperatures plotted against basement permeability, for the two suites of sediment permeabilities (LOW and HIGH). In each of the cases, temperature within the basin remains stable at basement permeabilities of less than 0.001 mD. Significant change in the temperature field within the graben occurs at basement permeability of greater than 0.1 and 0.001 mD, for the sediment permeability suites LOW and HIGH respectively. Therefore, as one might expect, the lower values of average sediment permeability necessitate higher basement permeability to produce a change in the temperature field within the basin (Central Graben).

4.2.2 *Basin Fluid Recharge through Basement?*

What then are the possible fluid velocities involved in fluid recharge to the Central Graben and what pattern do they follow? Do they influence petroleum migration directions?

I use a base-case model of the Central Graben to provide a broad estimate the regional fluid flow velocities and patterns of flow. The model has the same geometry and thermal properties of that shown in Figure 4.1. The poro-perm parameters are average values (see Table 4.2) between the

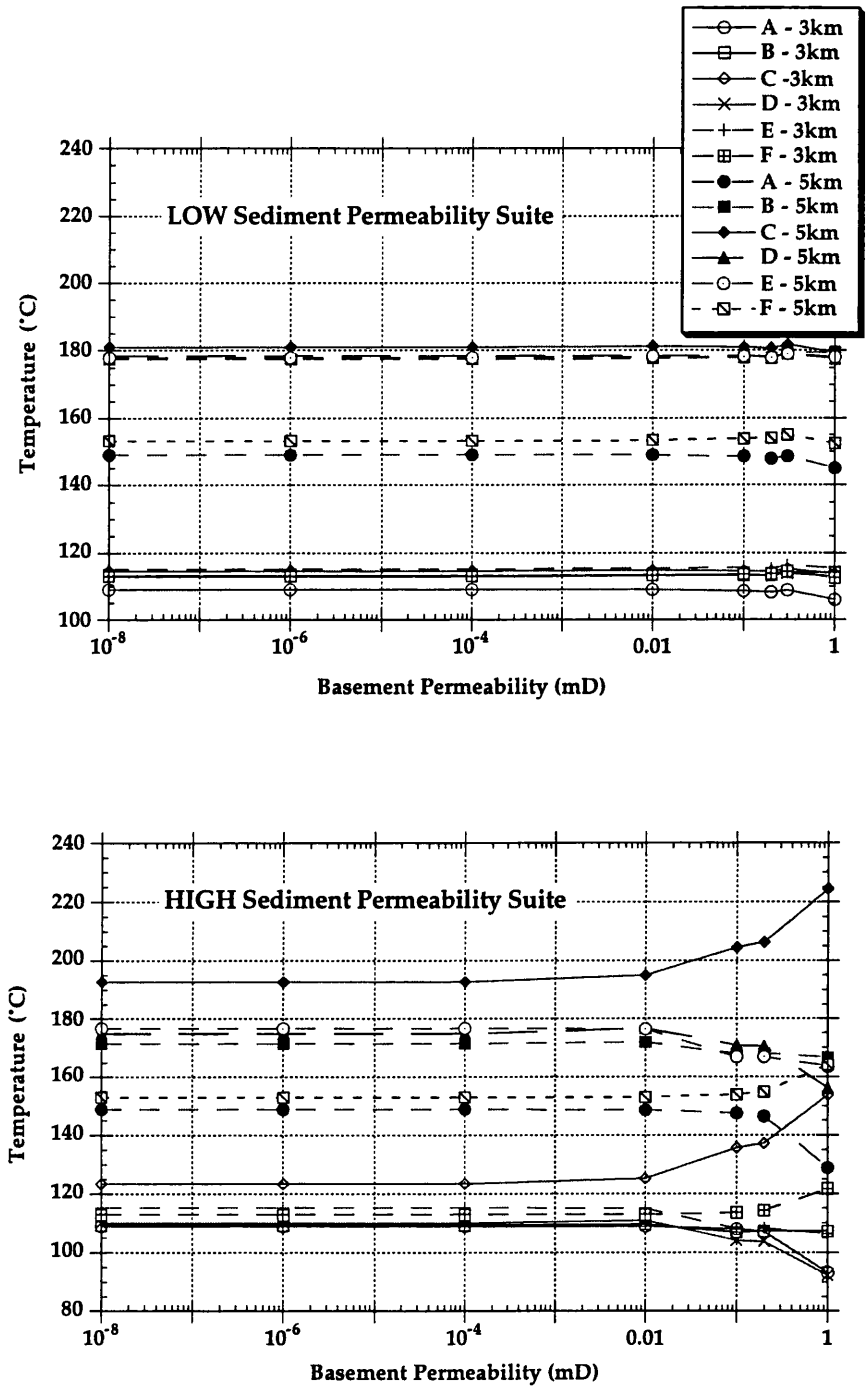

Figure 4.2 - Calculated temperatures from selected nodes (A - F and A' - F'; see Fig. 4.1) across the Central Graben (for sediment permeability suites LOW and HIGH) at varying basement permeabilities. Key for Low suite of measurements also applies to High suite.

two extremes of poro-perm (LOW and HIGH) used in the basement modelling of the previous section. Basement is held constant at 10^{-4} mD.

A plot of the calculated fluid velocities for this model is shown in Figure 4.3. The maximum groundwater velocity is 18 cma^{-1}, (the vectors in this plot are scaled between 5 cma^{-1} and 0.5 mma^{-1}, with X's marking flow velocities in this case of less than 0.5 mma^{-1}, not of no flow). The figure shows fluid recharge through basement to the graben, from the Norwegian high, of the order of mma^{-1}. This regional flow system (under normally-pressured conditions) would also be sufficient to effect petroleum migration directions (Fig. 4.4; same scale as Fig. 4.3). This model suggests that petroleum may be forced to migrate laterally towards basement highs (Fig. 4.4) at maximum velocities of 18 cma^{-1}.

4.2.3 *The Sedimentary Pile and Temperature*

I begin with the model shown in Figure 4.1 in which the sedimentary pile has *uniform* permeability but porosity varies with depth (the assigned porosities are; Tertiary and Cretaceous, 10%; Jurassic to Palaeozoic, 5%). By varying the permeability of the sedimentary pile over a range of scales it is possible to determine the threshold value of vertical permeability at which temperature change due to fluid flow occurs within the basin.

All units are assigned an anisotropy of 100 and permeability (horizontal) is varied between 0.01 mD and 1 Darcy. In order to determine the influence of basement permeability (if any) on this "threshold" sediment permeability, this range in sediment permeability is modelled at basement permeabilities of 10^{-2}, 10^{-4} and 10^{-8} mD. These permeabilities are well within the region of stable temperature (Fig. 4.2).

For each simulation, the temperature at three kilometres depth is extracted at nodes A to F across the basin (Fig. 4.1). These temperatures are

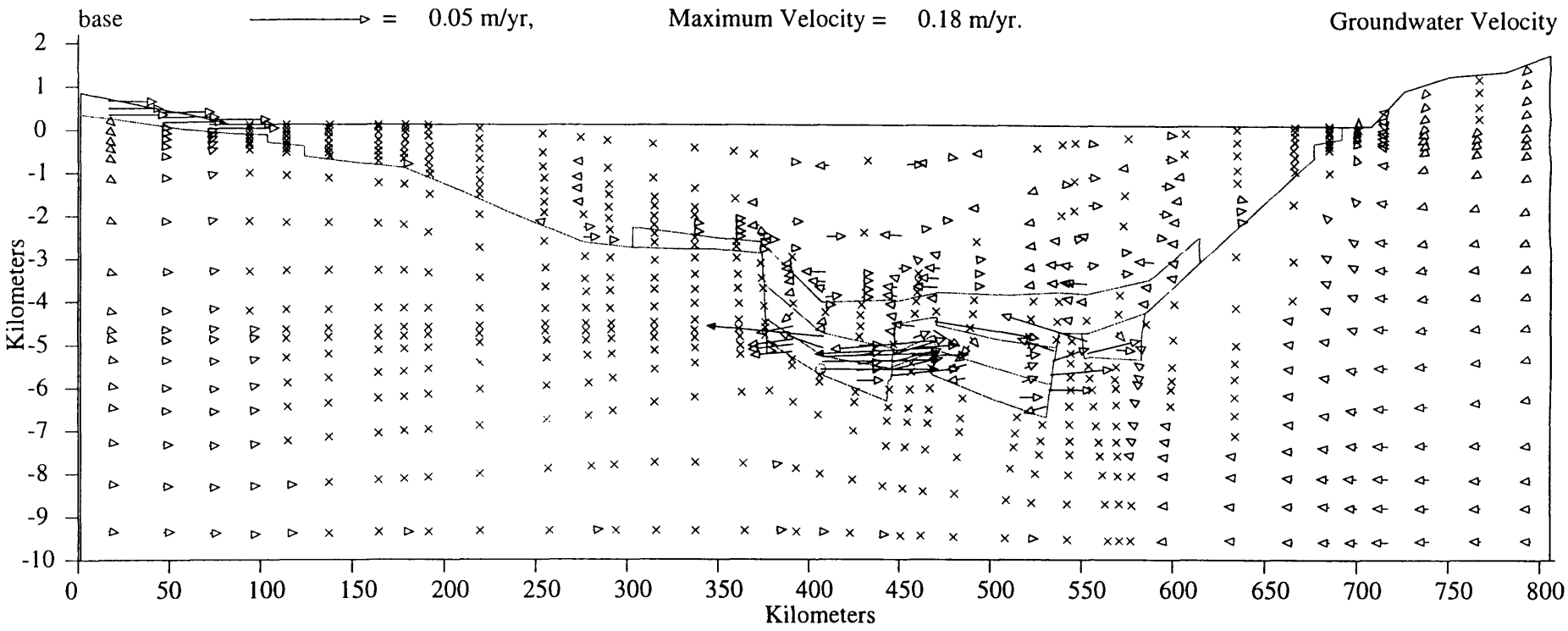

Figure 4.3 - Regional groundwater flow velocities within the Central Graben. The maximum groundwater velocity is 18 cma-1, (the vectors in this plot are scaled between 5 cma-1 and 0.5 mma-1, with X's marking flow velocities in this case of less than 0.5 mma-1, not of no flow). The figure shows fluid recharge through basement to the graben, from the Norwegian high, of the order of mma-1. Outline geometry corresponds to Figure 4.1.

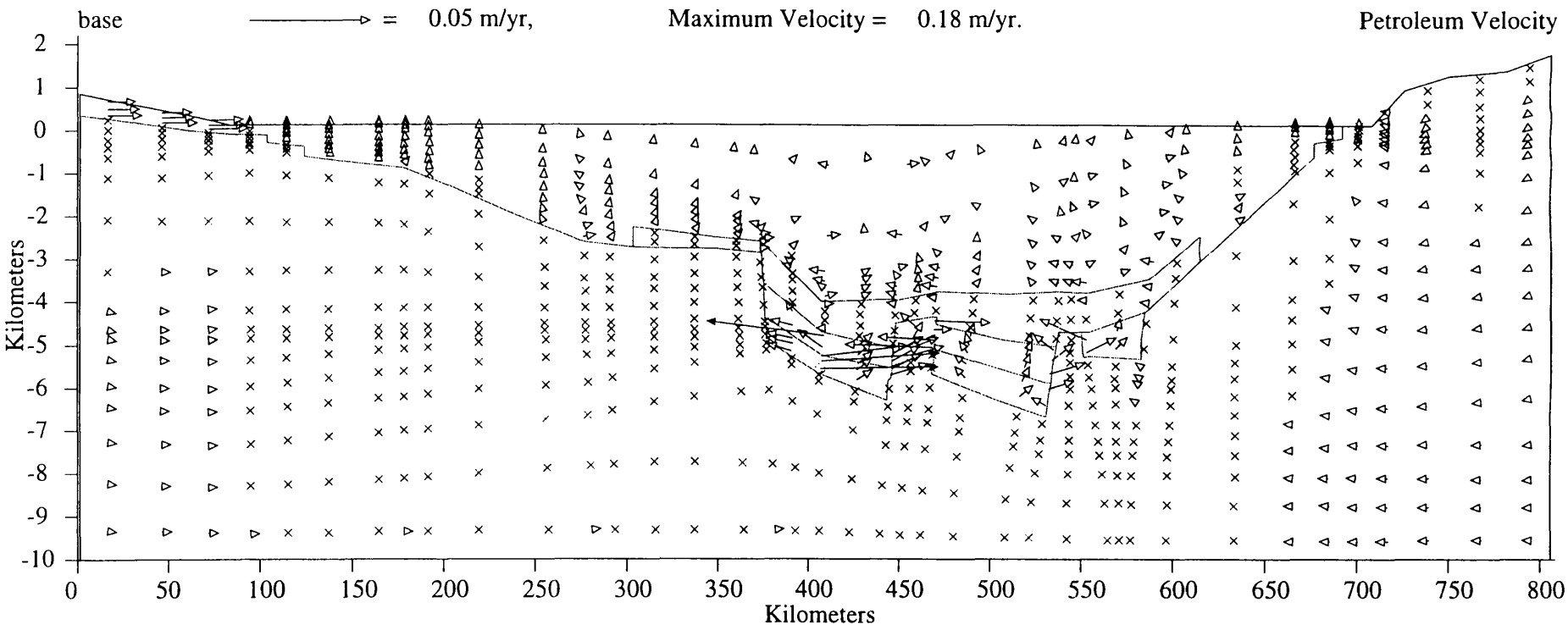

Figure 4.4 - Regional petroleum flow velocities within the Central Graben. Maximum petroleum velocity is 18 cma-1, (the vectors in this plot are scaled between 5 cma-1 and 0.5 mma-1, with X's marking flow velocities in this case of less than 0.5 mma-1, not of no flow). The figure shows lateral petroleum migration due to regional groundwater flow patterns (Fig. 4.3). Outline geometry corresponds to Figure 4.1.

plotted against sedimentary pile average permeability, for each value of basement permeability in Figure 4.5. The most striking feature of this figure is that for each value of basement permeability the calculated temperature field is identical across the range of sedimentary pile permeabilities. In each case there is no significant change in temperature within the basin at vertical sediment permeabilities of 0.05 mD and less, and only at vertical sediment permeabilities of greater than 0.1 mD do changes in temperature caused by regional fluid flow become detectable in terms of the resolution of our temperature data. It should also be noted that the temperature changes caused by regional fluid flow are most prominent within the East Central Graben (Nodes D and E, Fig. 4.1). However, in each case, the temperature anomaly formed is **not** comparable to the SWA's identified within the observed temperature profiles. For example, Figure 4.6 -- the calculated temperature field for a basement permeability of 10^{-4} mD and an average, vertical sediment permeability of 0.1 mD -- shows no significant (>10 °C) temperature "spikes" (SWA's) of less than 20 km wavelength.

In summary, topographically-driven fluid flow connected from basement to sediments, could cause temperature changes within the Central Graben at average vertical sedimentary permeabilities of greater than 0.01 mD. So there does exist the possibility for topographically-driven fluid flow to be affecting temperatures at the present-day. This temperature change however, would only be detectable from BHT data at vertical sediment permeabilities of greater than 0.1 mD, and in each case would be **independent** of basement permeability. The small potential thermal effects caused by regional fluid flow may modify the LWA established in Chapter 2, but do not compare favourably to the SWA's (Fig. 4.6).

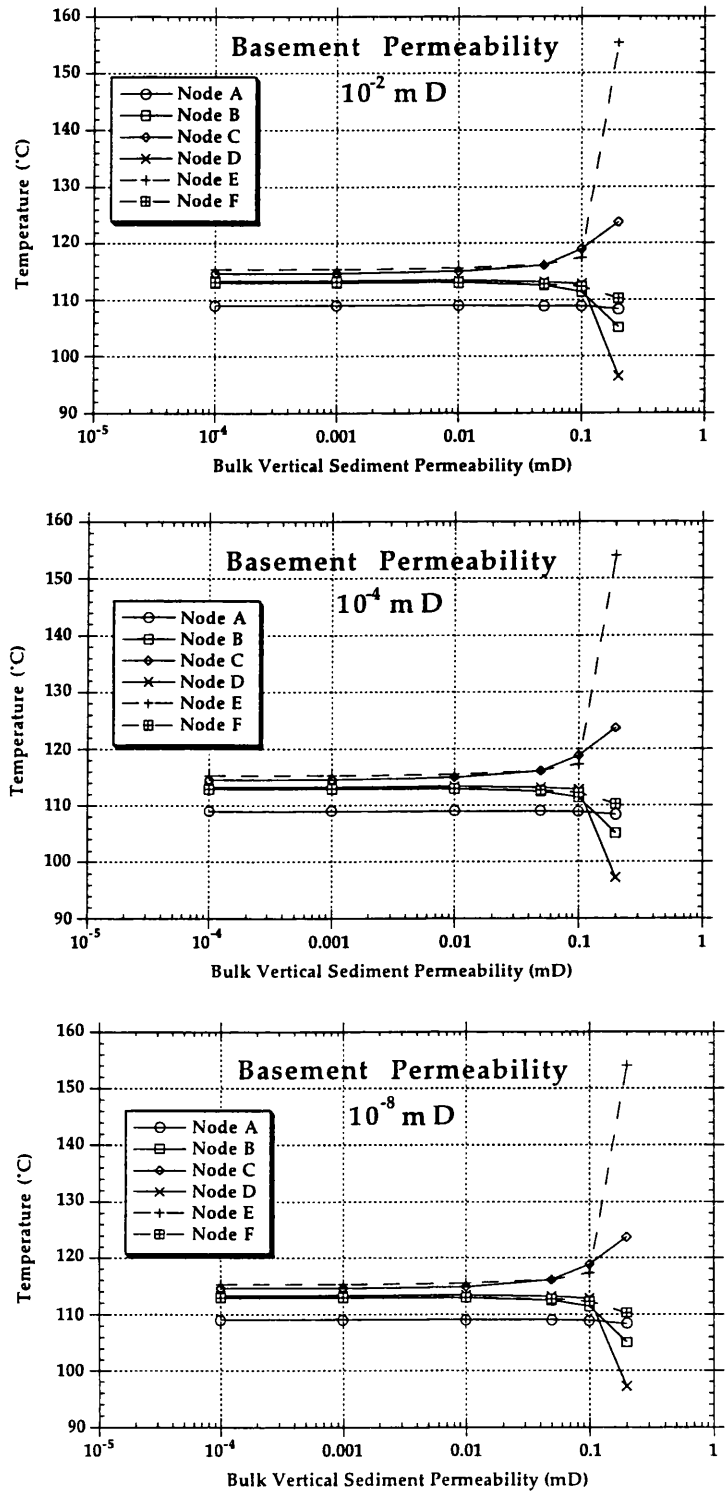

Figure 4.5 Calculated temperatures extracted from nodes A - F across the Central Graben (Fig. 4.3) for range in bulk sediment vertical permeability (suite of sediment permeabilities simulated at 10^{-2}, 10^{-4} and 10^{-8} mD basement permeability).

4.2.4 *Summary*

The basement permeability models (Fig. 4.1) are shown to have different threshold permeabilities for different sedimentary fill permeabilities (Fig. 4.2), with lower sediment permeability necessitating higher basement permeabilities to induce temperature change within the basin from the conductive temperature field. Where sediment permeabilities are relatively low (LOW models) basement permeability must exceed 0.1 mD, to produce any temperature change. Where the permeabilities are larger, in the HIGH suite of models, the threshold basement permeability is reduced to 0.001 mD due to the greater ease of penetration into the sedimentary pile of fluids moving through basement.

Published, "acceptable" values for basement permeability cover a wide range (Black (1987) and Clauser (1992)). However, from these models it is apparent that at realistic values for basement permeability (10^{-8} to 10^{-4} mD), fluid flow through basement plays no significant or detectable role in modifying the temperature regime of the Central Graben. Therefore, any major modification of temperature within the graben, from the purely conductive thermal regime, must take place within a higher permeability environment than homogeneous crystalline basement.

By modelling a sedimentary column of homogeneous permeability it is possible to predict at what bulk vertical permeability the resulting modelled temperature field will deviate from the purely conductive temperature field. Using the model shown in Figure 4.1 I can establish that the temperature regime behaves the same at basement permeabilities of 10^{-8}, 10^{-4} and 10^{-2} mD (Fig. 4.5) over a range of sediment permeabilities. This figure also shows that at a vertical bulk permeability of 0.05 mD or less for the sedimentary pile no significant temperature change is experienced across the entire basin. As the error margin in our BHT data is up to 10°C,

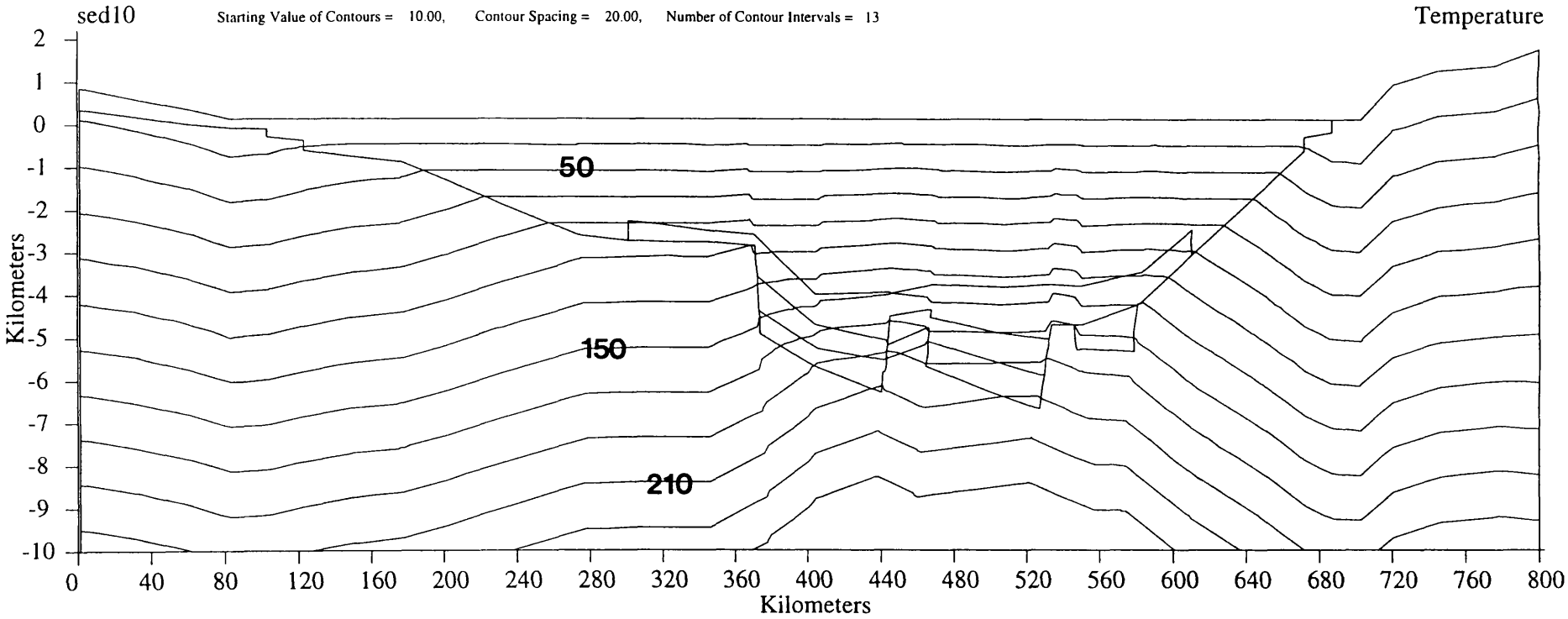

Figure 4.6 - Example temperature contour plot of Basement and the Sedimentary Pile: Bulk permeability model (Section 4.2.3). Temperature contours start at 10°C, and are in 20°C intervals. In this example, basement = 10^{-4} mD and average sediment vertical permeability of 0.1 mD.

the temperature effects of regional topographically-driven fluid flow would only be detectable at vertical, bulk sediment permeabilities above 0.1 mD. As the actual bulk permeability of the sedimentary pile most likely less than this value it is unlikely that the topographically-driven fluid flow affects temperature to any detectable degree within the basin. The shape of any potential anomaly would also NOT be comparable to the so far un-explained SWA's (Fig. 4.6).

4.3 Individual "Stratigraphic" Unit Model

Having established the vertical permeability required of the sedimentary pile as a whole, I now utilise the four unit geometry (Cenozoic, Cretaceous, Jurassic/Triassic and Palaeozoic sediments) for a more detailed study of sediment permeability and it's thermal effects (Fig. 4.7). I aim to define two parameters. Firstly, the threshold permeability within each unit at which the temperature field is significantly (10°C or greater) modified by fluid flow. Secondly, the maximum bulk vertical permeability possible in each unit (by comparing the simulated temperature profiles to the known interpolated temperature profiles established in Chapter 2 (Fig. 2.9).

For this "unit by unit" fluid flow modelling I assign Units 1 to 4 (Fig 4.7), and basement, a set of base-case poro-perm parameters (Table 4.2). Sediment permeabilities are approximated from: Unit 1 Garven and Freeze (1984); Unit 2, Brown (1987); Unit 3, Garven and Freeze (1984); Unit 4, Trewin and Bramwell (1991). Having shown previously that basement permeability between 10^{-2} and 10^{-8} mD does not significantly affect the temperature field within the Central Graben, I hold basement permeability constant throughout the rest of this chapters modelling at 10^{-4} mD. This base-case model, is essentially a coupled fluid and heat flow simulation of the best-case conductive model established in Chapter 2 with the thermal

UNIT	Base-Case Permeability (mD)	Porosity (%)	Anisotropy	Minimum Permeability Modelled (mD) horiz, **vert**	Maximum Permeability Modelled (mD) horiz, **vert**	Threshold Vertical Permeability /Theoretical Maximum Vertical Permeability (mD)
1	1.0	10	100	5.0, **0.05**	50, **0.5**	0.25
2	0.1	10	100	1.0, **0.01**	150, **1.5**	0.5
3	10	5	100	25, **0.25**	400, **4.0**	2.0
4	10	5	100	25, **0.25**	400, **4.0**	3.0

TABLE 4.2 - Model parameters, permeability ranges modelled and threshold permeability / theoretical maximum vertical permeability for Units 1 - 4. *The threshold permeability is defined as the maximum permeability at which the temperature deviation form background remains less than ± 10°C.* This also corresponds to the theoretical maximum vertical permeability. All models use a basement horizontal permeability of 10^{-4} mD (anisotropy of 5).

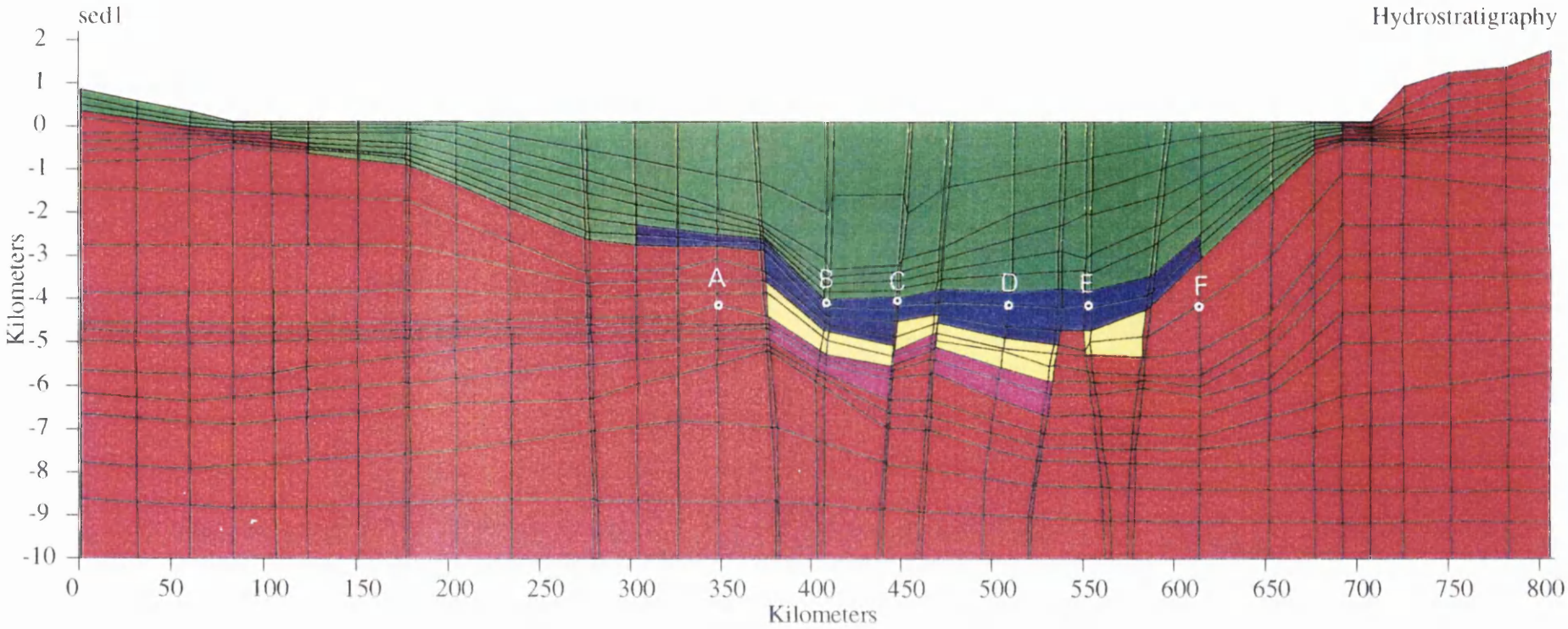

Figure 4.7 - Geometry of regional fluid flow model showing nodes of temperature extraction at 4 km (A - F). Units 1 - 4 are green, blue, yellow and purple, respectively. Basement is shown in red (see Table 3.2 for stratigraphic definition of Units 1 to 4).

properties of both models identical and provides the "background" temperature field, against which all subsequent simulations are compared. The temperature field for the base-case coupled model does not significantly differ from the conductive model.

4.3.1 *Threshold Permeabilities for Temperature Change*

Having established a background temperature field (in which fluid flow does not significantly alter temperatures) I increase the permeability of each unit in turn from the base-case value, and observe the associated temperature changes across the graben caused by the rising fluid velocities. Table 4.2 shows both the base-case permeabilities assigned to each unit and the range in permeability through which each unit is modelled.

For each simulation I extract the calculated temperature from six nodes (A - F), evenly spaced across the graben (Fig. 4.7) at an arbitrary depth of 4 km. From this data a composite plot of deviation in temperature from background, against Unit permeability is constructed for each of Units 1 - 4 (Fig. 4.8). This shows the magnitude of change in temperature caused at each value of sediment permeability across the graben. If I define a threshold permeability as being *the maximum modelled vertical permeability at which temperature deviation from background remains less than 10°C* (10°C being the maximum error in our temperature data) then it is apparent that Unit 1 has the lowest threshold permeability (0.25 mD) and Unit 4 the highest (3.0 mD) (see Table 4.2).

From this I can deduce that the vertical permeability of the lower units would need to be significantly greater than the shallower units, in order to create the same magnitudes of temperature change within the basin.

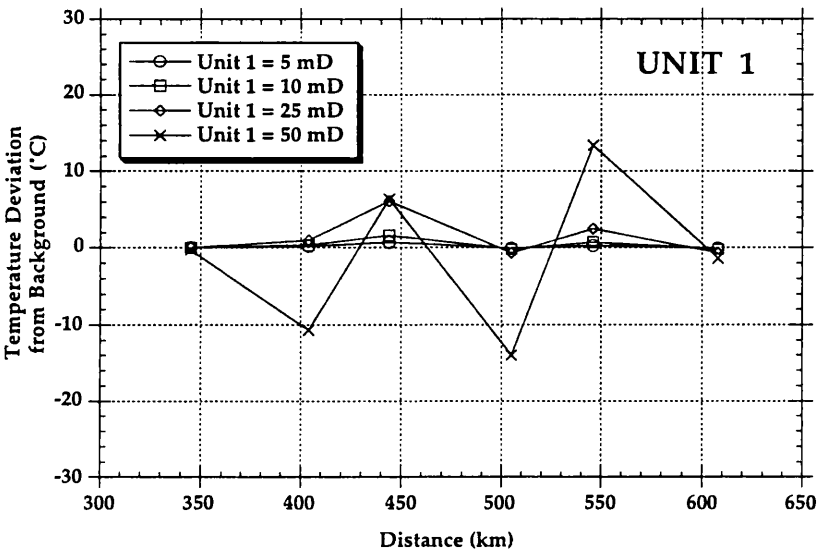

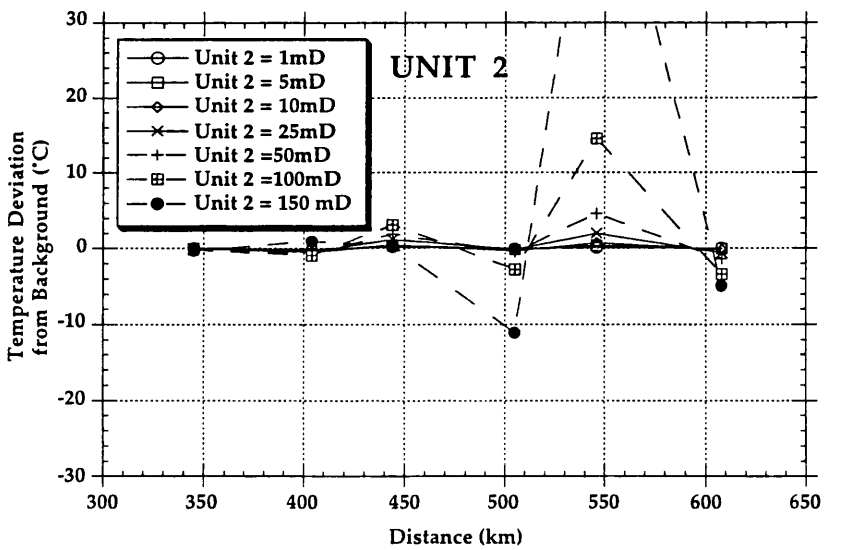

Figure 4.8 - Temperature deviation from background for Units 1 - 4 (see over for units 3 and 4) at varying horizontal permeabilities. In each case anisotropy is 100. These graphs are used to define the threshold permeability of each Unit. Threshold is defined as the maximum modelled permeability at which the temperature change from background remains less than 10°C. These are listed in Table 4.2.

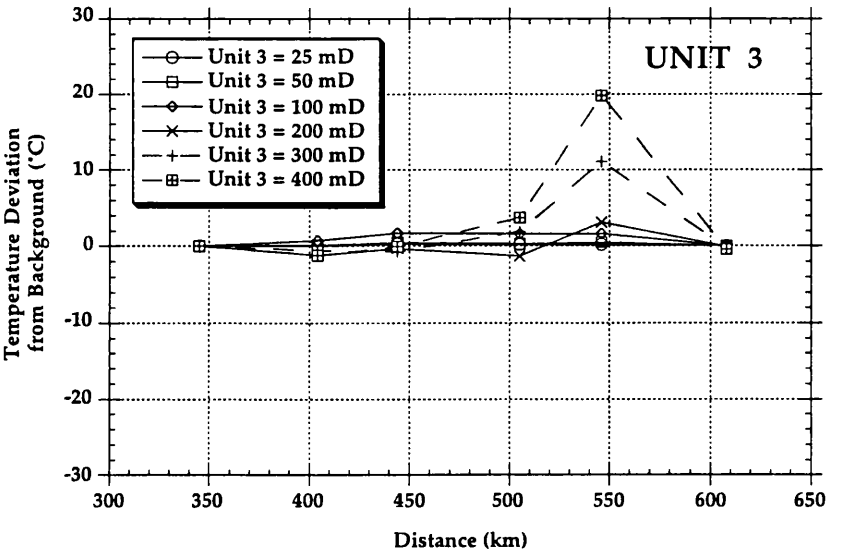

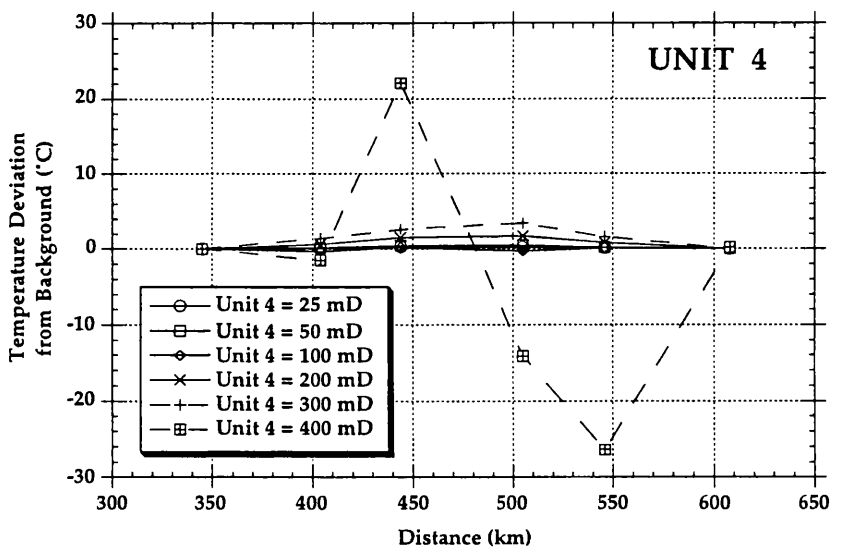

Figure 4.8 (cont.) - Temperature deviation from background for Units 3 and 4 at varying horizontal permeabilities. In each case anisotropy is 100. These graphs are used to define the threshold permeability of each Unit. Threshold is defined as the maximum modelled permeability at which the temperature change from background remains less than 10°C. These are listed in Table 4.2.

4.3.2 *Comparison to Interpolated Temperature Profiles*

Up to what value of permeability (for each individual Unit) do these resulting temperature profiles still compare favourably to reality? In order to assess this, for each Unit I plot the resultant temperature profile for each simulation against the interpolated-temperature profile at 4 km depth established from the BHT data. These plots (Fig. 4.9) show how realistic each simulation is relative the present-day temperature field. For example Fig. 4.9 (A), the plot for Unit 1, shows that vertical permeabilities of up to 0.25 mD produce a LWA temperature profile comparable to the interpolated profile calculated in Chapter 2 from the BHT data. Therefore the maximum (realistic) vertical bulk permeability modelled for Unit 1 is 0.25 mD. A vertical permeability of 0.5 mD for Unit 1 clearly produces an unrealistic LWA temperature profile. By this means I establish a theoretical maximum vertical permeability for each of Units 1 - 4 of 0.25, 0.5, 2.0, and 3.0 mD respectively (Fig. 4.9, Table 4.2).

These temperature changes, are NOT a result of topographically-driven regional fluid flow, but are caused by **convection** within each Unit as the vertical permeability approaches the previously established threshold value. Figures 4.10 (A) and (B) show plots of both groundwater velocity (Fig. 4.10A) and stream function (Fig. 4.10B) for Unit 3 at 200 mD horizontal permeability (2 mD vertical permeability). It is clear from this figure that although there is little temperature change due to convection at a horizontal permeability of 100 mD (Fig. 4.8), at 200 mD the convection cell is well established (with fluid velocities of up to 2.1 ma-1) and the resulting basin-wide temperature changes are much more significant (see Fig. 4.8). It should also be noted that the convection cell is almost entirely contained within Unit 3, (flow rates in Unit 2 and 4 (above and below) remaining relatively low; see Fig. 4.10A). This is true for each of the simulations i.e.

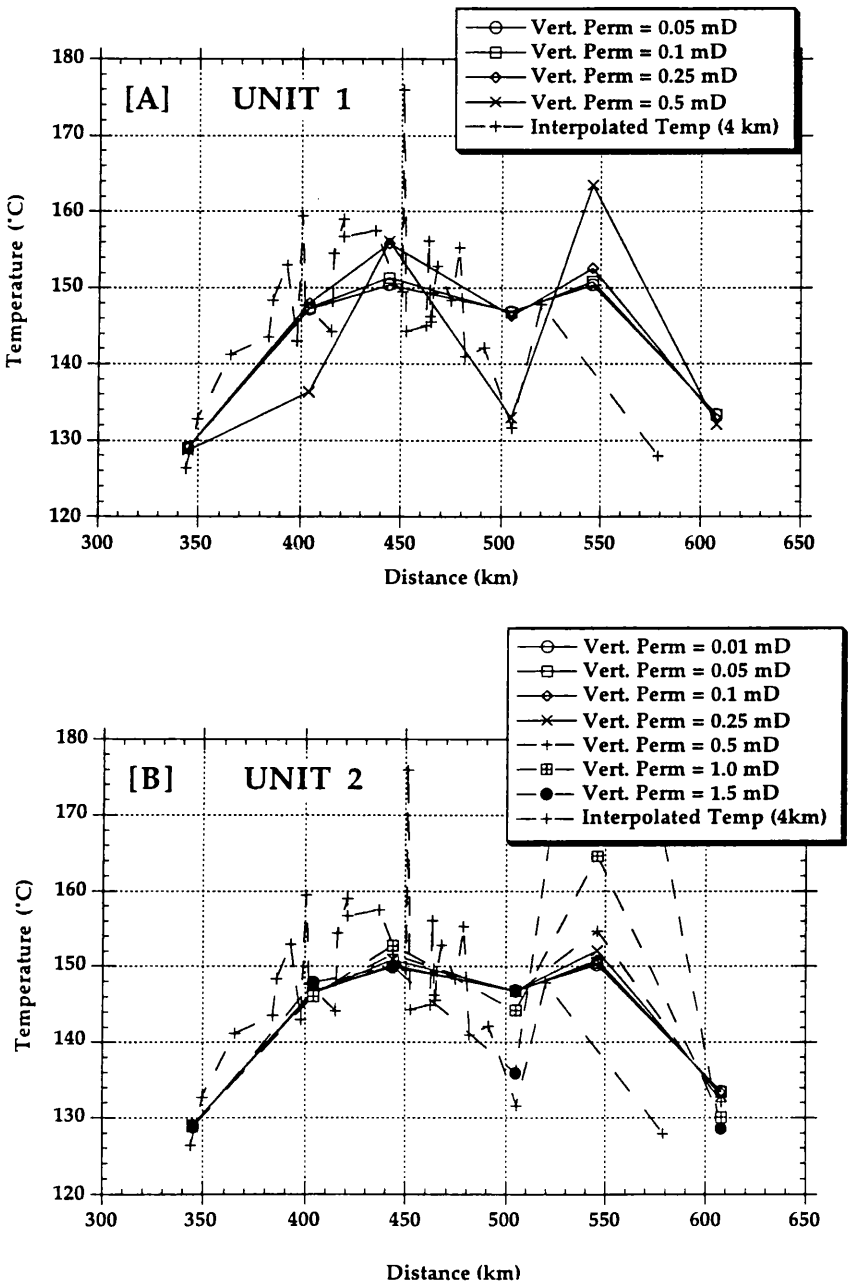

Figure 4.9 - Calculated temperature profiles at 4 km depth, (over a range in sediment vertical permeabilities) compared to the interpolated-temperature profile from 4km depth (Fig. 2.9) for each of Units 1- 4. These plots show how realistic each simulation is with respect to the present-day temperature field. Units 3 and 4 are shown overleaf.

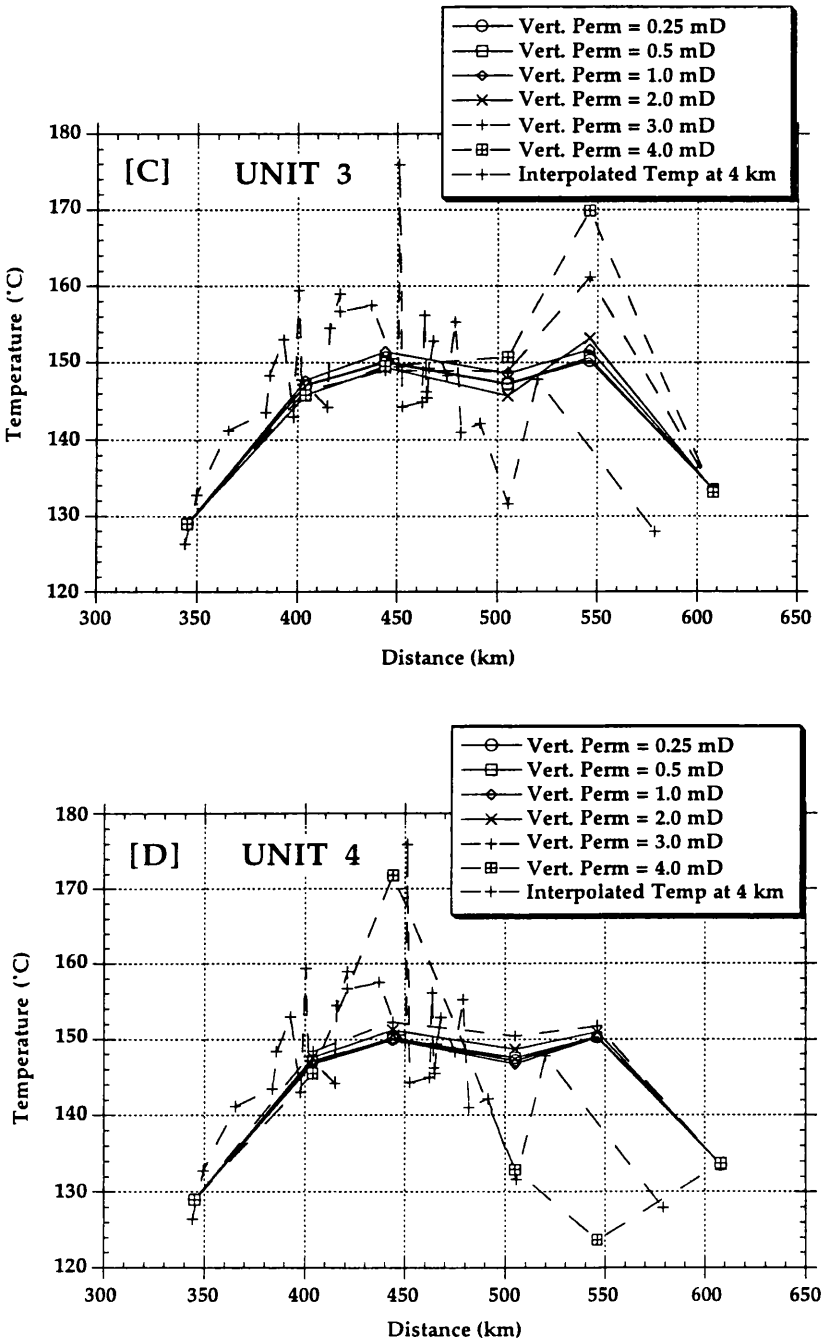

Figure 4.9 (cont.) - Calculated temperature profiles at 4 km depth, (over a range in sediment vertical permeabilities) compared to the interpolated-temperature profile from 4km depth (Fig. 2.9) for Units 3 and 4. These plots show how realistic each simulation is with respect to the present-day temperature field.

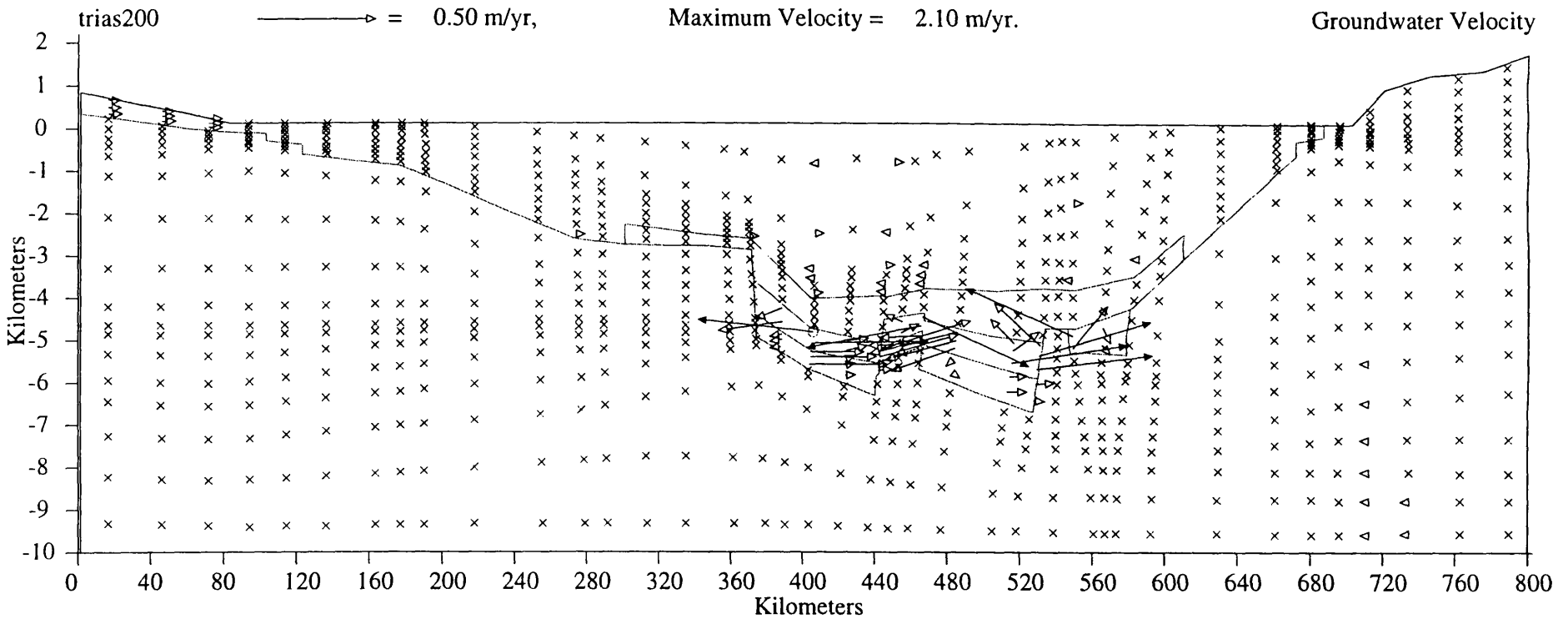

Figure 4.10A - Regional groundwater velociy plot for Unit 3 = 200 mD horizontal permeability (2 mD vertical permeability). Maximum groundwater velocity is 2.1 ma-1, (the vectors in this plot are scaled between 50 cma-1 and 0.5 cma-1, with X's marking flow velocities in this case of less than 0.5 cma-1, not of no flow). Increased fluid velocities (from those shown in Figure 4.3 - the base-case model) are restricted to the unit of raised permeability, in this instance Unit 3. Outline geometry corresponds to Figure 4.1.

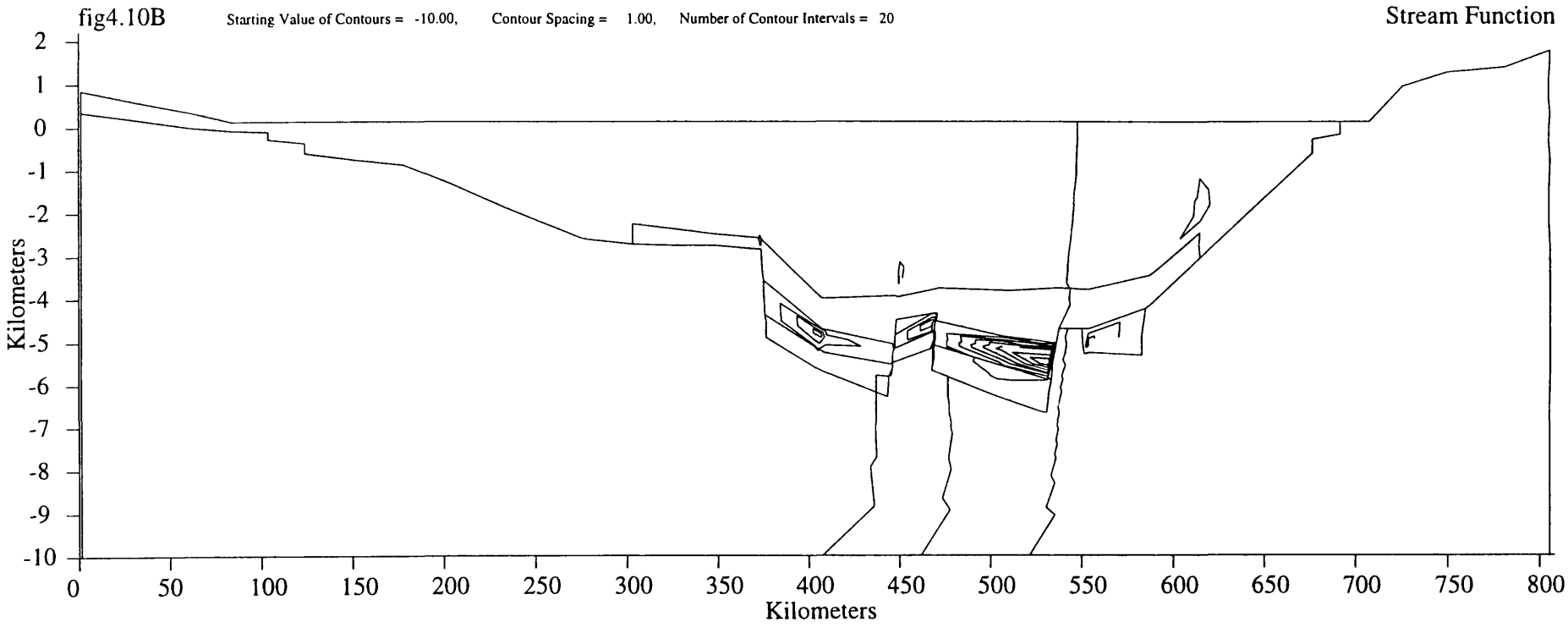

Figure 4.10B - Plot of stream function for Unit 3 = 200 mD horizontal permeability (2 mD vertical). Shows convection in the Jurassic/Triassic units more strongly evident within the eastern Central Graben. Outline geometry corresponds to Figure 4.7.

the convection cell established is almost entirely limited to the Unit of raised permeability (results not shown).

Although convective fluid flow has the potential to alter the temperature field within the Central Graben, the major convection modelled within the basin would only occur at values of permeability at or above the theoretical maximum. By establishing the true permeability of each Unit (potentially from borehole data), we can determine whether convection is likely to be affecting temperatures within the basin at the present day.

In geological terms, Units 1 and 2 are the least likely of the four to exceed the threshold permeability, induce convection and modify the temperature field. Unit 1 represents the Cenozoic sediments of which the majority are shales (Kent, 1975), and bulk permeability estimates are of the order of 1 mD or less (after Garven and Freeze, 1984). Unit 2, is dominated by the Cretaceous chalk (Kent, 1975) and horizontal matrix permeabilities are estimated at approximately 0.1mD (Brown 1987). Therefore these two units are not likely to be undergoing regional convection at the present-day.

However, Units 3 and 4 are more likely candidates for convective fluid flow and the associated transport of heat, consisting more dominantly of sandstones (Kent 1975; Glennie 1990). Unit 3 though, if it was indeed experiencing major convection, would form a shape of anomaly inconsistent with the known present day temperature profile (Fig. 4.9 C), so again it is very unlikely that the Jurassic and Triassic units within the Central Graben are experiencing major convection today. Unit 4 represents the Palaeozoic sediments, dominated by the Permian. Much of the Permian within the Central Graben is composed of Rotliegend "red beds" (Ziegler 1978), and in places dune sands (Kent, 1975) and is known to possess permeabilities of up to 1 D (Trewin and Bramwell, 1991) on the graben flanks (but is generally undrilled within the deep graben). Unit 4 may

therefore possess a high enough vertical permeability to allow significant convective fluid flow.

If convective fluid flow *is* taking place within the Central Graben, then would the shape of temperature anomaly formed be compatible with the known present day temperature field? An initial view of Figure 4.9 (D) suggests not, with the 400 mD model being significantly different. However, when an additional, more detailed range of Unit 4 permeabilities (350 to 390 mD) is modelled, it is apparent that at 350 to 360 mD (3.5 to 3.6 mD vertical permeability) the resultant temperature profiles are not only compatible with the overall shape of the present-day temperature field, but are a closer match to the present day temperature field than the purely conductive model (Fig. 4.11). The temperature anomalies formed due to this regional convection are in the form of temperature steps. The temperature distribution across the graben, with Unit 4 = 350 mD, is displayed in Figure 4.12.

Therefore, minor convective fluid flow may take place within the Central Graben over Unit 1 - 3, with small associated temperature effects, although is most likely *below* the Cretaceous chalk. The error within the measured temperature profiles however, leaves me unable to speculate further. By contrast, in the case of Unit 4, it appears that regional convective fluid flow may be taking place at the present-day at a magnitude detectable by our measured temperature data (Fig. 4.11 & 4.12).

4.3.3 *Summary*

Using the geometry in Figure 4.7 I investigate at what bulk vertical permeability each of the designated four units (Cenozoic, Cretaceous, Jurassic/Triassic, and Palaeozoic) significantly affect the temperature field, and define where possible a maximum vertical permeability for each unit by

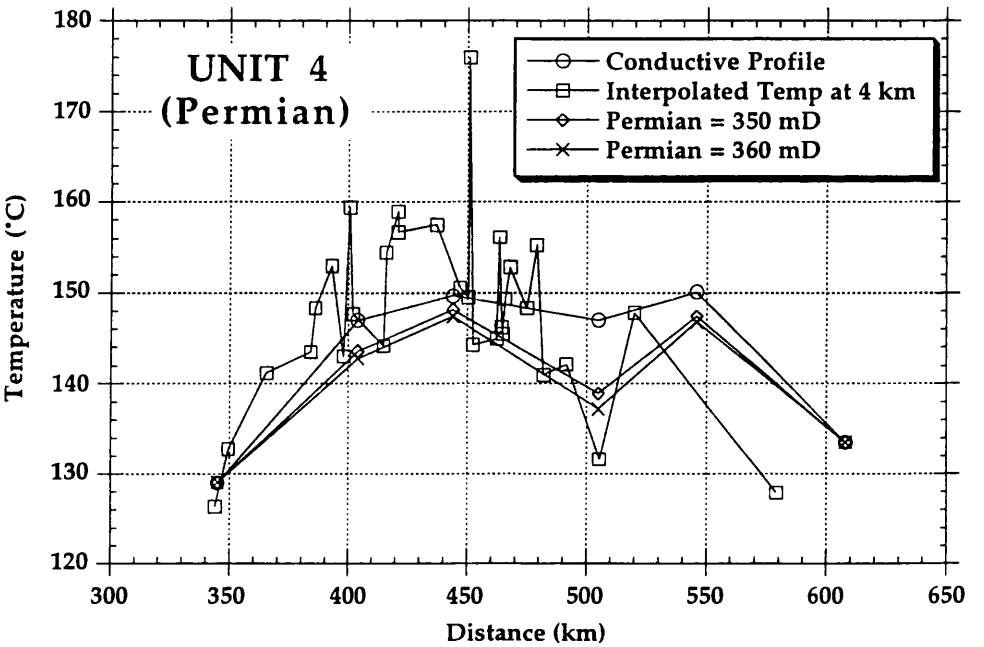

Figure 4.11 Conductive and interpolated temperature profiles compared to Permian model at 350 and 360 mD (Unit 4). Permian convection at 350 - 360 mD produces a closer match to the modern temperature profile than the purely conductive model. Permeabilities listed are horizontal (anisotropy = 100).

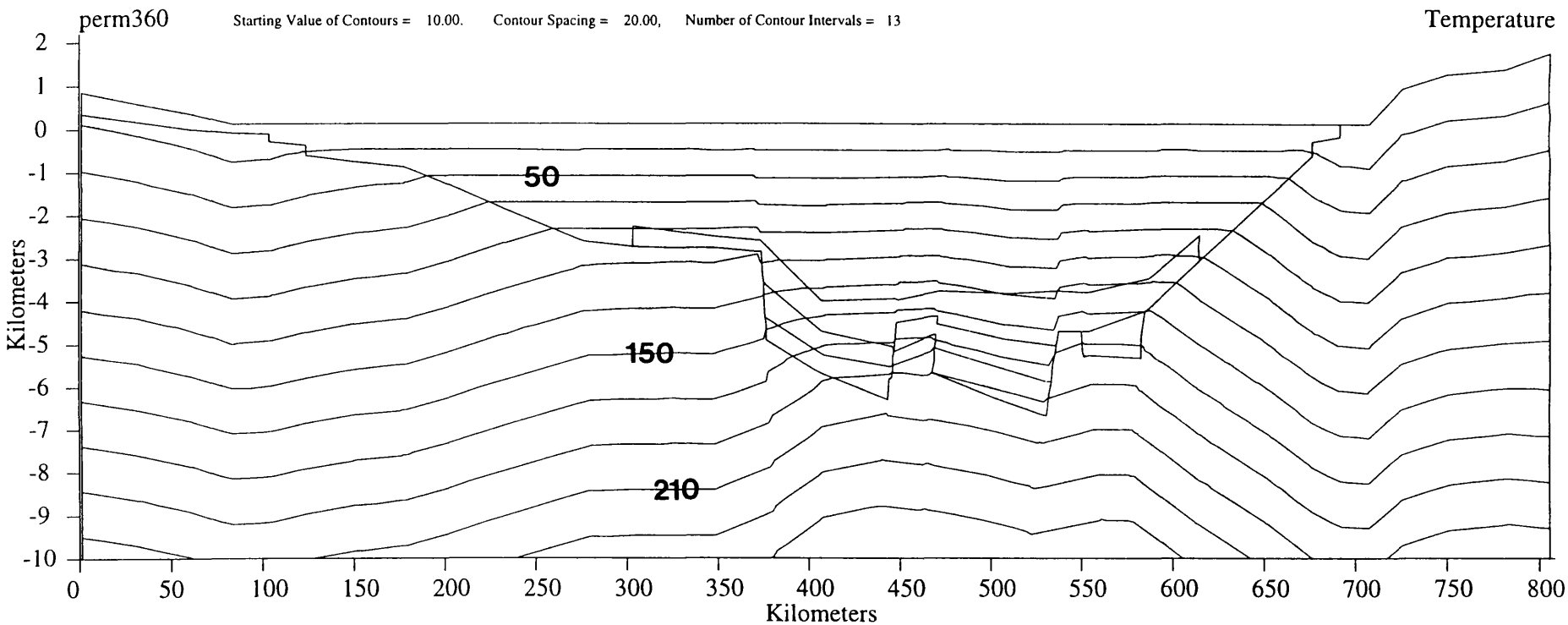

Figure 4.12 - Temperature contour plot for simulation of Unit 4 = 360 mD horizontal permeability (3.6 mD vertical). Temperature iostherms depressed in eastern Central Graben (compare to Fig. 4.11) due to regional fluid convection within Unit 4. Outline geometry corresponds to Figure 4.7.

comparison of the resultant temperature field to the temperature profiles established in Chapter 2. To achieve this I first assign base-case (realistic) values to each of the four Units. Then by raising the permeability of each unit in turn and recording the temperature changes at 4 km depth within the basin I can observe the difference or similarities between the simulated temperature profile and the observed (interpolated) profiles. A threshold permeability for each unit is defined as the maximum modelled vertical permeability at which the resultant temperature change remains less than 10°C. These are initially calculated as being 0.25, 0.50, 2.0, and 3.0 mD for Units 1 to 4 respectively (Fig. 4.7). At higher vertical permeabilities therefore, any temperature effect due to fluid flow within the Unit should be evident on the interpolated temperature profiles. By plotting the resultant (calculated) temperature profiles for each model, and comparing these with the interpolated temperature profile (Fig. 4.9), the theoretical maximum permeability can be established i.e. at what permeability the calculated temperature profile is still comparable to the "real" temperature profile. The theoretical maxima for each of Units 1 to 4 are calculated as being 0.25, 0.50, 2.0, and 3.0 mD vertical permeability respectively (the same as the threshold permeabilities). Units 1, 2 and 3 are in reality, unlikely to exceed the threshold permeabilities. Even if thresholds were exceeded they, would form anomalies of incompatible shape to the present day temperature field (Fig. 4.8 (A - C)). However, Unit 4, comprised of a significant thickness of Rotliegend "red beds" (Ziegler 1978) with some dune sand sequences (Kent 1975), would be expected to have relatively high permeability. More detailed modelling of Unit 4 suggests that not only is the resulting temperature profile (for a vertical permeability of either 350 or 360 mD) compatible with the interpolated profile, but it is a better fit than the conductive profile (Fig. 4.11). This suggests that fluid convection within the Permian at the present-day affects temperatures within the Eastern Central

Graben. Through examination of the stream function plots for these models it is apparent that temperature change within each Unit is the product of internal convection(Fig 4.10 and 4.13).

4.4 Conclusions

4.4.1 *Basement Permeability Effects on Temperature and Fluid Flow*

The geometry of the basement model is shown in Fig, 4.1. This geometry is modelled using a range in basement permeabilities of 10^{-14} to 1.0 mD at two different suites of sediment permeability (LOW and HIGH, see Table 4.1). Temperature within the basin remains unaffected by fluid flow through basement for the HIGH suite of sediment permeabilities at a basement permeability of less than 0.001 mD (10^{-3} mD). In the LOW suite of sediment permeabilities a basement horizontal permeability of 0.1 mD is required to change the temperature field within the basin from the conductive state (Fig. 4.2).

As realistic values for basement permeability are of the order of 10^{-4} mD or less (Black, 1987; Clauser, 1992), it is most unlikely that fluid flow through basement has any direct effect on temperature in and around the graben area. This is confirmed by the sedimentary pile bulk permeability modelling. Using the same geometry as the initial basement model (Fig. 4.1), a suite of sediment permeabilities are modelled at three values of basement permeability (10^{-2}, 10^{-4} and 10^{-8} mD), to observe at what threshold bulk sediment permeability temperature is affected within the basin. For each of the three suites of models the results are identical (Fig. 4.5). Thus, it is sediment permeability which is dictating fluid velocities and temperature change within the basin. Therefore basement, although possibly a conduit of meteoric fluid recharge to the graben, at realistic

permeabilities does not directly influence the fluid flow and temperature regime within the Central Graben.

4.4.2 *Sediment Permeability Effects on Temperature and Fluid Flow*

The sediment permeability models each use the same geometry (Fig. 4.1), with varying physical properties. In the case of a bulk sedimentary permeability being assigned to the basin, a threshold bulk vertical permeability of 0.05 mD (Fig. 4.2) is established for the sedimentary pile, below which there is no change in temperature across the basin due to fluid movement. Above 0.1 mD vertical permeability the temperature change caused by fluid movement is greater than 10°C (within the detection limits of our BHT data). However, it is unlikely that the sedimentary pile achieves such high bulk vertical permeabilities, and the resulting temperature plots are incompatible with the present-day temperature profile (for example Fig. 4.6) at a vertical bulk permeability of 0.1 mD. Therefore the modelled topographically or gravity-driven fluid flow causes no major temperature change within the sedimentary pile.

The individual stratigraphic unit models are a better representation of reality. By assigning base-case values of poro-perm to each Unit and varying the permeability of each of Units 1 to 4 individually, I establish a maximum theoretical sediment vertical permeability of 0.25 (Cenozoic), 0.50 (Cretaceous), 2.0 (Jurassic/Triassic) and 3.0 mD (Palaeozoic), by comparing the resulting modelled temperature profile against the observed BHT profile (Fig. 4.9). It is apparent from these plots (Fig. 4.9) that if significant temperature effects (10°C or greater, higher than the error of our temperature data) were caused by fluid movement within Units 1 to 3, that they would form temperature profiles incompatible with the present-day temperature profiles. Units 1 & 2 are also unlikely to achieve the high

permeabilities necessary. However Unit 4, at a vertical permeability of approximately 3.5 - 3.6 mD (anisotropy of 100), would result in a temperature profile closer in shape to the observed BHT temperature profile than the conductive profile (Fig. 4.11). Therefore it is likely that fluid flow within the Permian is significantly modifying the temperature field at the present-day. A plot of stream function for Unit 4 at 360 mD shows that this temperature change is a result of *convection* within the Permian (Fig. 4.13). The temperature anomaly associated with this regional convection is in the form of a temperature step (Fig. 4.12) and is NOT comparable to the SWA's identified within Chapter 2 which remain unexplained thus far.

4.4.3 *Implications*

From this regional fluid flow modelling, it is apparent that of the regional fluid processes simulated, only fluid convection has the potential to significantly affect the temperature field. Regional topographically/gravity driven flow *may* result in minor temperature changes of a few degrees but this cannot be confirmed due to the error associated with our BHT data (up to 10°C). However major topographic-driven flow regimes with associated temperature changes, as described by Garven (1989, 1995) do not take place within the Central Graben.

As the convection modelled in Unit 4 produces temperature *steps* as opposed to the temperature *spikes* (SWA's; Fig 4.12) observed within the interpolated temperature profiles, regional fluid flow (topographically or convection driven) cannot be responsible for the formation of SWA's. What process is then responsible for these SWA's?

It is apparent from the individual stratigraphic unit models that in order to induce temperature change, a relatively high vertical permeability environment of 10's to 100's of millidarcies is necessary, involving

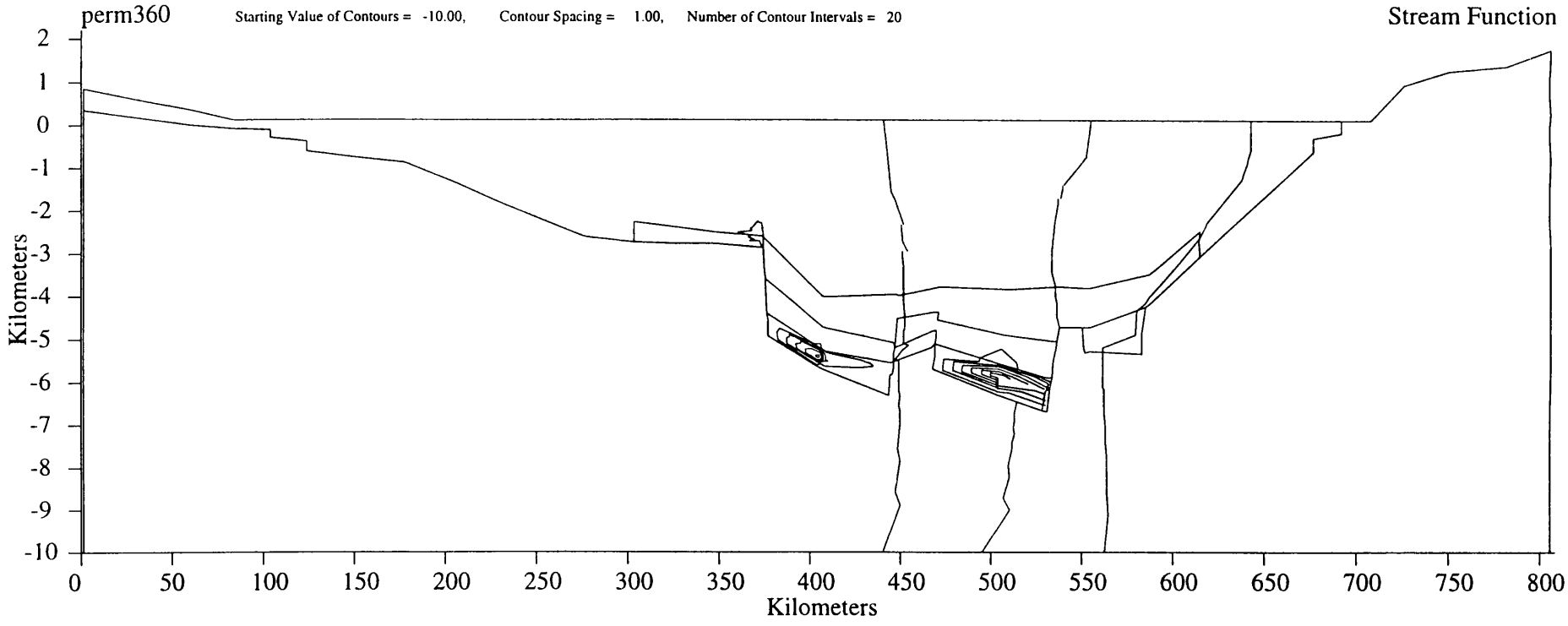

Figure 4.13 - Stream function plot for simulation of Unit 4 = 360 mD horizontal permeability (3.6 mD vertical). Regional fluid convection within Unit 4 strongly evident, especially within the eastern Central Graben. Outline geometry corresponds to Figure 4.7.

significant vertical fluid flow within a more localised setting than the regional flow models. Therefore, the environment in which these SWA's are formed must be permeable, small scale, and vertical or sub-vertical. It is possible then that fluid flow within vertical/sub-vertical fractures or faults is responsible for these short-wavelength temperature anomalies. The potential and likelyhood of this process to form these SWA's will be addressed in the next Chapter.

CHAPTER 5

LOCALISED FLUID FLOW AND ASSOCIATED THERMAL EFFECTS

5.1 Introduction

The previous two chapters have assessed the potential of firstly, thermal conduction processes (Chapter 3) and, secondly regional fluid flow mechanisms (Chapter 4), to explain the observed variability in the present-day temperature field (as established in Chapter 2). Neither of these processes independently, or combined, are able to provide a match for the SWA's established by the temperature profiles described in Chapter 2. The conclusion drawn was that a more localised process must be involved in the formation of these short-wavelength, high-magnitude temperature features.

Two possibilities are considered in this chapter: (a) the thermal effects of rapid convection of fluids within a small, isolated convection cell; and (b) the thermal effects of fluid flow within fault or fracture zones. Regarding the role of faults/fractures in fluid flow systems, Chapman (1987) states that "There is no true general statement of the form: 'Faults do/do not act as conduits for fluid flow'". There is evidence, though, to show that faults may focus fluid flow (Knipe, 1993; Sibson 1994). Circumstantial evidence from the concentrations of mineralisation around faults (Fowler, 1994), to fluid flow associated with earthquake activity (Sibson, 1975; 1994) and the presence of "dry" strata between source rocks and reservoirs (Knipe, 1993) points to the fact that faults **may** act as the key element for fluid flow. Therefore they must be considered in this study for any thermal effect that may be associated with fluid flow along faults or fracture zones.

5.1.1 *Summary of Methodology*

In each of the two areas of investigation (small scale convection, and fluid flow along faults), I first investigate the thermal effects caused by each process using test grids. These grids are designed to have a broad similarity to the geometry of the Central Graben (Fig. 3.1) along the original section line (Fig. 1.1), but they reduce the complexity of the natural system, thereby allowing cause/effect relationships to be more readily discerned.

In the case of the convection modelling, I use the test grid to establish a range in permeability values for both the sedimentary pile and the convection cell at which a significant disturbance occurs to the temperature regime. The Central Graben model is based on the best-fit model derived from thermal modelling described in Chapter 3 (Fig. 3.9 & 3.12), but with the addition of a high permeability unit within both the east and west Central Graben. Using conservative poro-perm values for the major "stratigraphic" units I observe the fluid velocities and temperature changes caused by increasing the permeability within the convection cell, and I compare the resulting temperature patterns to those observed in the temperature profiles described in Chapter 2 (Fig. 2.9).

In investigating the role of focused fluid flow within the Central Graben, I again use a series of test grids to assess the possibility of focused flow within an analogous Central Graben setting, for both a homogeneous and heterogeneous sedimentary pile. By this means I assess the ranges in fault and sediment permeability that are capable of producing significant temperature disturbances within the Central Graben. Again, I compare the resulting temperature anomalies with those described in Chapter 2.

The final set of simulations again use a modified Central graben model. It differs from the thermal modelling mesh (Fig. 3.2) by the addition

of a Palaeocene unit above the Cretaceous chalks, and by the addition of a 300 m wide fault zone in the east Central Graben. This model, and other similar models with minor variations of geometry, are used to assess the influence on the thermal regime of each sedimentary units permeability, the fault permeability, and the nature of the fault outlet zone.

5.2 Small Scale Convection

5.2.1 *Isolated High Permeability Units - Test Grids*

In order to test the ability of localised convection to significantly alter the temperature field within the Central Graben, I design a test grid (Fig. 5.1) which broadly reflects the geometry of the western half of the Central Graben (along the original section line described in Chapter 1, Figure 1.1). Modelling the fluid flow that occurs in this test grid, using OILGEN (Garven (1989) produces temperature contour maps which I compare against the conduction-only temperatures. The basic model (Fig. 5.1) has, as the Central Graben has, a maximum depth of sediment fill of approximately 6 km, and a typical North Sea "steers head" sediment geometry. A topographic high of 30 km width and a maximum height of 1 km is given to the south-western end of the section.

I have shown that the SWA's described in Chapter 2 are inexplicable in terms of either conductive heat transport, or regional fluid flow. The SWA's are of approximately 15 km half-wavelength or less, so if localised convection were responsible for the SWA's, the convection cell size responsible for the SWA may well be of a similar lateral width. Therefore, I approach the modelling of small scale localised convection by investigating several different thicknesses of convection cell, at 10 and 20 km widths, over a range of convection cell and sediment permeabilities.

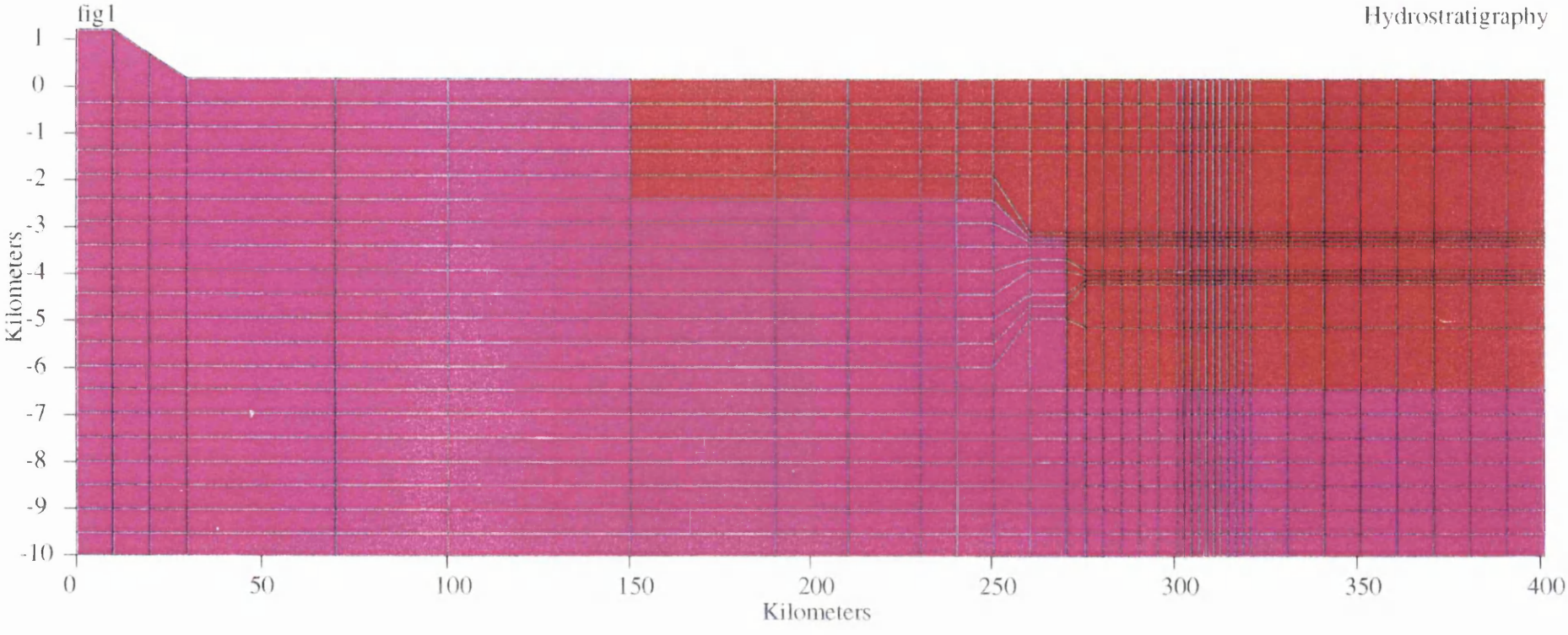

Figure 5.1 - Basic geometry of model used for convection cell modelling - test grids. Basement -purple, sediment fill - red. Topographic high of 1 km. This model is designed to be broadly analogous to the western Central Graben.

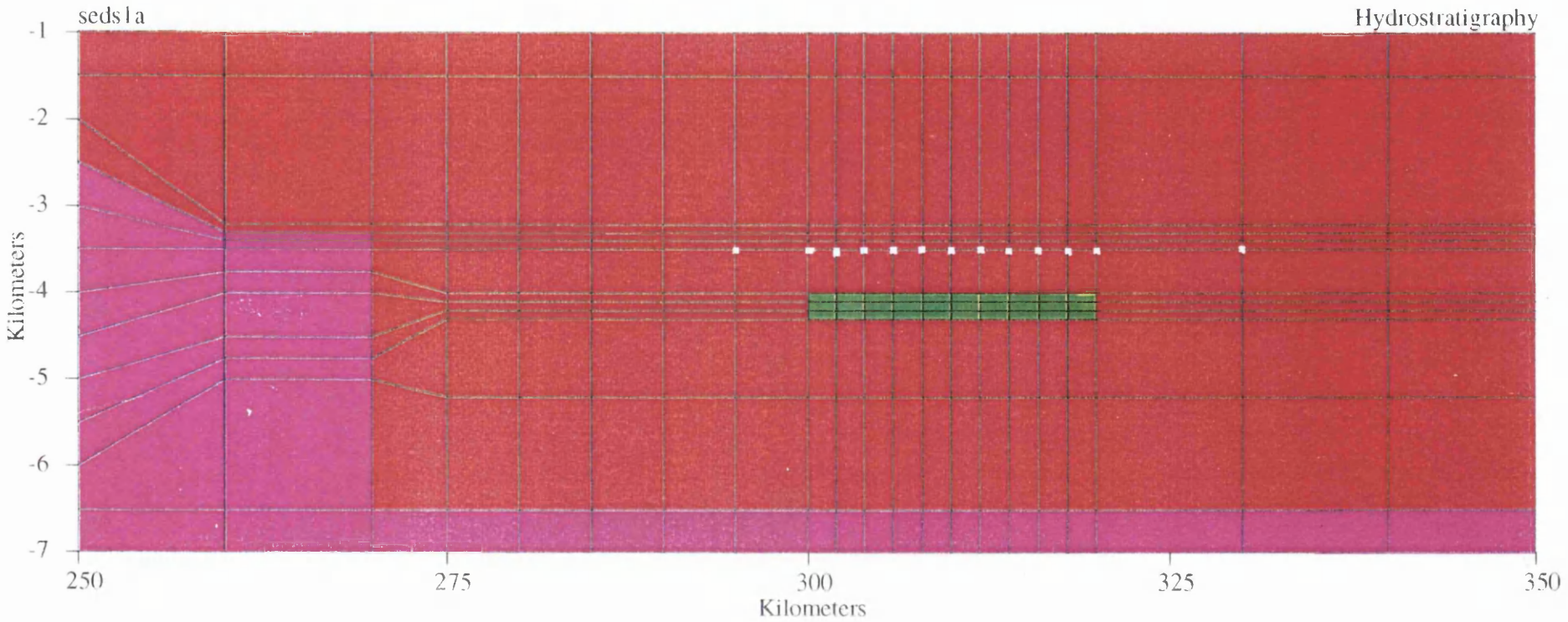

Figure 5.2 - Geometry of convection cell Models 1 and 2 (Section 2.1.1). Convection cell is 20 km wide by 400 m thick and lies at 4 km depth. This is an enlarged view of Figure 5.1, with basement geometry remaining constant. The nodes of temperature extraction are highlighted in white. NOTE Basement - purple, sediment fill - red and convection cell - green.

I firstly model a 20 km wide by 400 m thick cell (Fig. 5.2) surrounded by a homogeneous sedimentary fill (permeability 1 mD and anisotropy of 100; Table 5.1, Model 1), over a range of convection cell permeabilities. I then (using the same geometry) model the effects of a sedimentary fill permeability of 5 mD over the same range in convection cell permeabilities (Table 5.1, Model 2). In each simulation I recorded the temperature change from background (i.e. the conductive state) at the nodes highlighted in Fig. 5.2 above the convection cell. The magnitude and dimensions of any temperature disturbance due to convection are shown by plotting the recorded temperatures against distance for each value of convection cell permeability (Fig. 5.3A). This plot shows that at a sediment permeability of 1 mD (Model 1), a convection cell horizontal permeability of 4 Darcies (anisotropy of 100) is needed to produce a significant change in temperature from background. At 4 D two distinct fluid upflow zones form, giving rise to a temperature **step** at A of up to approximately 20 °C and a temperature **peak** of approximately 20°C at B (the temperature peak at B having a half-wavelength of approximately 12 km). Model 2 (Fig. 5.3B), with its sediment permeability of 5 mD, also requires a convection cell permeability of 4 D before there is a significant change in temperature from background. In this case, however, a composite temperature peak forms, of approximately 15 km half-wavelength, and almost 30 °C magnitude. Note that this temperature peak is depth-limited in nature (Fig. 5.4).

The next three model geometries assume a convection cell width of 10 km (this size of cell is used as the SWA's range from 5-15 km in width); the cells vary from 200 to 800 m in thickness (Models 3 - 5, Figure 5.5) with sediment permeability held constant at 1 mD (Table 5.1) in each case. Using the same method of investigation as employed for Models 1 and 2, I record the temperature at nodes shown in Figure 5.5 for a range of convection cell

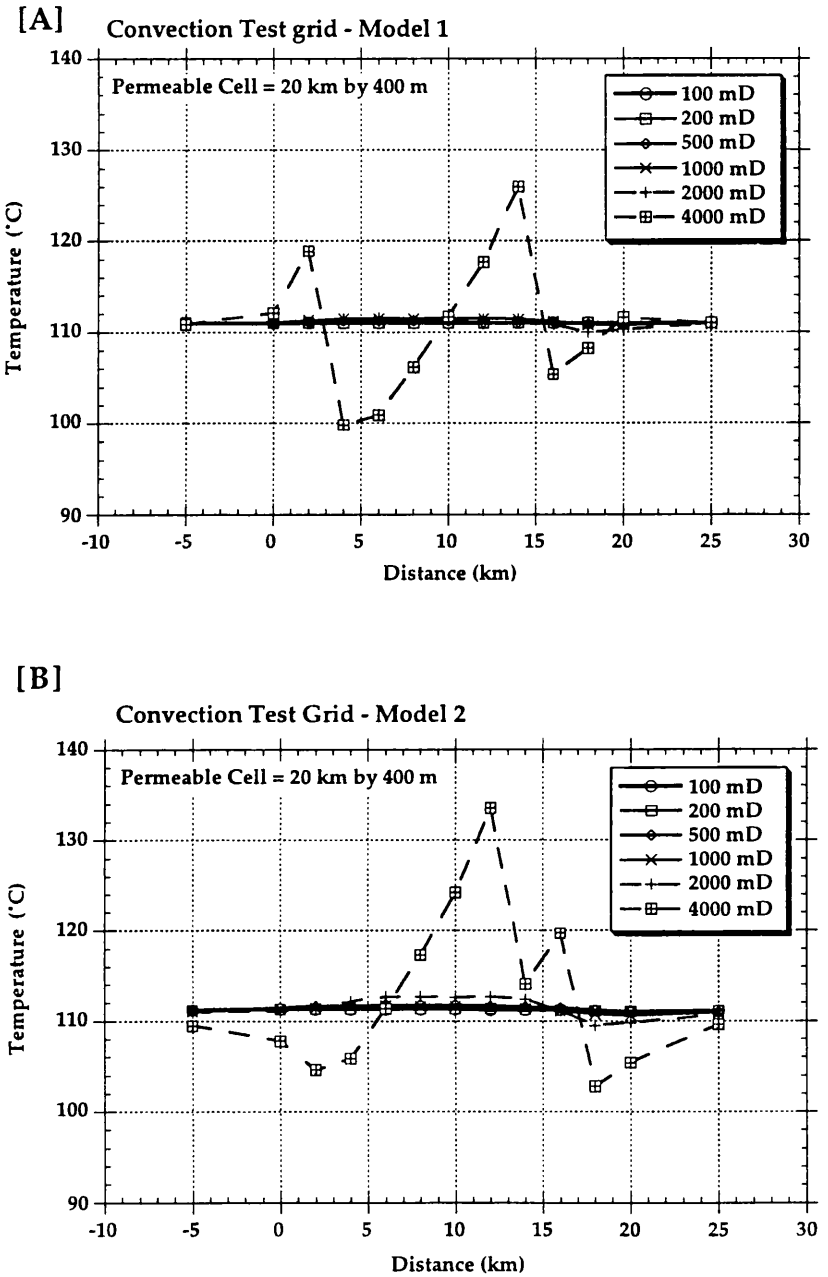

Figure 5.3 - Temperature variation over HPU shown in Figure 5.2 for a range in HPU permeabilities (Models 1 and 2). [A] - sediment horizontal permeability = 1 mD, [B] - sediment horizontal permeability = 5 mD.

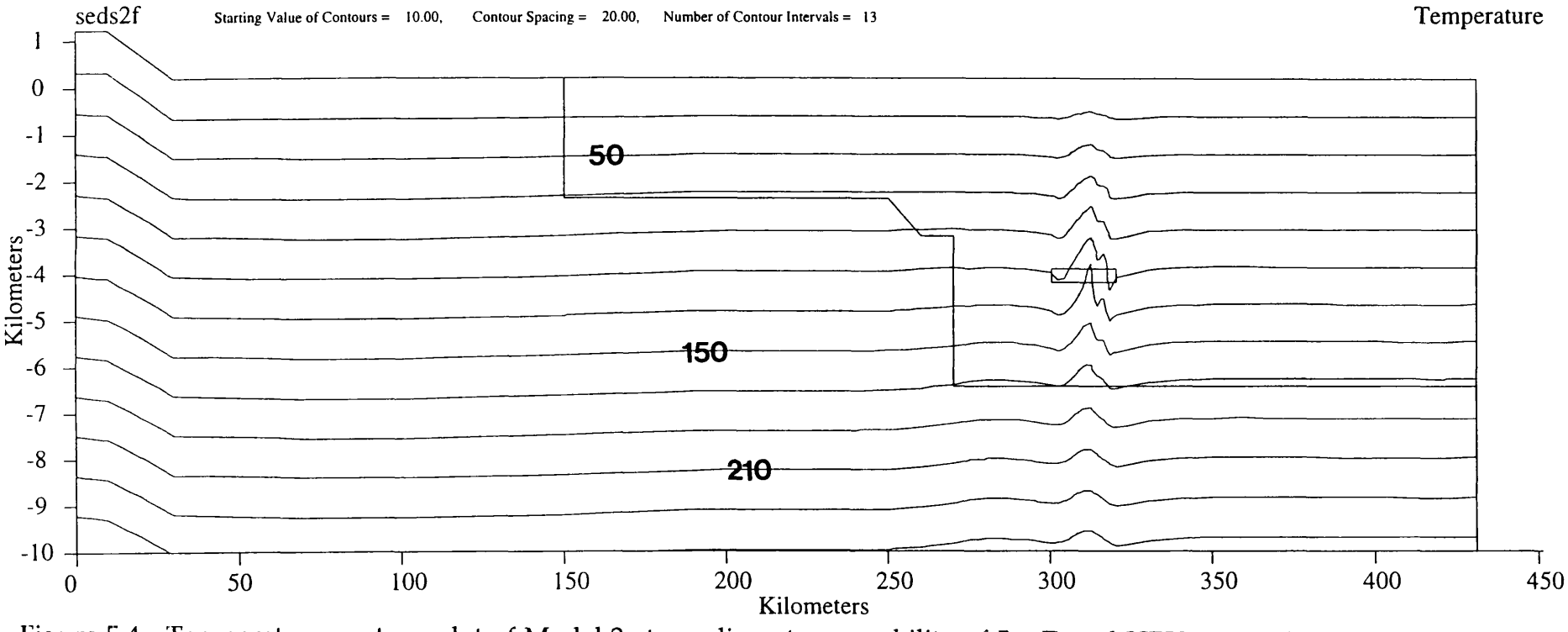

Figure 5.4 - Temperature contour plot of Model 2 at a sediment permeability of 5 mD and HPU permeability of 4D. Note that the temperature peak formed is a composite peak and is depth-limited. Temperature contours start at 10°C (surface) and are in 20°C intervals.

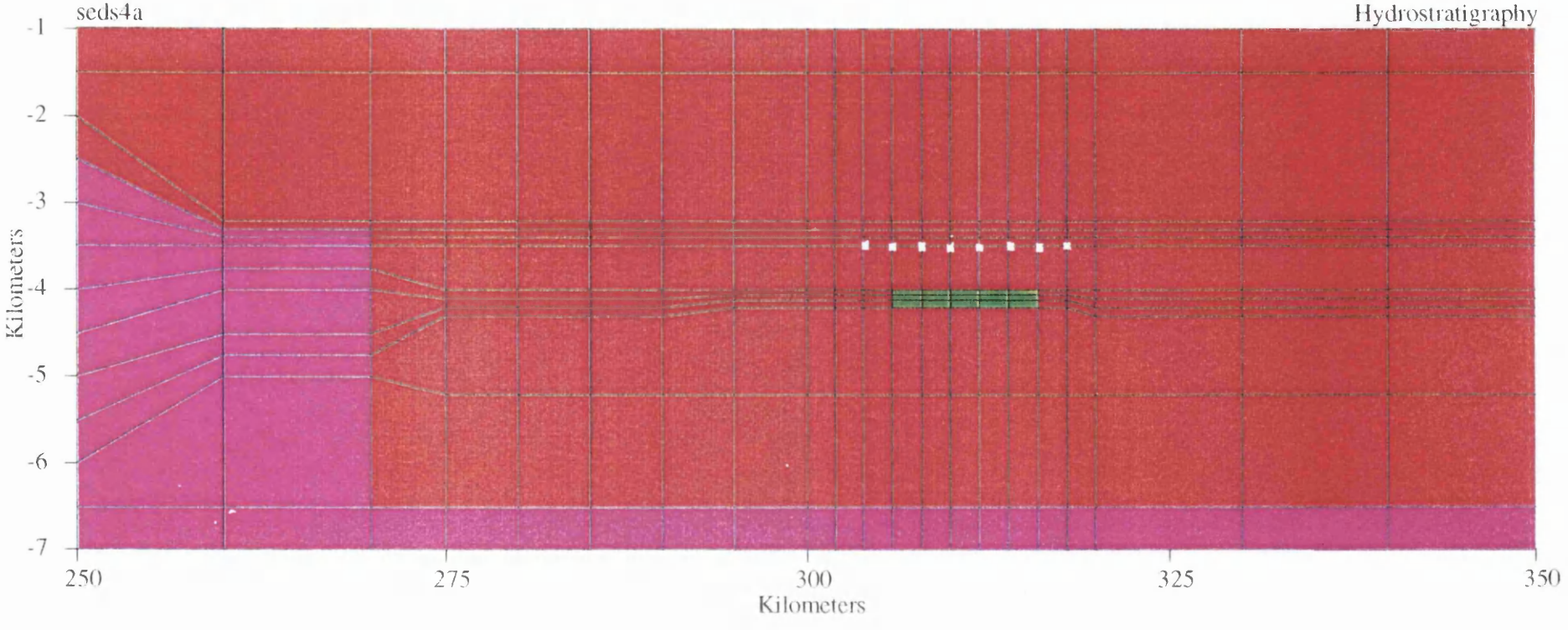

Figure 5.5A - Geometry of convection cell Model 3 (Section 2.1.1). Convection cell is 10 km wide by 200 m thick and lies at 4 km depth. This is an enlarged view of Figure 5.1, with basement geometry remaining constant. The nodes of temperature extraction are highlighted in white. NOTE Basement - purple, sediment fill - red and convection cell - green.

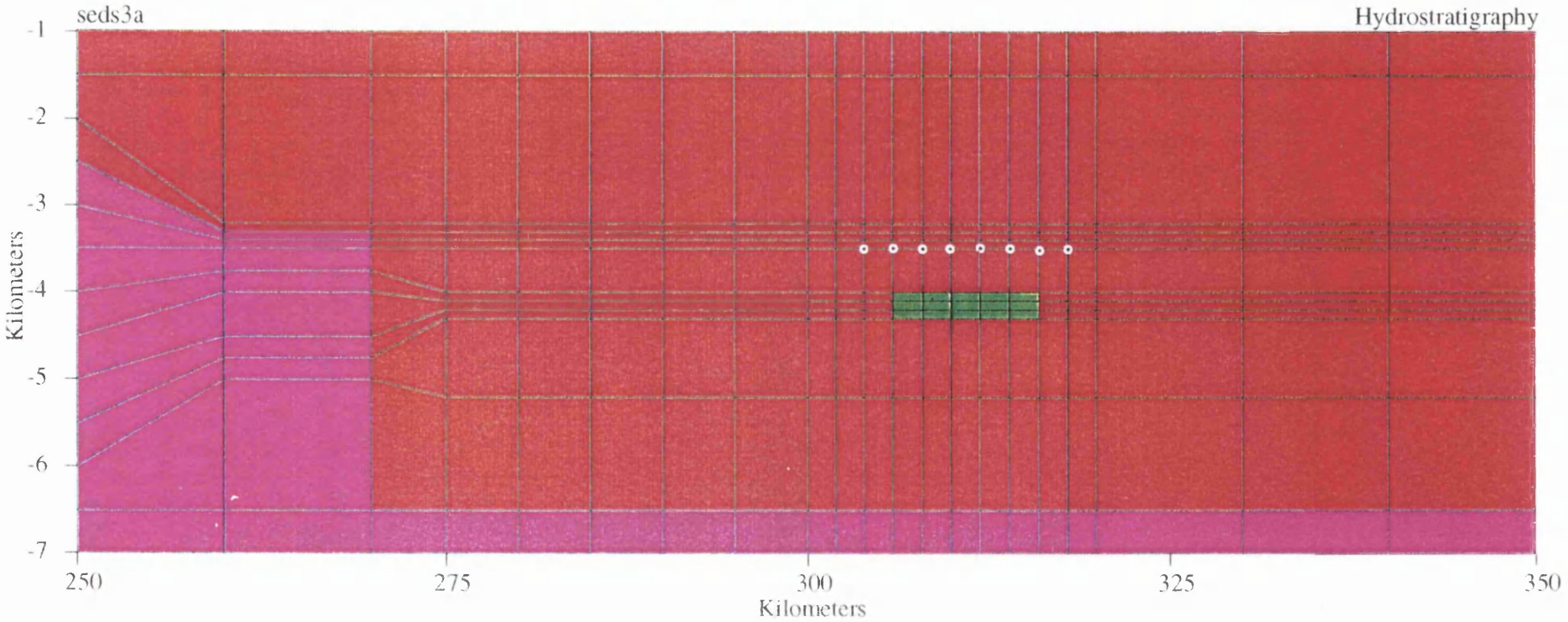

Figure 5.5B - Geometry of convection cell Model 4 (Section 2.1.1). Convection cell is 10 km wide by 400 m thick and lies at 4 km depth. This is an enlarged view of Figure 5.1, with basement geometry remaining constant. The nodes of temperature extraction are highlighted in white. NOTE Basement - purple, sediment fill - red and convection cell - green.

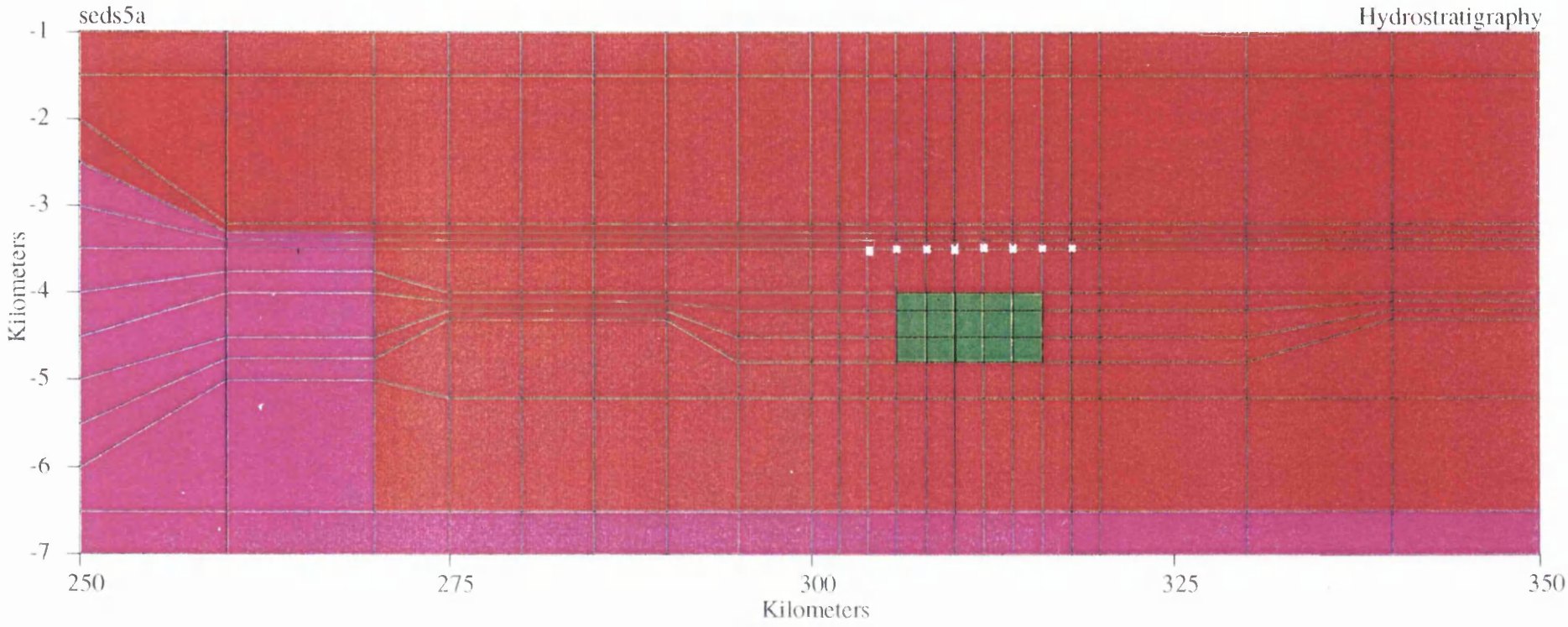

Figure 5.5C - Geometry of convection cell Model 5 (Section 2.1.1). Convection cell is 10 km wide by 800 m thick and lies at 4 km depth. This is an enlarged view of Figure 5.1, with basement geometry remaining constant. The nodes of temperature extraction are highlighted in white. NOTE Basement - purple, sediment fill - red and convection cell - green.

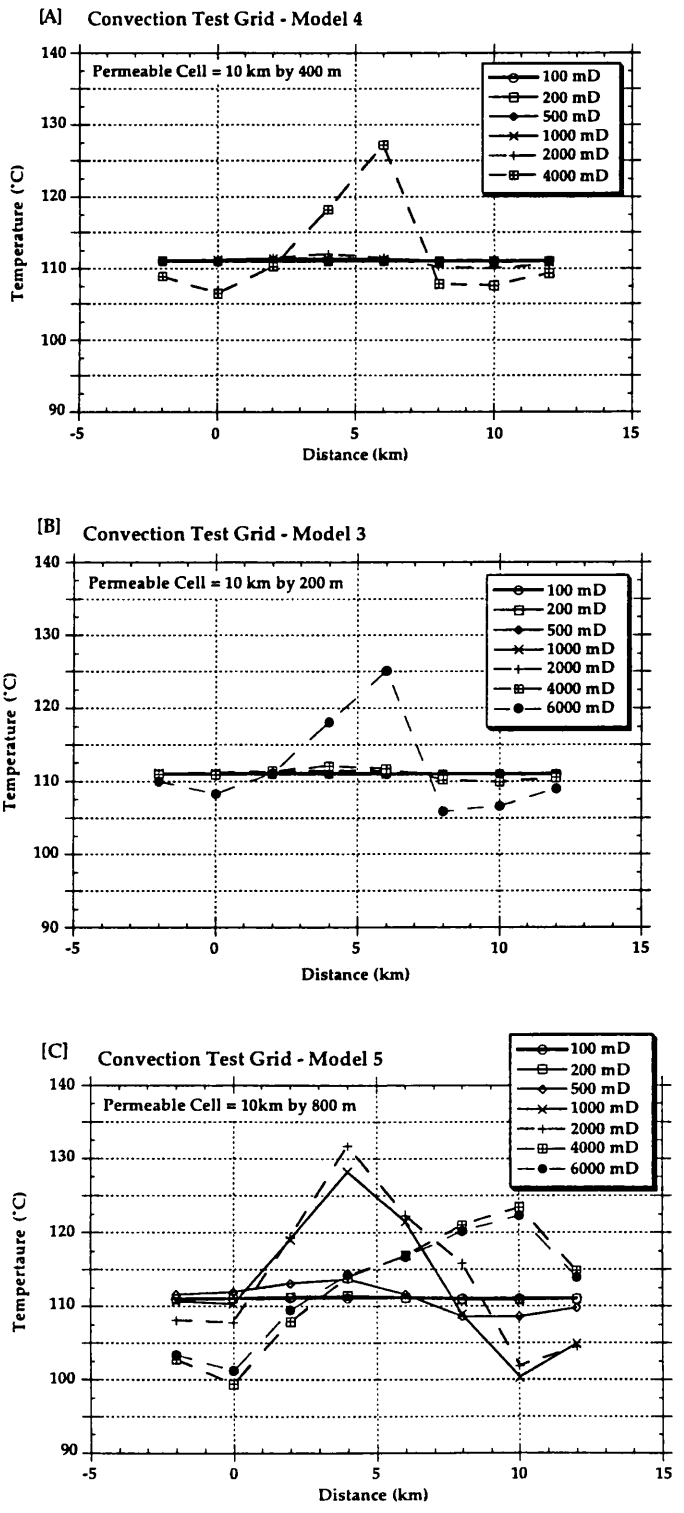

Figure 5.6 - Temperature variation over the HPU shown in Fig. 5.2 for a range in HPU permeabilities (Models 3, 4 and 5). [A] - sediment horizontal permeability = 1 mD, [B] - sediment horizontal permeability = 5 mD.

permeabilities (see Table 5.1 for convection cell poro-perm values). The resulting plots of temperature against distance for each value of convection cell permeability show that in Models 3 and 4 (Figure 5.6A & B, 10 km by 200 m and 10 km by 400 m respectively) significant disturbance of the temperature field occurs only at a convection cell permeability of 6 Darcies. In both cases a positive temperature anomaly forms of approximately 10 km half-wavelength; it is 15°C in magnitude for Model 3, and approximately 20°C in magnitude for Model 4.

Model	Sedimentary Pile Horizontal Permeability (mD)	Sedimentary Pile and Convection Cell Anisotropy	Convection Cell Dimensions	Horizontal Permeability Range of Convection Cell (mD)
Model 1	1.0	100	20 km * 400 m	100 - 4000
Model 2	5.0	100	20 km * 400 m	100 - 4000
Model 3	1.0	100	10 km * 200 m	100 - 6000
Model 4	1.0	100	10 km * 400 m	100 - 6000
Model 5	1.0	100	10 km * 800 m	100 - 6000

Table 5.1 - Sediment permeabilities, and ranges of modelled convection cell permeabilities (a series of models between 100 and 4000/6000 mD, investigate the effects of fluid flow within the convection cell), for Models 1 - 5, in Isolated High Permeability Units - Test Grids. Basement remains constant throughout modelling at 10^{-4} mD, with porosity held constant at 5% for both sedimentary pile and convection cell.

Model 5, however, displays very different behaviour. Due to its greater vertical thickness the convection cell in Model 5 is likely to begin convecting at lower permeabilities than will Models 1 to 4. As Figure 5.6 C shows, significant deviation in temperature occurs at 1 Darcy cell

permeability. For this 800 m thick cell, significant advective heat transport occurs at vertical permeabilities of above 5 mD (as opposed to 60 mD for Models 3 & 4). At 1 to 2 D horizontal permeability, an approximately 20°C temperature spike is formed due to this convection; it has a half-wavelength of 10 km. At even higher permeabilities (4 - 6 D), the convection pattern within the cell changes, and a more asymmetrical peak forms instead (20°C magnitude - 10 km in width).

In each case (Models 1 - 5) there exists the potential to produce short wavelength temperature anomalies -- albeit at relatively high permeabilities, or when thicknesses exceed 400 m.

5.2.2 *Isolated High Permeability Units - Central Graben*

I now simulate the effects of two deep (>3 km) high permeability units (HPU's) within the Central Graben (Fig. 5.7). This investigation is undertaken in order to assess the potential (using a more realistic model) of isolated convective fluid flow taking place within the Central Graben, and to quantify any resulting temperature effects. Each of the units measures 10 km horizontally, and is 400 m thick. They lie within the Jurassic, immediately below the Cretaceous chalk (Fig. 5.7).

In the models of the Central Graben, the poro-perm parameters of the surrounding sediments are held constant (at the values determined in Chapter 4), while the permeabilities of the two HPU's are increased until the onset of convection (Table 5.2). The effects on temperature and fluid velocity, caused by fluid flow and the onset of convection within these two HPU's, are observed over a range of HPU permeability from 100 mD to 3000 mD. For each HPU the steady-state temperatures are extracted from six points evenly spaced across the width of the HPU at a distance of 100 m above the top of the high-permeability cell (Fig. 5.8), and the average linear

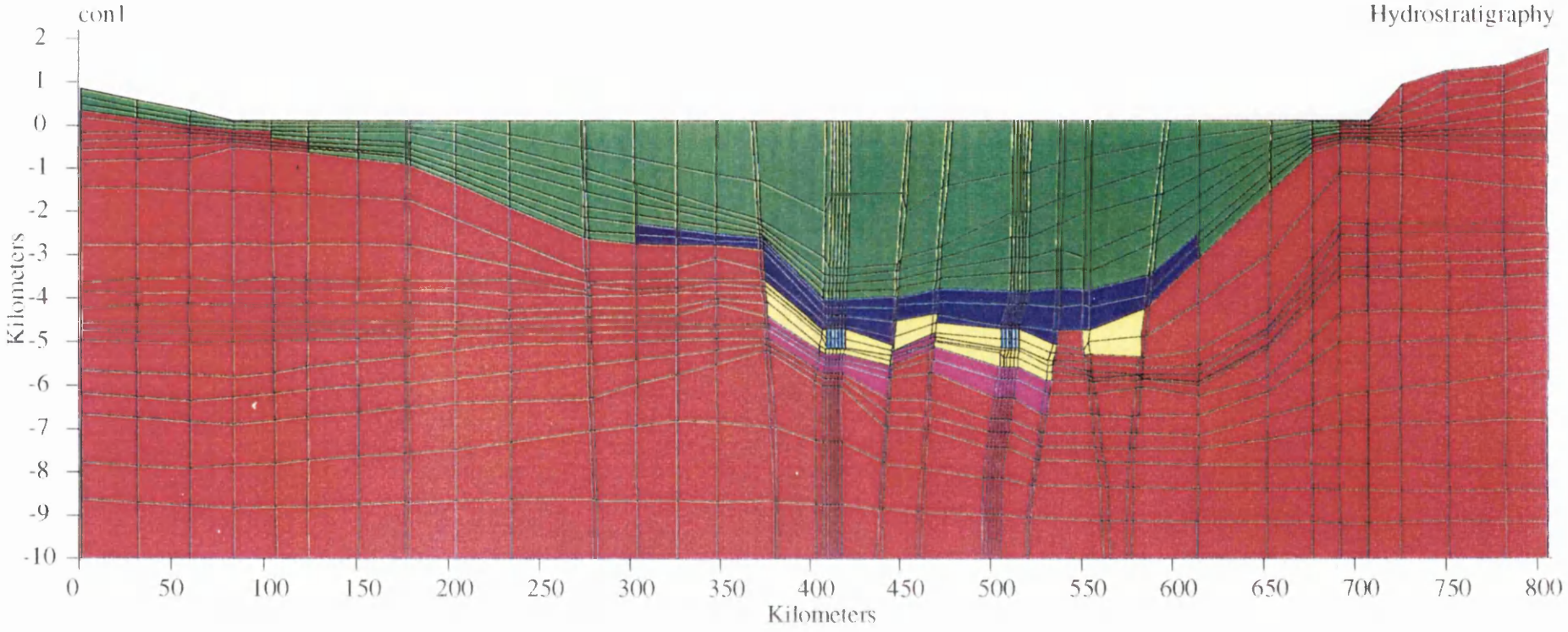

Figure 5.7 - Geometry (hydrostratigraphy) of Isolated High Permeability Units (HPU's) Model - Central Graben. Maximum depth of sedimentary fill approximately 6 km. Basement is shown in red, tertiary in green, Cretaceous in blue, Jurassic/Triassic in yellow and Permian in purple.The convection cells are light blue and measure 10 km wide by 400 m thick. They lie at approximately 4.5 km depth.

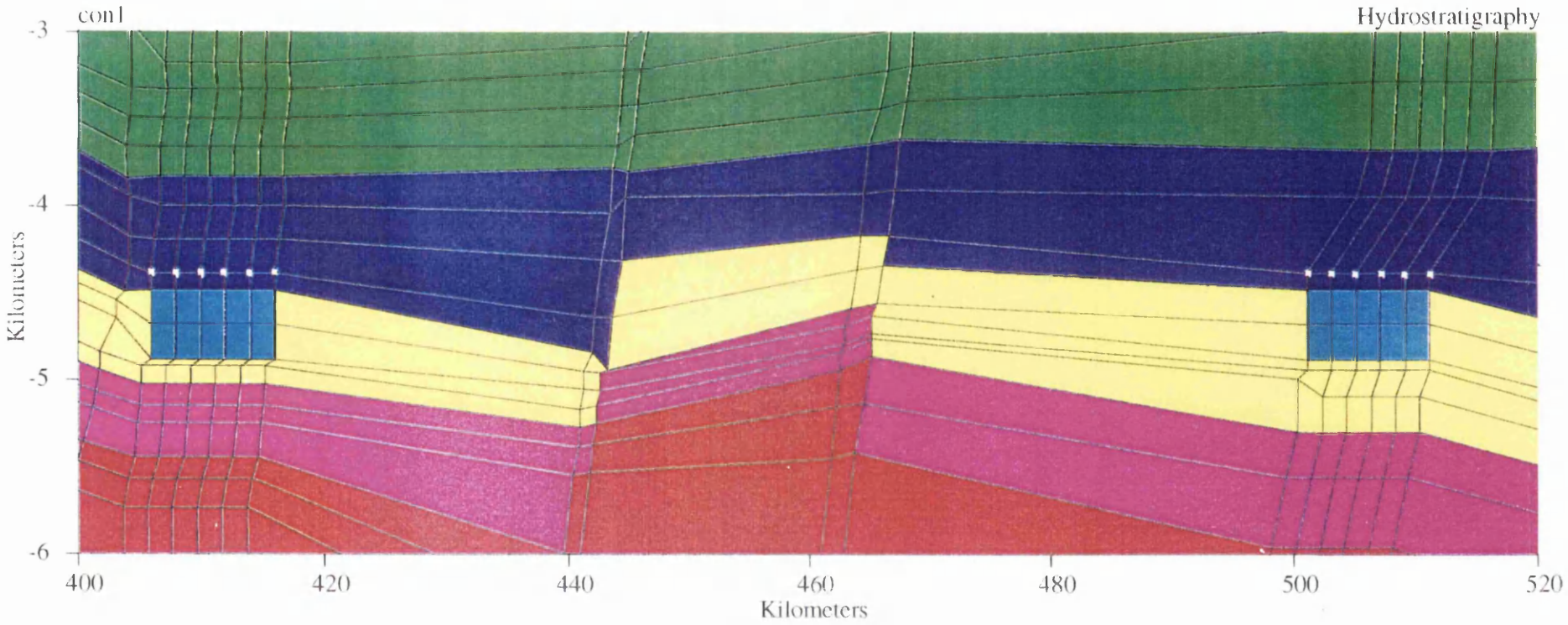

Figure 5.8 - Enlarged view of the geometry (hydrostratigraphy) of Isolated High Permeability Units (HPU's) Model - Central Graben. Basement is shown in red, tertiary in green, Cretaceous in blue, Jurassic/Triassic in yellow and Permian in purple. The convection cells are light blue and measure 10 km wide by 400 m thick. Nodes of temperature extraction for each cell are highlighted in white.

fluid velocity is calculated within each cell. The temperature profile across each convection cell (eastern Central Graben - ECG, and western Central Graben - WCG) is plotted at HPU permeabilities of 100, 1000, 1500, 2000, 2500, 2750 and 3000 mD (Fig. 5.9A & B).

UNIT	Horizontal Permeability (mD)	Anisotropy	Porosity (%)
1	1.0	100	10.0
2	0.1	100	10.0
3	10.0	100	5.0
4	10.0	100	5.0
High Perm. Unit	100 - 3000	100	5.0
Basement	10^{-4}	5	0.1

TABLE 5.2 - Poro-perm parameters for Units 1 to 4, Basement (as described in Chapter 4) and High Permeability Unit, for Isolated High Permeability Unit modelling (again a series of models with HPU permeabilities ranging from 100 to 3000 mD are used).

The western Central Graben plot (Fig. 5.9A) shows that at HPU permeabilities of 1500 mD or less, the thermal effects of fluid flow within the HPU remain undetectable by BHT accuracy standards (less than 10°C). Nevertheless, convective fluid flow is occuring. Temperature effects reach a peak at 2000 mD, producing a temperature spike of >15°C. At permeabilities above 2000 mD, the temperature anomaly formed by convection within the HPU decays (due to different convection patterns forming at higher velocities, and by secondary convection within the surrounding sediments). At 3000 mD the temperature deviation from background (100 mD curve) reaches a negative maximum of 10°C. The eastern Central Graben HPU

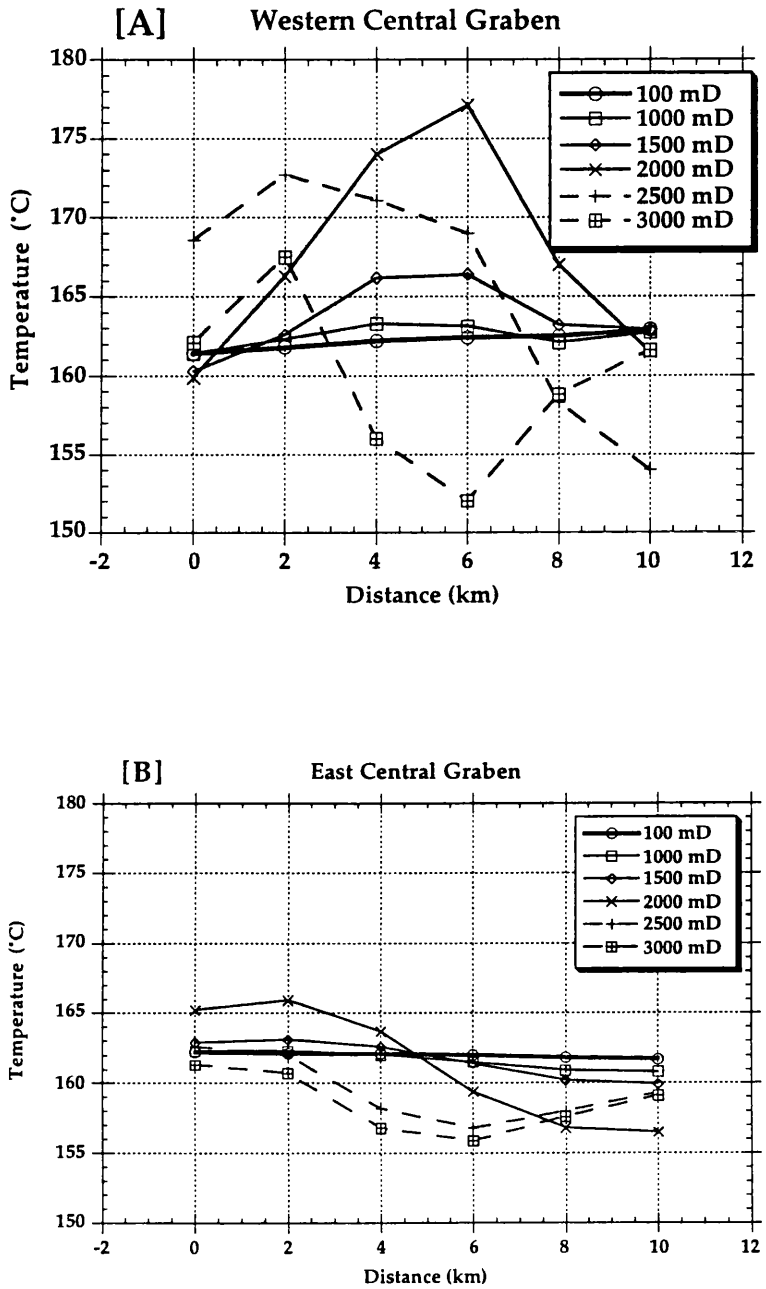

Figure 5.9 - Temperature variation over western and eastern Central Graben HPU's ([A] and [B] respectively), for a range in HPU permeability. The location of the convection cells (HPU's) is shown in Figure 5.7.

produces much smaller temperature effects over the same permeability range (Fig. 5.9 B). Again the temperature effects at or below 1500 mD are essentially undetectable by BHT data, and 2000 mD produces the maximum temperature anomaly. The magnitude of temperature change is much less for this HPU (10°C temperature **step** as opposed to the 15°C temperature **spike** formed in the WCG).

This difference in magnitude of temperature effect from ECG to WCG should be reflected in the magnitude of fluid velocities for each HPU. This is indeed the case, as Figure 5.10 shows. Above 100 mD the fluid velocities for the eastern Central Graben HPU are less than those for the western Central Graben HPU, although both HPU's are of equal dimensions, equal permeabilities and are at the same depth. At 1500 mD permeability or lower (the range in permeability over which there is no detectable temperature change), the average fluid velocities in both HPU's remain below 1.0 ma^{-1}. Fluid velocities for the western Central Graben thereafter increase more sharply with permeability than do fluid velocities within the eastern Central Graben, to a maximum of 6 ma^{-1} in the WCG, and 4.2 ma^{-1} ECG.

The temperature anomalies formed by localised convection in my Central Graben models are in most cases **step-shaped** unlike the temperature **spikes** observed within the temperature profiles established in Chapter 2. However, convective fluid flow within the western Central Graben is shown to have the potential to produce a 10 km wavelength 15°C temperature spike (see Fig. 5.9A & B).

5.2.3 *Summary*

The test grid geometries, as illustrated in Figures 5.2 and 5.5, are used to investigate the horizontal permeabilities necessary for convection to occur within cells of 10 to 20 km width, and up to 800 m in thickness

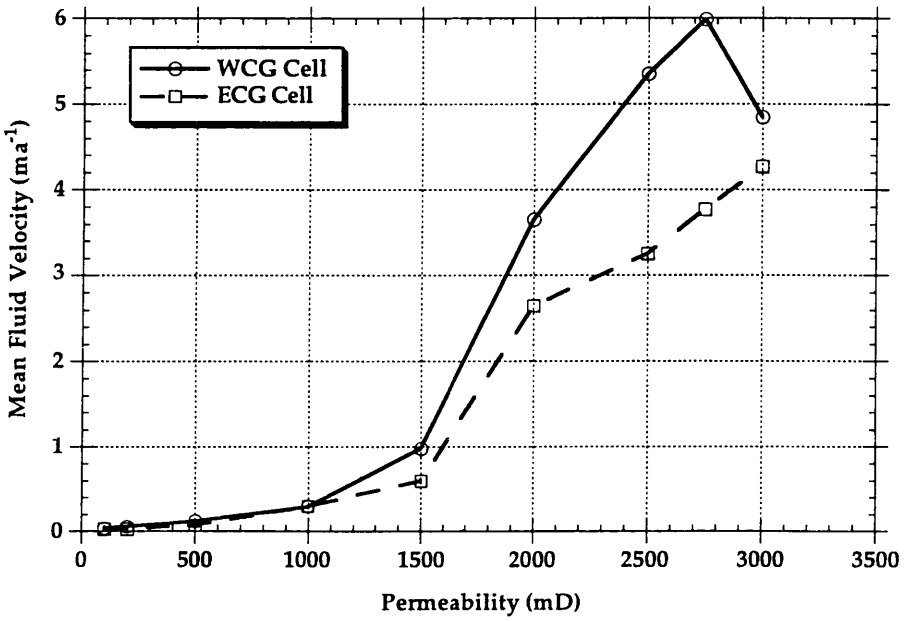

Figure 5.10 - Average fluid velocity within the eastern and western Central Graben HPU's, over a range in cell permeability from 100 to 3000 mD.

(anisotropy is constant at 100). Models 1 & 2 (of the same dimensions) although assuming different values of sediment permeability, both require a horizontal permeability of 4 D before the onset of major convection. However, the shape of the temperature anomaly formed at this permeability differs between these two models (Fig. 5.3), with a lower value of sediment permeability producing two distinct peaks whereas the higher values of sediment permeability produce a composite peak above the convection cell. This is due to the effect of increased fluid circulation within the sediments adjacent to the cell at higher sediment permeabilities.

Models 3 - 5 (Fig. 5.5, Table 5.1) have HPU's that range in thickness from 200 to 800 m. Modelling the effects of different permeabilities on fluid flow within the cells shows that cell thicknesses of 200 and 400 m require a horizontal permeability of 6 D to produce temperature anomalies of 15 - 20°C. Model 5, at 800 m thick, produces a 20°C temperature peak at between 1 and 2 Darcies.

Each of the test models, has the potential to produce a 10 - 20°C temperature anomaly. These anomalies are of similar magnitude and wavelength as the observed SWA's of Chapter 2 (Fig. 2.9), and like the SWA's, they are depth-limited. The permeabilities necessary to produce these anomalies are, especially in the cases of Models 3 & 4, unrealistically high.

I use a modified version of the finite-element mesh created for thermal modelling in Chapter 3 (Fig. 3.2) to investigate the role of convection within isolated cells in the Central Graben. This model (Fig. 5.7) has a 10 km wide by 400 m thick high permeability unit within both the ECG and WCG. The physical properties of the HPU's and those of the surrounding sedimentary pile, are as shown in Table 5.2. As Figure 5.9 shows, 2 D permeability produces the maximum temperature disturbance in each case -- an approximately 15°C temperature spike in the WCG, and a

10°C temperature step in the ECG. The maximum temperature disturbances are produced at average fluid velocities within the cell of approximately 1.0 ma^{-1}. The WCG convection cell is therefore capable of producing a temperature spike of 15°C (comparable to those of some SWA's) but no significant temperature spike is produced within the ECG cell even at 3 D permeability (Fig. 5.9).

A possible reason for this difference in behaviour between the two units may be the eastern Central Graben HPU's proximity to the Norwegian high (Fig. 5.7; PESGB, 1994). Higher regional flow velocities may suppress convective activity close to the Norwegian high, thus producing lower fluid velocities and lower temperature effects within the ECG cell, as compared to the WCG cell. In any case permeable units within the western Central Graben appear more prone to convection than their eastern Central Graben counterparts.

5.3 Fluid Flow Within Fault Zones - Test Grids

The test grids used within this section have the same "basement" geometry as the convection test grids, and they are again designed to be broadly analogous to the western Central Graben (see Fig. 5.1, [represents only half the graben]), having a maximum depth of sediment fill of approximately 6 km, and a typical North Sea "steers head" sediment geometry. The fault zone to be studied is in each case is 300m wide. It consists of three columns of elements in the finite element mesh. In order to increase the resolution of any temperature anomaly produced, column spacing around the fault zone is reduced to 1 km for a distance of 5 km (Fig. 5.11, "zoomed" fault zone).

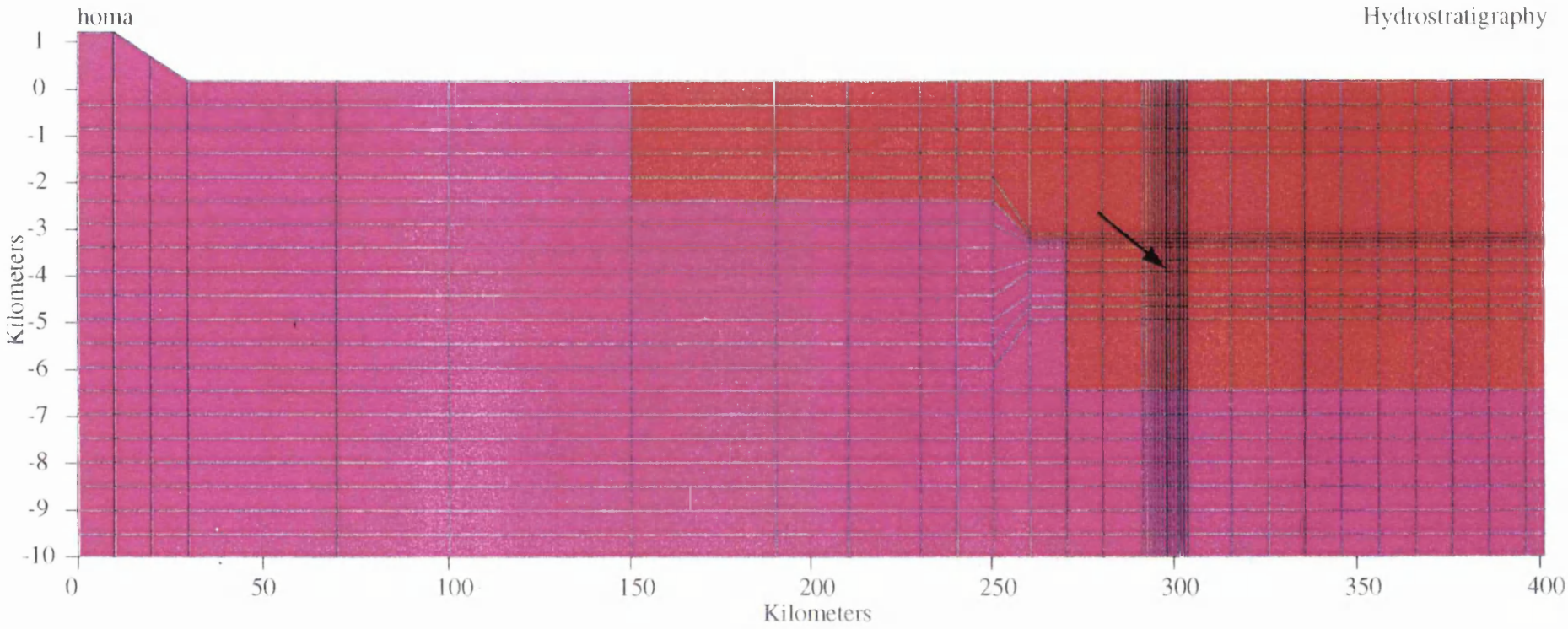

Figure 5.11 - Overall geometry of "Fault Zone Behaviour in a Sedimentary Pile" model (Section 5.3.1).Basement is purple and sedimentary fill is red. Approximate location of fault zone arrowed (see Fig. 5.12). Model again analogous to the western part of the Central Graben.

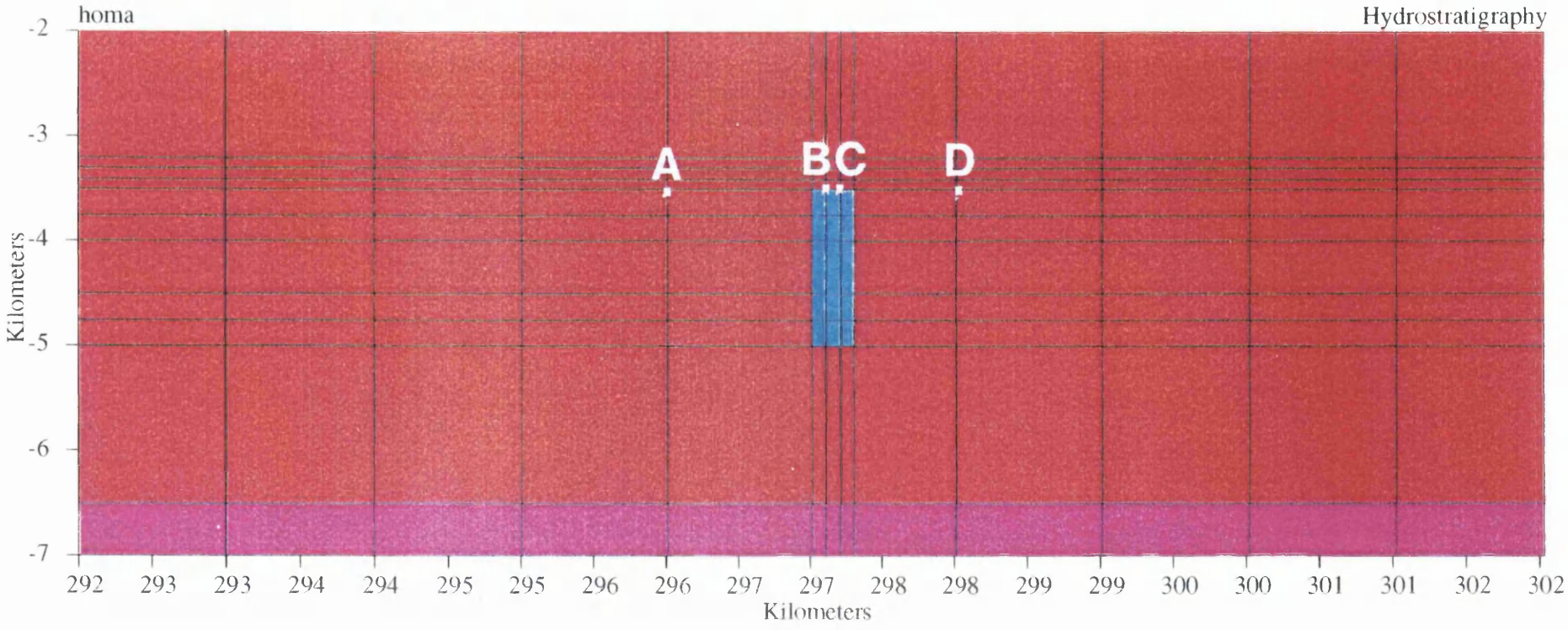

Figure 5.12 - Enlarged view of the geometry of "Fault Zone Behaviour in a Sedimentary Pile" model (Section 5.3.1).Basement is purple and sediment fill is red. The fault zone is shown in light blue and is 300 m wide. The nodes of temperature extraction A - D are shown in white.

5.3.1 *Fault Zone Behaviour within Homogeneous Sedimentary Pile*

The initial model used to investigate the potential of fluid flow within a fault zone consists only of basement (purple), sedimentary fill (homogeneous, red), and a single "fault" material (light blue; Fig. 5.12). The vertical fault zone spans 1.5 km depth from 3.5 km to 5km below the surface. Fluid energy is related to the small topographic expression at the western end of the section, analogous to the present-day land area of England.

In order to assess the effects of fault and sediment permeabilities on fluid flow velocities, and the resultant temperature effect around the fault zone, I model a range of sediment permeabilities for several values of fault permeability. I aim to establish a range of sediment and fault permeabilities at which vertical fluid flow within a fault zone produces a significant temperature effect (approx. 10°C or greater).

The poro-perm parameters assigned to the sedimentary pile and the fault zone are shown in Table 5.3. I proceed in modelling by assigning a fixed value to the fault zone of 50 mD (basement is fixed throughout the modelling at 10^{-4} mD), and simulate the effects of fluid flow on temperature in and near the fault zone at a range of sediment permeabilities. Temperatures are recorded from points A - D (Fig 5.12) for each simulation, and from these, the average temperature increase across the fault zone is calculated [using ((A+D)/2 - (B+C)/2), see Fig. 5.12]. By this means I can determine the effect of sediment permeability on fluid flow within the 50 mD fault zone. I then model the same suite of sediment permeabilities at fault permeabilities of 100 , 150, and 200 mD to determine the influence of fault permeability on fluid flow.

[It is worth noting that while I use a fault zone of 300 m width, the same results can be produced by smaller fault zone widths by increasing the

permeability of the fault zone. The relationship between fault zone width and vertical permeability is broadly linear. For example, a fault zone of 300 m width and 50 mD vertical permeability will produce a similar temperature disturbance as a 100 m wide fault of 150 mD vertical permeability.]

Unit	Modelled Permeability Range (mD)	Anisotropy	Porosity (%)
Sedimentary Pile	1 - 20 (Horizontal = Max.)	100	5
Fault Zone	50 - 200 (Vertical = Max.)	100	5

Table 5.3 - Poro-perm parameters and modelled ranges of fault and sediment permeabilities in simulations of Fault Zone Behaviour within a Homogeneous Sedimentary Pile. Basement remains constant at 10^{-4} mD.

From the above modelling a plot is constructed of temperature increase across the fault zone, as related to sediment permeability (Fig. 5.13). This shows that at horizontal sediment permeabilities (anisotropy = 100) lower than 7 mD, the temperature increase within the fault zone is less than 5 °C (and therefore undetectable from BHT data). Above 7 mD (sediment permeability) there is a sharp increase in the size of the temperature peak as sediment permeability increases, and by 12 mD sediment permeability, all faults with 50 mD to 200 mD permeability produce a 40°C temperature peak over the fault zone. However, closer examination of the temperature contour plots for each simulation reveals that at sediment permeabilities of **6 mD or less**, all temperature effects within the fault zone (<5°C) are caused by **convection within the fault zone** with minor circulation of fluids in the surrounding sediments. Figures 5. 14 A and B show an example of this

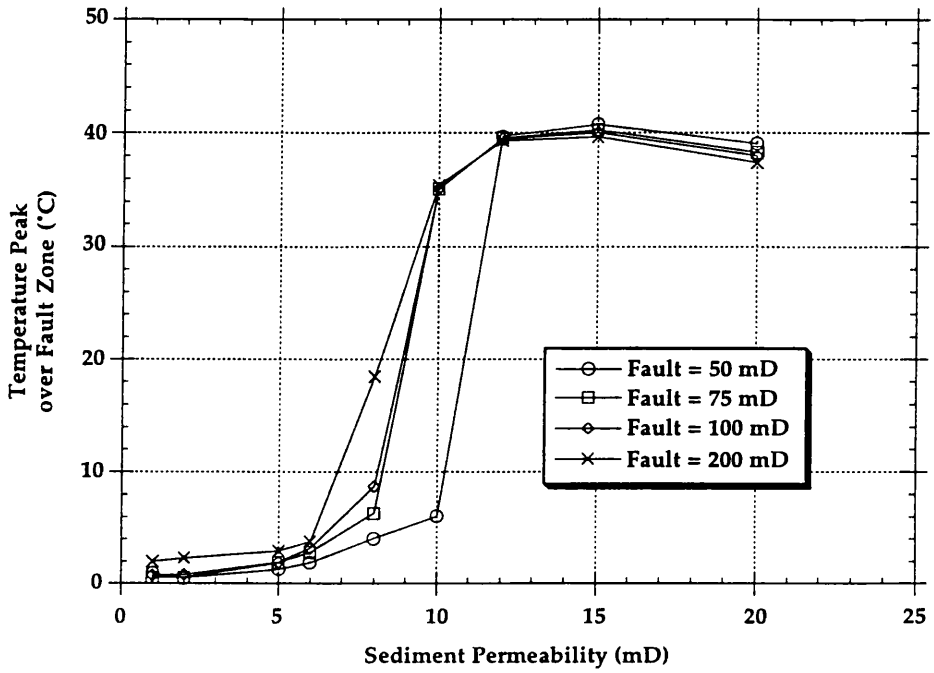

Figure 5.13 - Average temperature increase over the fault zone against horizontal sediment permeability, for fault permeabilities of 50 to 200 mD. Maximum temperature peak over the fault zone is 40°C.

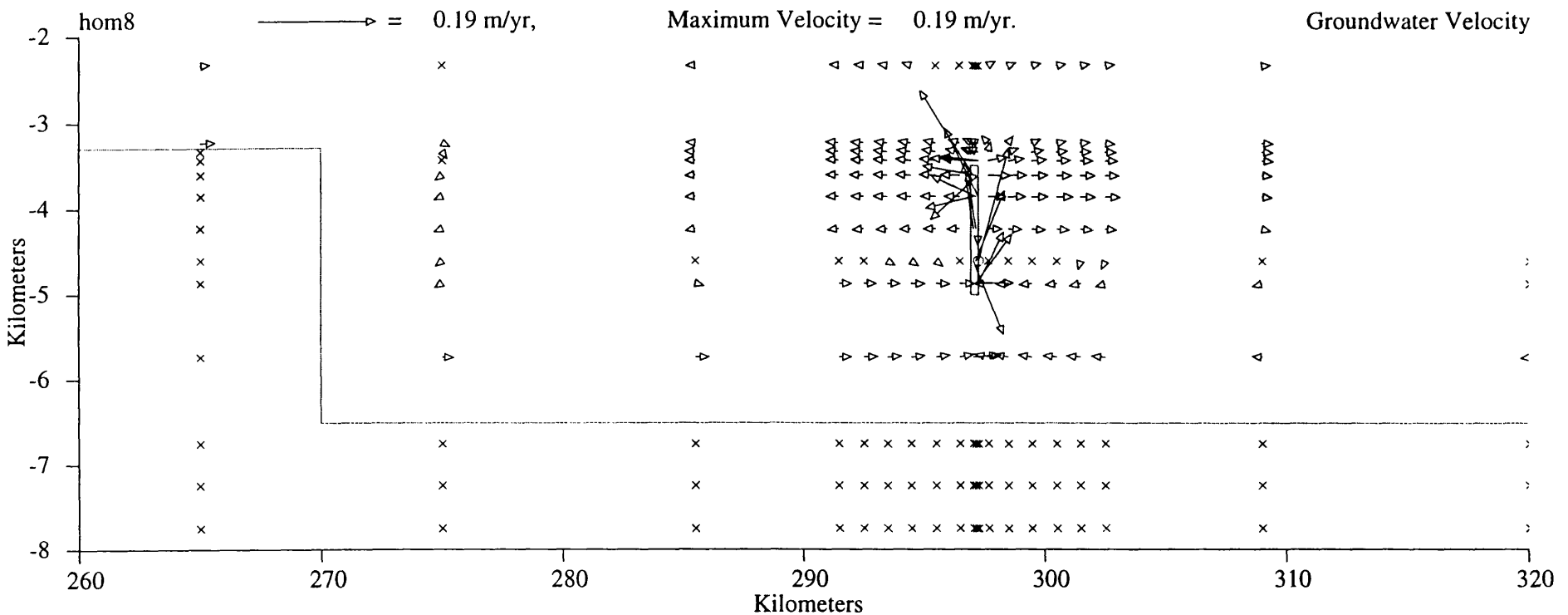

Figure 5.14A - Groundwater velocity plot of Fault Zone behaviour in a Homogeneous Sedimentary Pile for a sediment permeability of 5 mD and a fault permeability of 100 mD. Velocity vectors are scaled to 100th of the maximum velocity (0.19 ma-1). X's represent flow rates of less than 100th of the maximum, NOT no flow. note the convection within the fault zone and minor circulation within the surrounding sediments.

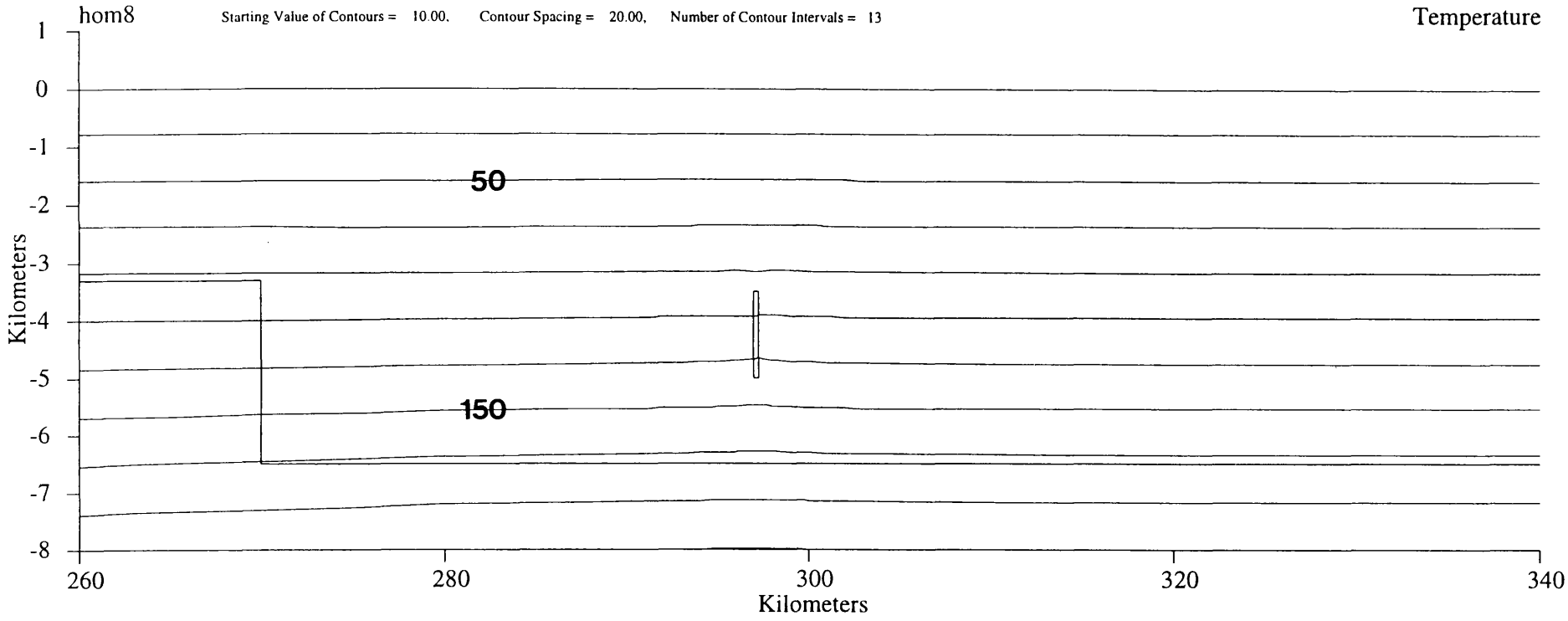

Figure 5.14B - Temperature contour plot of the Fault Zone behaviour in a Homogeneous Sedimentary Pile model at a sediment permeability of 5 mD, and a fault permeability of 100 mD. Temperature contours start at 10°C, and are in 20°C intervals. Less than 5°C temperature disturbance is caused by convection within the fault zone in this case.

convective flow (fault = 100 mD, sediment permeability 5 mD); the groundwater velocity plot (Fig. 5.14A) depicts an obvious circulation of fluids within the fault zone, producing virtually no temperature anomaly (Fig 5.14B). It is also notable that, at sediment permeabilities of approximately **7 - 15 mD,** there is upflow within the fault zone combined with convection in the sedimentary pile around the fault zone (Fig 5.15A), producing a large temperature anomaly (Fig. 5.15B). At permeabilities above 15 mD all the sedimentary pile convects and any effect of localised fluid flow within the fault zone is swamped by the regional fluid circulation (results not shown). The fault zone in each instance however, localises the fluid upflow zone, and its presence is critical to the development of these flow systems.

5.3.2 *Influence of Sediment Permeability Architecture*

The geometry of these models differs from the previous test-grid model by sub-division of the sedimentary pile into 4 distinct units: Tertiary, Palaeocene, Cretaceous and pre-Cretaceous (Fig. 5.16A). This model is designed to be broadly analogous to the Central Graben (thicknesses and edge of graben geometry are similar although all sedimentary units are in this case flat-lying) in architecture. The base-case poro-perm values are shown in Table 5.4 (comparable to those used in the regional fluid flow modelling, Section 4.3, Table 4.2).

The same fault zone geometry as shown in Figure 5.12 is used within the sub-divided sedimentary pile (the fault therefore initiates within the pre-Cretaceous sediments and terminates within the Palaeocene; see Fig. 5.16B). First, I assign the fault a vertical permeability of 50 mD (anisotropy of 100, i.e. horiz. permeability of 0.5 mD). A base-case simulation (all sedimentary units at base-case values (Table 5.4) and fault at 50 mD)

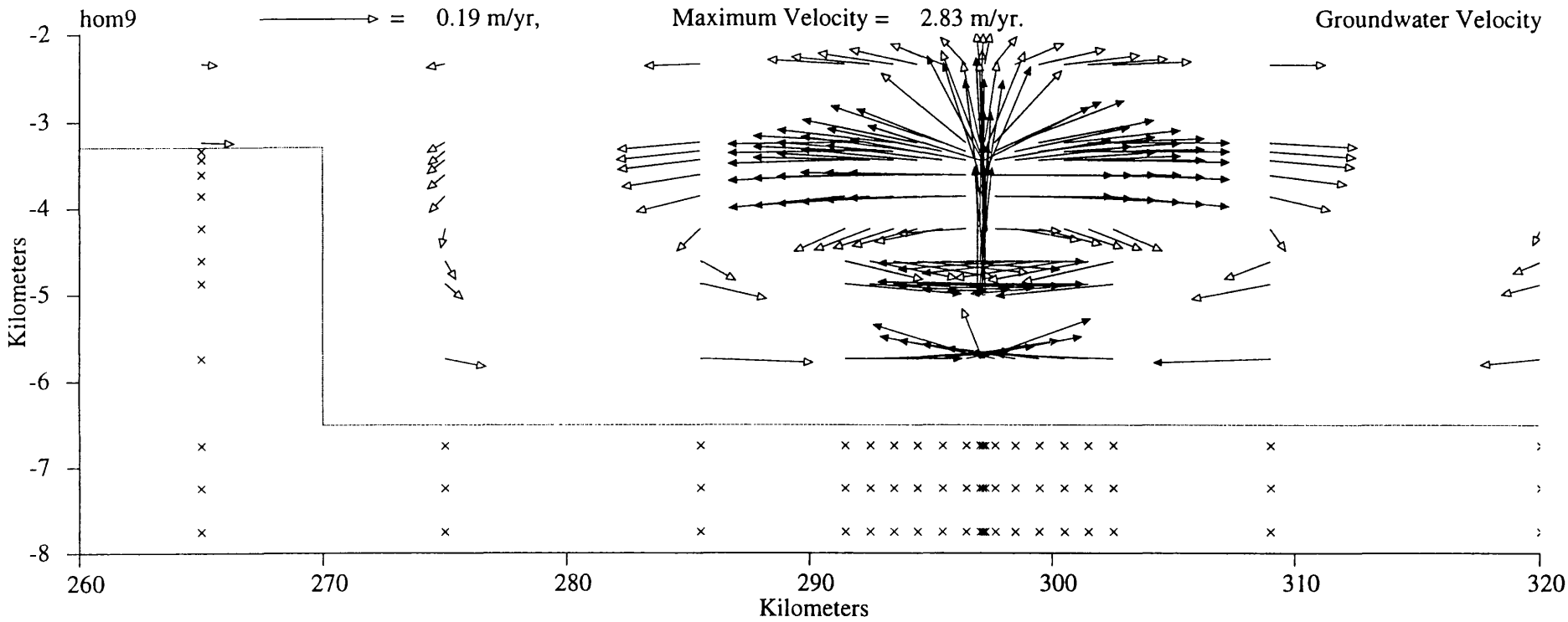

Figure 5.15A - Groundwater velocity plot of Fault Zone behaviour in a Homogeneous Sedimentary Pile for a sediment permeability of 10 mD and a fault permeability of 100 mD. The maximum groundwater velocity in this model is 2.83 ma-1, compared to 0.19 ma-1 for the same model with 5 mD sediment permeability. The longest vector represents 0.19 ma^{-1} so that this figure is directly comparable to Figure 5.14A. X's represent flow rates of less than 100th of longest vector (0.19 ma^{-1}), NOT of no flow. Note the circulation of fluids within the surrounding sediments, with dominantly upward flow within the fault zone.

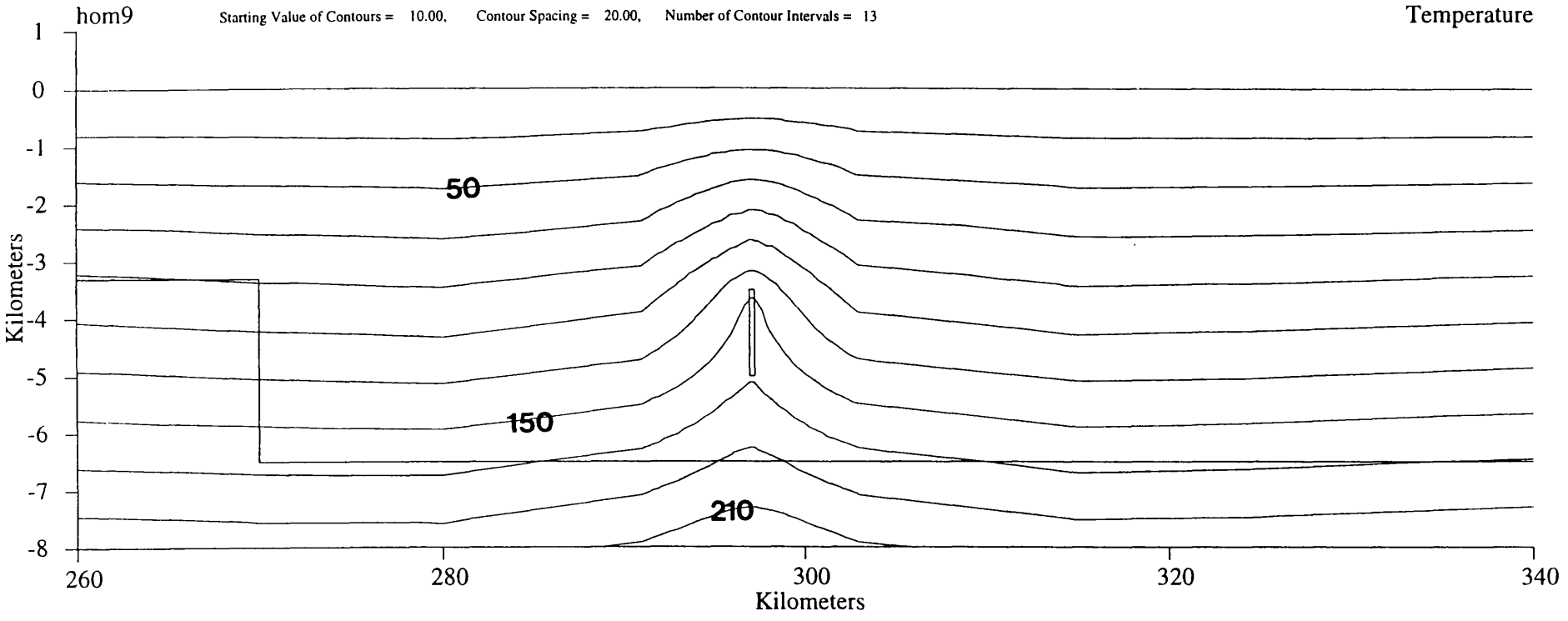

Figure 5.15B - Temperature contour plot of Fault Zone behaviour in a Homogeneous Sedimentary Pile model at a sediment permeability of 10 mD and a fault permeability of 100 mD. Temperature contours start at 10°C, and are in 20°C intervals. Note the the formation of a 30 - 40 °C temperature anomaly over the fautl zone. This anomaly is depth-limited.

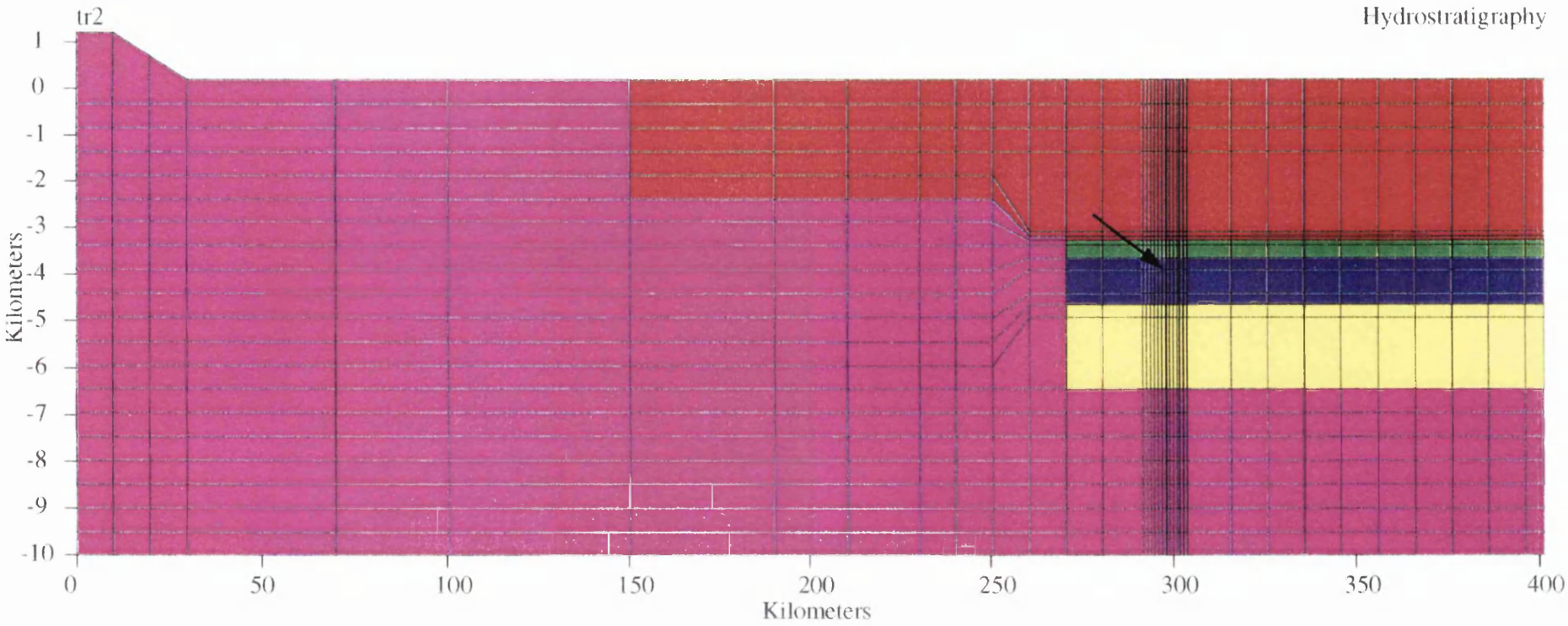

Figure 5.16A - Overall geometry of model used in "Fault Zone Behaviour in a Heterogeneous Sedimentary Pile". Basement is purple, Tertiary is red, Palaeocene is green, Cretaceous blue, and Jurassic to Permian yellow. Approximate location of fault zone shown.

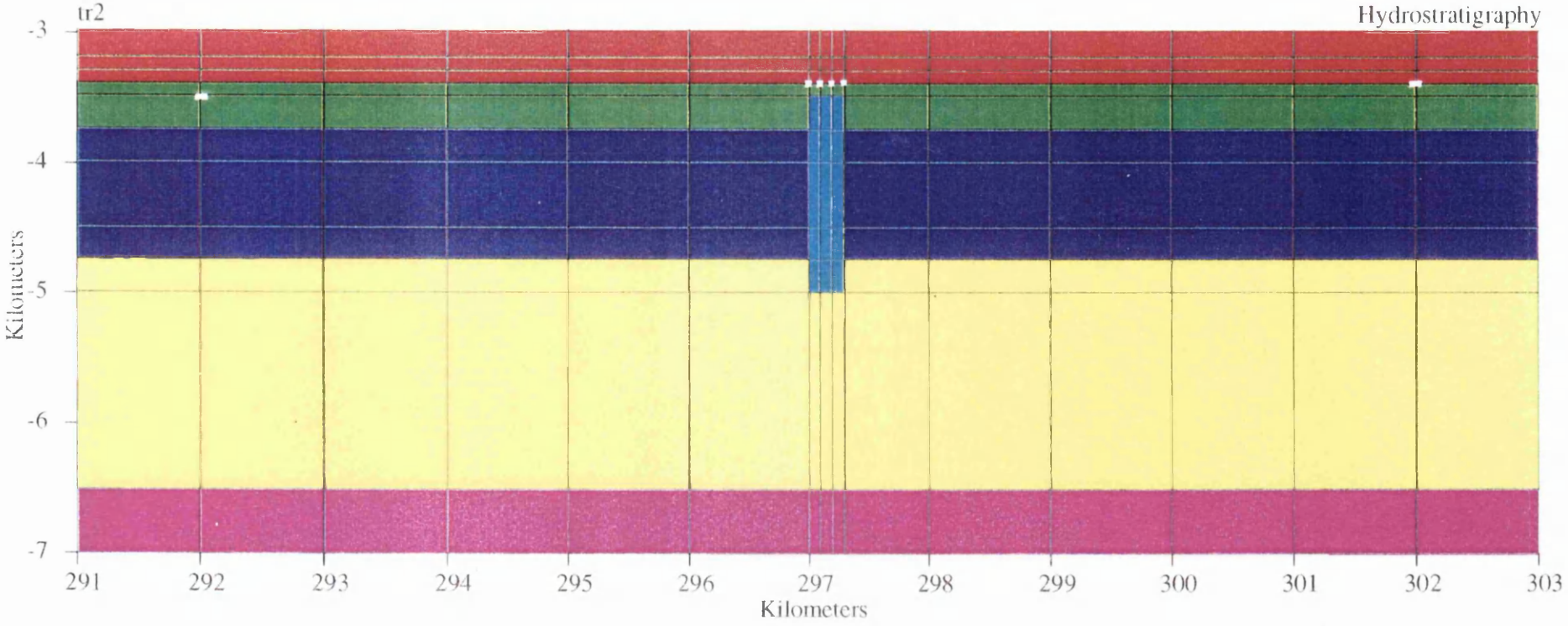

Figure 5.16B - Enlarged view of the geometry of the model used in "Fault Zone Behaviour in a Heterogeneous Sedimentary Pile". Colour coding as for Figure 5.16A. Approximate location of fault zone shown. Nodes of temperature extraction shown in white.

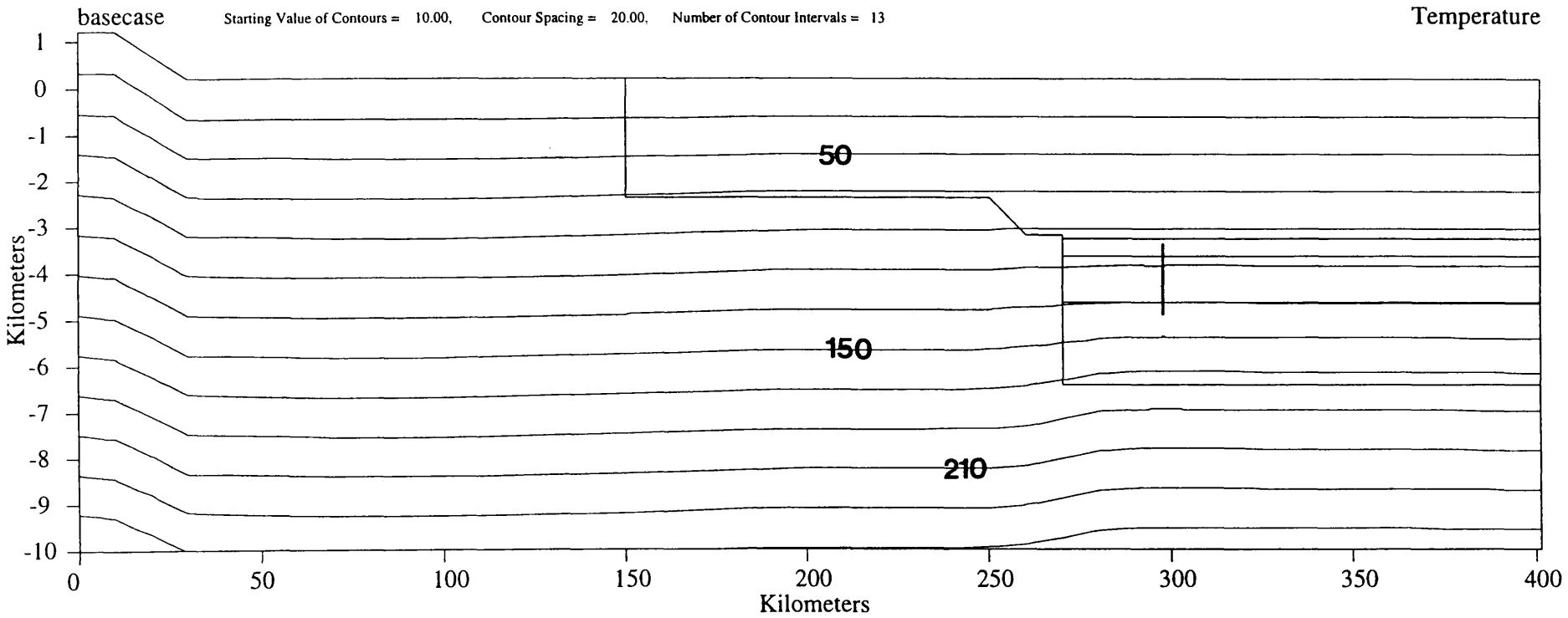

Figure 5.17 - Temperature contour plot for base-case model of "Fault Zone Permeability within a Heterogeneous Sedimentary Pile" (Section 5.3.2). Sediment permeabilities are listed in Table 5.4, fault zone vertical permeability is 50 mD. No apparent temperature disturbance due to fluid flow within the fault zone.

produces no significant temperature anomaly above the fault zone (Fig. 5.17). From this base-case scenario I simulate the thermal effects in and around the fault zone induced by increasing the horizontal permeability of a single major unit while holding the others constant (Table 5.4). By this means I can establish which stratigraphic units have the greatest effect on fluid flow (and therefore temperature effect) within the fault zone. The same suite of models is then run for a fault zone permeability of 200 mD.

Sedimentary Unit	Base-Case Horizontal Permeability (mD)	Base-Case Porosity (%)	Anisotropy	Range in Horizontal Permeability Modelled (mD)
Tertiary	1.0	10	100	5 -70
Palaeocene	100	10	100	200 - 1000
Cretaceous	0.1	5	100	1 - 30
Pre-Cretaceous	10	5	100	1 - 50

Table 5.4 - Base-case poro-perm parameters, and modelled range of sediment permeabilities, in simulations of Fault Zone Behaviour within a Heterogeneous Sedimentary Pile. Basement remains constant at 10-4 mD.

I extract the temperatures at the nodes shown in Figure 5.16B, for each simulation, and plot these temperatures against distance for each of the sedimentary units (Tertiary to pre-Cretaceous) for two fault-zone permeabilities. The resulting plots (Fig. 5.18) show that, for a fault permeability of 50 mD, a Cretaceous unit permeability of 30 mD can result in an approximately 7°C temperature anomaly across the fault zone. The pre-Cretaceous unit shows a rise in temperature across the fault zone up to a permeability of 40 mD. Above this permeability, however, the pre-Cretaceous units undergo major convection, and the resulting temperature

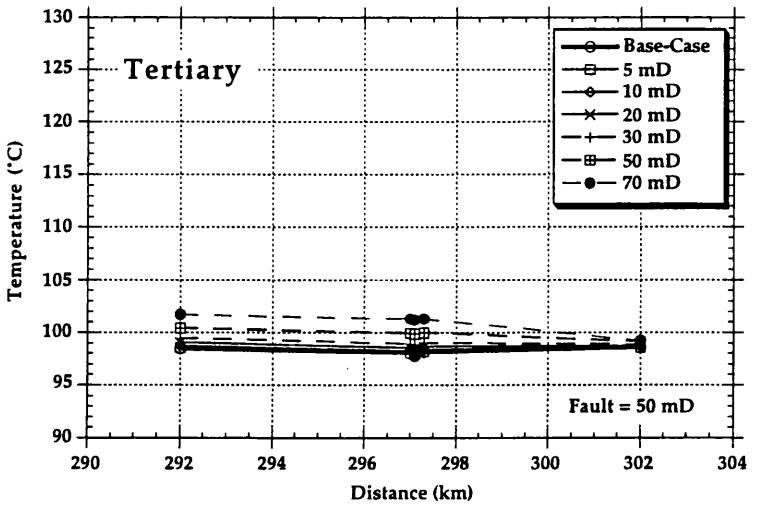

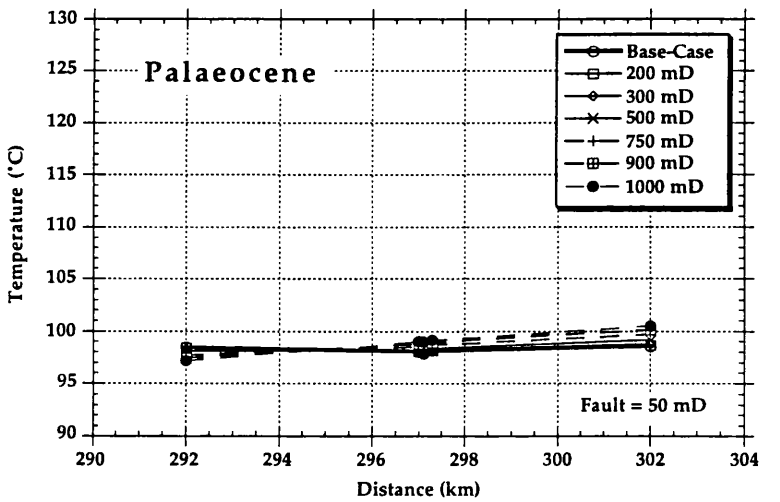

Figure 5.18 - Temperature across the fault zone plotted at a range of sedimentary unit permeabilities for the units described in Table 5.4. Fault zone permeability is constant at 50 mD. Cretaceous and Pre-Cretaceous are shown overleaf.

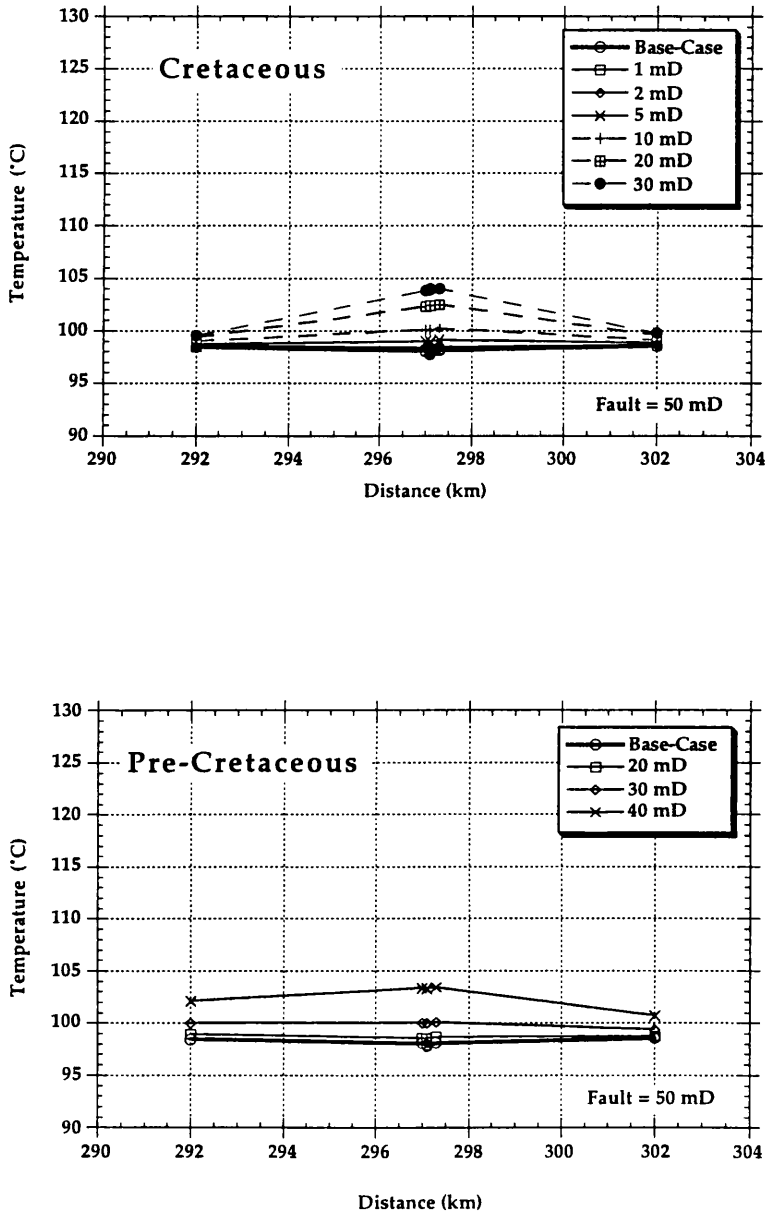

Figure 5.18 (cont.) - Temperature across the fault zone plotted at a range of sedimentary unit permeabilities for the units described in Table 5.4. Fault zone permeability is constant at 50 mD. Temperatures extracted from nodes shown in Figure 5.16B.

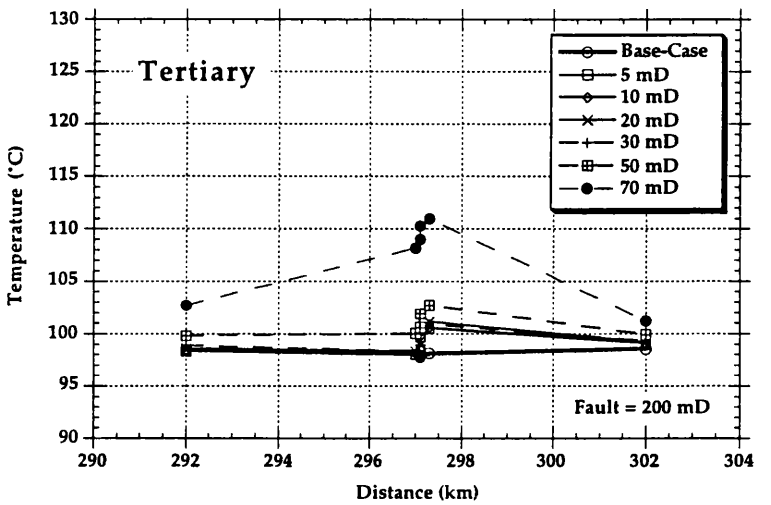

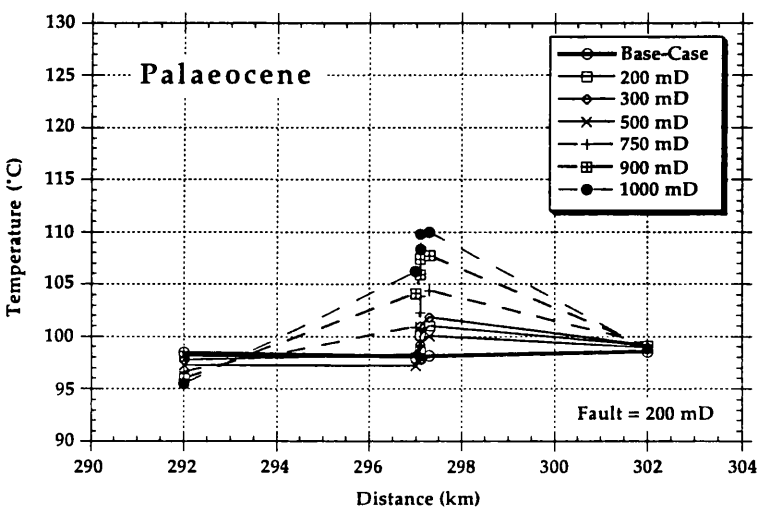

Figure 5.19 - Temperature across the fault zone plotted at a range of sedimentary unit permeabilities for the units described in Table 5.4. Fault zone permeability is constant at 200 mD. Cretaceous and Pre-Cretaceous are shown overleaf.

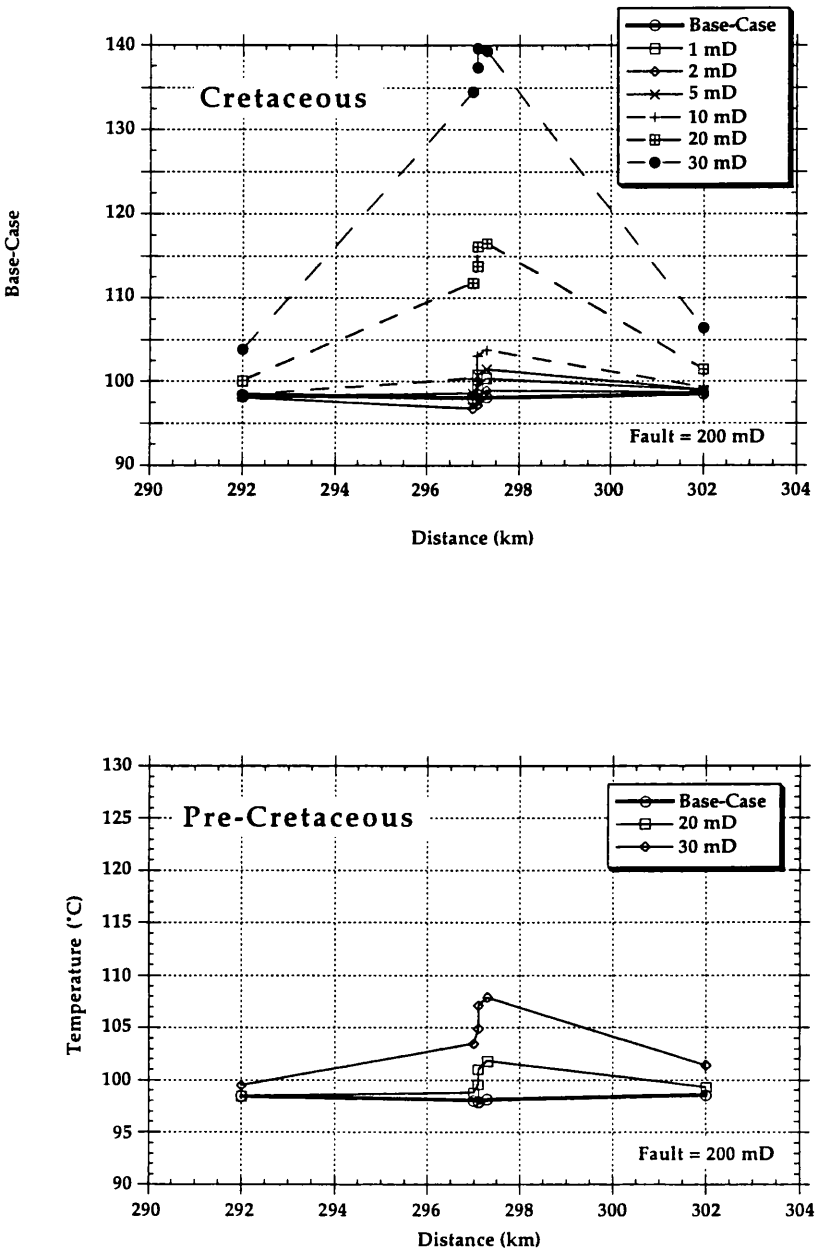

Figure 5.19 (cont.) - Temperature across the fault zone plotted at a range of sedimentary unit permeabilities for the units described in Table 5.4. Fault zone permeability is constant at 200 mD. Nodes of temperature extraction are shown in Figure 5.16B.

effects are no longer attributable to the presence of a fault zone. Therefore these high-permeability effects are disregarded in this section.

At a fault permeability of 200 mD (Fig. 5.19), horizontal sediment permeabilities of 70 mD in the Tertiary and 900-1000 mD in the Palaeocene units results in approximately 10 - 15°C temperature anomalies across the fault zone. A Cretaceous permeability of 30 mD (0.3 mD vertical) results in a temperature anomaly of 40°C, with an approximately 10 km width. The pre-Cretaceous unit remains relatively stable up to 30 mD, with an approximate 10°C temperature step formed. Above this value the pre-Cretaceous unit again undergoes major convection, and those results are not considered here (see previous section).

5.3.3 *Summary*

The test grids used to simulate the thermal effects of a permeable, vertical fault zone have a basement geometry broadly analogous to that of the Central Graben. Initially, a homogeneous sedimentary pile is assumed, and several values of fault zone permeability are modelled over sediment permeabilities ranging from 1 to 20 mD. A plot of average temperature increase across the fault zone against sediment permeability (Fig. 5.13) shows that only above sediment permeabilities of 7 mD is the temperature disturbance across the fault zone detectable in terms of the resolution of BHT data. Below this value (7 mD) any temperature deviation from background is caused by convection within the fault zone, not simply by upwelling fluids (Fig. 5.14). For any value of fault permeability, a maximum temperature peak of 40°C is possible across the fault zone at a sediment horizontal permeability of approximately 12 mD. At sediment permeabilities above 15 mD the entire sedimentary pile undergoes convection, and although the fault zone localises fluid upflow, the thermal

effects of fluid migration within the fault zone are swamped by the regional fluid circulation.

This initial model (Fig. 5.12) is then modified by the sub-division of the sedimentary pile into four units: Tertiary, Palaeocene, Cretaceous and pre-Cretaceous (Fig. 5.16). Using the same fault zone geometry as the previous section I first assign the fault zone a permeability of 50 mD and simulate the temperature effects of fluid flow within the fault zone for a range of sediment permeabilities (varying the permeability of each sedimentary unit independently). The same suite of models is then run for a fault permeability of 200 mD.

In plots of temperature against distance for each value of sediment permeability modelled (Figures 5.18 and 5.19), it is apparent that for the 50 mD fault zone, only the Cretaceous unit has the potential to influence fluid flow within the fault zone at realistic sedimentary permeabilities, with the Tertiary, Palaeocene and pre-Cretaceous having no effect on fluid flow within the fault zone. Note, however, that permeability values for the pre-Cretaceous of greater than 30 mD result in regional convection within that unit. At a fault permeability of 200 mD, both the Tertiary and Palaeocene have the potential to induce temperature peaks of approximately 15°C at horizontal sediment permeabilities of 70 and approximately 1000 mD, respectively. Fluid flow within the fault zone is again most sensitive to Cretaceous permeability, with a Cretaceous permeability of 40 mD (0.4 mD vertical) causing a temperature peak of 40°C and 10 km half-wavelength. The pre-Cretaceous unit again convects at permeabilities above 30 mD; below this value, the pre-Cretaceous does not significantly influence fluid flow within the fault zone.

The fault models in this section are capable of producing temperature anomalies of comparable magnitude and wavelength to the SWA's (Fig. 5.19). The SWA's are otherwise inexplicable in terms of

conductive heat transport, or thermal disturbances caused by regional fluid flow. Surprisingly, the potential for the formation of such temperature anomalies (SWA's) is equally dependent on sediment permeability as on fault permeability, especially that of the low permeability unit which the modelled fault transects.

5.4 Fluid Flow Within Fault Zones - Central Graben

The test grids show that fluid flow within fault zones is equally dependent on sediment permeability and fault permeability. The simulations also suggest that fluid flow within fault zones (at realistic permeabilities) is capable of producing SWA's of magnitude and wavelength similar to those noted in Chapter 2 from actual measurements (Fig. 2.9). It therefore seems appropriate to simulate the thermal effects of a sub-vertical, permeable fault zone within the setting of the Central Graben. The models used are adapted from the original Central Graben section described in Figure 4.1. However, I add several rows and columns; this allows simulations which include both the Palaeocene, and a sub-vertical fault zone (Figs. 5.20 and 5.21). The thermal conductivity parameters are the same as those for the final thermal model in Chapter 3 (Table 3.4 for thermal conductivity values). From a base-case model (no fault zone, see Table 5.5), I extract the temperatures at each of the nodes shown in Figure 5.21 (located across the subsequent position of the fault zone). For all other simulations I extract temperature values from the same set of points, thus allowing a comparison of any temperature effects due to flow within the fault zone to the "background".

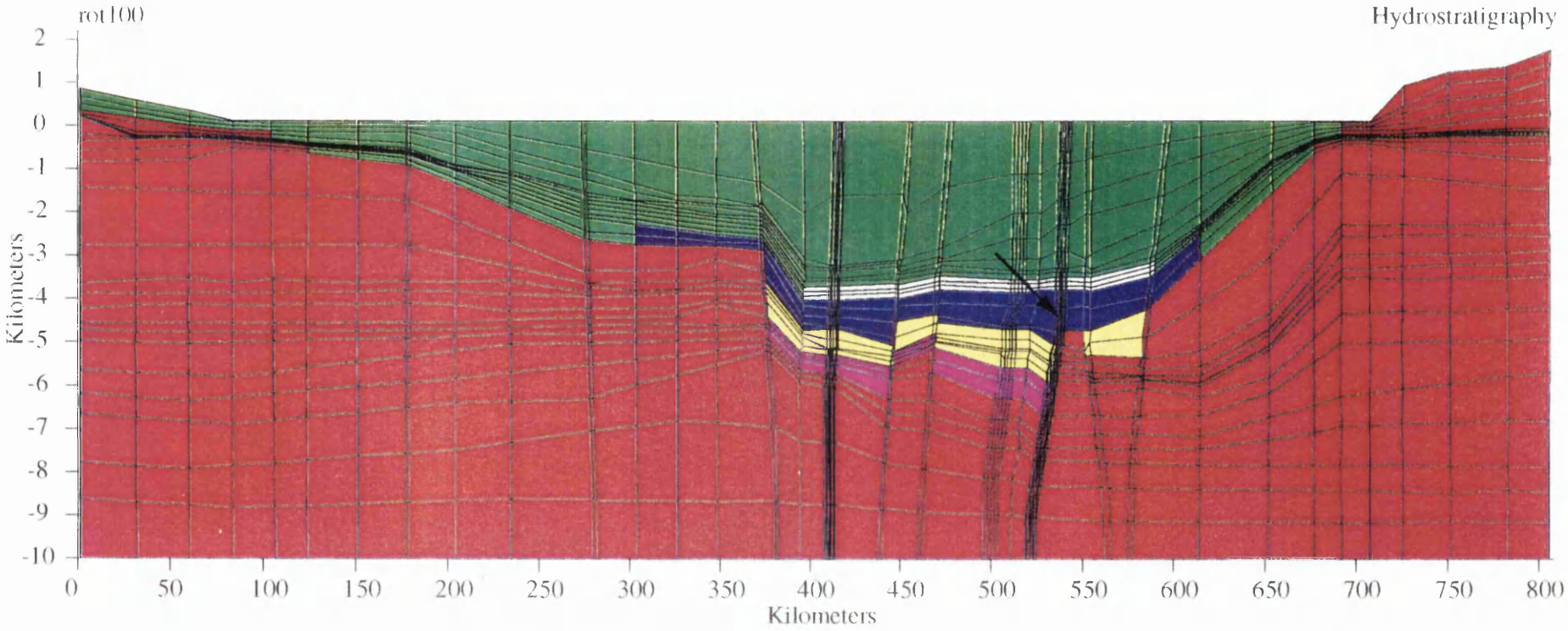

Figure 5.20 - Geometry of Fault zone model - Central Graben (Section 5.4). [Basement - red, Tertiary - green, Palaeocene - white, Cretaceous - blue, Jurassic/Triassic - yellow, Permian - purple.] Approximate location of fault zone arrowed (see Fig. 5.21).

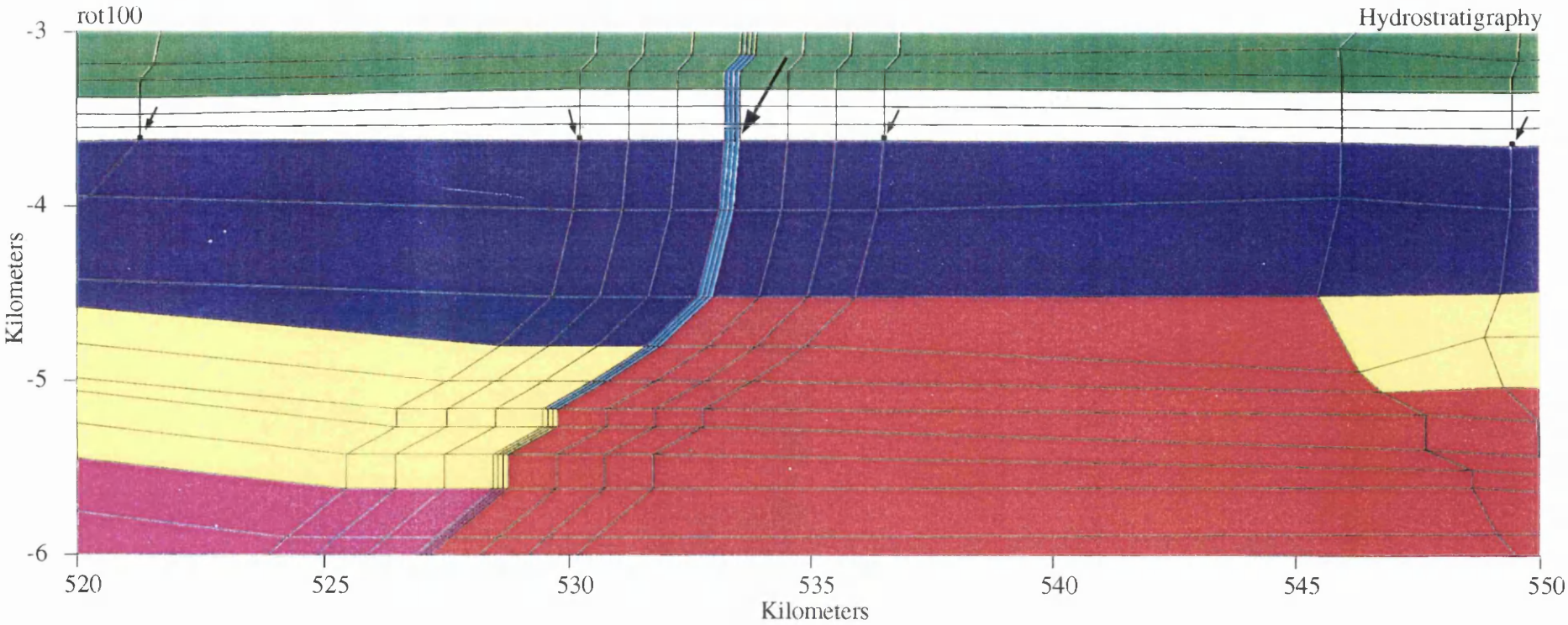

Figure 5.21 - Enlarged view of the geometry of the fault zone model - Central Graben (Section 5.4). [Basement - red, Tertiary - green, Palaeocene blue, Jurassic/Triassic - yellow, Permian - purple.] The fault zone is light blue in colour and 300 m wide. Note the nodes of temperature extraction shown in black (all four nodes that make up the fault zone are monitored).

5.4.1 *Influence of Sediment and Fault Zone Permeability on Temperature*

Using the modified version of the Central Graben section described above I proceed in a similar manner to the previous section on "influence of sediment permeability architecture" (Section 5.3.2). After adding a 300 m wide sub-vertical fault zone on the western edge of the basement high shown in Figure 5.21 (note the nodes for temperature extraction), I hold all sedimentary units at their base-case values and simulate the effects of a permeable fault zone. The simulations are over a range in fault zone permeability of 50 to 500 mD (it should be noted that all fault permeabilities quoted are vertical permeabilities, the horizontal permeability within the fault zone being 100th of the vertical in each case). The resulting temperature disturbance at these reference points is plotted in Figure 5.22. Up to a vertical permeability of 200 mD the temperature effect of the permeable fault zone is negligible. At 300 mD or above, a 15°C temperature anomaly of only approximately 5 km half-wavelength is formed. This is not the result of buoyancy-driven fluids moving upwards, from the pre-Cretaceous sediments into the Palaeocene as may be expected, but is a result of **convection within the fault zone** (Fig. 5.23).

Having established that wider reaching regional flow cannot be induced by the presence of a fault zone alone, I set the fault zone at a conservative 100 mD. I then proceed, by simulating the effect on flow (and therefore temperature) within the fault zone, over a range in permeabilities for each "stratigraphic" unit (Tertiary, Palaeocene, Cretaceous, Jurassic/Triassic, and pre-Triassic sediments). I note the resulting temperature effects in and around the fault zone for each simulation.

The range in permeability for each sedimentary unit is shown in Table 5.5. The resulting plots of temperature against distance for each value of permeability are shown in Figure 5.24. These plots show that, for elevated

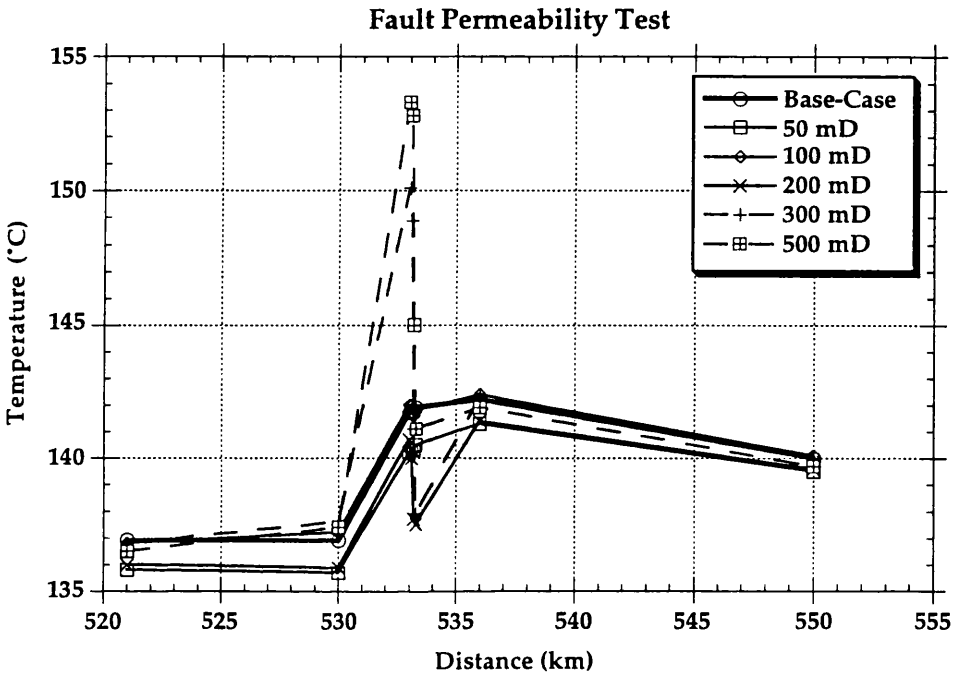

Figure 5.22 - Temperature profile across fault zone in Central Graben model for fault zone permeabilities of 50 to 500 mD. Sedimentary unit permeabilities held constant at values listed in Table 5.5. NOTE - fault permeabilties are vertical permeabilities, with horizontal fault permeabilities being 100th of the vertical.

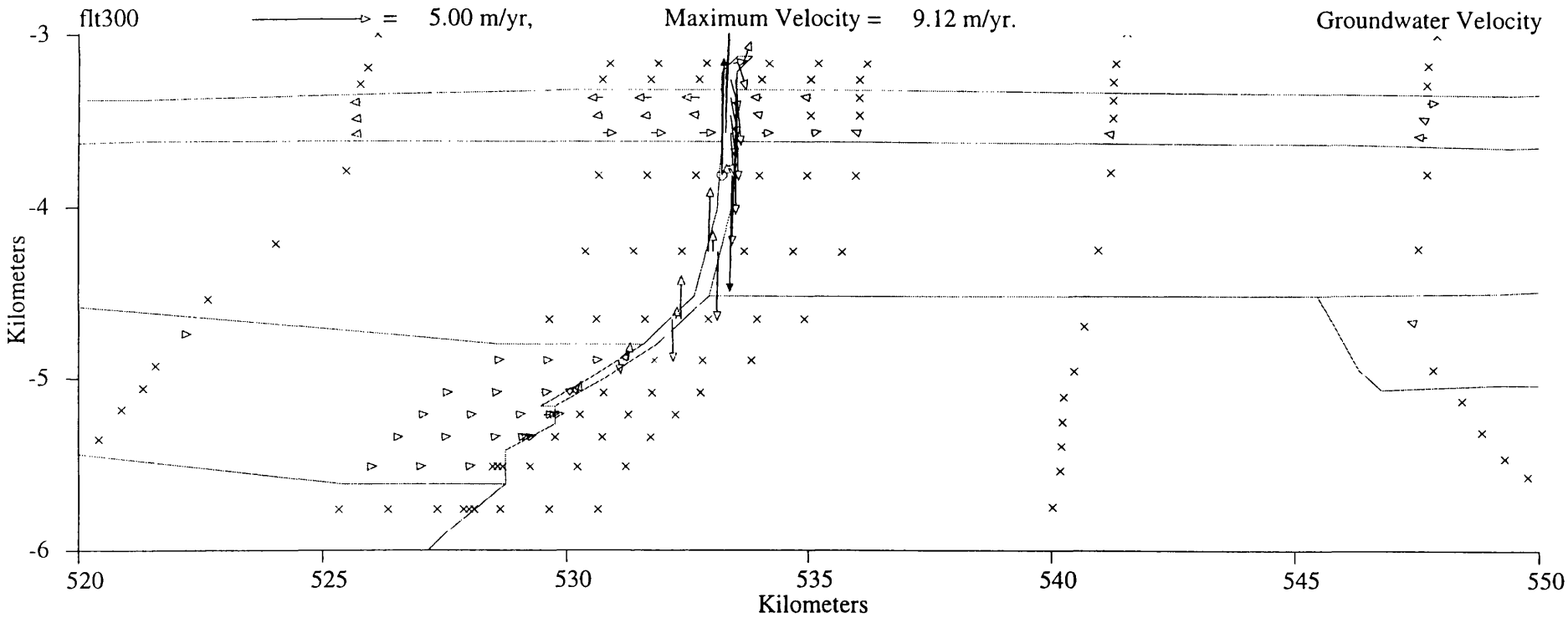

Figure 5.23 - Groundwater flow pattern for fault zone model - Central Graben, at a fault zone permeability of 300 mD. All sediment permeabilities at base-case values shown in Table 5.5. Maximum length of flow vector represents a flow velocity of 5ma*-1 or greater. All other vectors scaled to 100th of this value. X's represent flow velocities of less than 0.05 ma*-1. NOTE convection within the fault zone, and entrainment of fluid into the base of the fault zone. Minor convection also occurs within the Palaeocene. The geometry outlined corresponds to that shown in Figure 5.21.

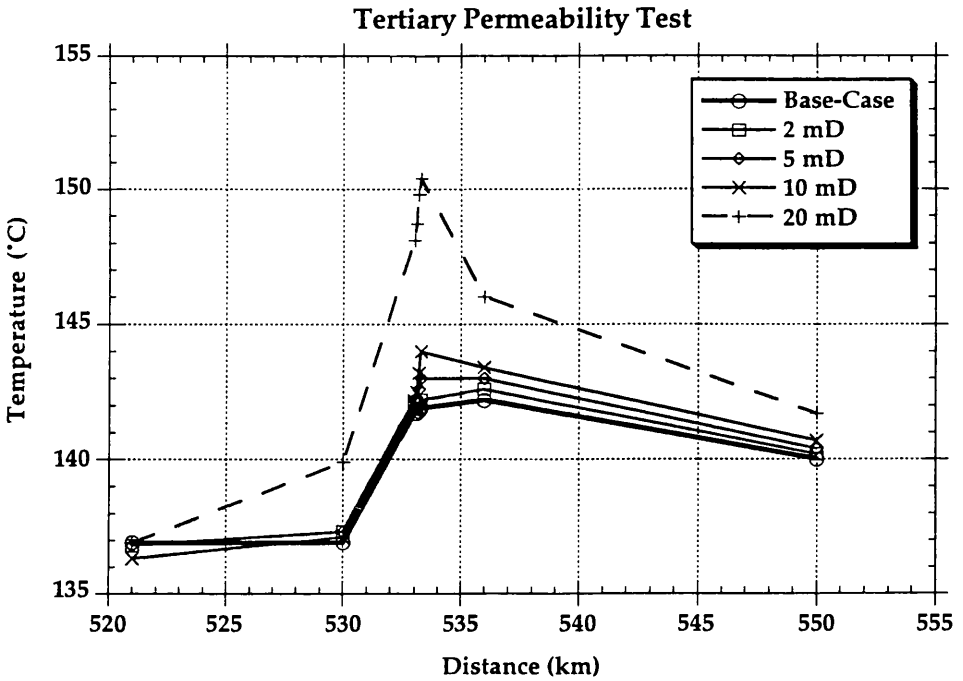

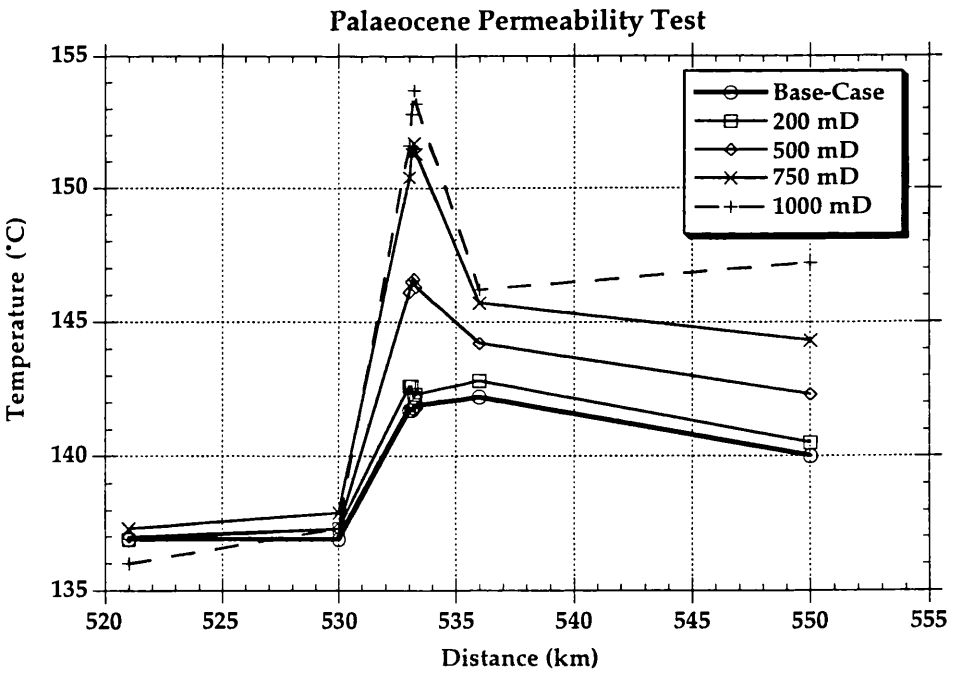

Figure 5.24 - Temperature profile across the fault zone for each unit described in Table 5.5, simulated at a range of horizontal sediment permeabilities. Cretaceous, Jurassic/Triassic, and Pre-Triassic are shown overleaf. The fault zone appears most sensitive to Cretaceous permeability variations.

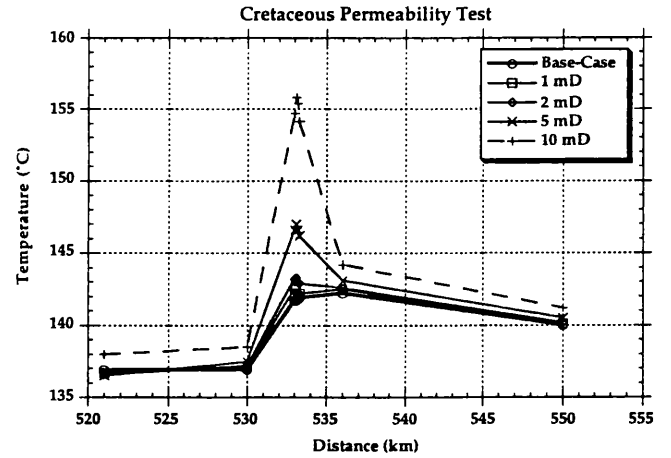

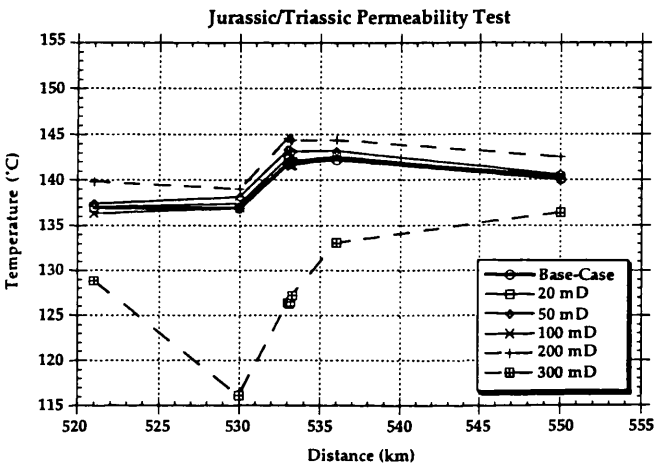

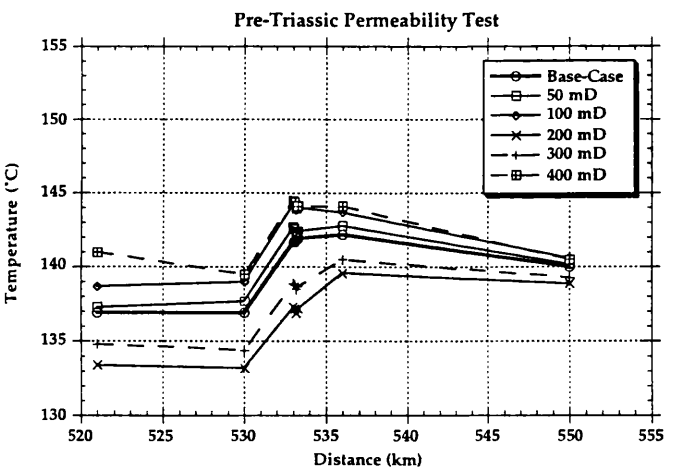

Figure 5.24 (cont.) - Temperature profile across the fault zone for each unit described in Table 5.5, simulated at a range of horizontal sediment permeabilities. The fault zone appears most sensitive to Cretaceous permeability variations.

permeabilities within the Tertiary and Palaeocene (of 20 mD and 500 mD+ respectively), 10 to 15°C temperature steps are formed with half-wavelengths of approximately 10 km. Flow velocities in fault zone are more sensitive to increases in permeability of the Cretaceous unit than any other unit; producing a 15°C temperature peak of approximately 5 km half-wavelength at 10 mD horizontal permeability (0.1 mD vertical permeability). Units lying below the Cretaceous appear to have minimal effect on the behaviour of flow within the fault zone, with the Jurassic/Triassic and pre-Triassic sedimentary units showing only minor temperature effects at up to 200 and 400 mD respectively.

Sedimentary Unit	**Base-Case Horizontal Permeability (mD)**	**Porosity (%)**	**Anisotropy**	**Range in Horizontal Permeability Modelled (mD)**
Tertiary	1.0	10	100	2 - 20
Palaeocene	100	10	100	200 - 1000
Cretaceous	0.1	5	100	1 - 10
Jurassic/ Triassic	10	5	100	20 - 200
Permian	10	5	100	50 - 400
Fault Zone	--	5	100	50 - 500 **(max. vertical, min. horizontal)**

Table 5.5 - Base-case poro-perm parameters, and modelled range of sediment and fault permeabilities, in simulations of Fault Zone Behaviour within the Central Graben model (Fig. 5.20). Basement remains constant at 10^{-4} mD (anisotropy of 5). NOTE - sediment permeabilities listed are horizontal, fault permeabilities listed are vertical.

5.4.2 *Fault Outlet Zone Investigation*

The models described up to this point, show that flow in and around the fault zone produces a maximum positive temperature disturbance of 15°C. One well within the Central Graben 2-D temperature plots (Figs. 2.6 & 2.9) shows a positive anomaly of 40°C. Could a positive anomaly of this magnitude be formed by fluid flow up a fault zone? One possibility is the exit of hot fluids from the top of the fault zone into a small (compartmentalised), more permeable unit allowing greater velocities of flow, and therefore a greater temperature disturbance.

To test this assumption, a suite of models is used with the same sediment poro-perm values as listed in Table 5.5, and the same overall geometry as Figure 5.20. However, the previous model is modified by the addition of a permeable unit at the top of the fault zone. The new geometries (around the fault zone) of Models 1 - 5 are shown in Figure 5.25 (A-C) with the poro-perm values of the additional permeable unit (black, see Fig. 5.25) listed in Table 5.6 (the fault remains at the conservative 100 mD vertical permeability). Models 1 & 2 are offset to the west of the fault zone, Model 3 is centred on the fault zone and Models 4 & 5 are offset to the east of the fault zone.

Models 1 and 2 share the same geometry (Fig. 5.25A) with the additional high permeability unit being approximately 2 km wide and 500 m thick. In the case of Model 1 the permeability of the outlet zone is isotropic, whereas in Model 2 it is anisotropic, with the maximum permeability being vertical (perhaps comparable to a highly fractured or brecciated unit or zone). A plot of temperature against unit permeability shows that Model 1 produces only an approximately 15°C temperature step (Fig. 5.26A). Model 2 however, with its enhanced vertical permeability, produces a maximum

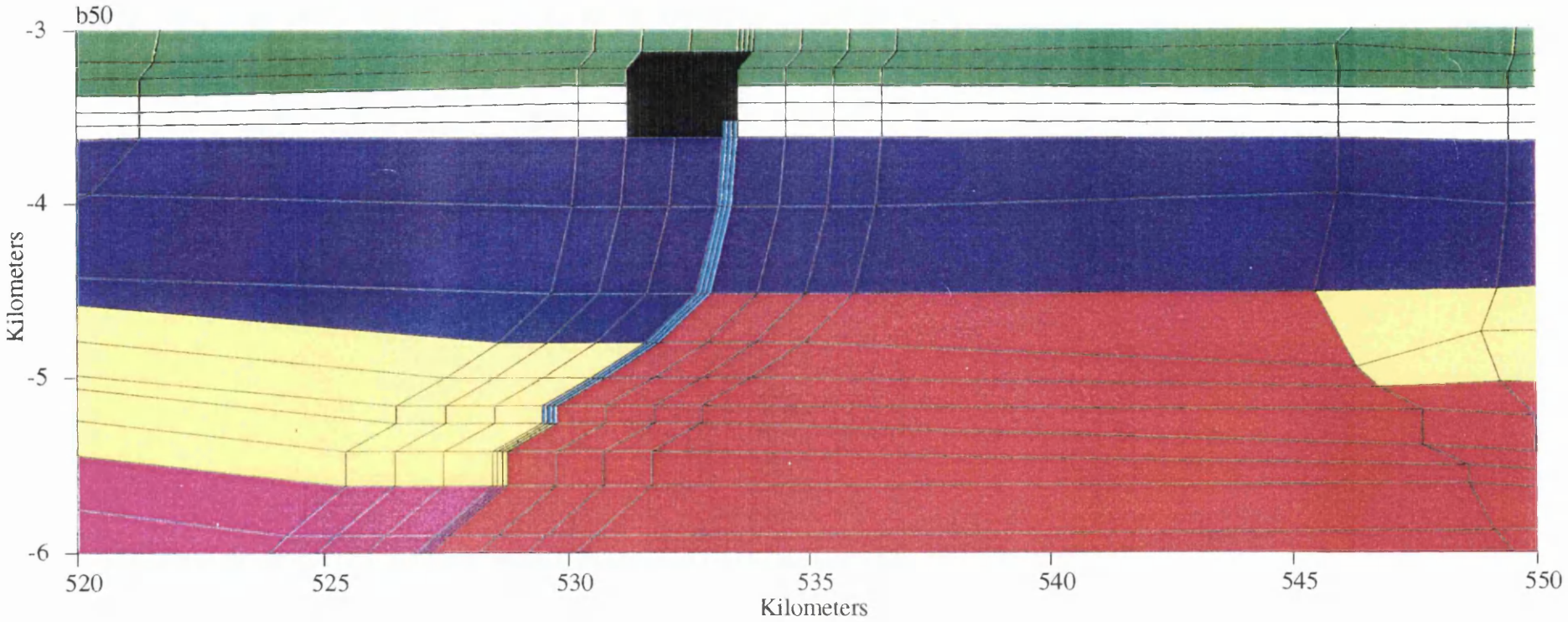

Figure 5.25A - Enlarged view of the geometry of Fault Outlet Zone Models 1 and 2 (Section 5.4.2). Fault outlet zone unit shown in black, other colours as Figure 5.21. Nodes for temperature extraction also the same as those used in Figure 5.21.

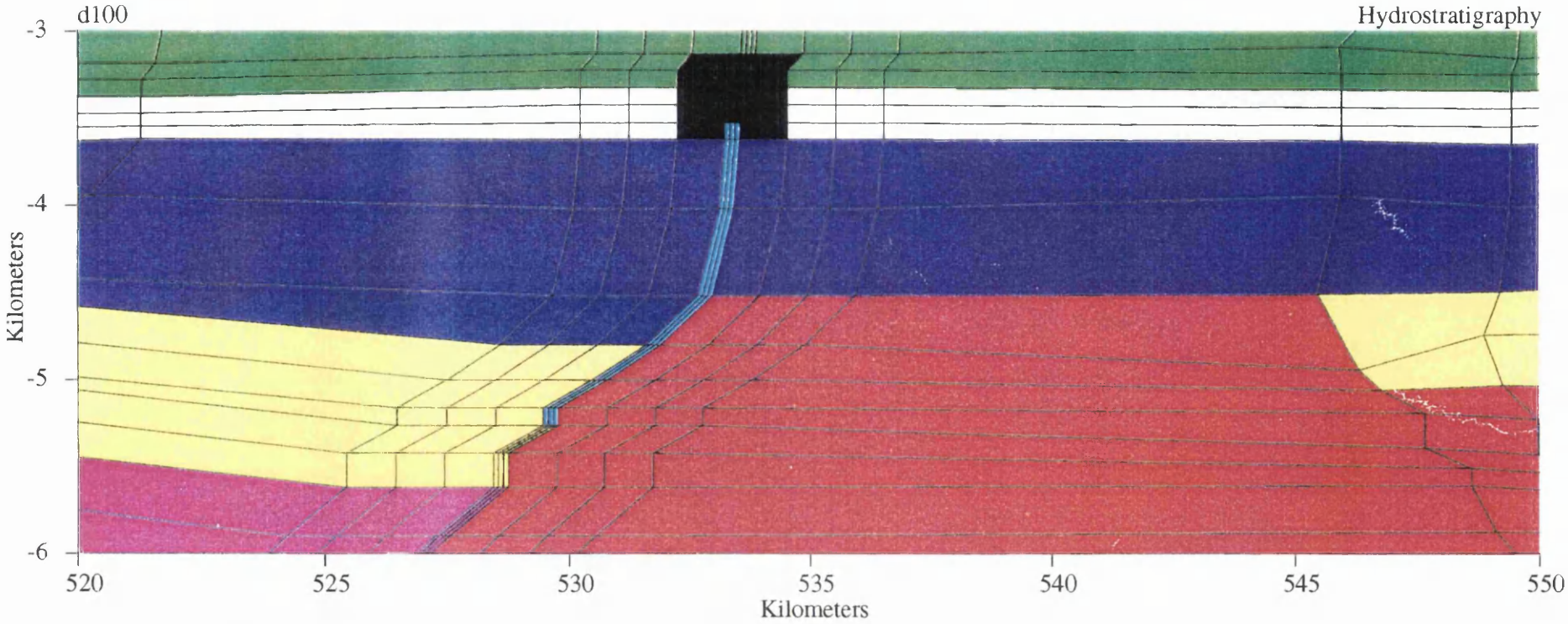

Figure 5.25B - Enlarged view of the geometry of Fault Outlet Zone Model 3 (Section 5.4.2). Fault outlet zone unit shown in black, other colours as Figure 5.21. Nodes for temperature extraction also the same as those used in Figure 5.21.

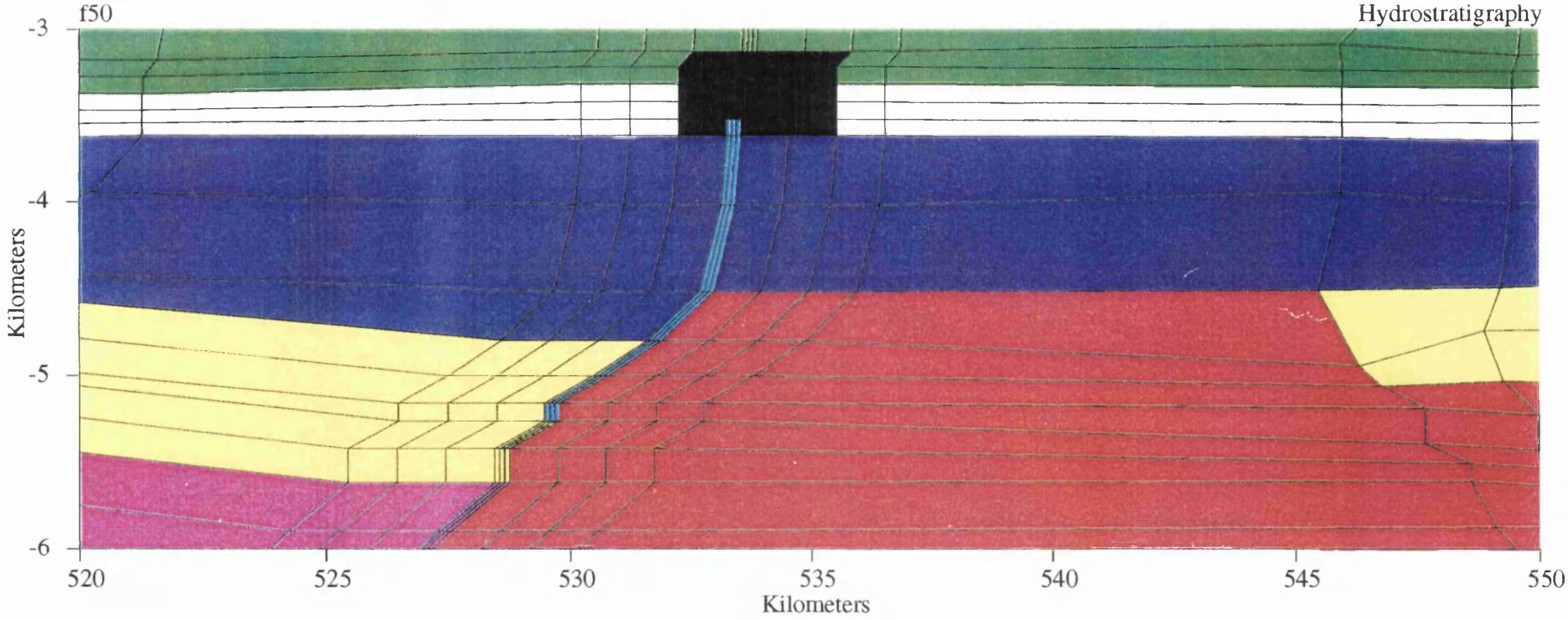

Figure 5.25C - Enlarged view of the geometry of Fault Outlet Zone Models 4 and 5 (Section 5.4.2). Fault outlet zone unit shown in black, other colours as Figure 5.21. Nodes for temperature extraction also the same as those used in Figure 5.21.

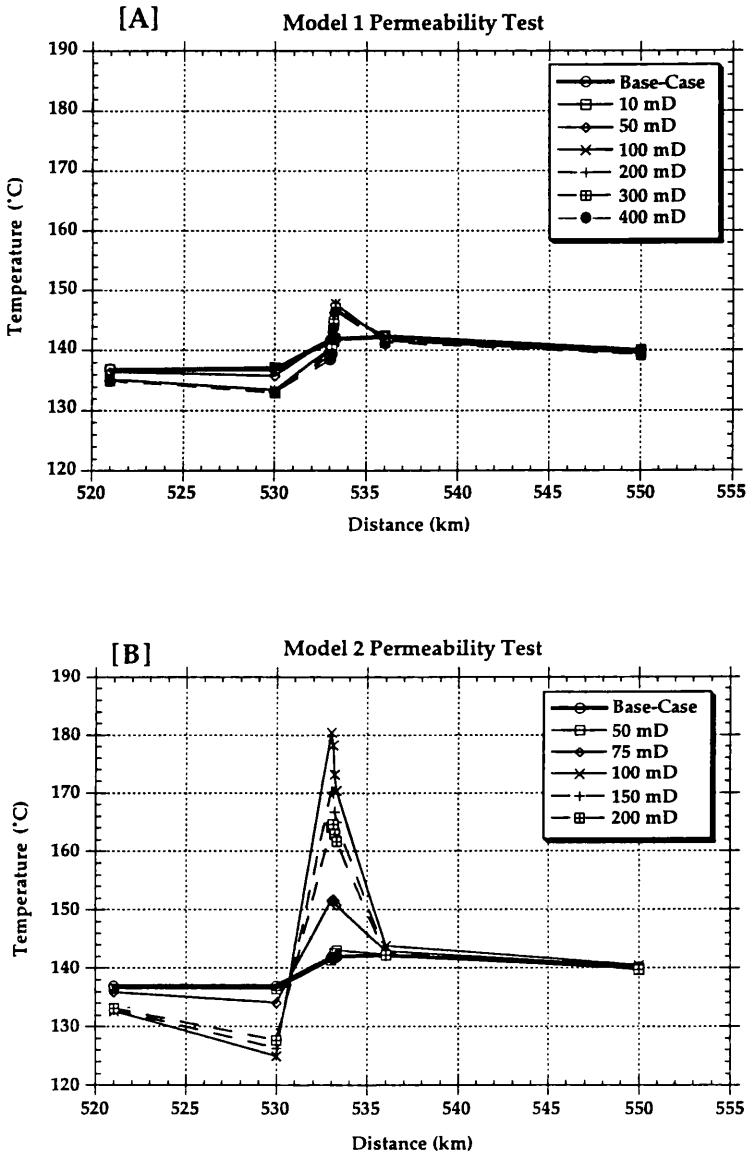

Figure 5.26 - Temperature profiles over the Central Graben fault zone for fault outlet zone Models 1 and 2. The fault zone permeability is held constant at 100 mD and all sedimentary units at their base-case values shown in Table 5.5.

temperature peak of 40°C (Fig. 5.26B) at a vertical permeability of 100 mD (equal to that of the fault zone). This magnitude of temperature peak is compatible with the largest of the observed SWA's.

Model 3 (Fig. 5.25B) has a 2.3 km wide sedimentary unit centred on the top of the fault zone. This unit is anisotropic, again with its vertical permeability 100 times horizontal. This model produces only a maximum 10°C temperature step (Fig. 5.27) over a range of permeabilities from 100 to 500 mD (vertical). This step deviates only from background temperatures by approximately 5°C.

Model	Maximum Permeability Angle (°)	Anisotropy (relative to maximum direction)	Permeability Range Modelled (mD)	Porosity (%)
Model 1	0 (horiz.)	1	10 - 400	10
Model 2	90 (vert.)	100	50 - 200	10
Model 3	90 (vert.)	100	100 - 500	10
Model 4	0 (horiz.)	1	25 - 125	10
Model 5	90 (vert.)	100	25 - 150	10

Table 5.6 - Poro-perm parameters of fault outlet zone, for Models 1 to 5 (Fig. 5.25) in Fault Zone Outlet Investigation (Section 5.4.2). All other sedimentary units at base-case parameters shown in Table 5.5. Fault Zone and Basement constant at 100 mD and 10^{-4} mD respectively.

In Models 4 and 5 the high permeability unit is offset to both the east and west of the fault zone (Fig. 5.25C) and is approximately 3 km wide by 500 m thick. Model 4 is isotropic, with Model 5 being anisotropic (see Table 5.6). The isotropic model (Model 4) produces an approximately 15°C temperature peak at 50 mD, with a negative temperature anomaly (of approximately

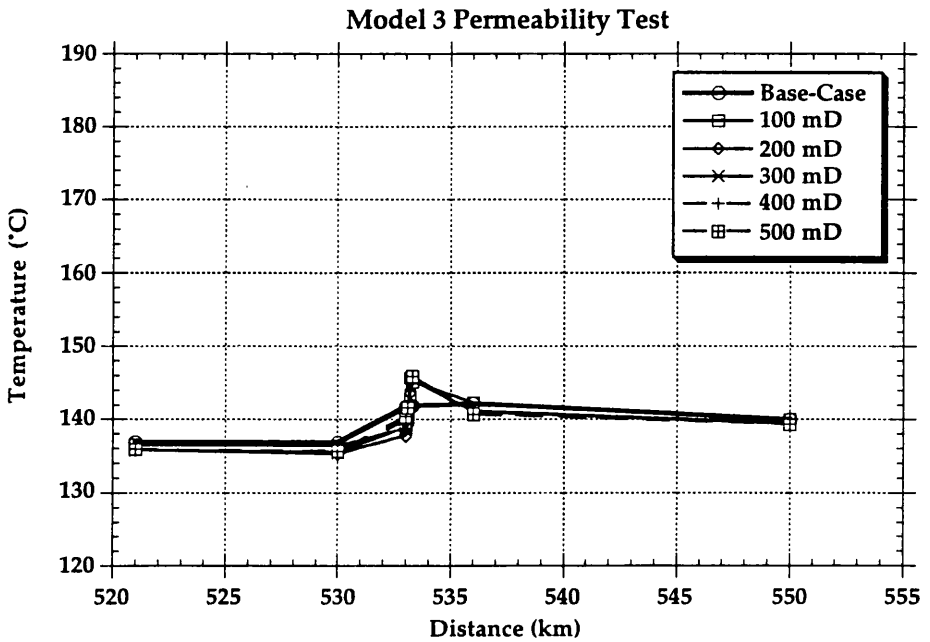

Figure 5.27 - Temperature profiles over the Central Graben fault zone for fault outlet zone Model 3. The fault zone permeability is held constant at 100 mD and all sedimentary units at their base-case values shown in Table 5.5.

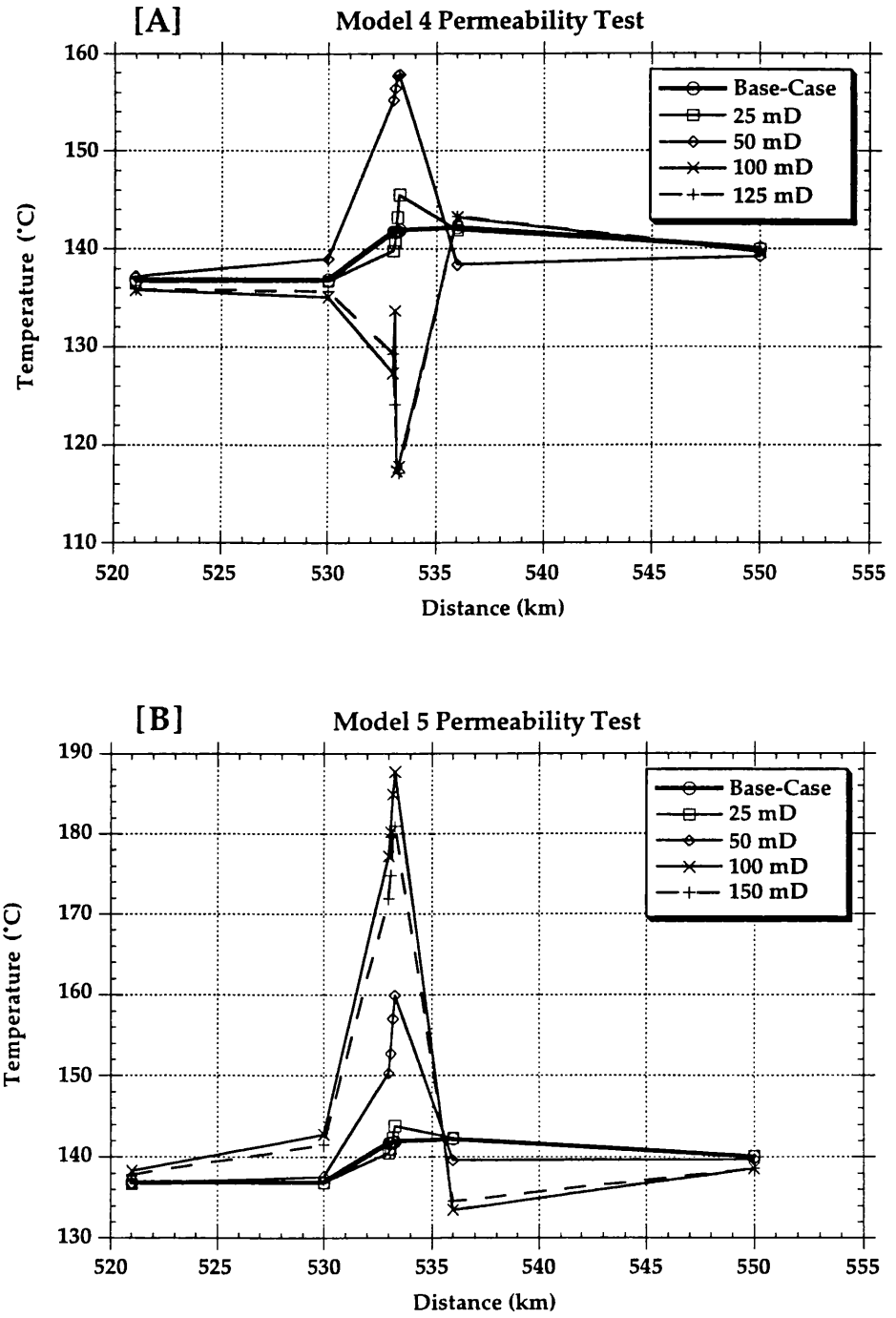

Figure 5.28 - Temperature profiles over the Central Graben fault zone for fault outlet zone Models 4 and 5. The fault zone permeability is held constant at 100 mD and all sedimentary units at their base-case values shown in Table 5.5.

15°C) being produced at higher permeabilities (Fig. 5.28A). Model 5 however, behaves in much the same manner as the other model of vertical maximum permeability (Model 2), and produces a **maximum temperature peak** at 100 mD of approximately **50°C** (Fig. 5.28B).

5.4.3 *Summary/Key Factors*

The thermal properties of the preferred conductive model reported in Chapter 3, along with a suite of base-case poro-perm parameters comparable to those used in the fault test-grid models, are used to assess the effects of fault zone fluid flow in a Central Graben setting (Figs. 5.20 & 5.21). Background, base-case temperatures are established and all subsequent simulations are compared to them. The influence of fault zone permeability is investigated first. Holding all sediment permeabilities at base-case values, the fault zone is modelled through vertical permeabilities ranging from 50 to 500 mD. At a fault zone permeability greater than 300 mD, a 15°C temperature anomaly is formed with a 5 km half-wavelength. This temperature disturbance is due to convection within the fault zone (Fig. 5.23) -- **not** to simple upwelling of buoyancy-driven fluids. Therefore the presence of a permeable fault zone alone does not induce more regional circulation of fluids.

I then set the fault zone at 100 mD vertical permeability for all subsequent simulations and vary the permeability of each sedimentary unit in turn (Table 5.5) noting the resulting temperature effects. Figure 5.24 shows that for Tertiary and Palaeocene horizontal permeabilities above 20 and 500 mD, respectively, 10 to 15°C temperature steps form with wavelengths of 10 km. As expected from the results of the test grids, fluid flow within the fault zone is most sensitive to Cretaceous permeability. A Cretaceous horizontal permeability of only 10 mD results in a 15°C, 5 km

half-wavelength temperature peak. The pre-Cretaceous units do not appear to have any major effect on flow within the fault zone, showing only minor temperature effects at up to 200 and 400 mD respectively. As observed in the test grid simulations, the Cretaceous is again the most influential unit on the behaviour of fluids within the fault zone, with units above the Cretaceous having a lesser effect and those below virtually no effect.

This suite of models described in Section 5.4.1 (Figs. 5.24) considers only a (conservative) base-case bulk permeability for each "stratigraphic" unit. What if the fault zone intersects a high permeability unit? This could be either a high permeability sedimentary unit within the Palaeocene, or an extremely fractured unit (wider fault zone, brecciated or hydrofractured unit). What does the model simulate the effect on temperature to be of a fault intersecting a smaller, permeable, compartmentalised unit? To investigate these questions I use five new geometries around the top of the fault zone shown in Figs. 5.25A - C (the overall geometry of the Central Graben model remains the same, poro-perm parameters of the additional unit(s) is shown in Table 5.6). Models 1 & 2 differ only in that the former is isotropic with the latter having its maximum permeability orientated vertically. The isotropic model produces a 15°C temperature step at compartment permeabilities of 100 mD and above (Fig. 5.26A), whereas Model 2 (anisotropic, vertical permeability maximum) produces a maximum temperature peak of 40°C and approximately 5 km width at only 100 mD vertical permeability (Fig. 5.26B).

Model 3 (maximum permeability vertical and centred on the fault zone) produces only a 5°C deviation in temperature from background at 500 mD vertical permeability (Fig. 5.27; 5 mD horizontal permeability); this geometry could not be responsible for any SWA's identified by this study. Models 4 & 5 (Fig. 5.28), although of different geometry to Models 1 & 2, behave in much the same manner. The isotropic model produces a

maximum temperature peak of 15°C at 50 mD, with a negative anomaly of 15°C occurring at higher permeabilities. Model 5 gives a maximum temperature peak of 50°C at only 100 mD vertical permeability (horizontal = 1 mD).

At the modelled permeabilities, fluid flow within fault zones is capable of producing temperature anomalies ranging in magnitude of up to 50°C. Such flow can adequately explain the SWA's observed within the temperature profiles of Chapter 2. Fault permeability however, is not the dominant factor, as might have been expected. Indeed at high fault permeabilities, convection within the fault zone dominates the flow system. Sediment permeability, and the permeability architecture of the unit into which the fault discharges, are of paramount importance in the magnitude of temperature anomaly produced.

5.5 Conclusions

5.5.1 *Convection*

The different geometries of convection cell I have modelled (Figs. 5.2 & 5.5) show that significant temperature disturbance is possible due to the effects of relatively small scale localised convection cells. The 800 m thick cell produces a 20°C temperature peak (Fig. 5.6 C) at only 1 Darcy horizontal permeability. However, the thinner cells (200 and 400 m thick), as expected, require higher horizontal permeabilities -- up to 6 D (anisotropy in both cases = 100). Like the SWA's identified in Chapter 2, Fig. 2.9, the resulting temperature anomaly is depth-limited (Fig. 5.4) and of similar magnitude.

In a more realistic model of the Central Graben (Fig. 5.7, 10 km by 400 m thick convection cells), temperature anomalies are produced (Fig. 5.9), but they are of smaller magnitude, and the maximum temperature anomalies

occur at 2 D horizontal permeabilities. This disturbance corresponds to an average fluid velocity within the convection cell of 1.0 ma^{-1} for both the ECG and WCG. The ECG, however, produces only a maximum 10°C temperature step compared to the >15°C temperature peak in the WCG at 2 D horizontal permeability. The WCG is apparently more prone to convection than the ECG.

Both sets of convection models have the potential to produce approximately 15°C magnitude SWA's. The permeabilities necessary for this effect are somewhat high compared to sediment at that depth. However, Darcy permeabilities may be possible within some of the Permian dune sand units within the graben (Trewin and Bramwell, 1991). Based on the results reported here, horizontal permeabilities of above 1 Darcy will certainly result in significant and potentially detectable (>10°C) temperature anomalies.

5.5.2 *Flow within fault Zones*

From both the test grids (Fig. 5.12 & 5.16), and the Central graben models (Fig. 5.21), it is apparent that fault or fracture zone permeability is not the sole/dominant factor in determining whether or not the temperature field will be significantly disturbed due to fluid flow within fault or fracture zones. Figure 5.13 shows that large fault zone permeabilities are not necessary for the formation of large thermal disturbances. A 50 mD vertical permeability fault zone can produce a 40°C temperature anomaly at bulk sediment horizontal permeabilities of only 10 - 12 mD!

In both of these types of model, if the fault-zone permeabilities are high, and the faults are located within a relatively low permeability sedimentary pile, the temperature disturbances that are formed are the result of convection within the fault zone. They are not related to simple

buoyancy-driven flow moving up the fault zone. Such convection within a fault or fracture zone is capable of producing a 15 to 20°C temperature anomaly of 5 km width for a fault zone 3 km wide. When the sedimentary pile is sub-divided into distinct hydrostratigraphic units (Figs. 5.12 & 5.21), the resulting temperature anomaly is most sensitive to the permeability of the "Cretaceous" -- in both the test grids, and the Central Graben models (compare Fig. 5.18 & 5.19 to Fig. 5.24). Underlying sedimentary units (beneath the Cretaceous) do not significantly affect the magnitude of the temperature anomaly formed, whereas the overlying Tertiary and Palaeocene units can influence the resulting temperature anomaly, although to a lesser degree than the Cretaceous (again see Figs. 5.18 & 5.19 to Fig. 5.24). The maximum magnitude of temperature anomaly modelled is approximately 15°C and of 5-10 km width.

To produce larger temperature anomalies, comparable to those of the largest identified SWA's, a fault-outlet zone of high vertical permeability is necessary (example Fig. 5.25A and 5.26B). This geometry is capable of producing up to 50 °C temperature anomalies.

In the Central Graben models, the fault permeability itself has less influence on the magnitude of fluid flow velocities, and the temperature anomalies formed, than does the permeability of the sedimentary pile, and the permeability and nature of the fault outlet area. For example, a 100 mD fault intersecting a small highly fractured (100 mD vertical permeability) unit above the Cretaceous produces a much greater temperature anomaly than the same fault intersecting an un-compartmentalised Palaeocene at a horizontal permeability of 1000 mD.

CHAPTER 6

DISCUSSION OF MODELLING AND MECHANISMS

6.1 The Modern Temperature Field and Conductive Heat Transfer

Understanding the temperature, and the temperature history, within an oil producing basin such as the North Sea, is of paramount importance, since the temperature history is a major controlling factor on the maturity of source rocks, and so on oil generation. A more accurate understanding of the modern temperature distribution, and of the factors influencing it, allows a better extrapolation into the geological past, and therefore, a better understanding of "kitchen" areas for oil generation within the basin.

Within the Central Graben I have identified two types of temperature anomaly - the LWA and the SWA. Through the use of 2-D conductive heat transfer models I am able to explain the LWA. These simulations allow me to estimate the variation in heat flow across the Central Graben. There is a 5 mWm^{-1} decrease from the West Central Graben (70 mWm^{-2}) to the East Central Graben (65 mWm^{-2}). A similar decrease in heat flow across the Central Graben is noted by Cermák (1979).

The SWA's superimposed onto the LWA are inexplicable in terms of conductive heat transfer. It is not possible to explain the SWA's by high conductivity features such as salt domes. The models I investigate --both a large salt dome and a salt wedge -- suggest a maximum temperature disturbance of less than 10°C (relative to the conductive temperature field) due to the presence of the anomalous salt features. A similar study by Petersen and Lerche (1996) of the temperature effects over a salt dome

within the Norwegian-Danish Basin show a maximum positive anomaly of 10°C over a 3 km "tall" salt dome. The only salt feature within my line of section of similar proportions lies within the Western Central Graben and therefore salt could not account for **all** the SWA's identified -- even if the temperature effects were sufficient to explain the observed SWA's.

Some temperature studies, confronted by areas of anomalous high or low temperatures, invoke changes in basal heat flow to account for these variations (Yu et al 1995). This may be the case when dealing with large areas (10's of km), but in the case of the Central Graben, the SWA's have wavelengths of 5 to 15 km, and, they are depth-limited. It does not seem possible that a local increase in basal heat flow can be responsible for the SWA's as any additional source of heat at depth (within the basement), which might cause such an increase in basal heat flow, would be greatly defocused within the basin sediments, and the resulting temperature anomaly at 1 - 5 km depths, would not be depth limited, and it would be broad.

Based on a wide range of modelled sediment and basement thermal conductivities, I have defined a best-fit conductive model for the Central Graben. However, this model cannot account for the SWA's observed within the temperature contour plots -- neither high thermal conductivity units such as salt, or changes in basal heat flow can produce SWA's of the appropriate geometry. The SWA's can only be explained by other heat transfer processes - e.g. advection of heated porefluids.

6.2 Fluid Flow and Heat Transfer Within the Central Graben

The transport of heat by moving groundwaters must now operate, or have recently been operative, within the Central Graben. Temperature studies undertaken by Carstens and Finstad (1981), and by Andrews-Speed et

al (1984), concluded that fluid flow must significantly influence the modern-day temperature field of the Central and Viking Grabens respectively. This study reaches similar conclusions. The fluid flow processes considered herein are large-scale gravity-driven fluid flow, convective fluid flow (on both a regional and localised scale), and fault-focused fluid flow. Fluid flow driven by overpressure is not explicitly considered, but I address this matter by analogy with the fault-focused models. Here I consider the viability of major fluid flow processes, and their effects or otherwise on modern temperatures, within the Central Graben. These processes and their effects are categorised in Table 6.1.

I did not investigate the effects of **compaction-driven** fluid flow. I concluded that sufficient work by others has already shown that compaction-driven fluid flow is typically of insufficient volume or velocity to significantly affect the temperature field of a compacting basin (Byorlykke, 1994; Bethke, 1985). For example, Bethke (1985) shows that compaction-driven flow within intracratonic basins (without the development of significant overpressure) is characterised by fluid flow rates of mma^{-1} or less. In the scope of this study fluid velocities of cma^{-1} to ma^{-1} are shown to be necessary for discernible (>1-2°C) temperature changes. Where rapid subsidence rates are coupled with the deposition of shaly strata (Gulf Coast) overpressure may form due to compaction disequilibrium (Bethke 1989; Dewers and Ortoleva 1994). However, I regard the process of trapping compactional fluids, and their subsequent rapid release at high pressure, as not truly compaction-driven fluid flow. I deal with the mechanism of overpressure-driven fluid flow later in terms of focused fluid flow.

Basement is generally excluded from basin models when dealing with fluid flow (Ungerer et al 1990, North Sea; Bethke 1986, Mississippi Valley, USA; Person and Garven 1989, Rhine Graben). However, recent investigations associated with the KTB borehole in Bavaria suggest that

Fluid Flow Process	**Affects LWA?** N = No Y = Yes	**Affects SWA?** N = No Y = Yes	**Magnitude/Half Wavelength of Anomaly**	**Significant Factors**
Compaction	N	N	--/--	Not significant (Bethke 1985)
Regional Gravity driven	N	N	--/--	Basement fluid flow - large volume recharge potential
Regional-Scale Convection	Y	N	up to 20°C/50 km	Permian sediments susceptible
Localised Convection	N	Y	up to 20°C/5-15 km	Pre-Cretaceous sediments most likely to convect
Fault/Fracture Flow	N	Y	up to 50°C/5 -15 km	Permeability of sediments surrounding fault zone and outlet (critical)

TABLE 6.1 - Summary of the potential thermal effects of major fluid flow processes within the Central Graben.

"basement fluids are present in great quantities and are able to migrate over considerable distances" (Harms et al 1993). The regional fluid flow simulations of the Central Graben reported in this study suggest that, while fluid flow **through basement** is not sufficiently fast to disturb the temperature regime, it provides a significant volume of fluids to the base of the sedimentary fill of the graben. The base-case model of the Central Graben used for regional fluid flow modelling indicates recharge through basement from the Norwegian high at flow rates of mma^{-1}. Therefore it is not realistic to automatically exclude basement from modelling studies within the North Sea (or elsewhere) without first conducting a regional overview that considers possible basement fluid flows. This additional fluid source to the deep graben may also have an effect on diagenetic studies within the sedimentary pile of the Central Graben.

Regional fluid flow in the base-case model (driven by topographic heads on the UK and Norwegian sides) produces a maximum fluid velocity of 18 cma^{-1} (within the Permian). This water flow pattern, and the associated flow of oil, suggests that petroleum migration directions may be severely affected by **topographically-driven** fluid flow (especially in the Pre-Cretaceous rocks). Although this model does not address overpressure, and the alteration of the flow system it causes, it may be that similar (cma^{-1}) fluid velocities have occurred in the past (during periods of no or low overpressure), and they may occur in the normally pressured portions of the basin at the present-day. If this is true, then **petroleum migration** directions, within the graben, may be partly determined by regional fluid flow (as opposed to only the buoyancy of oil; see Tóth 1991). In the base-case models petroleum flow is consistently **towards structural highs**; this motion is consistent with the known occurrences of oil within the Central Graben (Cayley, 1986).

Thermal effects associated with this topographically-driven flow system are not significant because flow rates are low. Although Andrews-Speed et al (1984) suggested that a regional fluid flow mechanism (cool groundwater descending off the Norwegian high) may be responsible for the patterns of heat flow they mapped. Jessop and Majorowicz (1994) believed there was not sufficient topographic relief to drive such a process. From the modelling reported here, it certainly appears that, although there exists some recharge to the Central Graben from the Norwegian High, it is insufficient to alter the conductive temperature field (unless there are permeable channels not identified or considered here). Therefore a process other than regional topographically-driven fluid flow must be responsible for any thermal disturbances.

Convection on a regional scale, and its potential to alter the conductive temperature field (see Le Carlier, 1994), is modelled by considering the effects associated with flows within individual stratigraphic units. Modern regional-scale convection within the Tertiary, Cretaceous and Jurassic/Triassic elements of the models can be discounted; the resultant temperature profiles associated with convection in these units are incompatible with the modern-day temperatures. Regional convection within the Permian of the Eastern Central Graben, however, may provide an alternative explanation for the shape of the modern LWA (instead of a decrease in basal heat flow from west to east), as this flow system produces a close fit to the LWA within the eastern Central Graben. However, without more detailed permeability data for the Permian of the deep graben, this possible flow system can remain only a hypothesis that may subsequently become testable.

Small scale (localised) convection has the potential to produce short-wavelength temperature anomalies of up to 20°C; such anomalies are comparable to some of the observed SWA's. The horizontal permeabilities

of sediments necessary to allow these convection cells are, however, relatively high (several Darcies). Pre-Cretaceous clastic units are the most likely sites for this form of fluid flow, with the Cretaceous chalk and Tertiary mudrock sequences unlikely to possess sufficient permeabilities. Therefore, the shallow, positive temperature anomaly (Tertiary) observed in the contour plots of temperature, and the 40°C SWA (Fig. 2.9), are not likely to be a result of localised convection.

6.3 Focused Fluid Flow - The Effects, Mechanism and Evidence

Focused fluid flow along faults or fracture zones is the only process modelled which can fully explain any of the observed SWA's within the modern temperature field. Simulations of fluid flow within a 300 m wide fault zone can produce temperature anomalies comparable to any of the SWA's identified in Chapter 2.

Interestingly, fault zone permeability does not appear to be the major factor governing flow within a fault (for the flow systems considered here). The rate of fluid flow within a fault zone (and therefore the magnitude of any temperature disturbance) is more sensitive to the permeability architecture around the **fault zone** than to the intrinsic fault permeability itself, and there is a particularly **critical dependence on the vertical permeability of the outlet zone**. The actual process of fluid flow within the fault zone (under the normally pressured conditions considered here) is one dominated by the buoyancy of fluids inducing convection within the upper permeable sediments at the top of the fault zone. A sketch model of my understanding of this fluid flow process is shown in Figure 6.1. This process can act at different stratigraphic levels within the basin and for different fault lengths given that a geometry like that shown in Figure 6.1 is present.

What is then the evidence for vertical fluid flow within fault or fracture zones? Cartwright (1994) presents evidence for large-scale dewatering of Tertiary mudrocks along the axis of the Central Graben. The primary mechanism proposed for this process is episodic release of overpressure through hydrofracturing, and the resulting sub-vertical migration of fluids within a hydrofractured fault network (this would be a geologically short-lived event). I observe a large temperature anomaly (SWA) within the Tertiary close to the axis of the Central Graben. This feature may represent physical temperature evidence for the process proposed by Cartwright (1994). Note however, that Cartwright infers episodes of flow from the Eocene to Miocene, and the temperature anomaly represents a modern phenomenon.

I propose that a similar mechanism of episodic build-up and release of overpressure in the deeper graben, also highly overpressured in part (Gaarenstroom 1992; Darby 1996a and 1996b, see Figure 6.1), may be responsible for the deeper SWA's within the Central Graben. The modelling package I have used (OILGEN) does not account for overpressure. However, I have shown that even within a normally pressured environment, at realistic fault and sediment permeabilities, SWA's may be formed due to buoyant fluid flow within fault zones. Therefore, the added fluid "drive" from an overpressured cell (due to the large pressure potential between the overpressured cell and normally or near-normally pressured strata above) would be even more likely to produce the ma^{-1} fluid velocities

6.1

necessary to result in the formation of SWA's. The process of episodic build-up and release of overpressure during basin evolution associated with hydrofracturing (Dewers and Ortoleva 1994) will enhance the vertical permeability in the zone of fluid release - a critical factor in the formation of the temperature anomalies. Furthermore, Miller (1995) shows that high pore pressures (overpressure) alone can cause "natural hydraulic fractures". Capuano (1993) also shows that under conditions of overpressure, even low permeability rocks such as shales may possess significant vertical fracture permeability, and can support flows comparable to that of sandstones.

Other studies of temperatures within sedimentary basins have shown the influence of fluid flow on temperature within fault zones. A study of the Rhine Graben by Person (1988) states that "the incorporation of high permeability fracture zones was found to be necessary to reproduce the observed geothermal conditions". More analogous to my study is the paper by Grauls and Baleix (1994) in which they show a positive temperature anomaly over a major fault network, **associated with overpressure release along that fault zone,** and the transfer of hydrocarbons from depth to a shallow reservoir over a short period of geological time. This process is directly comparable to what I would propose for the Central Graben (Fig. 6.1). Indeed, within the Central Graben, Cornford (1993) states that the bulk of oil migration is vertical (see also Thomas et al 1985, and Cayley 1986), and speculates on the likely pathways. Each pathway involves either faults, or fracture zones created by halokinesis.

My views on the processes most likely to be responsible for SWA's within the Central graben are summarised as:

- SWA's are explicable in terms of vertical (sub-vertical) migration of fluids along fault zones (at normal pressures).

- In studies by Cartwright (1994) and Grauls and Baleix (1994) overpressure release is the major driving force for migration of fluids within faults. In the case of Grauls and Baleix (1994) this process has also been shown to have detectable thermal effects.

- The Central Graben is known to have zones of extremely high overpressure (Darby 1996a, 1996b).

- Overpressure release within the North Sea may be episodic in nature (Cartwright 1994).

- Overpressure release provides enhanced vertical permeability through hydrofracturing (Dewers and Ortoleva 1994; Miller 1995).

- Oil migration within the Central Graben is dominantly vertical (Thomas et al 1985; Cayley 1986; Cornford 1993).

Therefore, I suggest that the observed (transient) SWA's that have formed within the Central Graben are the result of processes of episodic overpressure release, and the advection of heat by vertically moving fluids. However the modelling shows that such temperature anomalies may also form at normal pressures, and this may be significant in settings that lack an overpressure component.

6.4 Implications

A high degree of vertical fluid migration is necessary to account for oil migration patterns throughout the Central North Sea (Cayley 1986). Modelling carried out in this research shows that fluid velocities of greater

than 1 ma^{-1} along fractures/faults within the basin are possible at realistic permeabilities, and that this flow has the potential to greatly affect the temperature field (LWA [partly] and SWA's). These high velocities of vertical fluid migration may have implications for the time taken to charge oil fields, although charging could take place over one or more events.

A process such as episodic fluid release from the deeper portions of the Central Graben will have implications for not only the rates of oil migration, but also for diagenesis (Knipe 1993), and potentially for maturation around zones of successive overpressure release events through periodically raised temperatures.

This mechanism, allowing rapid vertical migration of fluids (water and oil) may help explain the observed low percentage of preserved oil in relation to the calculated volumes generated. Cornford (1993) suggests that the in-situ oil discovered represents only 1.25% of the total generated. Perhaps the suggested process of overpressure release and its implied rapid vertical migration of hydrocarbon-bearing fluids, and their subsequent loss accounts for part of the shortfall.

Modelling carried out in the course of this study implies a **dynamic hydrological regime** within the subsurface of the Central Graben. My understanding of each of the individual fluid flow mechanisms modelled (topographically-driven, regional and localised convection and focused fluid flow along faults) and their thermal effects, which are operative, or potentially operative, within the Central Graben is shown in Figure 6.2.

6.5 Shortcomings and Future Work

The 2-D models simulated using OILGEN do not consider overpressure or salinity variations across the basin. Models not inclusive of these factors are still valid in gaining a broad perspective of the hydrological

6.2

regime within the Central Graben. However, having established a general model of fluid processes within the Central Graben the present models could be refined by the use of a code which incorporated overpressure in calculating fluid velocities. Likewise, given enough salinity data for the line of section, the influences of salinity (and therefore density of fluids) on the fluid flow regime could also be determined. Note however, that rapid flows that cross "average" salinity gradients need to address fluid mixing; an issue involving a more complex modelling.

The horizontal top surface of the models (between the coasts of England and Norway) represents the sea bed (the height above sea-level of each land-mass is the topographic "head"). This flat top surface of the model provides no drive for fluids within the central portion of the models, and is therefore comparable to the effects of the North Sea. Such a geometry also provides the correct thermal datum for the area of interest (the graben) by using the average temperature of the North Sea as the boundary condition.

It would consider it useful to more fully investigate the temperature distributions within the North Sea basin using a 3-D visualisation tool. Such an investigation would provide information on heat flow and thermal conductivity variations within the basin and identify any other areas of anomalous temperature. Such a study linked to the distribution of overpressures may shed more light on the relationships between overpressure and temperature. Given modern computing power and software advances this seems a logical step forward compared to studies such as this one, Andrews-Speed (1984), or Carstens and Finstad (1984). Reaction-transport models could be used in modelling the diagenetic implications of the different proposed fluid flow mechanisms.

Geologists, when dealing with the subsurface, are faced with a lack of data and the problems of upscaling borehole data. Sensitivity studies of the

thermal and fluid flow regime appear essential to the characterisation of any basin whether in the pursuit of oil, minerals or geothermal power.

CHAPTER 7

CONCLUSIONS

This research was initiated to investigate the modern temperature field within the Central Graben, and attempt to generate models to match the resulting 2-D temperature profiles: first by conduction, and then subsequently by fluid advection. Transfer of heat within the graben by conduction is unable to fully explain the modern-day temperature field. Modelling of both regional and localised fluid flow processes and their effects on temperature is therefore undertaken, and a combination of conduction and localised fluid flow events are fully able to account for the modern day temperature distribution. A summary of the conclusions on a chapter by chapter basis follows:-

7.1 Chapter 2

- The modern temperature field of the Central Graben consists of a long-wavelength, positive temperature anomaly of low amplitude and approximately 120 km half-wavelength (LWA), and superimposed short-wavelength anomalies of up to 40°C in magnitude, and 5 - 15 km half-wavelength (SWA's).

7.2 Chapter 3

- Finite element models of conductive heat transfer in the Central graben are unable to **entirely** match the modern temperature field:

  - LWA can be matched by conduction - although if the

LWA is purely conductive, my models suggest a 5 mWm^{-2} decrease in basal heat flow (70 to 65 mWm^{-2}), across the Central Graben from west to east.

- SWA's remain unexplained even by high thermal conductivity units such as salt pillars and wedges.

7.3 Chapter 4

- Fluid flow through basement is of mma^{-1} in velocity, and may provide significant volumes of fluid recharge to the base of the sedimentary pile. Recharge to the basin is mainly through basement to the base of the graben not, as anticipated, off the highs through the sedimentary pile.

- At realistic sediment and basement permeabilities topographically-driven fluid flow does not significantly influence the temperature regime within the Central Graben.

- Regional convective fluid flow is only likely within the Permian and may modify the LWA in the eastern Central Graben.

- Regional fluid flow models are unable to account for the SWA's.

7.4 Chapter 5

7.4.1 *Convection*

- Small scale convection cells of the order of 10 km by several hundreds of metres thickness will require Darcy horizontal permeabilities to produce SWA's comparable to those observed in the temperature profiles of Chapter 2.

- The Western Central Graben is more prone to convection on a local scale than the Eastern Central Graben- possibly due to the lesser influence of gravity driven fluid flow off the Norwegian high.

7.4.2 *Fluid Flow within Faults/Fracture Zones*

- For a 300 m wide fault zone, fault permeabilities vertically of 50 mD are sufficient to form temperature anomalies of up to 50°C but the formation of a temperature anomaly is dependant on the permeability architecture of the surrounding sediments.

- Surrounding sediment permeability and geometry of the fault outlet zone are more influential on the formation of temperature anomalies than fault permeability itself. The permeability of the outlet zone being critical.

- High vertical permeabilities (100 mD) due to fracturing, in and around fault zones can result in SWA's of up to 50°C.

- Overpressure release is the most likely mechanism responsible for modern temperature anomalies (SWA's).

The modelling carried out within this project affirms the need for computational models in the investigation and understanding of basins. I

believe that this investigation of the thermal regime in the Central Graben, and the influence of fluid flow upon it, highlights the dynamic and complex nature of fluids within the subsurface.

Reference List

Abbots, I.L. (1991) *United Kingdom Oil and Gas Fields 25 Years Commemorative Volume.* Series .United Kingdom Oil and Gas Fields 25 Years Commemorative Volume, The Geological Society, London, 573 pp.

Andrews-Speed, C.P., Oxburgh, E.R. & Cooper, B.A. (1984) Temperatures and depth-dependent heat flow in Western North Sea. *The American Association of Petroleum Geologists*, **68**, 11, 1764-1781.

Barnard, P.C. & Bastow, M.A. (1991) Hydrocarbon generation, migration, alteration, entrapment and mixing in the Central and Northern North Sea. *In:* England, W.A. & Fleet, A.J. (eds) *Petroleum Migration.* The Geological Society, London,

Bethke, C.M. (1985) A numerical model of compaction-driven groundwater flow and heat transfer and its application to the palaeohydrology of intercratonic sedimentary basins. *Journal of Geophysical Research*, **90**, B8, 6817-6828.

Bethke, C.M. (1986) Hydrologic constraints on the genesis of the Upper Mississippi Valley mineral district from Illinois basin brines. *Economic Geology*, **81**, 2, 233-249.

Bethke, C.M. (1989) Modelling subsurface flow in sedimentary basins. *Geologische Rundschau*, **78**, 129-154.

Bjorlykke. (1994) Fluid flow processes and diagenesis in sedimentary basins. *In:* Parnell, J. (eds) *Geofluids: Origin, migration and evolution of fluids in sedimentary basins.* The Geological Society, London,

Black. (1987) Flow and flow mechanisms in crystalline rock. *In:* Williams, J.C.G.a.B.P.J. (eds) *Fluid flow in sedimentary basins and aquifers.* Blackwell Scientific Publications, London,

Brown, D.A. (1987) The flow of water and the displacement of hydrocarbons in fractured chalk reservoirs. *In:* Williams, J.C.G.a.B.P.J. (eds) *Fluid flow in sedimentary basins and aquifers.* Blackwell Scientific Publications, London, 18.

Burrus, J., Kuhfuss, A., Doligez, B. & Ungerer, P. (1991) Are numerical models useful in reconstructing the migration of hydrocarbons? A discussion based on the Viking Graben. *In:* England, W.A. & Fleet, A.J. (eds) *Petroleum Migration.* The Geological Society, London,

Cao, S., Lerche, I. & Hermanrud, C. (1988) Formation temperature estimation by inversion of borehole measurements. *Geophysics*, **53**, 979-988.

Capuano, R.M. (1993) Evidence of fluid flow in microfractures in geopressured shales. *The American Association of Petroleum Geologists Bulletin*, **77**, 8, 1303-1314.

Carstens, H. & Finstad, K.G. (1981) Geothermal gradients of the Northern North Sea basin, 59-62°N. *In:* (eds) *Petroleum geology of the continental shelf of North-West Europe.* London,

Cartwright, J.A. (1994) Episodic basin-wide hydrofracturing of overpressured Early Cenozoic mudrock sequences in the North Sea basin. *Marine and Petroleum Geology*, **11**, 5, 587-607.

Cayley, G.T. (1987) Hydrocarbon migration in the central North Sea, Petroleum Geology of North West Europe, Barbican Centre, London, Graham and Trotman.

Cermák, V. (1979) Heat flow map of Europe. *In:* Rybach, C.a. (eds) *Terrestrial Heat Flow in Europe.* Springer-Verlag, Berlin,

Clauser. (1992) Permeability of crystalline rocks. *Transactions of the American Geophysical Union*, **73**, 21,

Cornford, C. (1993) Hydrocarbon flux efficiences in the Central Graben of the North Sea, Geofluids '93, Torquay, England,

Darby, D., Haszeldine, R.S. & Couples, G.D. (1996a) Central North Sea overpressures: Insights into fluid flow from one- and two-dimensional modelling. *In:* Iliffe, J. & Duppenbecker, S. (eds) *Geological Society Special Publication "Basin modelling".* in press, The Geological Society, London,

Darby, D., Haszeldine, R.S. & Couples, G.D. (1996b) Pressure cells and pressure seals in the central North Sea. *Marine and Petroleum Geology*, in press.

Deming, D, Sass, J.H., Lachenbruch, A.H. & De Rito, R.F. (1992) Heat flow and subsurface temperature as evidence for basin-scale ground-water flow, North Slope of Alaska. *Geological Society of America Bulletin*, **104**, 528-542.

Dewers, T. & Ortoleva, P. (1994) Nonlinear dynamical aspects of deep basin hydrology: Fluid compartment formation and episodic fluid release. *American Journal of Science*, **294**, 713-755.

Evans, T.R. & Coleman, N.C. (1974) North Sea geothermal gradients. *Nature*, **247**, 28-30.

Fertl, W.H. & Wichmann, P.A. (1977) How to determine static BHT from well log data. *World Oil*, **184**, 1, 105-106.

Fowler, A.D. (1994) The role of geopressure zones in the formation of hydrothermal Pb-Zn Mississippi Valley typr mineralization in sedimentary basins. *In:* Parnell, J. (eds) *Geofluids: the origin, migration and evolution of fluids in sedimentary basins.* The Geological Society, 293-300.

Friche, S. & Schlosser, 9. (1980) Probleme der ermittelung von gesteintemperaturen durch Bohloch-messungen in ubertiefen Bohrlochern der DDR. *Z. Angew. Geol.*, 619-623.

Gaarenstroom, L., Tromp, R.A.J, de Jong, M.C. & Brandenburg, A.M. (1992) Overpressures in the Central North Sea: implications for trap integrity and drilling safety, Petroleum Geology of Northwest Europe, Barbican Centre, London, The Geological Society, London.

Garven, G. (1985) The role of regional fluid flow in the genesis of the Pine Point deposit, Western Canada sedimentary basin. *Economic Geology*, **80**, 307-324.

Garven, G. (1989) A hydrogeologic model for the formation of the giant oil sands deposits of the Western Canada sedimentary basin. *American Journal of Science*, **289**, 105-166.

Garven, G. (1995) Continental-scale groundwater flow and geologic processes. *Annual Review Earth and Planetary Science*, **24**, 89-117.

Garven, G. & Freeze, R.A. (1984) Theoretical analysis of the role of groundwater flow in the genesis of stratabound ore deposits. 1.Mathemetical and numerical model. *American Journal of Science*, **284**, 1085-1124.

Glennie, K.W. (1990) Outline of North Sea history and structural framework. *In:* Glennie, K.W. (eds) *Introduction to the petroleum geology of the North Sea.* Blackwell Scientific Publications, London,

Goff, J.C. (1983) Hydrocarben generation and migration from Jurassic source rocks in the E Shetland Basin and Viking Graben of the northern North Sea. *Journal of the Geological Society of London*, **140**, 445-474.

Grauls, D.J. & Baleix, J.M. (1994) Role of overpressures and in-situ stresses in fault-controlled hydrocarbon migration: a case study. *Marine and Petroleum Geology*, **11**, 6, 734-742.

Harms, U., Figgemeier, C., Huenges, E., Kessels, W. & Machon, L. (1993) Recent results of 7 km ultradeep drilling, KTB. Fluids and their pathways in the Variscan basement of Germany, Geofluids '93, Torquay, England,

Harper, M.L. (1971) Approximate geothermal gradients in the North Sea Basin. *Nature*, **230**, 235-236.

Hermanrud, C. (1988) Determination of formation temperature from downhole measurements, Ph.D. Thesis, University of South Carolina.

Hermanrud, C., Cao, S. & Lerche, I. (1990) Estimates of virgin rock temperature derived from BHT measurements: Bias and error. *Geophysics*, **55**, 7, 924-931.

Jessop, A.M. & Majorowicz, J.A. (1994) Fluid flow and heat transfer in sedimentary basins. *In:* Parnell, J. (eds) *Geofluids: Origin, Migration and Evolution of Fluids in Sedimentary Basins.* Special Publication No. 78, The Geological Society, London, 43-54.

Kent. (1975) Review of North Sea basin development. *Quarterly Journal of the Geological Society*, **131**,

Knipe, R.J. (1993) The influence of falult zone processes and diagenesis on fluid flow. *In:* Robinson, A.D.H.a.A.G. (eds) *Diagenesis and Basin Development.* The American Association of Petroleum Geologists, Tulsa, Oklahoma, USA,

Lachenbruch, A.H. & Brewer, M.C. (1959) Dissipation of the temperature effect of drilling a well in Arctic Alaska. *United States Geological Survey Bulletin*, **1083-C**, 73,

Le Carlier, C., Royer, J. & Leticia Flores, E. (1994) Convective heat transfer at the Soultz-sous-Forêts geothermal site: implications for oil potential. *First Break*, **12**, 11, 553-560.

Lovering, T.S. (1936) Heat conduction in dissimilar rock and the use of thermal models. *Bulletin of the Geological Society of America*, **47**, 87-100.

Majorowicz, J.A. & Jessop, A.M. (1981) Present heat flow and a preliminary palaeogeothermal histroy of the Central Prairies Basin, Canada. *Geothermics*, **10**, 81-93.

Miller, T.W. (1995) New insights on natural hydrualic fractures induced by abnormally high pore pressures. *American Association of Petroleum Geologists Bulletin*, **79**, 7, 1005-1018.

Neglia, S. (1979) Migration of fluids in sedimentary basins. *Bulletin of the American Association of Petroleum Geologists*, **63**, 573-597.

Oxburgh, E.R. & Andrews-Speed, C.P. (1981) Temperature, thermal gradients and heat flow in the southwestern North Sea. In: Illing, L.V. & Hobson, G.D. (eds.) *Petroleum Geology of the Continental Shelf of North-West Europe*. Institute of Petroleum, London.

Person, M. & Garven, G. (1989) Hydrologic constraints on the thermal evolution of the Rhine Graben. *In:* Beck, A.E., Garven, G. & Stegna, L. (eds) *Hydrogeological regimes and their subsurface thermal effects.* American Geophysical Union, Washington, D.C.,

Person, M. A. (1990) Hydrologic constraints on the thermal evolution of continental rift basins: Implications for petroleum maturation, Ph.D. Thesis, Johns Hopkins University, Baltimore.

Petersen, K. & Lerche, I. (1996) Self-consistent quantitative modelling of the dynamic evolution of salt and sediments: an example from the Norwegian-Danish Basin. *First Break*, **14**, 1, 19-28.

Raffensberger, J.P. & Garven, G. (1995) The formation of unconformity-type uranium ore deposits 1. Coupled groundwater and heat transport mechanisms. *American Journal of Science*, **295**, 581-636.

Rey, Del & Hamza. (1989) Terrestrial heat flow variations in the north-eastern part of the State of Sao Paulo: a case for transport of geothermal heat by interfracture Fluid Flows. *In:* A.E. Beck, G.G.a.L.S. (eds) *Hydrogeological regimes and their subsurface thermal effects.* Geophysical Monograph 47, American Geophysical Union, Washington DC,

Sclater, J.G. & Christie, P.A.F. (1980) Continental stretching: an explanation of the post-mid-Cretaceous subsidence of the central North Sea basin. *Journal of Geophysical Research*, **85**, 3711-3739.

Sibson, R.H. (1994) Crustal stress, faulting and fluid flow. *In:* Parnell, J. (eds) *Geofluids: the origin, migration and evolution of fluids in sedimentary basins.* The Geological Society, 69-84.

Sibson, R.H., Moore, J.McM. & Rankin, A.H. (1975) Seismic pumping - a hydrothermal fluid transport mechanism. *Journal of the Geological Society of London*, **131**, 653-659.

Smith & Chapman. (1983) Thermal effects of groundwater flow. *Journal of Geophysical Research*, **88**, 593-608.

Thomas, B.M., Møller-Pedersen, P., Whitaker, M.F. & Shaw, N.D. (1985) Organic facies and hydrocarbon distributions in the Norwegian North Sea. *In:* Thomas, B.M. (eds) *Petroleum Geochemistry in Exploration of the Norwegian Shelf.* Graham & Trotman, 3-26.

Tóth, J. (1980) Cross-formational gravity-flow of groundwater: a mechanism of the transport and accumulation of petroleum (the generalised theory of petroleum migration). *In:* Cordell, R.J. & Roberts, W.H. (eds) *Problems of petroleum migration:.* Studies in Geology No.10, American Association of Petroleum Geologists, 121-167.

Tóth, J., Maccagno, M.D., Otto, C.J. & Rostron, B.J. (1991) Generation and migration of petroleum from abnormally pressured fluid compartments: discussion. *American Association of Petroleum Geologists Bulletin*, **75**, 331-335.

Trewin & Bramwell. (1991) The Auk Field, block 30/16, UK North Sea. *In:* Abbots, I. (eds) *United Kingdom oil and gas fields 25 years commemorative volume.* The Geological Society, London, 227-236.

Ungerer, P., Burrus, J., Doligez, B., Chénet, P.Y. & Bessis, F. (1990) Basin evaluation by integrated two-dimensional modeling of heat transfer, fluid flow, hydrocarbon generation, and migration. *The American Association of Petroleum Geologists Bulletin*, **74**, 3, 309-335.

Wilkinson, M., Crowley, S.F. & Marshall, J.D. (1992) Model for the evolution of oxygen isotope ratios in the pore fluids of mudrocks during burial. *Marine and Petroleum Geology*, **9**, 1, 98-105.

Willett, S.D. & Chapman, D.S. (1989) Temperatures, fluid flow and heat transfer mechanisms in the Unita basin. *In:* Beck, A.E., Garven, G. & Stegna, L. (eds) *Hydrogeological regimes and their subsurface thermal effects.* American Geophysical Union, 29-34.

Yu, Z., Thomsen, O. & Lerche, I. (1995) Crystalline basement focusing of heat versus fluid flow/compaction effects: a case study of the I-1 well in the Danish North Sea. *Petroleum Geoscience*, **1**, 31-35.

Ziegler. (1978) North-Western Europe: Tectonics and basin development. *Geologie en Mijnbouw*, **57**, 4, 589-626.

Ziegler, P.A. (1982) *Geological Atlas of western and central Europe.* Shell International Petroleum Maatschappij B.V. and Elsevier, Amsterdam, 130 pp.

APPENDIX 1

Depth (m)	Temp. (°C)	Well No.
1232.9	66.7	29/23-1
2123.0	83.9	
3748.2	117.2	
1338.4	47.8	29/24-1
1440.5	50.6	
2325.7	83.3	
1203.1	36.1	29/25-1
2245.5	74.4	
3001.7	113.9	
3162.6	113.3	
1502.4	56.7	30/16-5
2742.6	106.1	
2750.2	105.0	
1822.1	68.9	30/17-8
3487.3	142.2	
3970.4	152.2	
4080.7	151.1	
4171.5	166.1	
4284.6	156.7	
491.04	35.0	30/17-7
1889.2	71.7	
3699.1	127.8	
3952.1	147.2	
1711.8	78.3	30/12-3
3764.6	143.3	
4182.2	170.6	
4883.0	192.8	
3226.7	122.2	30/12-2
3631.7	137.2	
4062.4	151.7	
4270.0	155.6	
4276.4	161.7	
4706.8	165.0	
4861.6	177.2	

3080.7	116.7	30/13-2
3636.0	117.8	
3878.6	127.8	
4277.0	173.9	
1783.7	62.8	30/13-1
2974.6	123.3	
3745.1	144.4	
4170.9	160.6	
1196.7	42.8	N1/5-2
3013.6	122.8	
3943.9	156.1	
4257.2	170.6	
1987.6	87.8	30/8-1
3644.5	145.0	
4419.3	167.2	
4685.7	183.3	
3252.3	131.7	N1/6-4
3775.0	147.8	
1160.4	38.9	N1/3-5
2435.1	80.6	
4103.0	146.1	
4349.9	163.9	
4359.9	167.8	
4675.1	172.8	
4769.9	189.4	
4779.0	181.7	
4815.0	183.3	
1409.7	52.8	N1/3-1
1509.1	53.9	
2966.0	102.8	
3102.6	123.3	
3743.3	160.6	
4563.5	151.7	
4841.8	186.1	
748.00	29.4	N1/3-4
1570.0	55.0	
2257.0	76.1	
2599.0	115.0	
2858.0	131.6	
3173.0	153.8	

1494.1	49.4	N1/3-2
1503.6	54.4	
3185.8	107.2	
3188.9	110.0	
3224.2	115.0	
3754.6	142.8	
4270.6	161.7	
717.00	36.1	N2/1-7
2452.0	95.5	
3839.0	128.8	
4252.0	163.3	
5039.0	178.3	
5160.0	183.8	
4299.0	169.4	N1/3-3
4327.0	170.5	
4849.0	182.7	
604.00	18.9	N2/1-4
1980.0	75.5	
3772.0	131.6	
4171.0	151.7	
4487.0	170.0	
609.90	23.3	N2/1-6
1990.9	77.2	
4096.0	140.0	
4557.0	172.7	
596.70	33.3	N2/1-8
1966.8	79.4	
3849.9	138.3	
4112.9	158.3	
527.60	48.9	2/1-3
1795.0	61.7	
3565.0	130.6	
3894.0	152.8	
3910.0	151.1	
4191.0	162.7	
4240.0	163.8	
474.00	46.1	2/1-2
2207.0	82.8	
3116.0	115.5	
3257.0	137.2	
3527.0	126.6	
3529.0	134.0	

2104.4	86.7	8/10-1
3012.1	118.3	
3063.9	122.2	
690.08	28.9	2/2-2
1940.4	78.9	
2543.0	105.0	
3098.9	100.0	
2779.2	107.2	8/10-2
2972.4	103.3	
2755.1	92.2	8/11-1
2755.7	93.9	
3771.3	125.6	
1079.0	38.3	8/12-1
1846.5	73.9	
1875.5	73.3	
2510.4	98.3	
2651.2	98.9	
2839.6	106.7	
473.06	25.6	10/5-1
1210.1	53.3	
1818.2	60.6	

APPENDIX 2

Temperature versus depth plots of individual wells listed in Appendix 1. The calculated temperature gradient (with an assigned surface temperature of 10°C) for each well is also shown.

29/23-1

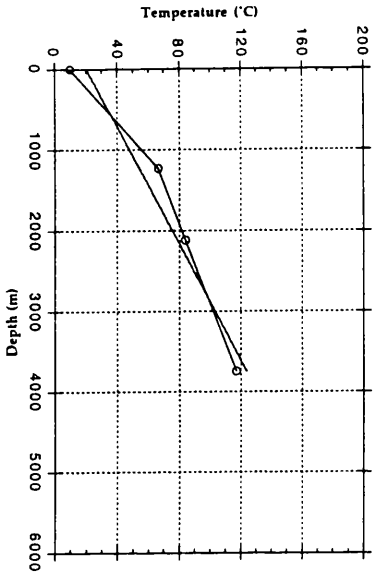

29/24-1

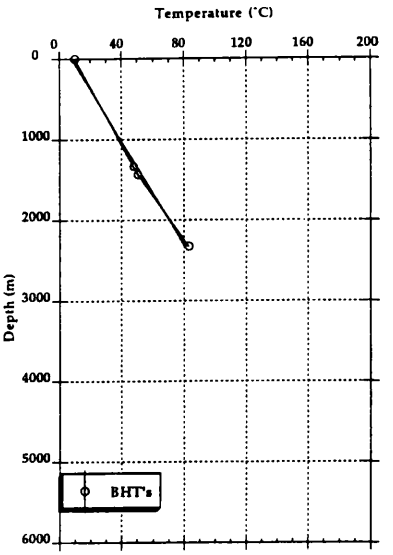

29/25-1

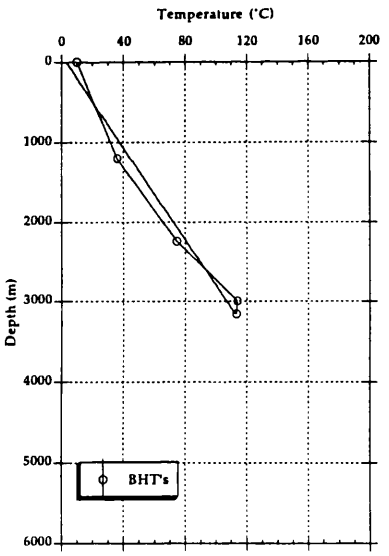

30/16-5

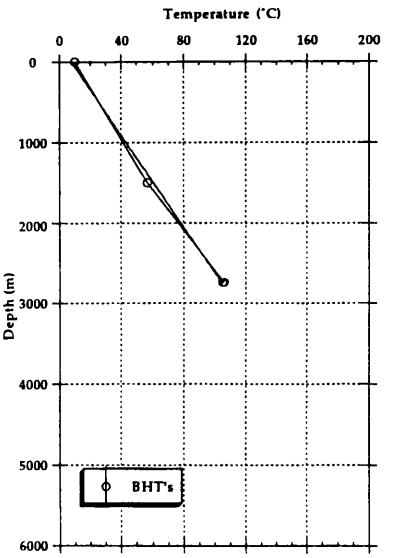

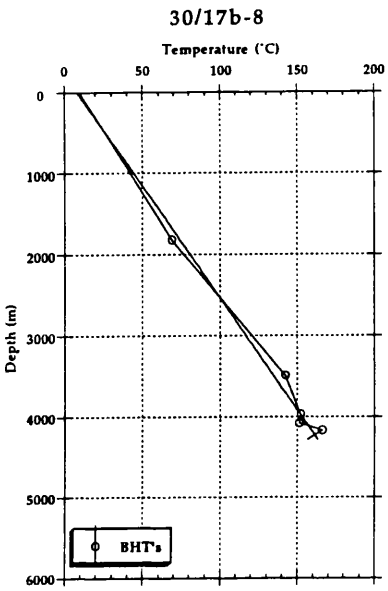
30/17b-8
Temperature (°C)
0
50
100
150
200
Depth (m)
1000
2000
3000
4000
5000
6000
BHT's

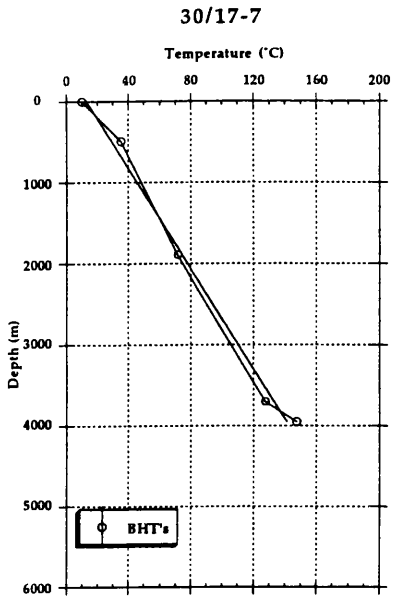
30/17-7
Temperature (°C)
0
40
80
120
160
200
Depth (m)
1000
2000
3000
4000
5000
6000
BHT's

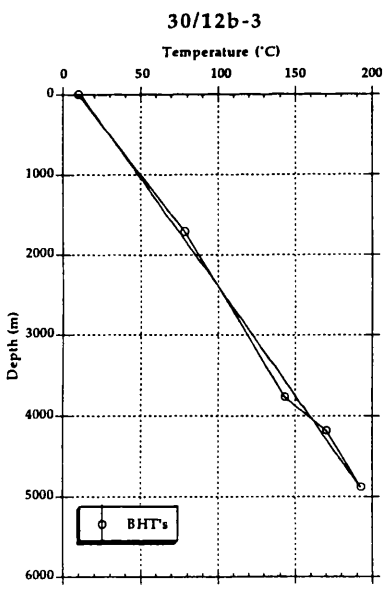
30/12b-3
Temperature (°C)
0
50
100
150
200
Depth (m)
1000
2000
3000
4000
5000
6000
BHT's

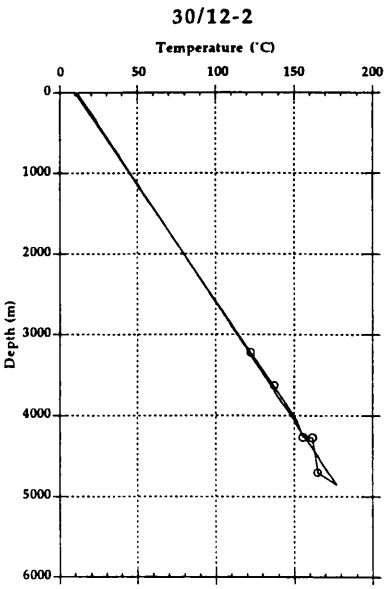
30/12-2
Temperature (°C)
0
50
100
150
200
Depth (m)
1000
2000
3000
4000
5000
6000

30/13-2

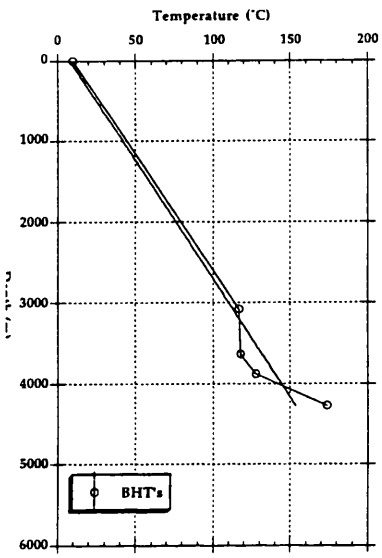

30/13-1

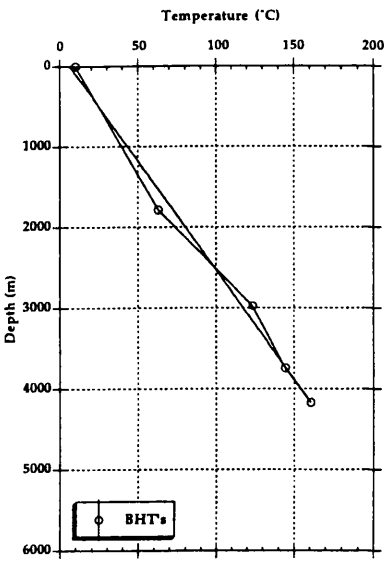

1/5-2

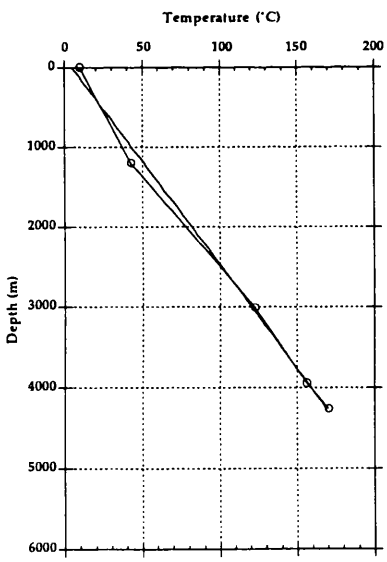

30/8-1

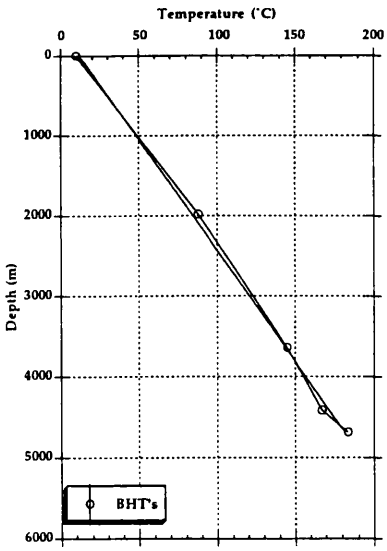

1/6-4

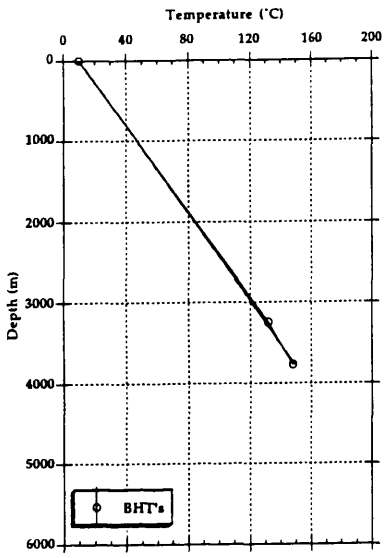

1/3-5

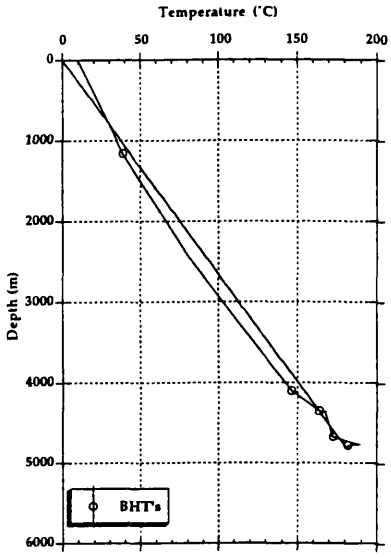

1/3-1

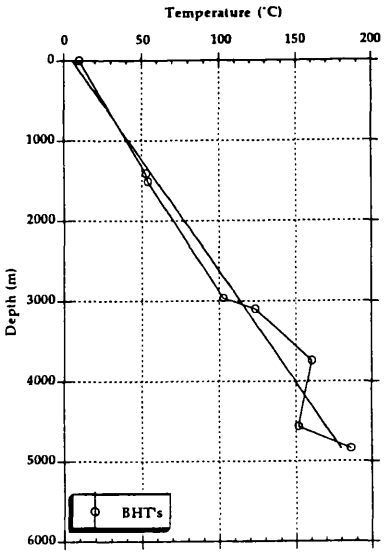

1/3-4

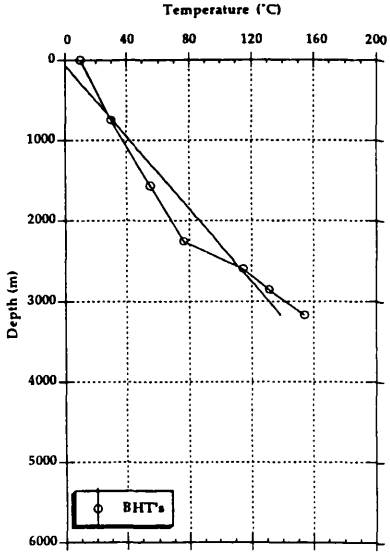

1/3-2

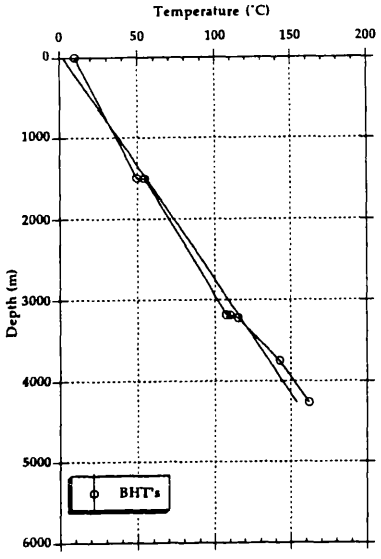

2/1-7

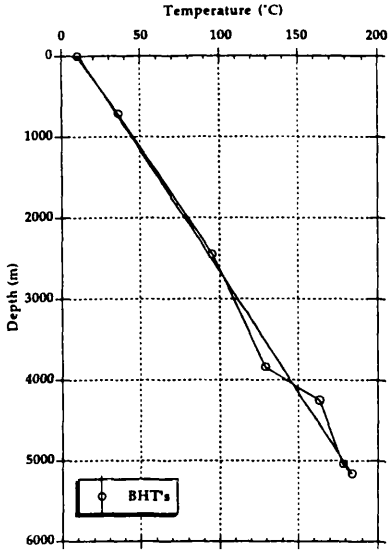

1/3-3

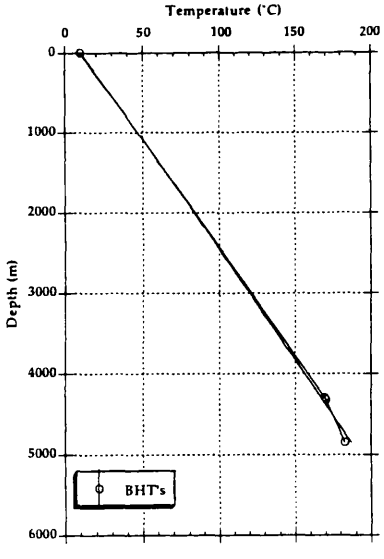

2/1-4

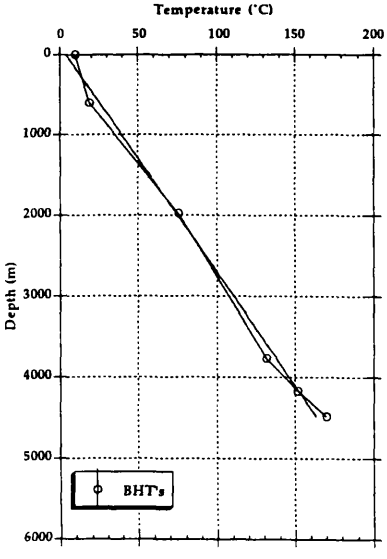

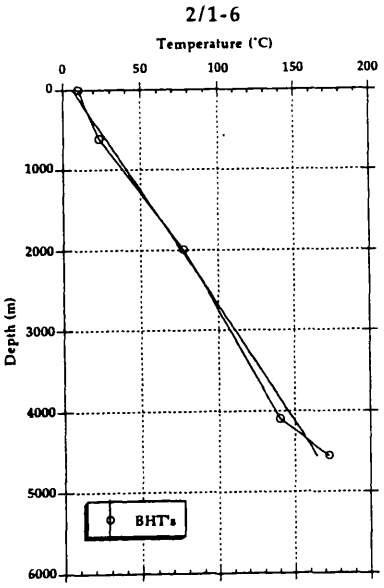
2/1-6
Temperature (°C)
0
50
100
150
200
Depth (m)
0
1000
2000
3000
4000
5000
6000
BHT's

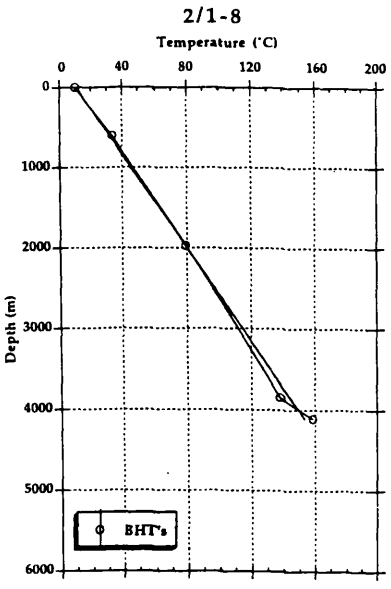
2/1-8
Temperature (°C)
0
40
80
120
160
200
Depth (m)
0
1000
2000
3000
4000
5000
6000
BHT's

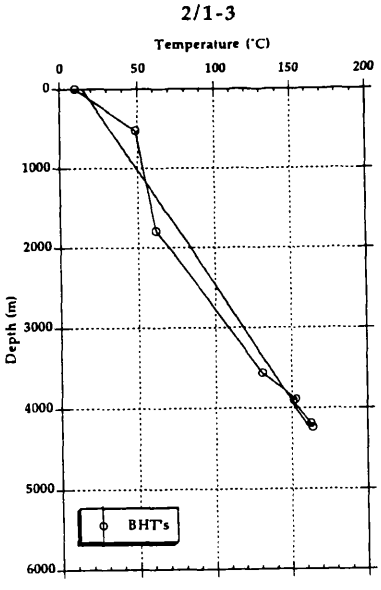
2/1-3
Temperature (°C)
0
50
100
150
200
Depth (m)
0
1000
2000
3000
4000
5000
6000
BHT's

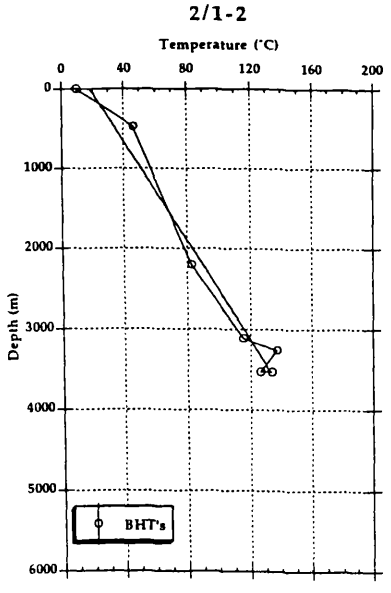
2/1-2
Temperature (°C)
0
40
80
120
160
200
Depth (m)
0
1000
2000
3000
4000
5000
6000
BHT's

8/10-1

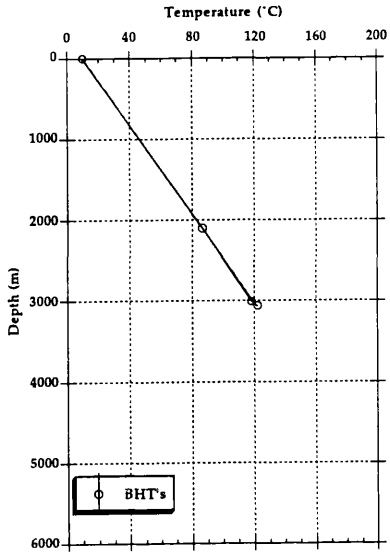

2/2-2

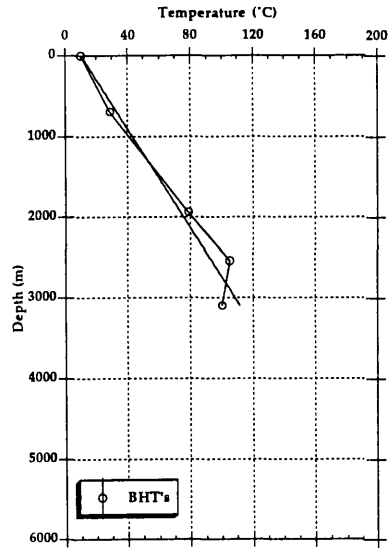

8/10-2

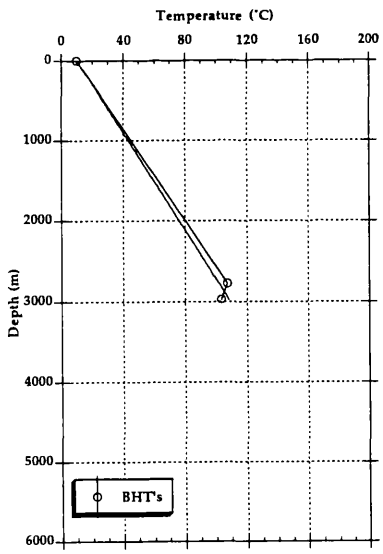

8/11-1